A HYBRID-PARALLEL FRAMEWORK FOR THE NONLINEAR SEISMIC ANALYSIS OF VERY TALL BUILDINGS

Thesis by

Abel Bermie R. Dizon

In Partial Fulfillment of the Requirements

for the Degree of

Doctor of Philosophy

California Institute of Technology

Pasadena, California

2016

(Defended December 1, 2015)

To

Jesus

My wife

My little one

Acknowledgements

I am very blessed to have Dr. John Hall as my advisor. I have learned so much through my conversations with him. He is encouraging, wise, and patient—qualities I want to emulate. His clear and logical way of thinking is something I hope to practice throughout my career. I thank Dr. Swaminathan Krishnan for giving me the opportunity to pursue this Ph.D. and for teaching me FRAME3D. His guidance through my first two years at Caltech was indispensable. And I thank Dr. Thomas Sabol from UCLA for being the first to believe in me as a civil engineer, even while I was a freshman in college. I thank the members of my candidacy and thesis defense committees: Dr. Domniki Asimaki, Dr. James Beck, Dr. Thomas Heaton, and Dr. Dennis Kochmann. Their insights are a great help to this work.

I wish to acknowledge my fellow graduate students, many who helped me through candidacy and my thesis work. In particular, I thank Pablo Guerrero who studied with me often during my first year at Caltech. I thank Anthony Massari for conversations regarding building design and structural engineering in general. It was nice having a Professional Engineer as a fellow classmate who was willing to help me out as much as he did. I also thank Kenny Buyco for his help in the final defense preparations.

I am proud to have had the opportunity to study at Caltech, which I consider to have one of the best learning environments in the world. I am grateful for the financial support, specifically from the Harold Hellwig Foundation and the George Housner Fellowship. I thank the administrative staff in the Mechanical and Civil Engineering Department for all their work.

I thank my church communities, NewLife Fellowship and Grace Communion International Los Angeles, for their prayers, encouragement, and moral support. I especially thank Dr. Michael Morrison for proofreading this manuscript.

I want to honor my parents Bermie and Carmelita Dizon, who are wonderful Christ-like role models and who encouraged me to pursue education. I wouldn't be the man I am today if it wasn't for them. I thank my siblings (and their families) Ben Dizon and Carmel Benavides, who grew to accept my quirkiness. I am especially glad to have a brother, David Dizon, who shares my interest in engineering. I thank the Ronquillos, my wife's family, who welcomed me as a son and brother.

I am very lucky to be married to the love of my life, Ana Dizon. Regarding this manuscript, I appreciate her help in preparing it. But more importantly, I am grateful that we are able to share our life-long dreams together. She inspires me to be the best version of myself, and the last few years would not have been the same without her constant loving support.

I hope that this work is an inspiration for my future children (such as the little one on the way), who are already in our hearts and thoughts. I pray that their dreams will come true, just as my dreams have and continue to come true.

Most of all, I am eternally grateful to my Lord and Savior, Jesus. His guidance through this life's journey is priceless.

Abstract

FRAME3D, a program for the nonlinear seismic analysis of steel structures, has previously been used to study the collapse mechanisms of steel buildings up to 20 stories tall. The present thesis is inspired by the need to conduct similar analysis for much taller structures. It improves FRAME3D in two primary ways.

First, FRAME3D is revised to address specific nonlinear situations involving large displacement/rotation increments, the backup-subdivide algorithm, element failure, and extremely narrow joint hysteresis. The revisions result in superior convergence capabilities when modeling earthquake-induced collapse. The material model of a steel fiber is also modified to allow for post-rupture compressive strength.

Second, a parallel FRAME3D (PFRAME3D) is developed. The serial code is optimized and then parallelized. A distributed-memory divide-and-conquer approach is used for both the global direct solver and element-state updates. The result is an implicit finite-element hybrid-parallel program that takes advantage of the narrow-band nature of very tall buildings and uses nearest-neighbor-only communication patterns.

Using three structures of varied sized, PFRAME3D is shown to compute reproducible results that agree with that of the optimized 1-core version (displacement time-history response root-mean-squared errors are $\sim 10^{-5}$ m) with much less wall time (e.g., a dynamic time-history collapse simulation of a 60-story building is computed in 5.69 hrs with 128 cores—a speedup of 14.7 vs. the optimized 1-core version). The maximum speedups attained are shown to increase with building height (as the total

number of cores used also increases), and the parallel framework can be expected to be suitable for buildings taller than the ones presented here.

PFRAME3D is used to analyze a hypothetical 60-story steel moment-frame tube building (fundamental period of 6.16 sec) designed according to the 1994 Uniform Building Code. Dynamic pushover and time-history analyses are conducted. Multi-story shear-band collapse mechanisms are observed around mid-height of the building. The use of closely-spaced columns and deep beams is found to contribute to the building's "somewhat brittle" behavior (ductility ratio ~2.0). Overall building strength is observed to be sensitive to whether a model is fracture-capable.

Table of Contents

List of Figures

List of Tables

Chapter 1

Introduction

1.1 General

The structural engineering discipline has greatly been aided by the rise of structural analysis programs. Today, many such programs like SAP2000, ETABS, RAM, PERFORM-3D, OpenSees, and LS-DYNA are used by industry and research groups to solve complex problems. Yet computational challenges limit the capabilities of even the most popular software packages.

In the past two decades, the California Institute of Technology (Caltech) has developed FRAME, a program for the nonlinear analysis of steel structures subjected to

ground motion. FRAME2D and 3D are capable of simulating building response well up to the point of collapse. They do this by automatically including in their algorithm formulations that address the challenges that some programs approach in an ad-hoc manner, challenges like geometric nonlinearity, robust convergence schemes, weld fracturing, and material models that match experimental data over many loading cycles.

1.2 Literature review

Of the many structural programs available, PERFORM-3D (CSi 2011) and OpenSees (Mazzoni et al. 2009) are two of the most widely used programs for highly nonlinear structural analysis.

PERFORM-3D is a commercial finite-element program, generally considered the industry standard. It has a large user base among practicing professionals and is suitable for deformation-based design. Although P-Δ effects are considered, true large-displacement analysis requires that equilibrium be taken at the structure's deformed position, which is not done in PERFORM-3D. Material models are approximated using a five-line backbone curve, and hysteresis follows these lines. In a study (Bjornsson and Krishnan 2014) comparing FRAME3D and PERFORM-3D, PERFORM-3D frame elements were found to deviate from experimental data sooner (fewer loading cycles) than FRAME3D frame elements. PERFORM-3D also had more difficulty capturing the slow degradation of structures than FRAME3D.

OpenSees is an open-source finite-element program intended for both structural and geotechnical analysis. Because of its modular design, it has a large element library and is versatile. This also means that a user determines the level of nonlinearity intended, the solution algorithms, etc. specific for their project. Features like panel zones, geometric nonlinearity, large-displacement effects, and strength degradation can be included. The material models in its database are similar to that of PERFORM-3D, in that they are based on backbone curves composed of line segments. Although no comparison study between OpenSees and FRAME3D has been conducted, FRAME3D uses a more realistic steel backbone and hysteretic material model, and the above features (e.g., panel zones, geometric nonlinearity, etc.) are automatically included for the context of steel frame buildings.

The FRAME program is the starting point of the current research. A brief history of FRAME is presented in the remainder of this section. Recounted are the works of Caltech professor John Hall and some of his Ph.D. students since the 1990s.

In 1992, Challa completed his thesis, "Nonlinear seismic behavior of steel planar moment-resisting frames" (Challa 1992). Before this work, the behavior of steel under cyclic loading was well known from extensive experimental data (e.g., Kent 1969; Popov and Petersson 1978). Yet few structural analysis programs captured the nonlinear behavior well over several loading cycles. Challa proposed two computational beam-column element models: (1), the plastic-hinge element, a simple model, and (2), the fiber element, a comprehensive model. The plastic-hinge element behaves elastically between two nodes and is allowed to hinge plastically when end moments exceed a yield value. It accounts for strain hardening approximately by including an elastic rotational spring after

hinging occurs. The more robust fiber element is discretized transversely into subelements (i.e., segments), where each segment is discretized longitudinally into fibers. Each fiber follows the backbone curve and hysteretic rules of a steel bar under uniaxial stress, based on experimental data (Kent 1969; Popov and Petersson 1978). The joints of the frames have finite size and match the experimental shear stress-strain curves well (Tsai and Popov 1988). Additionally, Newmark's method (Newmark 1959) was used to solve the incremental equations of motion (§2.2). The result of this work was the NDA2 program, a precursor to FRAME2D.

Hall and Challa developed and published the formulation of FRAME2D (Hall and Challa 1995). The 1994 Northridge earthquake revealed a flaw in pre-Northridge moment-resisting buildings: welds fractured below design levels. Thus, the fiber formulation was updated to simulate weld fractures (Hall 1995; Hall 1998).

In the first efforts to extend FRAME2D to three dimensions, Carlson and Hall developed a 3D fiber discretization of columns and a 3D joint (Carlson and Hall 1997). Carlson also developed 3D constraint equations that represent the effect of rigid diaphragms, so that a 3D building can be studied using planar frames. The work resulted in the ANDERS program and Carlson's thesis "Three dimensional nonlinear inelastic analysis of steel moment-frame buildings damaged by earthquake excitations" (Carlson 1999). Carlson compared fracture-incapable models with fracture-capable models and found little correlation between their behaviors, which suggests that for large motions, fracture-incapable models would be insufficient. ANDERS, however, was not "fully 3D"; it neglected some 3D effects such as the biaxial bending of non-corner columns.

Krishnan reformulated FRAME2D into FRAME3D, fully accounting for 3D effects. He examined irregularly shaped buildings, those with a center of mass and rigidity that do not coincide, and observed that torsional demand can be significant. He documented the 3D transition in his thesis "Three dimensional nonlinear analysis of tall irregular steel buildings subject to strong ground motion" (Krishnan 2003). A 3D analog replaced every 2D element. For example, 3D plastic-hinge elements can hinge in two orthogonal directions. 3D fiber segments are discretized to account for biaxial bending. For computational efficiency, Krishnan introduced the three-segment elastofiber element, which was calibrated to replace the fiber element. The descriptions and formulations of the 3D plastic-hinge and three-segment elastofiber elements can be found in §2.3 and §2.4, respectively.

In 2009, Krishnan added the five-segment elastofiber element to FRAME3D's element library to efficiently capture geometric nonlinearities and buckling. A description and formulation of the five-segment elastofiber element can be found in §2.5.

1.3 Objectives of the present study

Since the 1990s, FRAME2D and FRAME3D have contributed to the structural engineering community's knowledge of steel frame buildings up to 20 stories, their response in strong earthquakes, and their collapse mechanisms. The primary goal of the current thesis is to extend the capability of FRAME3D to steel buildings much taller than 20 stories. It is achieved with the following intermediate objectives:

- Review the existing formulation of FRAME3D. It is important to understand how the program works before improving it.
- Propose revisions to the formulation of FRAME3D. The goal of these revisions is to improve the program's ability to handle highly nonlinear situations, such as building collapse, and improve the realism of the steel material model.
- Develop a computationally efficient, parallel FRAME3D. FRAME3D's nonlinear formulation is complex and detailed enough that for systems larger than 20 stories, a sequential dynamic time-history collapse simulation may take days or weeks complete. This thesis aims to significantly reduce the computation times of tall-building simulations.
- Develop and study an example 60-story steel building. The primary purpose of this example is to showcase PFRAME3D's computational performance. A secondary purpose is to analyze the 60-story building's nonlinear behavior and collapse mechanisms. (The secondary purpose will be achieved with greater detail in future work.)

1.4 Outline of thesis

This thesis consists of three parts.

Part I presents a review of and the revisions to FRAME3D's formulations. Chapter 2 reviews the FRAME3D formulation. It covers the global equations of motion and the

element contributions to the equations. Chapter 3 presents revisions to the FRAME3D formulation, including their effect on improving the robustness of the program.

Part II focuses on the development of the parallel version of FRAME3D. Chapter 4 provides a general orientation to parallel computing. Chapter 5 discusses the direct solver. Several algorithms are considered and a divide-and-conquer solver is chosen for PFRAME3D. Chapter 6 covers domain decomposition and parallel updating. Chapter 7 demonstrates that PFRAME3D produces nearly identical results as FRAME3D in significantly less time.

Part III covers the application of PFRAME3D to a 60-story example building. Chapter 8 explains the design considerations according to pre-Northridge (UBC 94) provisions, the modeling considerations for creating the PFRAME3D model, and the results of dynamic pushover and dynamic time history analysis. Finally, Chapter 9 is the conclusion of this report and presents future directions.

PART I

FRAME3D Reviewed and Revised

Chapter 2

A Review of the

FRAME3D Formulation

2.1 General

A structural finite element program works by defining a set of elements connected at nodes, and then solving equations of equilibrium that describe how those elements respond to external input generally applied at the nodes. For a 2D model, the elements lie on a plane; for a 3D model, they lie in 3D space. The equations of equilibrium depend on many variables—such as element properties, model geometry, boundary conditions—and

for dynamic problems, mass, damping, and initial conditions, too. A review of FRAME3D's equations is the focus of this chapter.

The discussion here begins with the global equation of motion (§2.2) and ends with how each type of element contributes to the global equation (§§2.3 – 2.8).

The element library consists of:

- the plastic-hinge element (§2.3)
- the three-segment elastofiber element (§2.4)
- the five-segment elastofiber element (§2.5)
- the panel-zone element (§2.6)
- the four-noded diaphragm element (§2.7)
- the translational/rotational spring element (§2.8).

An example arrangement of these elements (except the spring) is shown in Figure 2.1 to provide context. Three right-handed orthogonal coordinate systems are used: (1) the global XYZ system, where X and Y are horizontal and Z is vertical; (2) the panel-zone $\bar{X}\bar{Y}\bar{Z}$ system, where $\bar{X}$, $\bar{Y}$, and $\bar{Z}$ are initially defined to match the longitudinal, major, and minor axes, respectively, of the panel zone's "associated column" (typically the column immediately beneath the panel zone); and, (3) the beam segment/element $X'Y'Z'$ system, where X', Y', and Z' are the longitudinal, major, and minor axes, respectively, of the beam segment/element chord. The coordinate systems, elements, and nodes are further explained in §2.2 – 2.8. In-depth explanations can be found in Krishnan (2003), Krishnan and Hall (2006a, 2006b), and Krishnan (2009a).

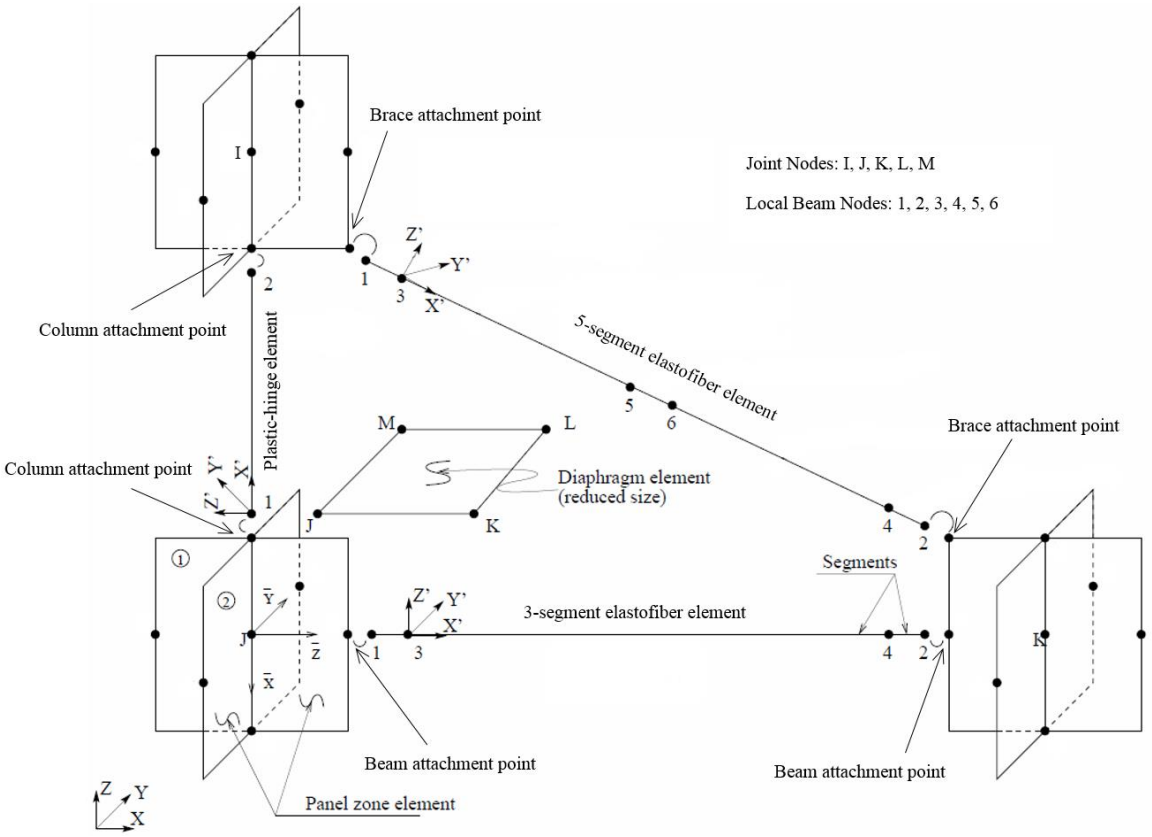

Figure 2.1: Example element arrangement in FRAME3D, showing plastic-hinge, three-segment elastofiber, five-segment elastofiber, panel-zone, and diaphragm elements, with global nodes, local nodes, attachment points, and coordinate systems (Krishnan 2009a, edited).

2.2 Global solution

The dynamic solution of FRAME3D is based on the matrix equation (Cook et al. 1989):

$$[M]\{\ddot{U}(t)\} + [C]\{\dot{U}(t)\} + \{R(t)\} = \{f_g\} - [M][r]\{\ddot{U}_g(t)\} \qquad \text{(Eq. 2.1)}$$

where $\{\ddot{U}(t)\}$ and $\{\dot{U}(t)\}$ are vectors of global accelerations and velocities, respectively, over time ($\{U(t)\}$, not shown in Eq. 2.1, is a vector of global displacements); $[M]$ is the

mass matrix, diagonal because masses are lumped at global nodes; $[C]$ is the Rayleigh damping matrix: $[C] = a_0[M] + a_1[K]$, where $[K]$ is the initial elastic stiffness matrix and a_0 & a_1 are Rayleigh damping parameters; $\{R(t)\}$ is the vector of nonlinear stiffness forces (i.e., internal or restoring forces); $\{f_g\}$ is the static external force vector, typically of gravity forces; $\{\ddot{U}_g(t)\}$ is the three-component (global X, Y, and Z) input ground motion vector; and $[r]$ is the participation matrix (so that $\{\ddot{U}_g(t)\}$ can be applied as inertial forces through $[M]$).

In 3D, $\{U(t)\}$, $\{\dot{U}(t)\}$, $\{\ddot{U}(t)\}$, $\{R(t)\}$, etc. have 6 to 8 degrees of freedom (DOFs) per node. At each node, DOFs 1 – 3 are translations in global X, Y, and Z directions (Figure 2.1). DOF 4 is the rigid body rotation of the panel-zone element about the $\bar{X}$ axis (Figure 2.1). DOFs 5 – 8 define the deformations of the 2 orthogonal panel zones; each panel zone can deform in 2 modes (Figure 2.2). When one or both panel zones are absent or rigid, DOFs 5 – 6 and DOFs 7 – 8 consolidate to define up to 2 rigid body rotations, i.e., the node has 6 or 7 DOFs instead of 8. It should be noted that the global rotational DOFs are not about the fixed global axes XYZ, but rather are defined by the panel-zone $\bar{X}\bar{Y}\bar{Z}$ system.

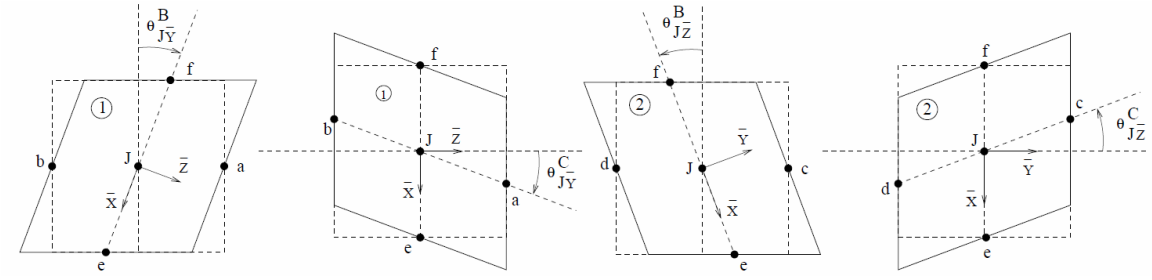

Figure 2.2: Global DOFs 5 – 8 based on deformations of panel zones (Krishnan 2009a).

Discretizing time (Δt), applying constant average acceleration, and recognizing that a time step often cannot be completed in a single iteration, Eq. 2.1 at global iteration l of time step t becomes

$$\left[\frac{4}{(\Delta t)^2}M + \frac{2}{\Delta t}C + K_T^l\right]\{\Delta U\} = \{f_g\} - \{R^l\} - [M][r]\{\ddot{U}_g(t)\} \qquad \text{(Eq. 2.2)}$$
$$+[M]\left\{\frac{4}{(\Delta t)^2}U(t) + \frac{4}{\Delta t}\dot{U}(t) + \ddot{U}(t)\right\}$$
$$+[C]\left\{\frac{2}{\Delta t}U(t) + \dot{U}(t)\right\} - \left[\frac{4}{(\Delta t)^2}M + \frac{2}{\Delta t}C\right]\{U^l\}$$

where $\left[K_T^l\right]$ is the global iterating matrix. Although the subscript T suggests that $[K_T^l]$ is a "tangent stiffness matrix," it includes an elastic term, too; also, the fiber material model may use non-tangent slopes (discussed more in §2.4); and, because analysis is dynamic, whether an element loads or unloads is not necessarily certain at a given global iteration; thus, the true "tangent stiffness matrix" is often not used.

$[K_T^l]$, $\{\Delta U\}$, $\{U^l\}$, and $\{R^l\}$ are updated in every iteration. $\{U(t)\}$, $\{\dot{U}(t)\}$, $\{\ddot{U}(t)\}$, and $\{\ddot{U}_g(t)\}$ are updated at the beginning of every time step. $[M]$, $[C]$, and $\{f_g\}$ are constant throughout the dynamic analysis.

A typical global iteration l follows these steps:

(0) Get the right-hand side (RHS) using iteration $l-1$ or the previous time step. The RHS is known as the force residual, which physically represents the difference between internal and external forces (including dynamic effects) at every DOF at the current global iteration.

(1) Check convergence. The system is considered to be converged if the infinity norm of the RHS is nearly zero, within a tolerance. Physically, a zeroed infinity norm implies dynamic force equilibrium at every node. If the system

converged, proceed to the next time step; the current configuration $\{U^l\}$ is regarded as the solution for the current time step $\{U(t+\Delta t)\}$. If the system did not converge, continue iterating.

(2) Assemble $\left[K_T^l\right]$, the tangent stiffness matrix, based on every element in the structure, and on the nodal configuration at iteration l. Add $\left[K_T^l\right]$ to the constant $\frac{4}{(\Delta t)^2}[M]$ and $\frac{2}{\Delta t}[C]$ terms to get the left-hand side (LHS) matrix $\left[\frac{4}{(\Delta t)^2}M + \frac{2}{\Delta t}C + K_T^l\right]$.

(3) Solve for $\{\Delta U\}$ using the LHS matrix and the RHS. $\{\Delta U\}$ represents the incremental difference between $\{U^l\}$ and $\{U^{l+1}\}$. The solution process has two parts:

   a. Factor the LHS matrix with Cholesky or LDL^T factorization.

   b. Solve the factored system.

   For more details on this step, see §5.

(4) Update the geometry of the system—including element geometric parameters, nodal locations/attachment points, and $\{U^{l+1}\}$. This updated geometry will be used at the next convergence check (step 1 of global iteration $l+1$). Because of this step, geometric nonlinearities and P-Δ effects are automatically included.

(5) Assemble $\{R^{l+1}\}$, the internal force vector, based on every element in the structure, and on the updated $l+1$ geometry. Go to iteration $l+1$.

The primary task at each global iteration is to update $\left[K_T^l\right]$ and $\{R^l\}$, both of which are assembled from finite elements (§§2.3 – 2.8). For each element in the model, a static specified-displacement problem is solved; i.e., given an incremental displacement $\{\Delta U\}$,

element stiffness and internal forces are determined such that static equilibrium is satisfied. The individual element contributions are combined to form $\left[K_T^l\right]$ and $\{R^l\}$. The remainder of this chapter covers, for each element type, the formulations of these "local" calculations.

2.3 Plastic-hinge element

The plastic-hinge (PH) element is a computationally efficient element, useful for preliminary analysis or for modeling secondary elements. Its formulation assumes doubly symmetric cross sections, centroidal axes, uniform cross sections along element length, and no warping restraint. The 12-DOF equation (6 DOFs per node) in incremental form describes the element:

$$\left\{dR'_{ph}\right\}_L = \left[K'_{T,ph}\right]_L \left\{dU'_{ph}\right\}_L \quad \text{(Eq. 2.3)}$$

where $\left\{dR'_{ph}\right\}_L$, $\left[K'_{T,ph}\right]_L$, and $\left\{dU'_{ph}\right\}_L$ are the element's incremental internal force vector, tangent stiffness matrix, and incremental displacement, respectively, in its local $X'Y'Z'$ coordinate system (§2.1; Figure 2.1). The 6 DOFs per node are 3 translational and 3 rotational DOFs, as indicated by the subscript L. Before Eq. 2.3 is solved, the global displacement increments $\{\Delta U_{ph}\}$ (extracted from $\{\Delta U\}$) are transformed to $\left\{\Delta U'_{ph}\right\}_L$ using

$$\left\{\Delta \overline{U}_{ph}\right\} = [T_1]\{\Delta U_{ph}\} \quad \text{(Eq. 2.4)}$$

$$\left\{\Delta \overline{U}_{ph}\right\}_L = [T_2]\{\Delta \overline{U}_{ph}\} \quad \text{(Eq. 2.5)}$$

$$\left\{\Delta U_{ph}\right\}_L = [T_3]\left\{\Delta \overline{U}_{ph}\right\}_L \quad \text{(Eq. 2.6)}$$

$$\{\Delta U'_{ph}\}_L = [T_4]\{\Delta U_{ph}\}_L \qquad \text{(Eq. 2.7)}$$

where $[T_1]$ transforms the global displacement increments from the XYZ to the $\bar{X}\bar{Y}\bar{Z}$ system; $[T_2]$ from the global node (e.g., J & K in Figure 2.1) to the local attachment point (e.g., 1 & 2 in Figure 2.1), which reduces the number of DOFs per node from 6 – 8 to 6 as denoted by the subscript L; $[T_3]$ from the $\bar{X}\bar{Y}\bar{Z}$ system to the XYZ system; and $[T_4]$ from the XYZ system to the $X'Y'Z'$ system. The result of the transformations is $\{dU'_{ph}\}_L$. $\{dR'_{ph}\}_L$ and $[K'_{T,ph}]_L$ are determined from $\{dU'_{ph}\}_L$ using Eq. 2.8 – 2.10, and are transformed back to the 6 – 8 DOFs per node in the global XYZ system.

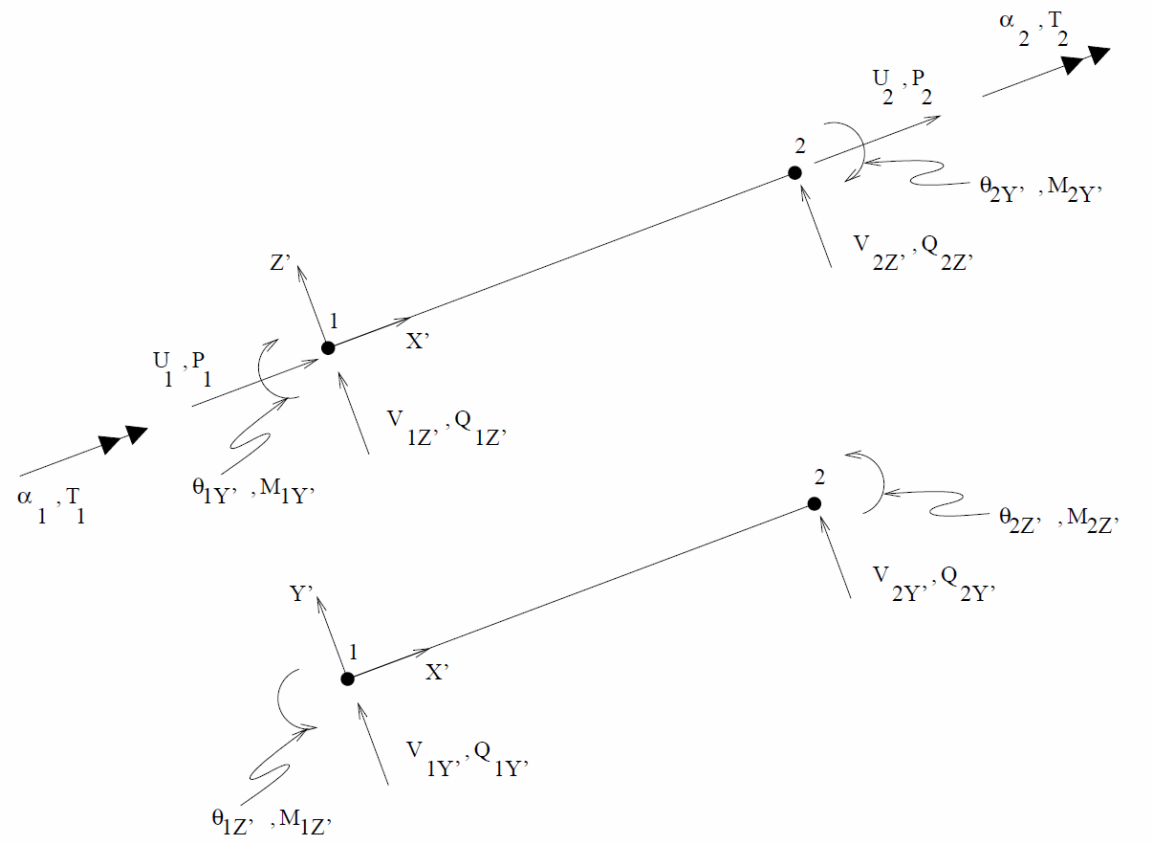

Figure 2.3: Nodal forces/moments and displacements/rotations in local coordinates of a plastic-hinge element (Krishnan 2003).

Each term in $\{dR'_{ph}\}_L$ and $[K'_{T,ph}]_L$ is computed from beam theory, and accounts for axial, flexural, shear, and twisting contributions (Figure 2.3). Axial (P, U) and twisting (T, α) contributions come from:

$$\begin{Bmatrix} dP_1 \\ dP_2 \end{Bmatrix} = \frac{E_T A}{L_0} \begin{bmatrix} 1 & -1 \\ -1 & 1 \end{bmatrix} \begin{Bmatrix} dU_1 \\ dU_2 \end{Bmatrix} \quad \text{(Eq. 2.8)}$$

$$\begin{Bmatrix} dT_1 \\ dT_2 \end{Bmatrix} = \frac{GJ}{L_0} \begin{bmatrix} 1 & -1 \\ -1 & 1 \end{bmatrix} \begin{Bmatrix} d\alpha_1 \\ d\alpha_2 \end{Bmatrix} \quad \text{(Eq. 2.9)}$$

where the subscripts 1 and 2 denote the local element node number; E_T is the tangent Young's modulus as independently computed using axial force only; A is the cross sectional area; L_0 is the original element length; G is the elastic shear modulus; and J is the torsional inertia. E_T is determined by a bilinear material model defined by the elastic modulus E, the yield stress σ_y, and the strain-hardening (i.e., post-yield) modulus E_{sh}, and unloading is elastic. Eq. 2.9 neglects warping restraint. The flexural (M, θ) and shear (Q, V) contributions about the major axis (Y') come from:

$$\begin{Bmatrix} dQ_{1Z'} \\ dM_{1Y'} \\ dQ_{2Z'} \\ dM_{2Y'} \end{Bmatrix} = \left[\begin{bmatrix} \frac{-1}{L_0} & \frac{-1}{L_0} \\ 1 & 0 \\ \frac{1}{L_0} & \frac{1}{L_0} \\ 0 & 1 \end{bmatrix} \begin{bmatrix} a_T & b_T \\ b_T & c_T \end{bmatrix} \begin{bmatrix} \frac{-1}{L_0} & 1 & \frac{1}{L_0} & 0 \\ \frac{-1}{L_0} & 0 & \frac{1}{L_0} & 1 \end{bmatrix} + \frac{P}{L_0} \begin{bmatrix} 1 & 0 & -1 & 0 \\ 0 & 0 & 0 & 0 \\ -1 & 0 & 1 & 0 \\ 0 & 0 & 0 & 0 \end{bmatrix} \right] \begin{Bmatrix} dV_{1Z'} \\ d\theta_{1Y'} \\ dV_{2Z'} \\ d\theta_{2Y'} \end{Bmatrix}$$

(Eq. 2.10)

where a_T, b_T, and c_T depend on E, G, P, major-axis moment of inertia $I_{Y'}$, major-axis effective shear area $A_{SZ'}$ (Figure 2.4), and major-axis plastic-hinge conditions at nodes 1 and 2 (Krishnan 2003; Krishnan and Hall 2006a).

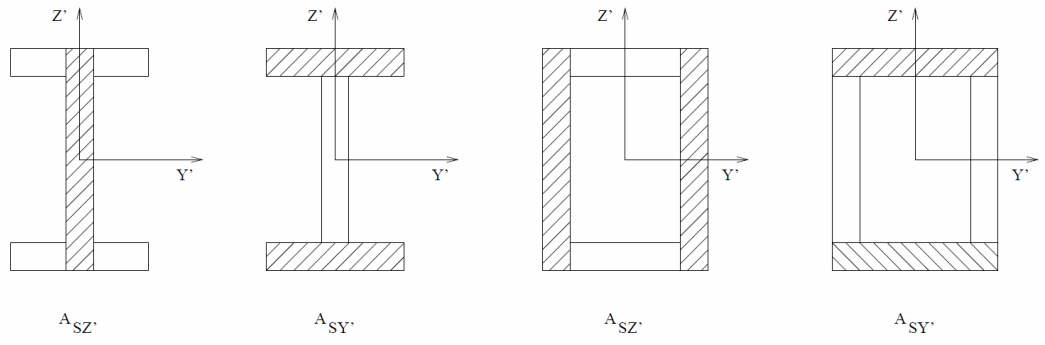

Figure 2.4: Effective shear areas for W-flanged and box sections (Krishnan 2003).

A plastic hinge occurs when the moment at node 1 or 2 exceeds the yield moment $M_{pY'}$ or $M_{pZ'}$ as defined by a P-$M_{pY'}$-$M_{pZ'}$ (PMM) interaction relationship. FRAME3D has two types of interaction curves. The first, shown in Figure 2.5 (top), accounts for the effect of P on the plastic moment capacities, but not the effect of major-axis bending on minor-axis plastic moment capacity and vice versa. The second is a PMM surface, constructed from a user-defined section (Krishnan 2009b); e.g., the PMM interaction relationship for a W6X20 section is shown in Figure 2.5 (bottom). Between nodes, the element is elastic in flexure. Switch Z' and Y' in Eq. 2.10 to get the flexural and shear formulation about the minor axis. The PH element, although efficient, is suited for secondary and pinned elements. To more accurately capture beam behavior for high levels of inelasticity, a more complicated fiber-based element is required.

The next two sections describe the formulation of two fiber-based elements: the three-segment and five-segment elastofiber elements.

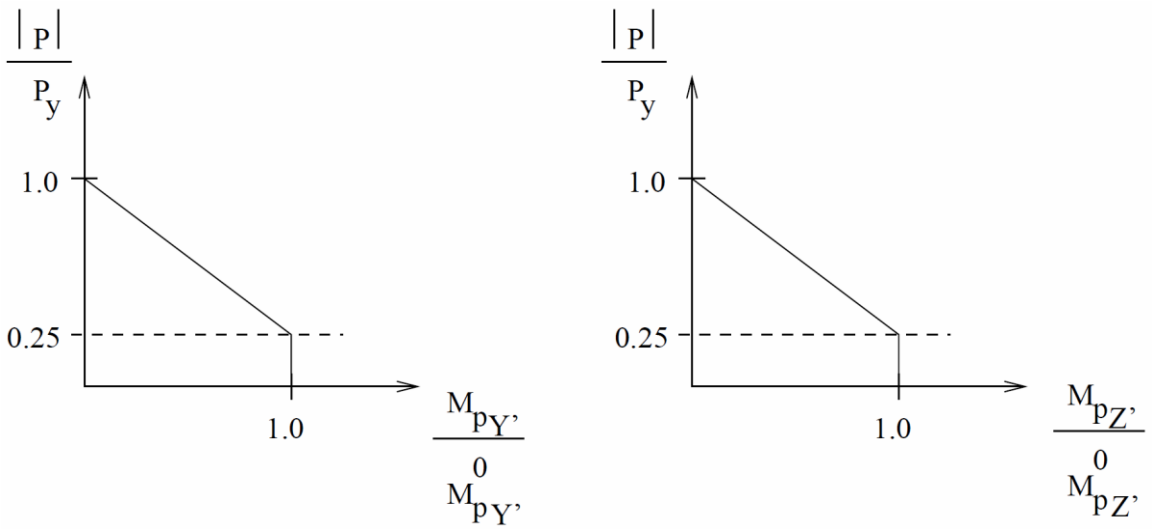

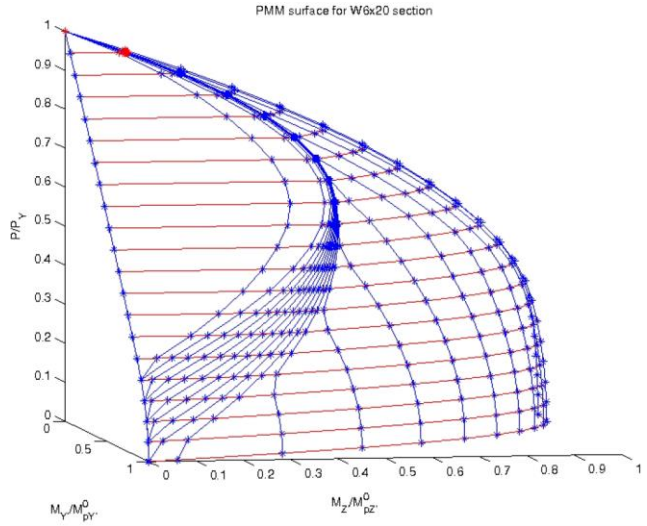

Figure 2.5: P-$M_{pY'}$ -$M_{pZ'}$ relationships for PH elements. $M^0_{pY'}$ and $M^0_{pZ'}$ are the plastic moment capacities when P=0 (top: Krishnan 2003, bottom: Krishnan, 2009b).

2.4 Three-segment elastofiber element

The three-segment elastofiber (EF3) element is suited for accurately modeling beams over many loading cycles. It can capture flexural behavior similar to a fully

discretized fiber element with significantly less computational cost (Krishnan 2003). It consists of 3 segments (fiber-elastic-fiber) and 4 nodes (2 interior and 2 exterior) (Figure 2.6).

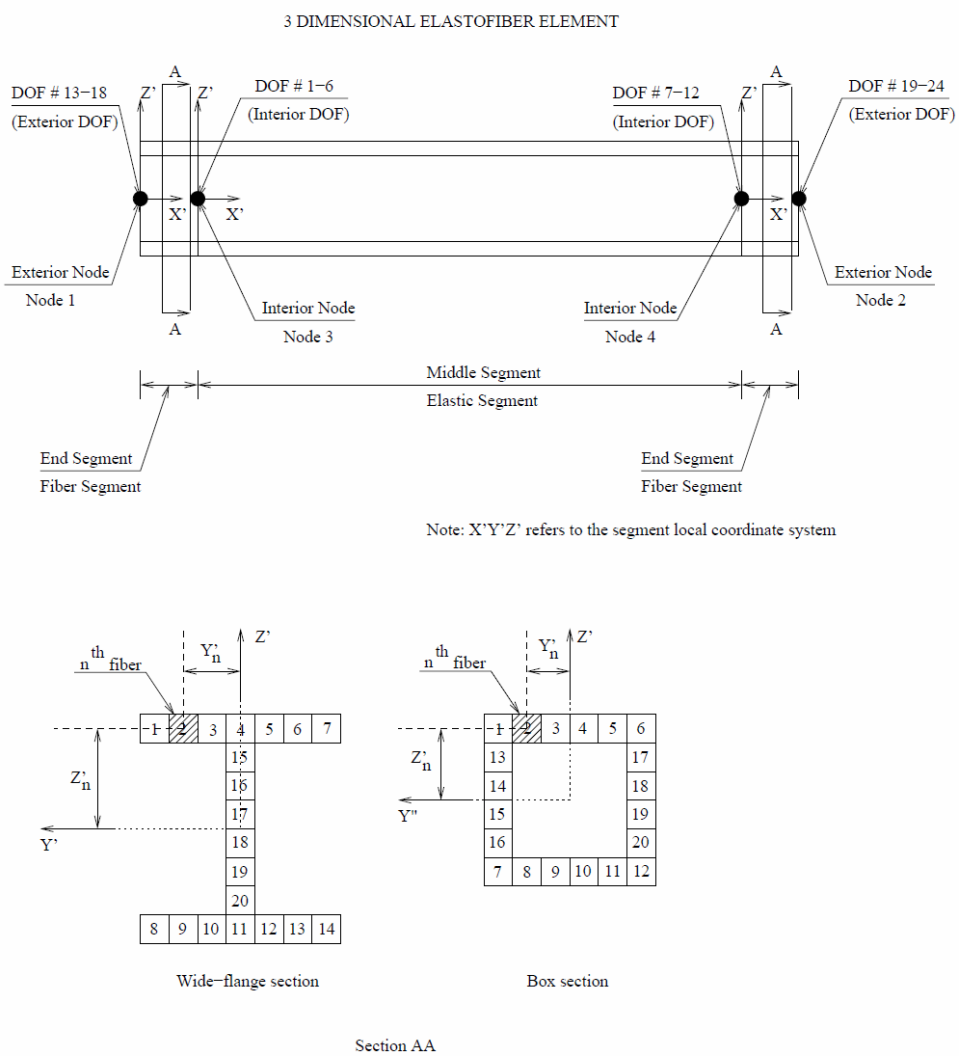

Figure 2.6: Three-segment elastofiber element layout (Krishnan 2003).

Because displacement increments are specified at the exterior nodes and the EF3 element has 2 interior nodes, it is treated like a local structural analysis problem. Thus, Newton-Raphson iterations (Eq. 2.11; similar to §2.2) are used to achieve local force equilibrium. For local iteration (k),

$$\begin{bmatrix} K_{T,II}^{(k)} & K_{T,IE}^{(k)} \\ K_{T,EI}^{(k)} & K_{T,EE}^{(k)} \end{bmatrix} \begin{Bmatrix} \Delta U_I \\ \Delta U_E \end{Bmatrix} = \begin{Bmatrix} 0 \\ F_E \end{Bmatrix} - \begin{Bmatrix} R_I^{(k)} \\ R_E^{(k)} \end{Bmatrix} \quad \text{(Eq. 2.11)}$$

where the (k) denotes local iterations within global iteration l; the subscripts I and E indicate the 12 internal and 12 external DOFs, respectively, of the EF3 element (6 DOFs per node using the XYZ system); $\{\Delta U_E\}$ is the known displacement increment $\{\Delta U_{ef}\}_L$ applied at the exterior nodes (transformed from $\{\Delta U_{ef}\}$ using $[T_1]$, $[T_2]$, and $[T_3]$); $\{F_E\}$ represents unknown external forces (which can be ignored as shown in Eq. 2.12 – 2.13); $\begin{bmatrix} K_{T,II}^{(k)} & K_{T,IE}^{(k)} \\ K_{T,EI}^{(k)} & K_{T,EE}^{(k)} \end{bmatrix}$ and $\begin{Bmatrix} R_I^{(k)} \\ R_E^{(k)} \end{Bmatrix}$ are assembled from segment contributions (after the contributions are transformed using $[T_4]$ from segment $X'Y'Z'$ systems to the XYZ system); and $\{\Delta U_I\}$ is solved from

$$\left[K_{T,II}^{(1)}\right]\{\Delta U_I\} = -\left[K_{T,IE}^{(1)}\right]\{\Delta U_E\} - \left\{R_I^{(1)}\right\} \quad \text{(Eq. 2.12)}$$

$$\left[K_{T,II}^{(k)}\right]\{\Delta U_I\} = -\left\{R_I^{(k)}\right\}. \quad \text{(Eq. 2.13)}$$

In Eq. 2.12, i.e., $(k) = 1$, the effect of $\{\Delta U_E\}$ is an applied force on the upper I equations of Eq. 2.11. At local convergence, the internal DOFs are condensed out of $\begin{bmatrix} K_{T,II}^{(k)} & K_{T,IE}^{(k)} \\ K_{T,EI}^{(k)} & K_{T,EE}^{(k)} \end{bmatrix}$ and $\begin{Bmatrix} R_I^{(k)} \\ R_E^{(k)} \end{Bmatrix}$ using partial factorization, resulting in $\left[K_{T,ef}^{l+1}\right]_L$ and $\left\{R_{ef}^{l+1}\right\}_L$, which are then

transformed into $\left[K_{T,ef}^{l+1}\right]$ and $\left\{R_{ef}^{l+1}\right\}$ using $[T_3]$, $[T_2]$, and $[T_1]$, and assembled into the global $\left[K_T^{l+1}\right]$ and $\{R^{l+1}\}$ arrays.

$\begin{bmatrix} K_{T,II}^{(k)} & K_{T,IE}^{(k)} \\ K_{T,EI}^{(k)} & K_{T,EE}^{(k)} \end{bmatrix}$ and $\begin{Bmatrix} R_I^{(k)} \\ R_E^{(k)} \end{Bmatrix}$ are assembled from segment contributions. The center segment has an elastic beam formulation, without axial yielding or plastic hinging capabilities. The two outer fiber segment formulations can be derived from individual fibers (Figure 2.6).

Consider fiber n in a segment. Fiber n has an incremental strain $d\varepsilon_n$ that depends on the incremental (axial) translations dU and incremental (relative to the chord) rotations $d\varphi$ of the segment nodes i, j:

$$d\varepsilon_n = \frac{dU_j - dU_i}{L_{s0}} + \frac{Z_n'\left(d\varphi_{jY'} - d\varphi_{iY'}\right)}{L_{s0}} - \frac{Y_n'\left(d\varphi_{jZ'} - d\varphi_{iZ'}\right)}{L_{s0}} \qquad \text{(Eq. 2.14)}$$

where Z_n' and Y_n' is the location of fiber n along the cross section (Figure 2.6), and L_{s0} is the original segment length.

A robust material model (Figure 2.7 and Figure 2.8, Hall and Challa 1995) defines the fiber's current tangent stiffness $E_{T,n}$ and stress σ_n based on its stress-strain history and $d\varepsilon_n$. The user-defined backbone curve has an initial elastic region, a yield plateau, and a strain-hardening/softening curve defined by a cubic ellipse. In this curve, E is the elastic modulus, σ_y is the yield stress, E_{sh} is the tangent modulus at the onset of strain-hardening, ε_{sh} is the strain at the onset of strain-hardening, σ_u is the ultimate stress, and ε_u is the fiber ultimate strain. The cubic ellipse (ε, σ) in Figure 2.7 is determined by

$$\frac{(\varepsilon - \varepsilon_0)^3}{a^3} + \frac{(\sigma - \sigma_0)^3}{b^3} = 1 \qquad \text{(Eq. 2.15)}$$

where ε_0 and σ_0 define the center of the ellipse, and a and b are the diameters of the ellipse. ε_0, σ_0, a, and b are functions of σ_y, E_{sh}, ε_{sh}, σ_u, and ε_u. At the plateau region of the backbone curve (between point A and the point of strain-hardening onset in Figure 2.7), E_{AB} is used as $E_{T,n}$, where the A-B line segment is tangent to the cubic ellipse at point B. Beyond the ultimate point (between points C and D in Figure 2.7), 0 is used as $E_{T,n}$. The Extended Masing's hypothesis, described in Challa (1992), governs the hysteretic behavior (Figure 2.8). Fibers may also fracture in tension if a predetermined probabilistic fracture strain is exceeded; a fractured fiber may carry compressive loads.

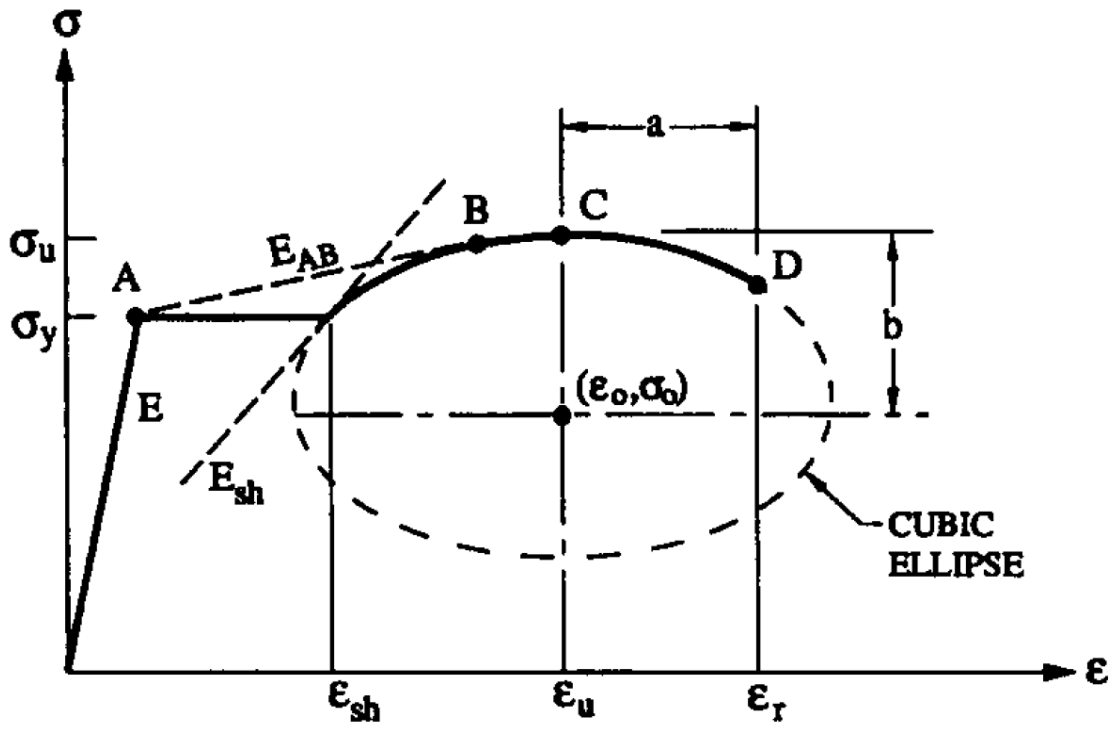

Figure 2.7: Stress-strain backbone curve of a fiber (Hall and Challa 1995).

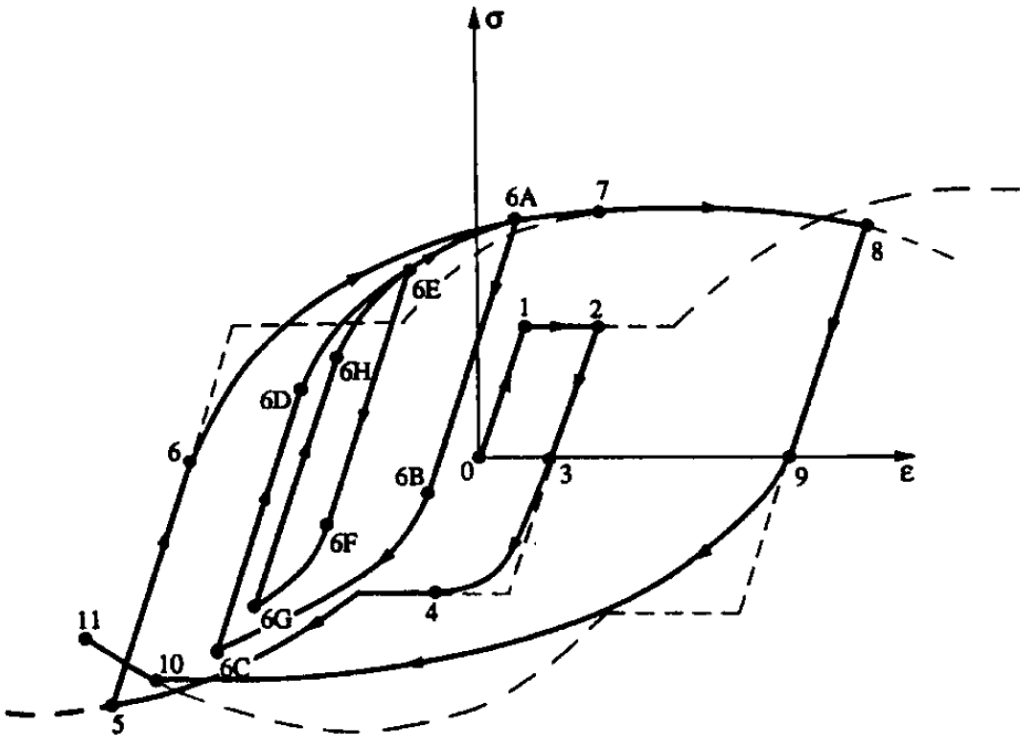

Figure 2.8: Hysteretic stress-strain paths of a fiber (Hall and Challa 1995).

Fiber contributions are combined to get the segment's incremental axial force (dP) and moment (dM):

$$dP = \sum_n E_{T,n} A_n d\varepsilon_n \quad \text{(Eq. 2.16)}$$

$$d\bar{M}_{Y'} = -\sum_n E_{T,n} A_n Z'_n \, d\varepsilon_n \quad \text{(Eq. 2.17)}$$

$$d\bar{M}_{Z'} = \sum_n E_{T,n} A_n Y'_n \, d\varepsilon_n \quad \text{(Eq. 2.18)}$$

where A_n is fiber area. The overbar indicates that dM corresponds to the segment center.

Shear (dQ) is elastic and computed independently:

$$d\bar{Q}_{Y'} = -A_{SY'} G \frac{\left(d\varphi_{iZ'} + d\varphi_{jZ'}\right)}{2} \quad \text{(Eq. 2.19)}$$

$$d\bar{Q}_{Z'} = A_{SZ'} G \frac{\left(d\varphi_{iY'} + d\varphi_{jY'}\right)}{2} \quad \text{(Eq. 2.20)}$$

where $A_{SY'}$ and $A_{SZ'}$ are the cross-sectional shear areas (Figure 2.4). Twisting (dT) is computed in the same way as PH element twisting. Eq. 2.14 is substituted into Eq. 2.16 – 2.20, and Eq. 2.16 – 2.20 and Eq. 2.9 are combined to form the matrix equation

$$\begin{Bmatrix} dP \\ d\bar{M}_{Y'} \\ d\bar{M}_{Z'} \\ d\bar{Q}_{Y'} \\ d\bar{Q}_{Z'} \\ dT \end{Bmatrix} = [C_T] \begin{Bmatrix} \frac{dU_j - dU_i}{L_{s0}} \\ -\frac{d\varphi_{jY'} - d\varphi_{iY'}}{L_{s0}} \\ -\frac{d\varphi_{jZ'} - d\varphi_{iZ'}}{L_{s0}} \\ -\frac{d\varphi_{iZ'} + d\varphi_{jZ'}}{L_{s0}} \\ \frac{d\varphi_{iY'} + d\varphi_{jY'}}{L_{s0}} \\ \frac{d\alpha_j - d\alpha_i}{L_{s0}} \end{Bmatrix} \quad \text{(Eq. 2.21)}$$

where

$$[C_T] = \begin{bmatrix} \sum_n E_{T,n}A_n & -\sum_n E_{T,n}A_n Z'_n & \sum_n E_{T,n}A_n Y'_n & 0 & 0 & 0 \\ & \sum_n E_{T,n}A_n Z'^2_n & -\sum_n E_{T,n}A_n Y'_n Z'_n & 0 & 0 & 0 \\ & & \sum_n E_{T,n}A_n Y'^2_n & 0 & 0 & 0 \\ & \text{symmetric} & & A_{SY'}G & 0 & 0 \\ & & & & A_{SZ'}G & 0 \\ & & & & & GJ \end{bmatrix}. \quad \text{(Eq. 2.22)}$$

By substituting

$$\begin{Bmatrix} \frac{dU_j - dU_i}{L_{s0}} \\ -\frac{d\varphi_{jY'} - d\varphi_{iY'}}{L_{s0}} \\ -\frac{d\varphi_{jZ'} - d\varphi_{iZ'}}{L_{s0}} \\ -\frac{d\varphi_{iZ'} + d\varphi_{jZ'}}{L_{s0}} \\ \frac{d\varphi_{iY'} + d\varphi_{jY'}}{L_{s0}} \\ \frac{d\alpha_j - d\alpha_i}{L_{s0}} \end{Bmatrix} = \frac{1}{L_{s0}}[S] \begin{Bmatrix} dU_i \\ dV_{iY'} \\ dV_{iZ'} \\ d\alpha_i \\ d\theta_{iY'} \\ d\theta_{iZ'} \\ dU_j \\ dV_{jY'} \\ dV_{jZ'} \\ d\alpha_j \\ d\theta_{jY'} \\ d\theta_{jZ'} \end{Bmatrix} \quad \text{(Eq.2.23)}$$

where

$$[S] = \begin{bmatrix} -1 & 0 & 0 & 0 & 0 & 0 & 1 & 0 & 0 & 0 & 0 & 0 \\ 0 & 0 & 0 & 0 & 1 & 0 & 0 & 0 & 0 & 0 & -1 & 0 \\ 0 & 0 & 0 & 0 & 0 & 1 & 0 & 0 & 0 & 0 & 0 & -1 \\ 0 & -1 & 0 & 0 & 0 & -\frac{L_{s0}}{2} & 0 & 1 & 0 & 0 & 0 & -\frac{L_{s0}}{2} \\ 0 & 0 & -1 & 0 & \frac{L_{s0}}{2} & 0 & 0 & 0 & 1 & 0 & \frac{L_{s0}}{2} & 0 \\ 0 & 0 & 0 & -1 & 0 & 0 & 0 & 0 & 0 & 1 & 0 & 0 \end{bmatrix} \quad \text{(Eq. 2.24)}$$

into Eq. 2.21, and accounting for geometric nonlinearity through the geometric stiffness matrix

$$[G] = \frac{P}{L_{s0}} \begin{bmatrix} 0 & 0 & 0 & 0 & 0 & 0 & 0 & 0 & 0 & 0 & 0 & 0 \\ 0 & 1 & 0 & 0 & 0 & 0 & 0 & -1 & 0 & 0 & 0 & 0 \\ 0 & 0 & 1 & 0 & 0 & 0 & 0 & 0 & -1 & 0 & 0 & 0 \\ 0 & 0 & 0 & 0 & 0 & 0 & 0 & 0 & 0 & 0 & 0 & 0 \\ 0 & 0 & 0 & 0 & 0 & 0 & 0 & 0 & 0 & 0 & 0 & 0 \\ 0 & 0 & 0 & 0 & 0 & 0 & 0 & 0 & 0 & 0 & 0 & 0 \\ 0 & 0 & 0 & 0 & 0 & 0 & 0 & 0 & 0 & 0 & 0 & 0 \\ 0 & -1 & 0 & 0 & 0 & 0 & 0 & 1 & 0 & 0 & 0 & 0 \\ 0 & 0 & -1 & 0 & 0 & 0 & 0 & 0 & 1 & 0 & 0 & 0 \\ 0 & 0 & 0 & 0 & 0 & 0 & 0 & 0 & 0 & 0 & 0 & 0 \\ 0 & 0 & 0 & 0 & 0 & 0 & 0 & 0 & 0 & 0 & 0 & 0 \\ 0 & 0 & 0 & 0 & 0 & 0 & 0 & 0 & 0 & 0 & 0 & 0 \end{bmatrix}, \quad \text{(Eq. 2.25)}$$

Eq. 2.21 is rewritten as

$$\begin{Bmatrix} dP_i \\ dQ_{iY'} \\ dQ_{jY'} \\ dT_i \\ dM_{iY'} \\ dM_{iZ'} \\ dP_j \\ dQ_{iZ'} \\ dQ_{jZ'} \\ dT_j \\ dM_{jY'} \\ dM_{jZ'} \end{Bmatrix} = \frac{1}{L_{s0}} [S^T C_T S + G] \begin{Bmatrix} dU_i \\ dV_{iY'} \\ dV_{iZ'} \\ d\alpha_i \\ d\theta_{iY'} \\ d\theta_{iZ'} \\ dU_j \\ dV_{jY'} \\ dV_{jZ'} \\ d\alpha_j \\ d\theta_{jY'} \\ d\theta_{jZ'} \end{Bmatrix}, \quad \text{(Eq. 2.26)}$$

which is the segment's incremental force-displacement relation

$$\{dR'_s\} = \left[K'_{T,s}\right]\{dU'_s\}. \quad \text{(Eq. 2.27)}$$

As stated above, $\left[K'_{T,s}\right]$ and $\{dR'_s\}$ are transformed using $[T_4]$ from the segment $X'Y'Z'$ system to the XYZ system before being assembled into $\begin{bmatrix} K_{T,II}^{(k)} & K_{T,IE}^{(k)} \\ K_{T,EI}^{(k)} & K_{T,EE}^{(k)} \end{bmatrix}$ and $\begin{Bmatrix} R_I^{(k)} \\ R_E^{(k)} \end{Bmatrix}$.

2.5 Five-segment elastofiber element

The five-segment elastofiber (EF5) element is suitable for modeling columns, braces, and other elements that may exhibit first-mode buckling. It has 5 segments (fiber-elastic-fiber-elastic-fiber) and 6 nodes (4 interior and 2 exterior) (Figure 2.9). The five-segment formulation is very similar to the three-segment formulation, except it has 24 internal DOFs instead of 12.

Interior nodal coordinates are updated at every local iteration in order to account for geometric nonlinearity and buckling. (Coordinate updating is done in the EF3 element, too, but this feature is more relevant for the EF5 element.)

It is also worth nothing, for both EF3 and EF5 elements, that axial yielding is concentrated at the fiber segments, which may not be realistic behavior particularly when modeling braces in tension.

When using the brace attachment points (Figure 2.1), pinned connections are not necessarily assumed (unlike FRAME2D). Krishnan (2009a) explains how gusset plates can be modeled at the brace attachment points.

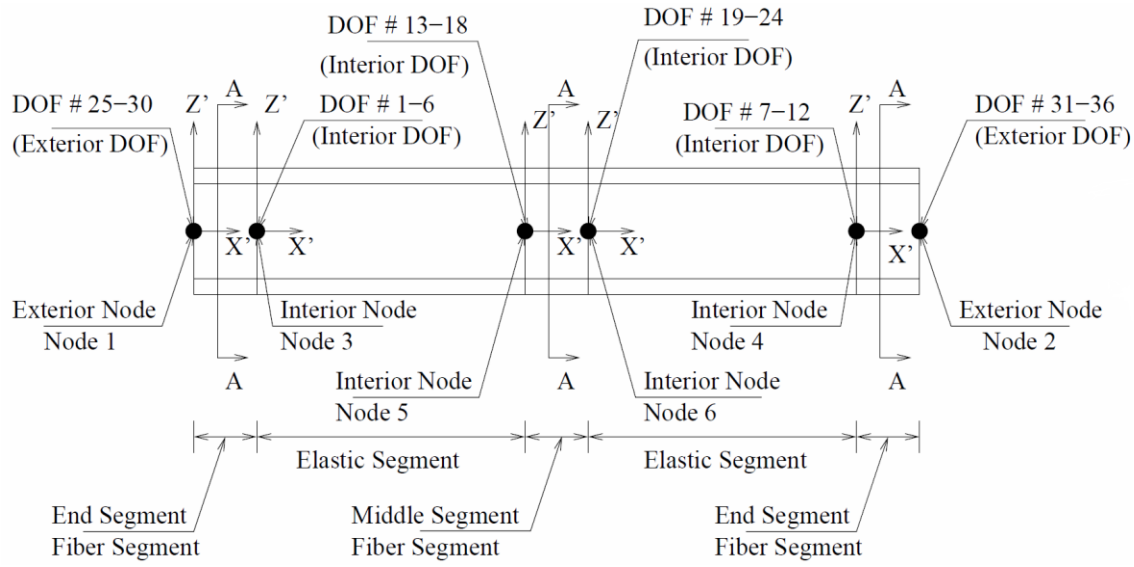

Figure 2.9: Five-segment elastofiber element layout (Krishnan 2009a).

2.6 Panel-zone element

The panel-zone (PZ) element captures the nonlinear hysteretic behavior of the part of the column within the depths of the intersecting beams. Building joints are deformable; therefore, the PZ element contributes to the model's stiffness and internal forces. The PZ element consists of two orthogonal rectangles, with attachment points for beams, columns, and/or braces (Figure 2.1). Each PZ deforms in shear due to the moments and shears from attached beams and columns.

The 4-DOF formulation has the form:

$$\{dR_{pz}\} = [K_{T,pz}]\{dU_{pz}\} \qquad \text{(Eq. 2.28)}$$

where $[K_{T,pz}]$ is assembled from the two orthogonal panels (Figure 2.10). A PZ that corresponds to the web of the associated column (panel ①) is described by the 2-DOF equation:

$$\begin{Bmatrix} dM_{J\bar{Y}}^{B} \\ dM_{J\bar{Y}}^{C} \end{Bmatrix} = G_T t_p HD \begin{bmatrix} 1 & -1 \\ -1 & 1 \end{bmatrix} \begin{Bmatrix} d\theta_{J\bar{Y}}^{B} \\ d\theta_{J\bar{Y}}^{C} \end{Bmatrix}. \quad \text{(Eq. 2.29)}$$

The tangent stiffness G_T is based on the backbone curve in Figure 2.11 with hysteretic behavior similar to that of a fiber, t_p is the thickness of the web (plus any doubler plates), H is the height (i.e., the depth of an attaching beam), and D is the depth of the column. For panel ②, t_p is the thickness of both column flanges (plus any doubler plates), and the column width W is used instead of D. The relevant DOFs for each PZ are shown in Figure 2.2.

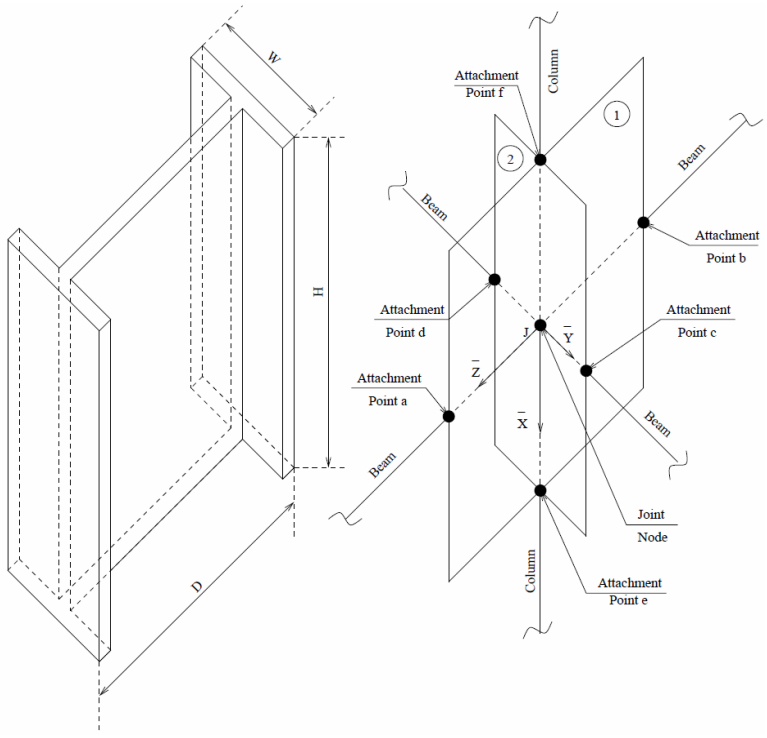

Figure 2.10: Beam-column joint represented as a panel-zone element (Krishnan 2003). Braces and brace attachment points are not shown.

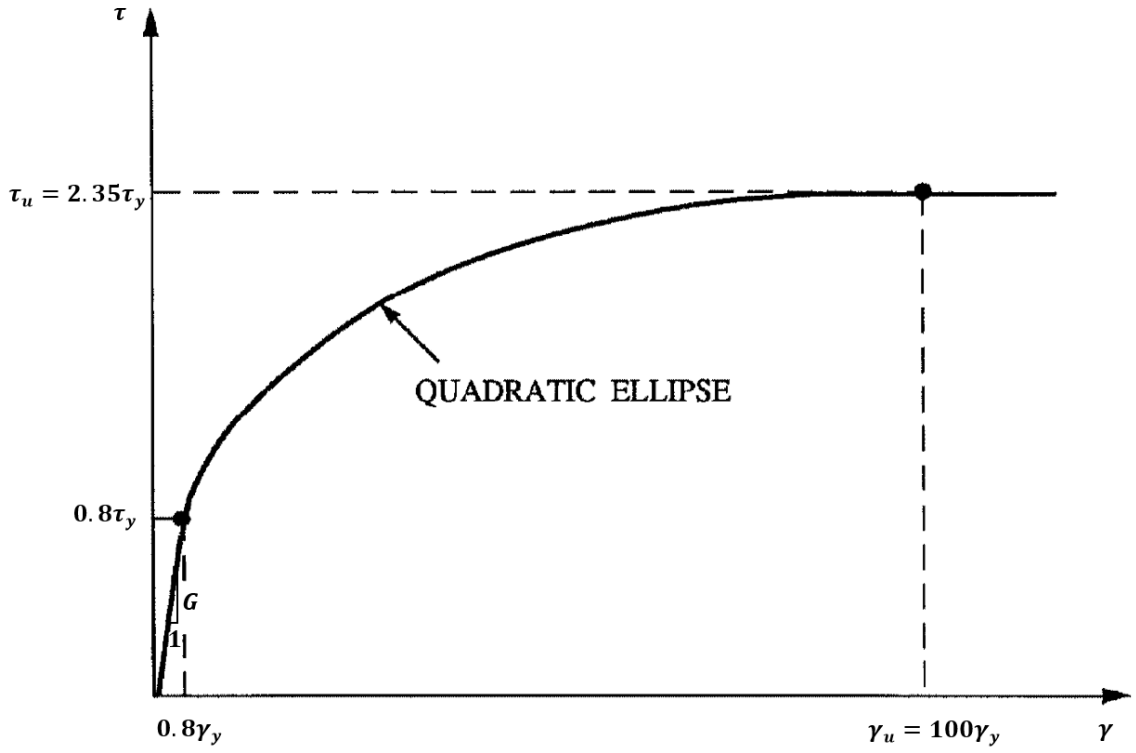

Figure 2.11: Shear stress-strain backbone curve of a panel zone (Challa 1992, edited).

The quadratic ellipse (γ, τ) in Figure 2.11 is determined by

$$\frac{(\gamma-\gamma_0)^2}{a^2} + \frac{(\tau-\tau_0)^2}{b^2} = 1 \qquad \text{(Eq. 2.30)}$$

where γ_0 and τ_0 define the center of the ellipse, and a and b are the diameters of the ellipse. γ_y, γ_0, τ_0, a, and b depend on τ_y and G. Because the PZ element has no internal nodes, $\{dR_{pz}\}$ and $[K_{T,pz}]$ are computed without iterations.

When assembled, the PZ element contributes to global stiffness of DOFs 5 – 8 (rotational DOFs) at each node. No transformation is required.

2.7 Diaphragm element

The diaphragms of a building, i.e., the floor slabs, are modeled as four-node linearly elastic plane-stress (PS) elements. A PS element provides in-plane-only resistance defined by elastic modulus E and Poisson's ratio ν, and its formulation can be found in many finite element textbooks (also in Krishnan 2003). A three-node version is achieved by mapping two local nodes to the same global node. Unlike FRAME3D's beam and PZ elements, its PS elements are always elastic; thus, the global stiffness matrix due to PS elements $[K]^{ps}$ is calculated only once, before analysis begins. Coordinate updating is not included in the PS element formulation.

2.8 Spring element

The simplest element in FRAME3D is the 1-node linear-elastic spring element, which resists a node's motion along a user-defined global DOF 1 – 8. It is added directly to the diagonal of the global stiffness matrix. Its implementation is straightforward and 1-dimensional.

2.9 Conclusion

This chapter reviewed the global equation of motion (§2.2) and various element formulations (§2.3 – 2.8). The remainder of the thesis discusses the contributions of the present research: improvements in the serial code (§3), the development of a parallel version (Part II), and an analysis of a 60-story high-rise building (Part III).

Chapter 3

Revisions to the

FRAME3D Formulation

3.1 General

FRAME3D is designed for highly nonlinear, large displacement analysis. In a study comparing FRAME3D with the industry standard PERFORM-3D, Bjornsson and Krishnan (2014) showed that both programs can track structures to the onset of collapse. They used both programs to analyze the collapse of a low-complexity water-tank tower (with fundamental period ~1.31 sec). A FRAME3D element was shown to capture more

loading cycles more accurately than an "equivalent" PERFORM-3D element. The FRAME3D water-tank tower degraded gradually until collapse onset. Immediately following the onset of collapse, the FRAME3D model encountered numerical instabilities that terminated the program. PERFORM-3D encountered similar numerical instabilities but terminated at larger roof displacements. However, the PERFORM-3D model collapsed suddenly with a large work-energy imbalance, an indication of error.

Neither program can collapse the water-tank tower "to the ground"; in fact, few structural engineering programs have this capability. Researchers are concerned primarily with the structural response leading up to the formation of the collapse mechanism. However, the above-mentioned numerical instabilities may prevent a model from even reaching this point. Thus, the present work improves FRAME3D's convergence capabilities by reformulating some of the core components of the solution procedure. Even though the structural models themselves may fail to capture all of the behavioral features of extremely large deformations associated with collapse conditions, it is important that a code not be limited by convergence problems.

One approach to avoid non-convergence is to one-by-one attempt various nonlinear solution algorithms (e.g., Newton-Raphson, modified Newton-Raphson, Newton Line Search, Krylov-Newton, etc.) until convergence is achieved (Haselton et al. 2009). This procedure may be time-consuming because several algorithms are used and it may not directly address some underlying causes of non-convergence.

In the case of FRAME3D, convergence implies force equilibrium—for both the global (Eq. 2.2) and the local problem (Eq. 2.11). The global problem is dynamic and the LHS matrix tends to have an effective stiffness controlled by $[M]$ and $[C]$, so global

convergence is usually reliable. The local problem is static and there are often large changes in stiffness due to unloading and yielding, so local convergence can be a challenge.

Recall (§2.4) the purpose of the local iterations: a multi-segmented beam problem with specified displacement increments at the ends is solved, as illustrated in Figure 3.1. The displacement/rotation increments are denoted as ΔU_1 and ΔU_2. Of interest are the beam's end forces/moments and condensed tangent matrix—but to determine these, the state of the interior segments must be solved via a static structural analysis; element-level iterations are hence needed.

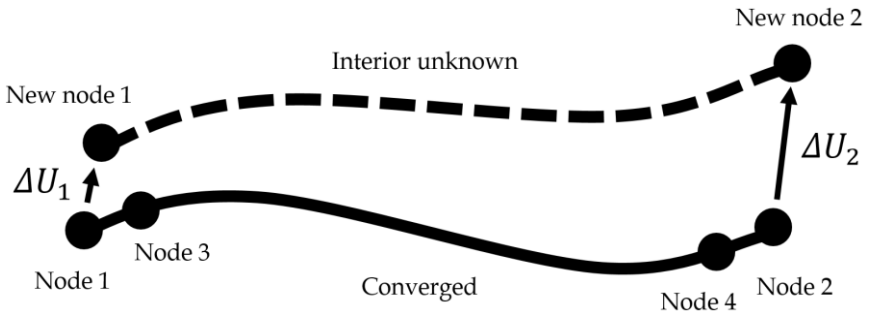

Figure 3.1: Pictorial representation of element-level iterations. Although not pictured, incremental rotations are included in ΔU_1 and ΔU_2.

The previous FRAME3D addresses local convergence issues with these features:

- For the first local iteration ($k = 1$) the elastic matrix is used; this is beneficial if one or more fibers are unloading because the unloading slope is the elastic slope E.
- If the element force residual grows, it iterates with an elastic matrix for 2 iterations.

- Otherwise, it iterates with the tangent matrix plus a user-defined fraction of the elastic matrix (the author uses 5%).
- In addition to the above strategies, it uses a "backup-subdivide algorithm" (discussed in §3.3).

But even with these remedies, the local problem can have trouble converging in some cases. In this chapter, elements and nodes are tracked more carefully and FRAME3D is revised to account for software bugs and limitations that arise in specific nonlinear situations. These situations involve:

- Large displacement/rotation increments (§3.2)
- The backup-subdivide algorithm (§3.3)
- Element failure (§3.4)
- Extremely narrow joint hysteresis (§3.5).

The improvements in convergence due to the §§3.2 – 3.5 revisions are demonstrated in §3.6. The revisions above are shown to produce identical structural response compared to that of the previous FRAME3D with a greater ability to track collapse.

This chapter also documents the modification of the fiber backbone curve to allow for:

- Post-rupture compressive strength (§3.7).

This modification simultaneously provides a more realistic representation of fiber behavior at large compressive strains and addresses a non-convergent situation in the fiber-segment formulation. Because this last modification alters structural response it is discussed separately from the §§3.2 – 3.5 revisions.

3.2 Large displacement/rotation increments

In the present section, the algorithm that is used to create the Eq. 2.11 elastofiber element stiffness matrix for the local iterations is revised to handle large displacement/rotation increments more appropriately.

Recall (Eq. 2.11) that $\begin{bmatrix} K_{T,II}^{(k)} & K_{T,IE}^{(k)} \\ K_{T,EI}^{(k)} & K_{T,EE}^{(k)} \end{bmatrix}$ (denoted as $\left[K_T^{(k)}\right]$ for convenience in the present discussion) uses DOFs at both exterior and interior nodes. In the previous FRAME3D, when local iteration $k = 1$, the values of the exterior DOFs come from the incremented state ("New node 1" and "New node 2" in Figure 3.1), and the values of the interior DOFs come from the most recently converged state ("Node 3" and "Node 4")—updating gradually until local convergence is achieved (and matches the incremented state). Using this original algorithm leads to successful convergence in most cases. However, Figure 3.2 shows that if displacement/rotation increments are large enough, the end segments can be very deformed, leading to an unrealistic $\left[K_T^{(k)}\right]$ and a difficulty with convergence.

Figure 3.2: Pictorial representation of a large displacement/rotation increment. Highlighted (grey) is the configuration used by the previous FRAME3D to construct $\left[K_T^{(k)}\right]$ *for local iteration k=1; the end segments are shown to be highly deformed.*

Thus, FRAME3D is revised, for local iteration $k = 1$ only, such that $\left[K_T^{(1)}\right]$ is constructed from values of the DOFs from the most recently converged state ("Nodes 1 – 4," not the "New nodes"). Only the construction of $\left[K_T^{(1)}\right]$ is different; the rest of Eq. 2.11 is unchanged.

For subsequent iterations $k > 1$, the interior nodes are located in the neighborhood of the incremented state, so no revision is implemented: $\left[K_T^{(k)}\right]$ is constructed from the "New nodes 1 & 2" and the updating interior nodes.

The revision described in this section matches FRAME2D's formulation, except it is in 3D.

3.3 The backup-subdivide algorithm

The backup-subdivide algorithm was originally created to address large displacement/rotation increments for the local element-level problem. In the present section, the previous algorithm is reviewed and then revised to improve convergence capabilities efficiently.

The previous backup-subdivide algorithm can be summarized by Figure 3.3. If local equilibrium at the fully incremented state ("Attempt 1") cannot be achieved within a (user-defined) maximum allowable number of local iterations, then:

(1) It *backs up* to the "Most recently converged state," and *subdivides* the displacement increment. (The increment is halved in FRAME3D.)

(2) It applies the subdivided increment ("Attempt 2") for which the element should converge more easily.

(3) If the element does not converge, the program backs up and subdivides again ("Attempt 3").

(4) If the element converges (suppose at "Attempt 3"), then "Attempt 3" becomes the "Most recently converged state," and the program attempts the remaining increment ("Attempt 1" again). Any future back-ups in the current global iteration return to the newly converged state. It is worth noting, that in order to avoid unrealistic effects such as artificial unloading, the fibers themselves are always updated using the overall strain increments since the previously converged time step.

(5) The loop continues until the entire ΔU_1 and ΔU_2 are applied successfully, or until the subdivided increment is less than a "small" percentage (e.g., 25% in FRAME3D) of the original ΔU_1 and ΔU_2. The latter implies non-convergence, in which case the program will "accept" the last attempt and reapply the remaining increment (with the backup-subdivide algorithm); the element may become convergent if the entire ΔU_1 and ΔU_2 end up successfully applied.

(6) If the remaining increment is less than the small percentage (from step 5), then the algorithm accepts the remaining increment's "Attempt 1" as the solution, whether or not it converged. A warning is issued if local convergence is not achieved.

The previous (above) backup-subdivide algorithm ends in successful convergence in most cases. However, it is found that accepting step 6's "Attempt 1" is sometimes insufficient

in terms of helping the model, as a whole, approach global convergence. Thus, step 6 is revised:

(6) If the remaining increment is less than the small percentage (from step 5) and the remaining increment's "Attempt 1" did not converge, then the algorithm accepts "Attempt 2," reapplies the remaining half, and repeats (the revised) step 6. But if the remaining increment is also less than a much smaller percentage (e.g., 0.1%), then the remaining increment's "Attempt 1" is accepted as the solution. A warning is issued if local convergence is not achieved.

This revision allows further subdivisions at the end of the algorithm—when the remaining increment is less than 25% of the complete increment. It is more efficient than simply reducing the 25% to a smaller percentage (which also increases the number of subdivisions at the beginning of the algorithm). It is also observed that this revision tends to reduce the number of global iterations needed before convergence. For example, in the first 16 sec (3200 time steps) of the water-tank tower collapse simulation, the revised FRAME3D uses 32% less global iterations overall than the previous FRAME3D.

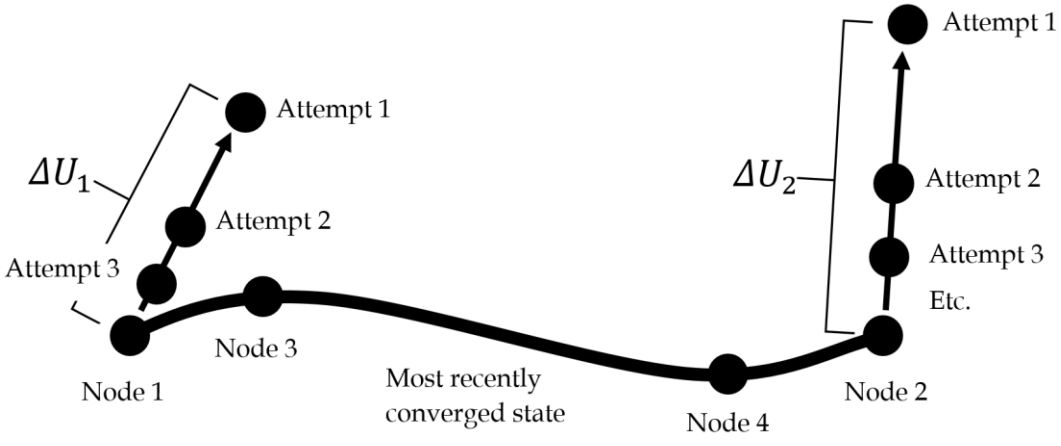

Figure 3.3: Backup-subdivide algorithm.

3.4 Element failure

Realistic building collapses likely include element failure. In the present section the handling of failing elements is reconsidered for FRAME3D. For the discussion in the present section, the following rules define fiber, segment, and element failure:

- Fiber n is considered as failed if it has reached or exceeded the rupture strain in either tensile or compressive directions, i.e., $|\varepsilon_n| \geq |\varepsilon_r|$.
- A segment is considered as failed if every fiber in it has failed, i.e., $\min_{\forall n} |\varepsilon_n| \geq |\varepsilon_r|$.
- An element is considered as failed if any segment in it has failed.

(The above failure criteria are modified in §3.7, but that revision will be discussed then.)

A fiber, segment, or element failure means that that fiber, segment, or element is omitted from the formulation thereafter, i.e., it no longer contributes to the stiffness or strength of the remaining structure. In the context of a single time step with global and local iterations, the previous FRAME3D mistakenly defines "thereafter":

- If an element fails at global iteration l, it is omitted from subsequent global iterations l.

This definition sometimes leads to a computational "snowball effect" where many other elements fail in the same time step; the forces that cause the first element to fail are "redistributed" in the next global iteration (because the first element is omitted) to adjacent elements, which may cause them to fail, and so on. At the numerical instability of Bjornsson and Krishnan (2014), roughly 100 elements apparently fail simultaneously in a single time step (at t = 16 sec), which is physically improbable because time-step size

$\Delta t = 0.005\ sec$ is very small. Thus, FRAME3D's handling of element failure in the context of a single time step is revised to match that of FRAME2D:

- If an element failed at a previous time step, it is omitted from all iterations of the current time step.
- Otherwise, it is included in all iterations—global and local—of the current time step.

This revision applies to fiber and segment failures, too. Essentially, the convergence of the global iterations at the current time step determines whether a fiber, segment, or element actually fails then.

3.5 Extremely narrow joint hysteresis

FRAME3D's material models are unique because they feature cubic and quadratic ellipses to define the backbone curves and hysteresis. (Other programs such as PERFORM-3D and OpenSees use multi-segmented lines to approximate material behavior.) Of interest in the present section is joint hysteresis (i.e., for PZ elements), which for FRAME3D is governed by the Extended Masing's hypothesis as stated in §2.6 and explained in Challa (1992). A part of the hypothesis is reviewed, a non-convergent scenario is identified, and the program is revised to account for the scenario.

There are many rules in the hypothesis, but for the present discussion consider a branch originating from a PZ backbone curve. As shown in Figure 3.4, when unloading takes place (starting at point "3" or "6"), a linear-elastic path is taken until zero load is

reached (point "4" or "7"), after which a cubic ellipse is followed until the symmetric point on the translated opposite backbone curve is reached (point "5" or "8"). The entire path (from "3" to past "5," or from "6" to past "8") is functionally smooth and the cubic ellipse is computed internally to ensure that this constraint is met. Although not detailed here, the portion that represents the cubic ellipse is computed from one of two explicit functions: for a negative or a positive hysteresis loop.

The hypothesis accounts for the case where unloading occurs with a very small amount of inelastic deformation because it may not be possible to construct a cubic ellipse that smoothly connects point "4" with point "5" (or "7" with "8"). In this case, the linear-elastic path is extended beyond point "4" (or "7") toward the yield point "4A" (or "7A") of the translated opposite backbone curve until a cubic ellipse can be properly fitted. The above rules have been used effectively for many years to accurately model joint hysteresis.

Although the hysteretic rules themselves are not revised in the present work, it is observed that if unloading occurs with a much smaller amount of inelastic deformation (plastic strain about 10^{-6}), the program might use the wrong function to compute the path of the cubic ellipse, resulting in global non-convergence whenever a PZ element transitions from the linear-elastic to the cubic portion of an extremely narrow hysteresis loop. The author identified this issue, and Hall fixed it by ensuring that an appropriate function is used. The revision is implemented in the present work for FRAME3D.

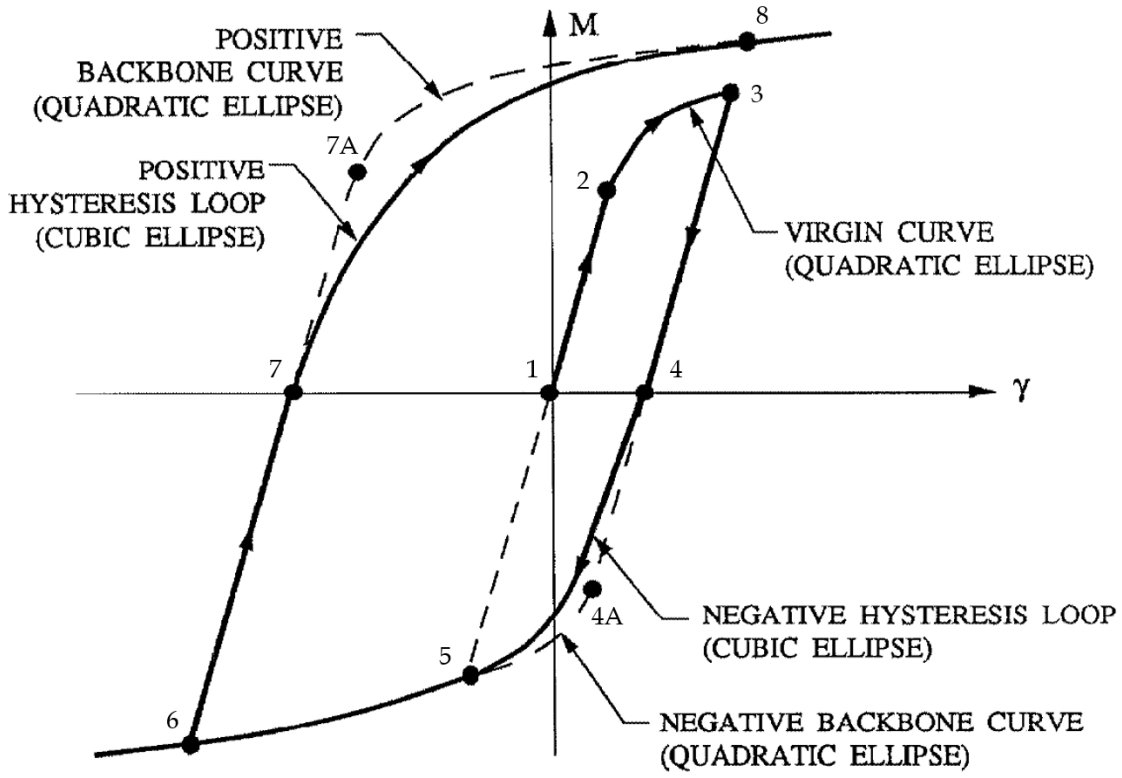

Figure 3.4: Joint hysteresis example featuring a negative hysteresis loop branching from a positive panel-zone backbone curve, and a positive hysteresis loop branching from a negative panel-zone backbone curve (Challa 1992, numbers added).

3.6 Demonstration of convergence capabilities

Because of the revisions in §§3.2 – 3.5, FRAME3D is more robust for simulating structural collapse. For example, the water-tank tower in §3.1 (Bjornsson and Krishnan 2014) can now collapse "to the ground." Although the collapse mechanism forms before $t = 16\ sec$ (the numerical instability observed by Bjornsson and Krishnan 2014), Figure 3.5 (left) shows that the mechanism is not obvious in a plot of unscaled deformations. Figure 3.5 (right) shows that, with the revision, the tank can be seen clearly collapsing

with unscaled deformations at $t = 20\ sec$. The revised FRAME3D converges beyond $t = 20\ sec$, but this is not shown because some members are below "ground level" ($Z = 0\ m$).

It is shown in Figure 3.6 that the water-tank roof displacement histories, with and without the §§3.2 – 3.5 revisions, are nearly identical until $t = 16\ sec$; for the first 16 seconds of the simulation, the root-mean-square error (against the previous FRAME3D) of the revised FRAME3D's "X Displacement" history in Figure 3.6 is $6.14 \times 10^{-6}\ m$, which can be considered as negligible for the present context.

However, the reader must be cautioned. Even though the simulation is convergent through collapse, the structural behavior may not be modeled appropriately at large deformations. For example, the mass-proportional component of Rayleigh damping resists absolute velocity and is unphysical (Hall 2005); when (and before) the water-tank tower falls, it may be significant. Also, the stiffness-proportional damping may be generating excessive resisting forces (Hall 2005).

It is recommended to improve FRAME3D's damping formulation (this will be done in a future study). For example in FRAME2D, the contribution from stiffness-proportional damping can be bounded, and damping elements can be incorporated. Nevertheless, the present research makes FRAME3D more robust for collapse simulations.

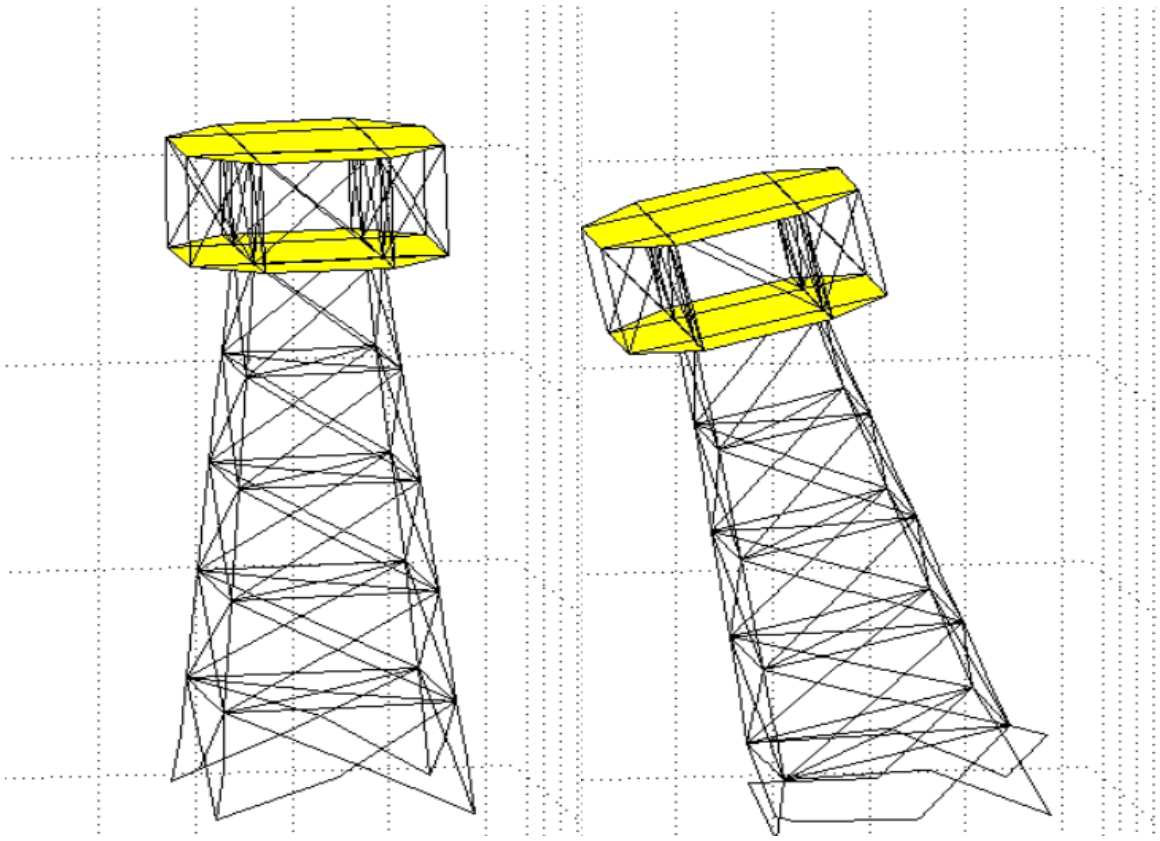

Figure 3.5: Unamplified deformations of water-tank tower at t=16 sec (left) and at t=20 sec (right), due to the Kobe earthquake ground motion at Takatori (Figure E.1) scaled to 32%. Elements that failed during analysis are not shown. Deformations are unamplified.

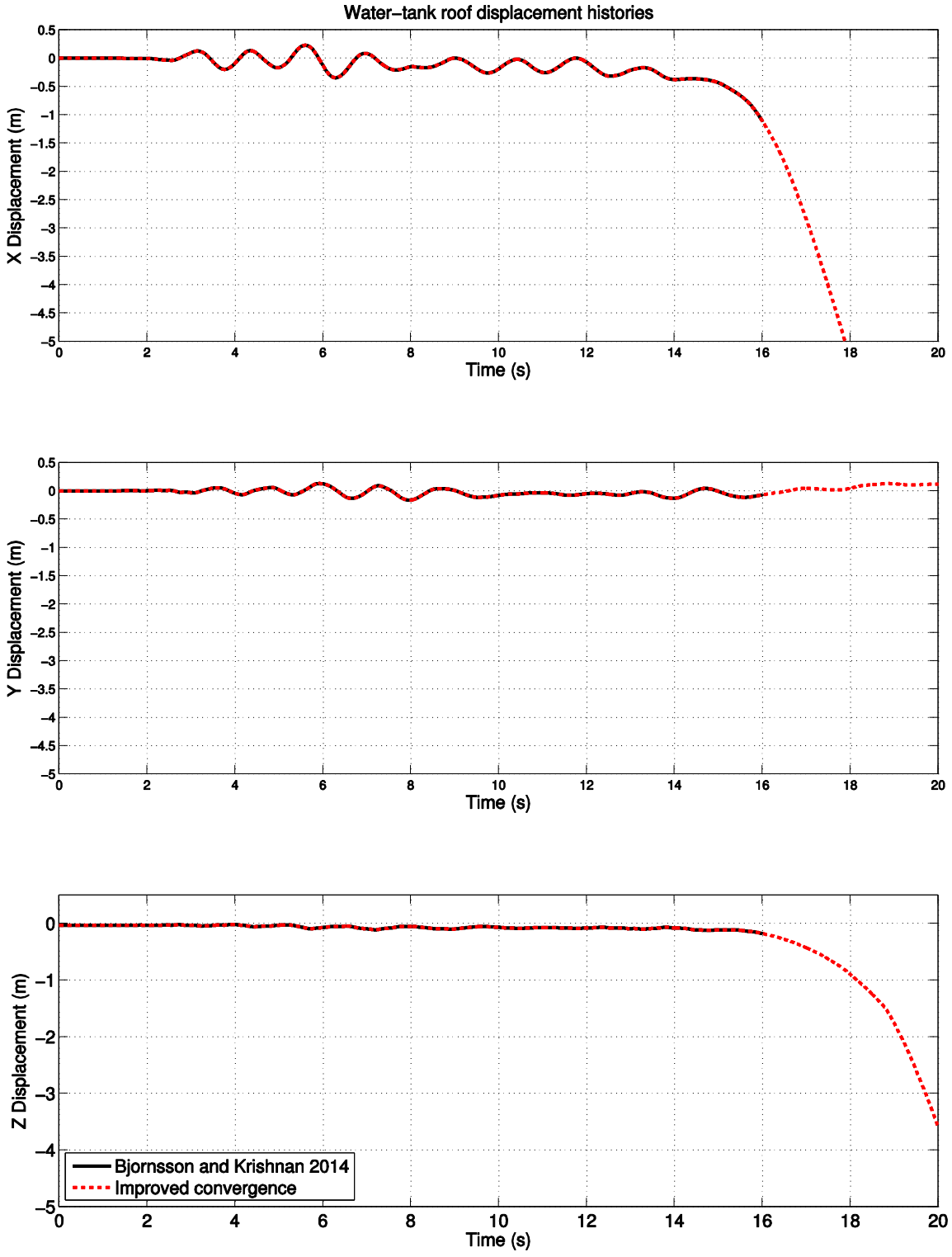

Figure 3.6: Water-tank tower roof displacement histories, due to the Kobe earthquake ground motion at Takatori (Figure E.1) scaled to 32%, as observed by Bjornsson and Krishnan 2014 (solid), and with the §§3.2 – 3.5 revisions (dashed).

3.7 Post-rupture compressive strength

In the present section, the fiber backbone curve from Figure 2.7 is modified to allow the presence of a post-rupture compressive strength (Figure 3.7). Without this modification, non-convergence is sometimes observed because segment nodes might move close to and even past each other, creating unphysical or "inside-out" segment configurations. This behavior is not realistic and is observed because post-rupture compressive strength is omitted. The modified backbone curve improves realism by adding such strength.

The modification can be summarized as follows. Consider fiber n with current fiber stress σ_n, current fiber strain ε_n, rupture strain ε_r, and "final" post-rupture strength σ_{fin}.

- In compression, if $\varepsilon_n \leq \varepsilon_r < 0$, then $\sigma_n = \sigma_{fin} < 0$. Although not done here, a user may adjust σ_{fin} according to experimental data.
- In tension, if $\varepsilon_n \geq \varepsilon_r > 0$, then $\sigma_n = 0$, i.e., fiber n fractures at the rupture point.

In other words, fiber n can never "completely fail"—it can only fracture in tension. Therefore, the element failure criteria is revised (see §3.4 for previous criteria):

- Fiber n can never fail. Even fractured fibers have potential compressive capabilities.
- A segment is considered as failed if every fiber in it has fractured.
- An element is considered as failed if any segment in it has failed.

With the above modification, segment nodes might still eventually pass each other and create an "inside-out" segment configuration that provides compressive resistance. This situation, too, is unphysical. Therefore, an additional failure criterion is added:

- The segment can also fail, as a whole, in compression if the segment strain $\varepsilon_s = \frac{L_s - L_{s0}}{L_{s0}} \leq \varepsilon_{sf} < 0$, where L_s and L_{s0} are the current and original segment lengths, respectively, and ε_{sf} is the segment failure strain.

$\varepsilon_{sf} = -0.9$ is used presently so that segments fail before L_s reaches a length of 0, but a more appropriate value may be determined according to experimental data.

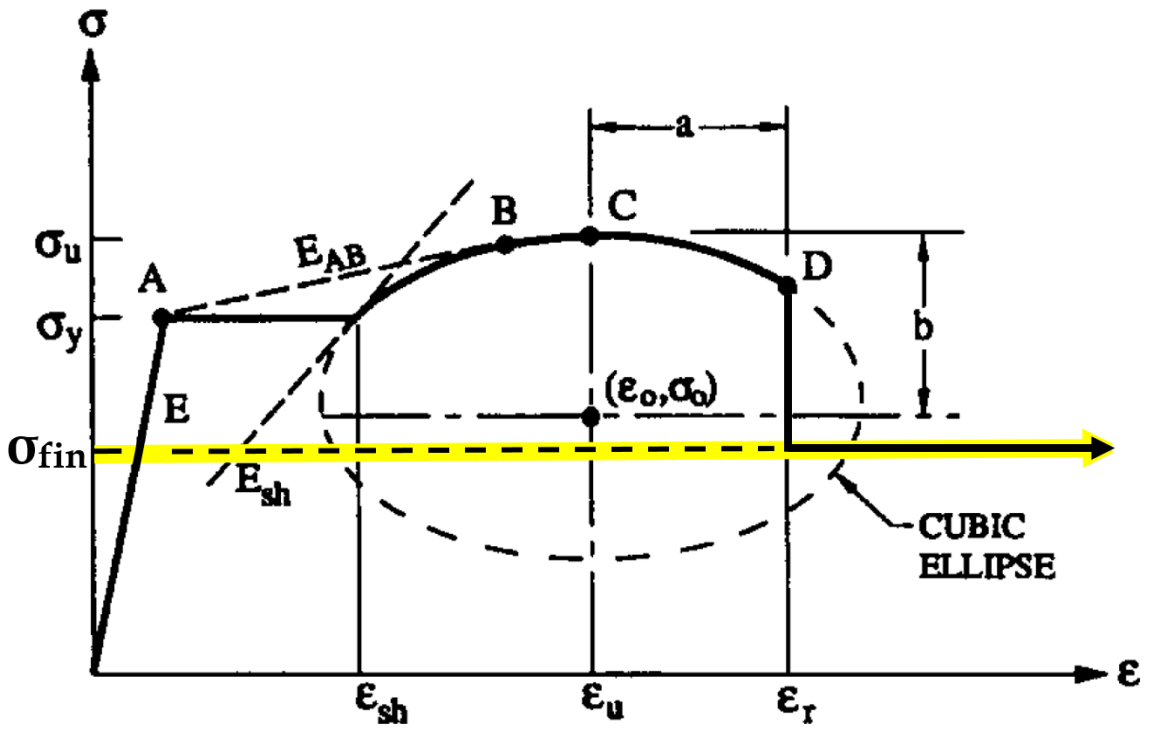

Figure 3.7: Positive stress-strain backbone curve of a fiber with non-zero post-rupture strength σ_{fin}, highlighted (Challa 1992, post-rupture strength added).

With the modifications of the present section, it is worth noting that the collapse mechanism in §3.6 is no longer observed when the water-tank tower is subjected to the 32% Kobe earthquake ground motion at Takatori. Assuming $\sigma_{fin} = 0.60\sigma_u$, Figure 3.8 shows that the water-tank tower needs a higher scale factor in order to collapse—37.3% instead of 32% of the prescribed ground motion—an indication that a true higher strength was not previously captured. Figure 3.8 also suggests that the material model at post-rupture strains can affect collapse behavior significantly. At 37.3%, the response without the modified backbone curve (green) collapses almost $30\,sec$ sooner than with the modifications (cyan). More experimental data is recommended to properly characterize steel at post-rupture compressive strains. But presently, it can just be said that including some post-rupture compressive strength is more realistic than omitting it altogether.

3.8 Conclusion

Therefore, FRAME3D's geometric nonlinearity and convergence capabilities are improved such that collapse can be further tracked, and the backbone curve is modified to more realistically characterize post-rupture compressive strength. The formulation in §2 and revisions in §3 are included for the remainder of this report.

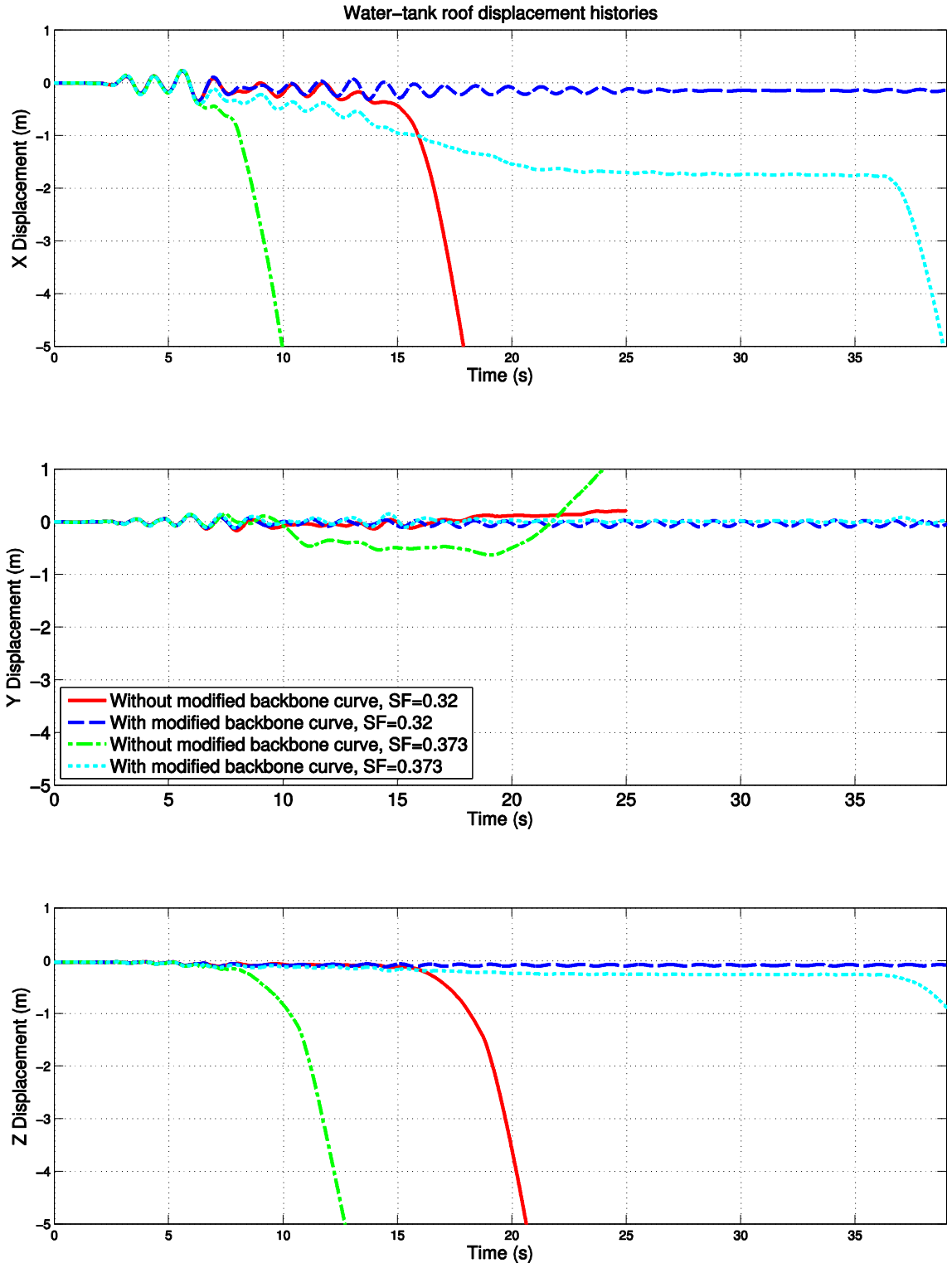

Figure 3.8: Water-tank tower roof displacement histories, due to the Kobe earthquake ground motion at Takatori (Figure E.1) scaled to 32% and 37.3%, with and without the §3.7 modified backbone curve.

PART II

A Computationally Efficient, Parallel FRAME3D

Chapter 4

Overview of Parallel Computing

4.1 General

The revised FRAME3D at the conclusion of Part I exhibits superior convergence capabilities compared to previous versions. The next goal of the present work is to improve FRAME3D's computational performance so that the nonlinear response of very tall buildings can be computed more quickly. For example, Part I's FRAME3D (an unoptimized serial code) would compute the nonlinear dynamic time-history collapse of a 60-story building (designed in §8) with a *wall time* (i.e., from the user's perspective; defined in §4.4.2) of 27 days.

In Part II (§§4 – 7), a computationally efficient, parallel FRAME3D (PFRAME3D) is developed. The serial code is optimized, reducing the wall time of the same computation to 3.5 days. Then the optimized serial code is parallelized, further reducing the wall time to 5.7 hours (using 128 cores).

The current chapter, which presents an overview of parallel computing, is organized as follows:

- Review of parallel computing in structural engineering (§4.2)
- Terminology (§4.3)
- Parallel performance measures (§4.4)
- Computer architecture (§4.5)
- Speedup strategy (§4.6).

4.2 Review of parallel computing in structural engineering

Parallel computing for finite-element programs is becoming an increasingly important topic due to rapidly improving computer environments. For dynamic programs that use explicit integration, distributed-memory parallel-computing strategies are well established. However, explicit integration is not preferred for large buildings because stiff elements require the use of unreasonably small time steps. Additionally, explicit dynamic analysis requires non-zero mass at every DOF in order to invert the mass matrix in the solution phase, but building models often assume zero mass at rotational DOFs. Thus, implicit integration schemes are usually preferred in structural engineering.

In the literature, there is yet to be a parallel framework intended specifically for the analysis of very tall buildings. Industry standards like PERFORM-3D and ETABS are currently limited to the shared-memory platform (one computer with multiple cores).

A distributed-memory (multiple computers) parallel version of OpenSees (OpenSeesSP) (McKenna and Fenves 2007) was developed and addressed the general case of sparse systems (uses sparse linear solvers like MUMPS, Petsc, and SuperLU). It was reported, however, to not scale well when using implicit integration (McKenna 2012). A bottleneck is present due to communication overhead with a "head-node." Thus, it was recommended to use OpenSeesSP with explicit integration, which as stated above is not ideal for building structures.

Another distributed-memory parallel version of OpenSees (OpenSeesMP) (McKenna and Fenves 2007) has also been developed and achieves scalability for the naturally parallel case that is commonly used in parameter studies (i.e., many concurrent simulations). To use OpenSeesMP, a user must write parallel scripts—and account for potential deadlock (cyclic dependencies when message passing), race conditions (non-determinism due to parallelization and variable CPU speeds), and load imbalances. OpenSeesMP also allows for the analysis of a single large structure, but it requires a user to specify subdomains. For example, a large model must be re-created if the user wants to split up the problem differently (e.g., to use 4 computer nodes instead of 2). This framework may not be ideal for highly complex structures.

Cho (2012) developed a parallel framework for the implicit finite-element analysis of reinforced concrete walls. He observed scalability and his work is referenced in §B.1, but a different framework is found to be more suitable for very tall buildings. Essentially,

Cho (2012) addressed the parallelization of wide-band systems, but of interest here are narrow-band systems.

Therefore, the parallel framework developed in the current report is unique in that it is intended for the nonlinear implicit analysis of large narrow-band systems representing tall buildings. To the knowledge of the author, it is the first of its kind.

4.3 Terminology

The reader may not be familiar with some of the terminology used by the parallel computing (PaC) and/or structural finite element modeling (FEM) communities. To add confusion, word usage may overlap between these two disciplines. For example, *node* refers to a computer in a computer cluster in PaC, but to a joint in a FEM model. Or, *local* refers to a single node in PaC, but to the element-level calculations in FEM. And *global* refers to a set of nodes in PaC, but to the structure-level calculations in FEM. §A.1 defines terms as they are used in this paper.

4.4 Parallel performance measures

4.4.1 General

To quantify the effectiveness of parallelization, two performance measures are defined:

- Wall time (§4.4.2)
- Speedup (§4.4.3).

4.4.2 Wall time

Perhaps the most intuitive way to assess performance is to consider *wall time*; the ultimate goal of parallelization is to minimize this quantity. *Wall time* refers to the elapsed time as perceived by a user. When plotted against the number of cores used, wall time can help quantify how *scalable* a program is. Specifically, two notions of scalability are used: *strong-scaling* and *weak-scaling*.

Strong-scaling involves varying the number of cores used to complete a constant overall "workload." This notion addresses the effectiveness of parallelization for completing a single large computation as quickly as possible.

Weak-scaling involves simultaneously varying both the number of cores used and the total workload such that the "workload per core" is constant. This notion addresses the effectiveness of parallelization for completing larger computations (using more parallelism) in the same amount of time as smaller computations (using less parallelism).

For clarity in the present discussion (to account for both notions of scalability) wall time is written as $T(N, W)$, a function of the number of cores used N, and the number of "workload units" performed W (e.g., if 1 "workload unit" is performed, then $W = 1$; if N "workload units" are performed, then $W = N$, etc.). In a strong-scaling study, wall time is denoted as $T(N, W = 1)$; in a weak-scaling study, it is $T(N, W = N)$.

Consider wall time vs. the number of cores used (i.e., T vs. N). Strong-scaling is "ideal" if $T(N, 1)$ halves when N doubles, and "poor" if $T(N, 1)$ is constant vs. N. The latter

condition is typically approached as more cores are added (Amdahl 1967). Weak-scaling is "ideal" if $T(N,N)$ is constant vs. N, and "poor" if $T(N,N)$ doubles when N doubles.

(The terms "ideal" and "poor" are used for convenience. It is possible to have "better than ideal" scaling, e.g., Cho (2012) due to favorable cache-effects, or "worse than poor" scaling, i.e., "parallel slowdown," due to excessive communication costs. Nevertheless, "ideal" and "poor" serve as appropriate reference points.)

4.4.3 Speedup

Speedup, the relative wall times between serial (1-core) and parallel (N-cores) computations, is a unitless metric that measures "how much faster" a parallel program is than its serial counterpart. It is most often defined (as is done here) in the strong-scaling sense, or

$$Speedup(N) = \frac{T(1,1)}{T(N,1)}. \quad \text{(Eq. 4.1)}$$

Speedup is "ideal" if it is 1:1 proportional to N, and "poor" if it is constant vs. N. As stated in §4.4.2, the latter condition is typically approached as more cores are added.

4.5 Computer architecture

All analyses are run using *Garuda*, a high-performance computer cluster at Caltech. The cluster has 75 nodes with 8 cores per node (a *core* is assumed to be the basic unit that can execute a single stream of commands); up to 600 cores may be simultaneously used in analysis. More specifically, it has 75 Dell PowerEdge 1950s, each with 2.33 GHz dual

quad-core processors, an 8 GB RAM, and a 148 GB hard drive. It has a Rocks operating system, and uses Qlogic Infiniband equipment and a MOAB/Torque scheduler. Additional background on computer architecture can be found in §A.1.

4.6 Speedup strategy

The strategy for developing a parallel framework of an existing program depends on the algorithm of the existing program. Recall that FRAME3D solves the iterative dynamic equation (Eq. 2.2):

$$\left[\frac{4}{(\Delta t)^2}M + \frac{2}{\Delta t}C + K_T^l\right]\{\Delta U\} = \{f_g\} - \{R^l\} - [M][r]\{\ddot{U}_g(t)\}$$
$$+[M]\left\{\frac{4}{(\Delta t)^2}U(t) + \frac{4}{\Delta t}\dot{U}(t) + \ddot{U}(t)\right\}$$
$$+[C]\left\{\frac{2}{\Delta t}U(t) + \dot{U}(t)\right\} - \left[\frac{4}{(\Delta t)^2}M + \frac{2}{\Delta t}C\right]\{U^l\}.$$

For the discussion in Part II, Eq. 2.2 is simplified to

$$[A]\{x\} = \{b\} \quad \text{(Eq. 4.2)}$$

Where

$$[A] = \left[\frac{4}{(\Delta t)^2}M + \frac{2}{\Delta t}C + K_T^l\right], \quad \text{(Eq. 4.3)}$$

$$\{x\} = \{\Delta U\}, \text{ and} \quad \text{(Eq. 4.4)}$$

$$\{b\} = \{f_g\} - \{R^l\} - [M][r]\{\ddot{U}_g(t)\} \quad \text{(Eq. 4.5)}$$
$$+[M]\left\{\frac{4}{(\Delta t)^2}U(t) + \frac{4}{\Delta t}\dot{U}(t) + \ddot{U}(t)\right\}$$
$$+[C]\left\{\frac{2}{\Delta t}U(t) + \dot{U}(t)\right\} - \left[\frac{4}{(\Delta t)^2}M + \frac{2}{\Delta t}C\right]\{U^l\}.$$

Thus, the solution procedure (§2.2) simplifies to five general steps (referred to as *Steps 1 – 5* in Part II). For each global iteration l:

(1) Check convergence

(2) Update* $[A]$

(3) Solve for x in $[A]\{x\} = \{b\}$

(4) Update geometry

(5) Update $\{b\}$

*Most of the work for Step 2 involves iterating locally (element-level) to determine EF3/EF5 element tangent stiffnesses. This work is already done in Step 5 and is not included in Step 2's wall time.

By recording the wall time (sec) per simulation time step, using three example nonlinear dynamic time-history collapse simulations (small/medium/large), it is shown in Figure 4.1 and Figure 4.2 that Steps 3 and 5 are usually the costliest—based on Part I's FRAME3D, an unoptimized serial code. These three systems are discussed further in §7, along with performance results. In terms of strategy, it can be seen that as system size increases, Step 3 becomes more significant. Step 5 is significant for all sizes and cannot be ignored.

Thus, the speedup strategy here prioritizes Steps 3 and 5. §5 focuses on Step 3, and §6 focuses on step 5. Steps 2 and 4 are similar to step 5, and therefore, are also covered in §6. Step 1, though it uses insignificant computation time, is automatically sped up due to the implementations of §5 and §6. As a result, every step is made parallel.

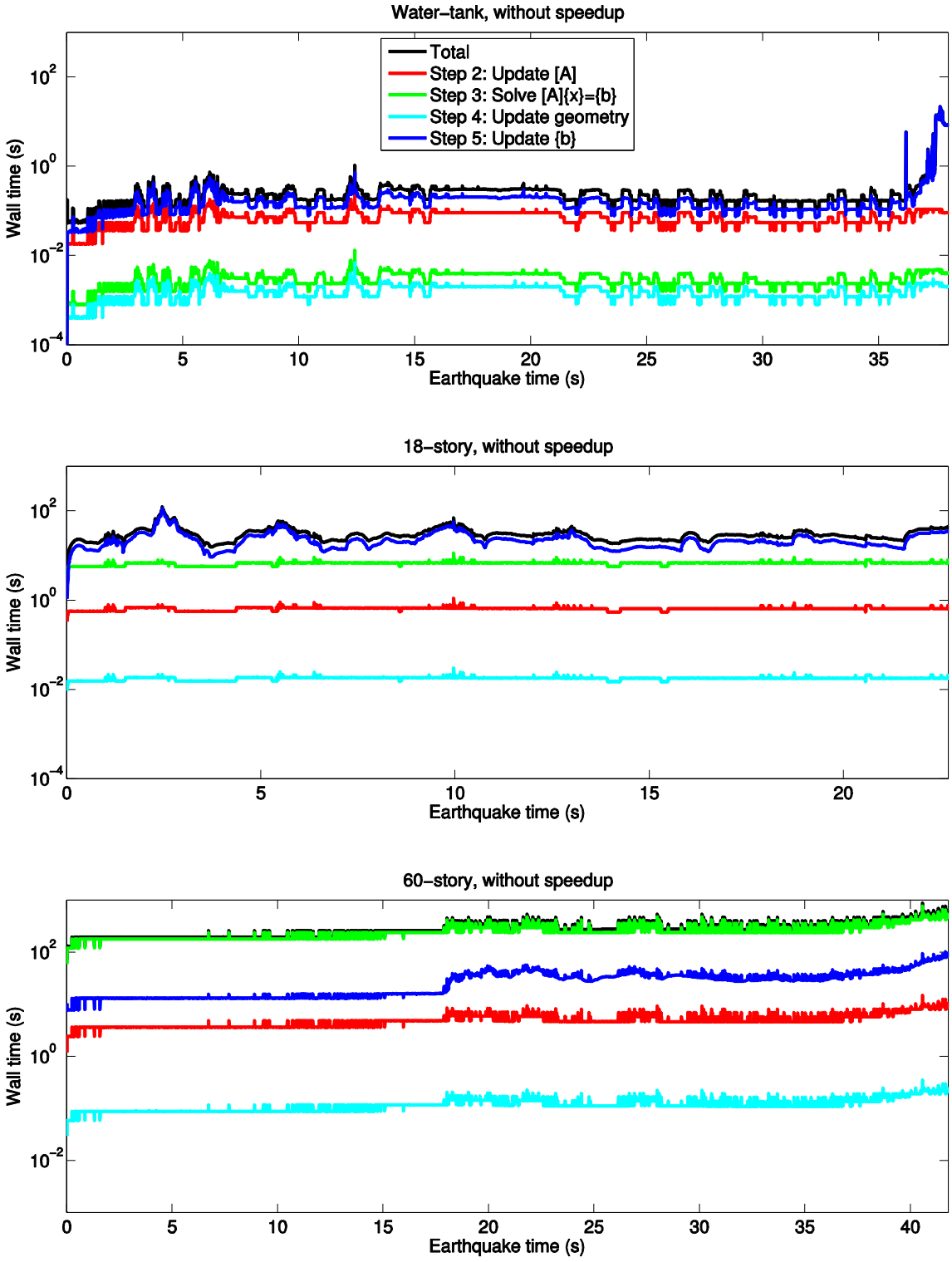

Figure 4.1: Wall time (sec) per earthquake-simulation time step, from 3 example collapse simulations: a small (top), a medium (middle), and a large (bottom) system. Part I's unoptimized FRAME3D is used.

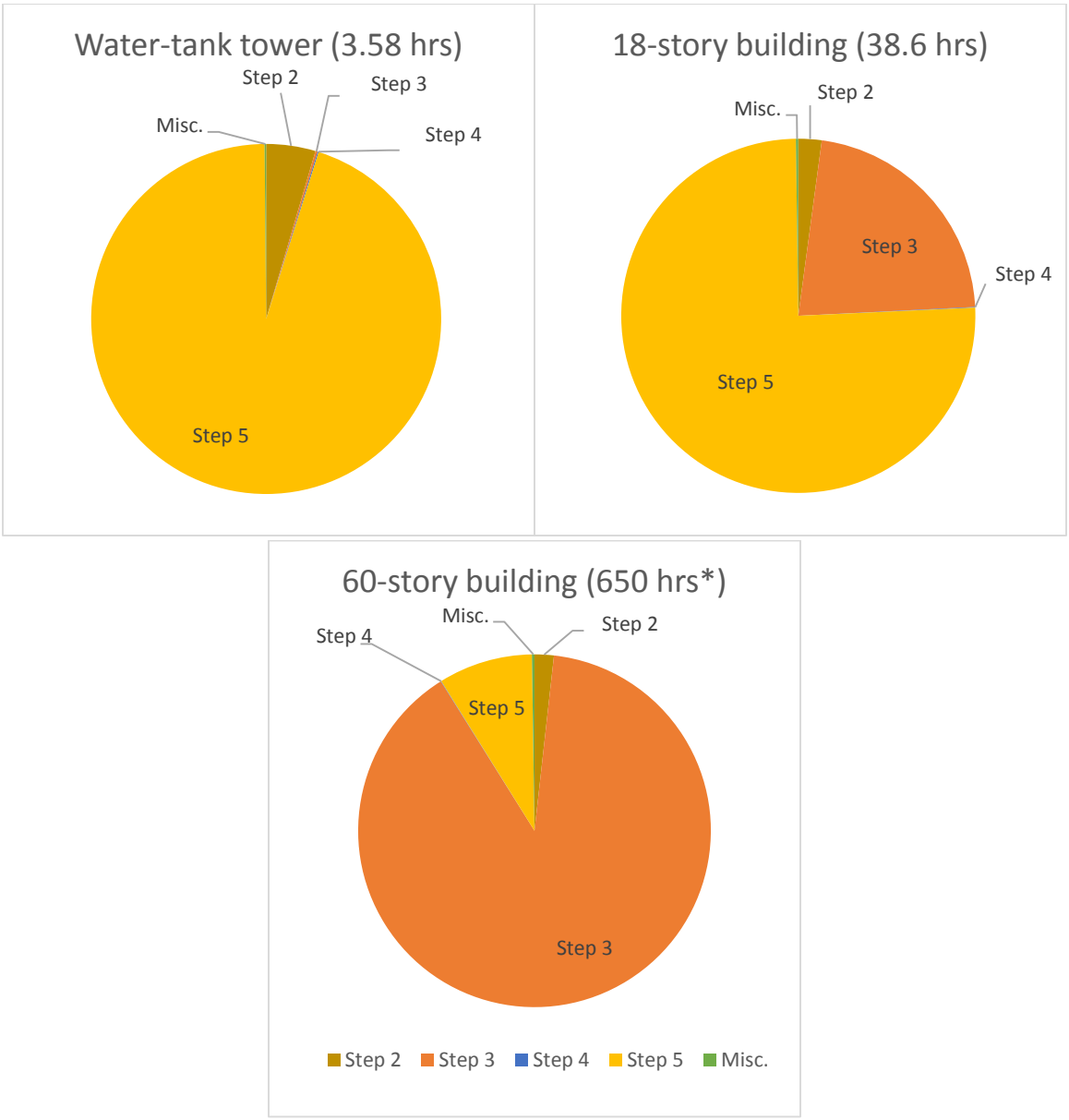

Figure 4.2: Computational cost breakdown of significant steps, from three collapse simulations. Part I's unoptimized FRAME3D is used.

*The 650 *hr* (27 *day*) simulation never actually ran. It is estimated based on: (1) the wall time of an optimized 1-core analysis, and (2) the relative speeds of optimized and unoptimized 1-core code.

Chapter 5

The Direct Solver

5.1 General

Many researchers have studied efficient solutions to the n-DOF linear equation $[A]\{x\} = \{b\}$ (Step 3 in §4.6). In this chapter, various LU-type direct solvers are explored:

- LU and Cholesky solvers in general (§5.1)
- Row-based solver (§5.2; the original FRAME3D solver)
- Column-based solver (§5.2)
- Blocked solver (§§5.2-5.3)
- Divide-and-conquer solver (§5.4).

The divide-and-conquer solver implemented with hybrid parallelism is chosen for PFRAME3D.

The LU solution procedure, which assumes that $[A]\{x\} = \{b\}$ can be solved without shifting, has two sub-steps: factorization and substitution.

(3.1) Factorization: Factor $[A]$ to an $[L][D][U]$ or $[L][U]$ system, where $[L]$ and $[U]$ are lower and upper triangular matrices, respectively, and $[D]$ is a diagonal matrix. This sub-step is often written as

$$[A] = [L][D][U] \text{ (or } [L][U]). \quad \text{(Eq. 5.1)}$$

(3.2) Substitution: Solve the factored system $[L][D][U]\{x\} = \{b\}$ with three equations:

$$[L]\{z\} = \{b\} \quad \text{(Eq. 5.2)}$$

$$[D]\{y\} = \{z\} \quad \text{(Eq. 5.3)}$$

$$[U]\{x\} = \{y\} \quad \text{(Eq. 5.4)}$$

where $\{z\} = [D][U]\{x\}$. Eq. 5.2 and 5.4 use forward and back substitution, respectively, because $[L]$ and $[U]$ are triangular. Eq. 5.3 is present if the system was factored as LDU (skipped if LU). Sub-steps 3.1 and 3.2 use about $\frac{n^3}{3}$ and n^2 multiplications, respectively, for an $n \times n$ linear system.

For algorithmic efficiency and storage savings, symmetry and positive-definiteness are considered. For a symmetric positive-definite $[A]$, $[L]^T = [U]$ and the factored system is $[L][D][L]^T\{x\} = \{b\}$ (or $[L][L]^T\{x\} = \{b\}$). The resulting procedure, called LDL^T or LL^T (Cholesky) factorization, requires $\frac{n^3}{6}$ multiplications—half of the LU factorization multiplication count.

For a banded $[A]$, the terms outside of the band can be skipped, reducing wall time and storage. As a result, factorization and substitution need $\frac{nm^2}{6}$ and nm multiplications, respectively, where m is the system half-bandwidth. And because $[A]$ is symmetric and banded, storage requirements reduce from n^2 to nm. A tall building has a narrow-band symmetric positive-definite $[A]$ matrix where m is roughly the number of DOFs per story level; e.g., for a 60-story building, $m \approx \frac{n}{60}$. Therefore, only banded Cholesky-type solvers are considered. The above simplifications are summarized in Table 5.1.

Table 5.1: Multiplication-division count and storage for LU and Cholesky factorization.

Factorization type	**# Multiplications in factorization**	**# Multiplications in substitution**	**Storage**
LU (or LDU), non-banded	$\frac{n^3}{3}$	n^2	n^2
Cholesky or LDL^T, non-banded	$\frac{n^3}{6}$	n^2	n^2
Cholesky or LDL^T, banded	$\frac{nm^2}{6}$	nm	nm

The Cholesky solvers in this chapter are subjected to a series of performance tests (solving $[A]\{x\} = \{b\}$ with varied system sizes n and half-bandwidths m). Increasing the size of a tall building usually means increasing its height. When considering increasing building height, n generally increases much faster than m. For example, if 1 story is added to a tall building, m is constant and n increases by m. That is not to say that increases in m are unimportant. On the contrary, taller buildings also tend to have larger footprints (higher m, or more DOFs per story) than shorter buildings. And the factorization costs

depend on m^2, a stronger than linear relationship. Nevertheless, the relationship between n and m is one where $\frac{n}{m}$ approximately reflects the number of stories in a building. Thus, to test a solver's suitability over a range of building heights, it is reasonable to vary n with a constant m.

For each solver in this chapter, performance results are reported first and algorithms explained afterwards.

5.2 Serial (1-core) solvers

This section shows that serial optimizations can significantly improve the performance of the direct solver. Four solvers are considered:

- a row-based solver (the original FRAME3D solver),
- a column-based solver,
- an optimized column-based solver, and
- a blocked solver.

Performance tests, where n ranges from 2500 to 160,000 with a constant $m = 1000$, show (Figure 5.1) that serial optimizations alone can make the direct solver much faster than the original row-based solver. For example, if $n = 80{,}000$ and $m = 1000$, factorization wall time is reduced from 753 sec (row-based) to 12.9 sec (blocked). These improvements are achieved using 1 core.

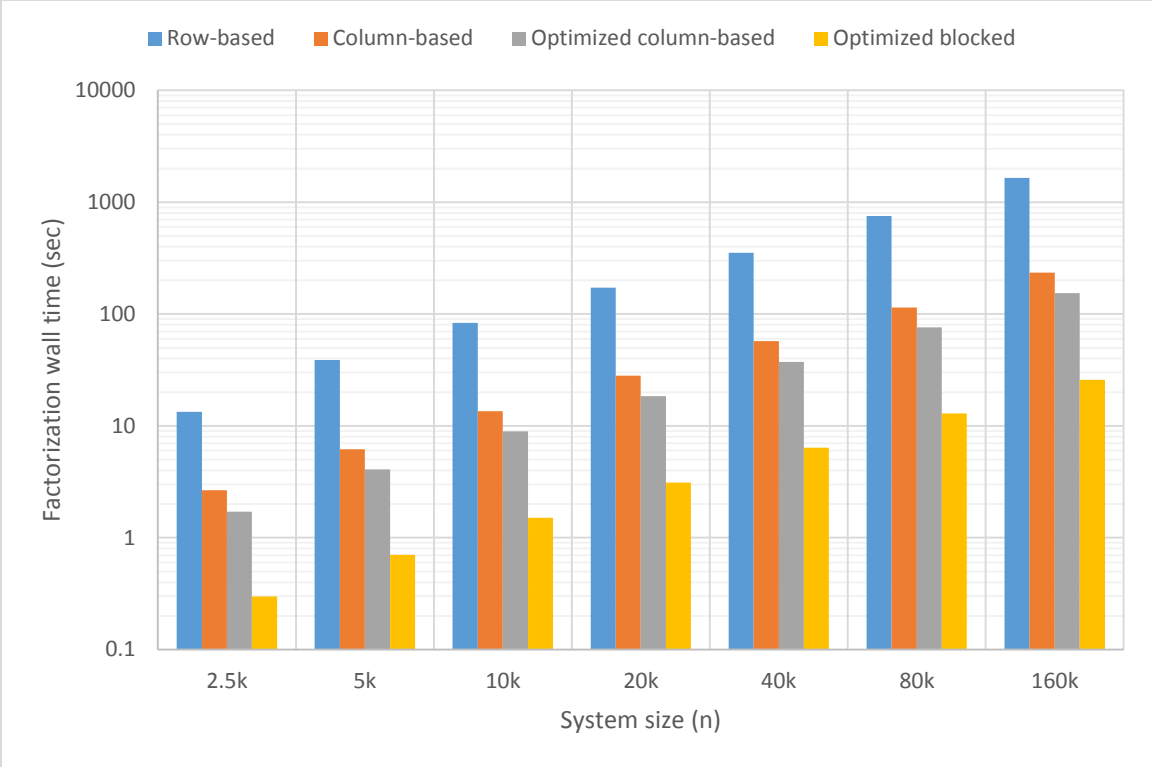

Figure 5.1: Wall times (sec) of serial factorization, using row-based, column-based, and blocked solvers, where m=1000. Intel MKL is used for the "optimized" solvers.

Begin with the original FRAME3D solver. It is a row-based variant of the LDL^T solver; it uses $[U]$ instead of $[L]$, where $[U]^T = [L]$. $[A]$ is stored as an $n \times m$ matrix (Table 5.2), and factored to $[U]^T[D][U]$ using the algorithm on the left of Table 5.3.

A column-based version of the original solver is shown on the right of Table 5.3. Table 5.3 shows that the only difference between the row- and column-based solvers is the switching of indices (and the renaming of mincol to minrow—but this is trivial). The column-based solver is more efficient (~6 times faster than row-based) because it considers *cache effects* (§A.2). Essentially, computer code is more efficient when data arrangement matches the data access pattern. In a column-major language (FORTRAN),

this means that factorization is more efficient when $[A]$ is stored as $m \times n$ (Table 5.3). For similar reasons, substitution is sped up with the $m \times n$ arrangement.

*Table 5.2: Storage schemes for a banded matrix [A], where * represents symmetry. In this example, n=5 and m=3.*

$n \times n$	$n \times m$	$m \times n$
$\begin{bmatrix} a_{00} & * & * & & \\ a_{10} & a_{11} & * & * & \\ a_{20} & a_{21} & a_{22} & * & * \\ & a_{31} & a_{32} & a_{33} & * \\ & & a_{42} & a_{43} & a_{44} \end{bmatrix}$	$\begin{bmatrix} a_{00} & a_{10} & a_{20} \\ a_{11} & a_{21} & a_{31} \\ a_{22} & a_{32} & a_{42} \\ a_{33} & a_{43} & \\ a_{44} & & \end{bmatrix}$	$\begin{bmatrix} a_{00} & a_{11} & a_{22} & a_{33} & a_{44} \\ a_{10} & a_{21} & a_{32} & a_{43} & \\ a_{20} & a_{31} & a_{42} & & \end{bmatrix}$

Table 5.3: Row- and column-based pseudocodes for the serial factorization of a banded positive-definite matrix.

Row-based	**Column-based**
$[A]$ is $n \times m$ $[A] = [U]^T[D][U]$	$[A]$ is $m \times n$ $[A] = [L][D][L]^T$

do i=1,n
  mincol = min(m,n-i+1)
  do j=2,mincol
  st = A(i,j)/A(i,1)
  do k=j,mincol
  A(i+j-1,k-j+1) =
  A(i+j-1,k-j+1) - A(i,k)*st
  continue
  A(i,j) = st
  continue
continue
	do i=1,n
	  minrow = min(m,n-i+1)
	  do j=2,minrow
	  st = A(j,i)/A(1,i)
	  do k=j,minrow
	  A(k-j+1,i+j-1) =
	  A(k-j+1,i+j-1) - A(k,i)*st
	  continue
	  A(j,i) = st
	  continue
	continue

Although much of the initial wall time reduction in Figure 5.1 can be attributed to the switch from a row- to a column-based solver, the equivalent *optimized* column-based factorization from the Intel Math Kernel Library (MKL), *dpbtf2*, is even faster. Intel MKL routines, designed specifically for Intel processors, include many additional optimizations (e.g., loop unrolling, vectorization, machine-level optimizations, etc.) that make it difficult to outperform (*dpbtf2* is ~1.5 times faster than un-optimized column-based).

Wall time is further reduced by switching to a *blocked solver*. The blocked solver is a generalization of the column-based solver; it factors by block columns instead of scalar (1 × 1 block) columns (Remon, Quintana-Orti, and Quintana-Orti 2007). Figure 5.1 shows that an optimized 1-core blocked solver is ~6 times faster than the optimized 1-core column-based one. Although the total operation count is similar, working with blocks reduces cache misses (Ballard et al. 2009). Used here is the Intel MKL version of the blocked factorization, *dpbtrf*, where block sizes are optimized for the processors' cache sizes.

To understand blocked factorization, consider the matrix $[A]$, which is split into blocks such that

$$[A] = \begin{bmatrix} [A_{00}] & * & * & & \\ [A_{10}] & [A_{11}] & * & * & \\ [A_{20}] & [A_{21}] & [A_{22}] & * & * \\ & [A_{31}] & [A_{32}] & [A_{33}] & * \\ & & [A_{42}] & [A_{43}] & [A_{44}] \end{bmatrix} \quad \text{(Eq. 5.5)}$$

where $*$ represents symmetry. Assume that the first block column ($[A_{i0}]$, $i \in 0,1,2$) has been factored already. To continue (using the next block column, $[A_{i1}]$, $i \in 1,2,3$):

(1) Factor the diagonal block

$$[A_{11}] = [L_{11}][L_{11}]^T \quad \text{(Eq. 5.6)}$$

(2) Update the block column

$$[A_{21}](=[L_{21}]) = [A_{21}][L_{11}]^{-T} \quad \text{(Eq. 5.7)}$$

$$[A_{31}](=[L_{31}]) = [A_{31}][L_{11}]^{-T} \quad \text{(Eq. 5.8)}$$

(3) Update across

$$[A_{22}] = [A_{22}] - [L_{21}][L_{21}]^{T} \quad \text{(Eq. 5.9)}$$

$$[A_{32}] = [A_{32}] - [L_{31}][L_{21}]^{T} \quad \text{(Eq. 5.10)}$$

$$[A_{33}] = [A_{33}] - [L_{31}][L_{31}]^{T}. \quad \text{(Eq. 5.11)}$$

The serial optimizations in this section are shown to significantly improve the performance of the direct solver. Without adding computer resources (still using 1 core), the $n = 80{,}000$ and $m = 1000$ factorization wall time is reduced from 753 sec (row-based) to 12.9 sec (blocked).

Single-core optimizations are also included for the substitution step; e.g., for $n = 80{,}000$ and $m = 1000$, substitution wall time is reduced from 2.37 sec (row-based) to 0.36 sec (optimized Intel MKL *dpbtrs*).

For small systems (e.g., elastofiber elements with interior nodes, where $n \leq 36 <$ typical block size ≈ 64), the optimized column-based solver is most efficient, with factorization and substitution about 1.6 and 1.2 times faster, respectively, than the original row-based solver.

5.3 Multi-threaded blocked solver

The blocked solver from §5.2 is easily parallelized in the shared-memory context (multiple cores in a computer node) because only matrix-matrix operations (Eq. 5.6 – 5.11) are performed. Shared-memory parallelism is also known as *multi-threading* (§A.1) where each core executes 1 thread. Figure 5.2 shows that multi-threading the blocked solver further reduces factorization wall time, e.g., for $n = 80{,}000$ and $m = 1000$, from 12.9 sec (1 core) to 3.47 sec (8 cores).

Shared-memory parallelism is often efficient because there is no communication cost; however, a maximum of 8 cores (the number of cores in 1 node) may be utilized. To further reduce wall time (by using more than 8 cores), a distributed-memory solver must be considered.

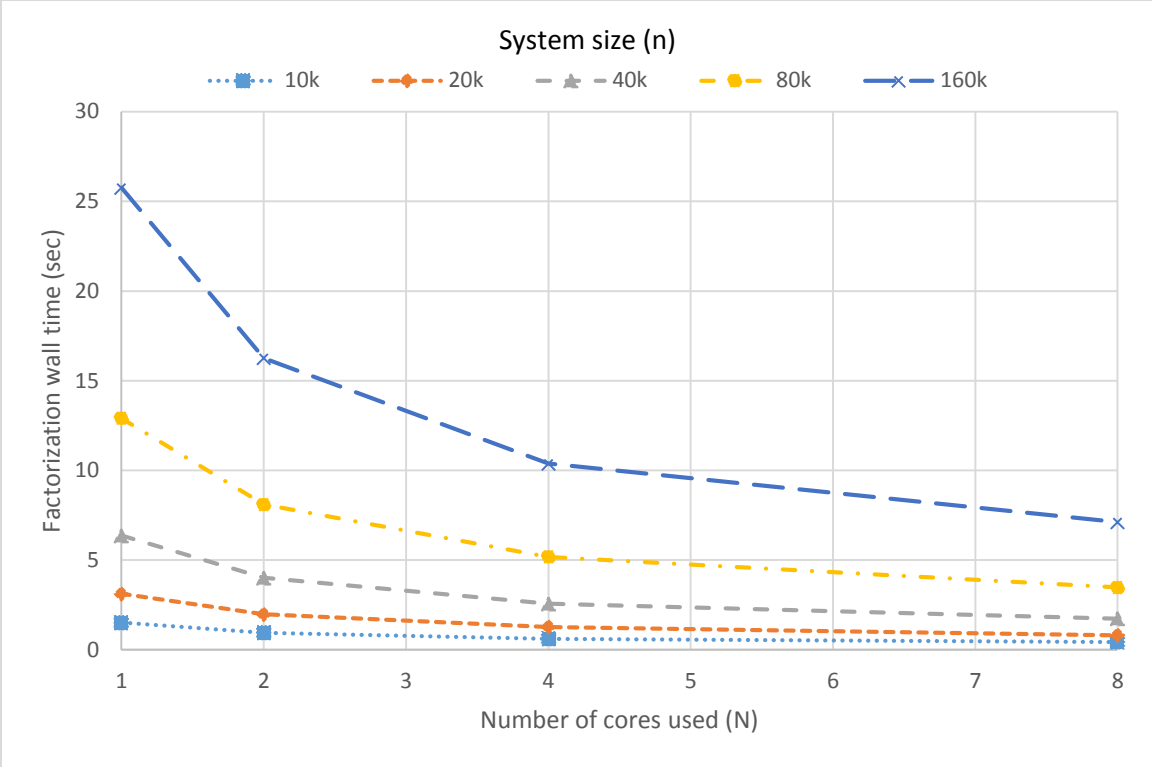

Figure 5.2: Wall times (sec) of multi-threaded blocked factorization (dpbtrf) with 1 to 8 cores. Each curve corresponds to a different system size n with m=1000.

5.4 Divide-and-conquer solver

The divide-and-conquer solver is a distributed-memory extension of the multi-threaded blocked solver in §5.3. Figure 5.3 shows that for large enough systems, it can factor faster than the 8-core blocked solver. For example, with 256 cores, it factors the $n = 80{,}000$, $m = 1000$ system in 2.10 sec.

Figure 5.3 shows an initial "penalty," where the 8-core blocked solver is faster than a 16- or 32-core divide-and-conquer solver. This penalty is a result of "fill-in," which

increases the overall operation count by about 4 (Cleary and Dongarra 1997). It is further described below, as part of the discussion on the divide-and-conquer algorithm.

A weak-scaling curve (defined in §4.4) is constructed in Figure 5.3 (solid green). This curve shows, for example, that if workload doubles from $n = 80{,}000$ to $n = 160{,}000$ with a constant $n = 5000$ workload per 8 cores, factorization wall time increases by a factor of about 1.22. (Recall from §4.4.2 that weak-scaling is "ideal" if this factor is 1.0 and "poor" if it is 2.0.)

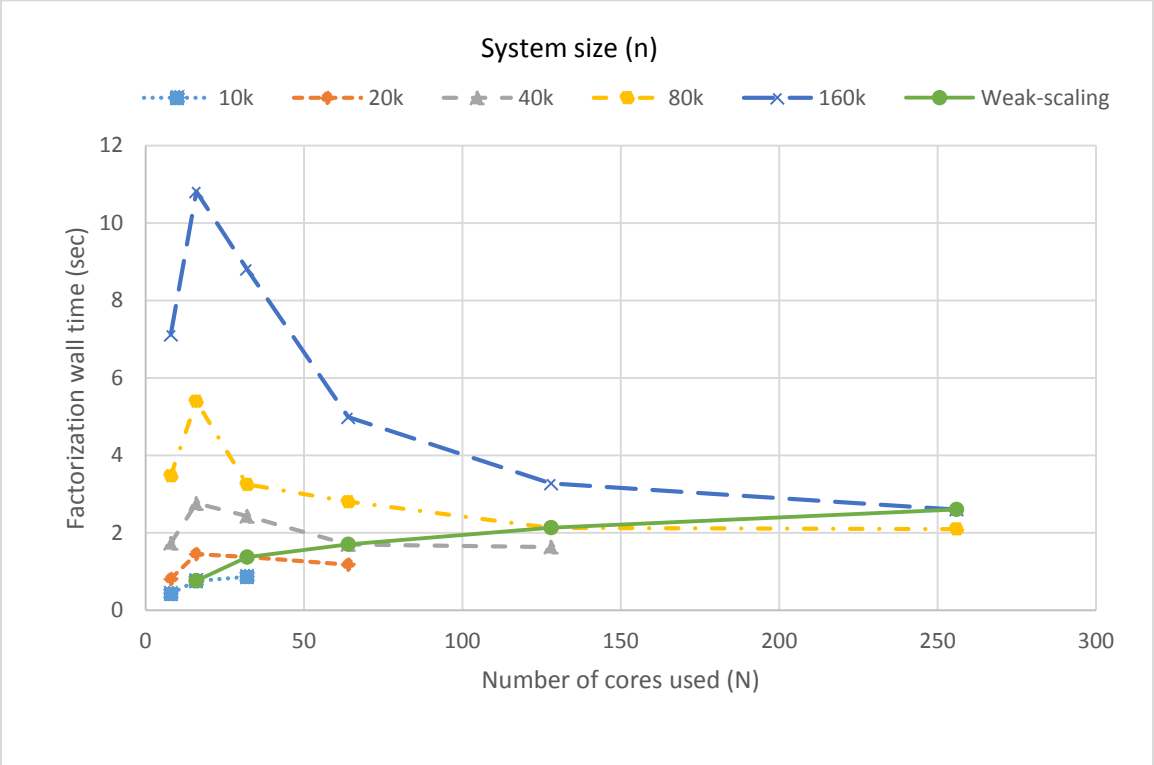

Figure 5.3: Wall times (sec) of divide-and-conquer factorization with 8 to 256 cores. Each curve corresponds to a different system size n with m=1000. With 8 cores, the multi-threaded blocked factorization from §5.3 is used. A weak-scaling curve (solid green) is constructed (where workload is n = 5000 per 8 cores).

Performance results for divide-and-conquer substitution (Figure 5.4) show that "fill-in" has little effect on parallel substitution and that the weak-scaling curve is relatively constant. For example, if workload doubles from $n = 80{,}000$ to $n = 160{,}000$ with a constant $n = 5000$ workload per 8 cores, substitution wall time increases by a factor of 1.17.

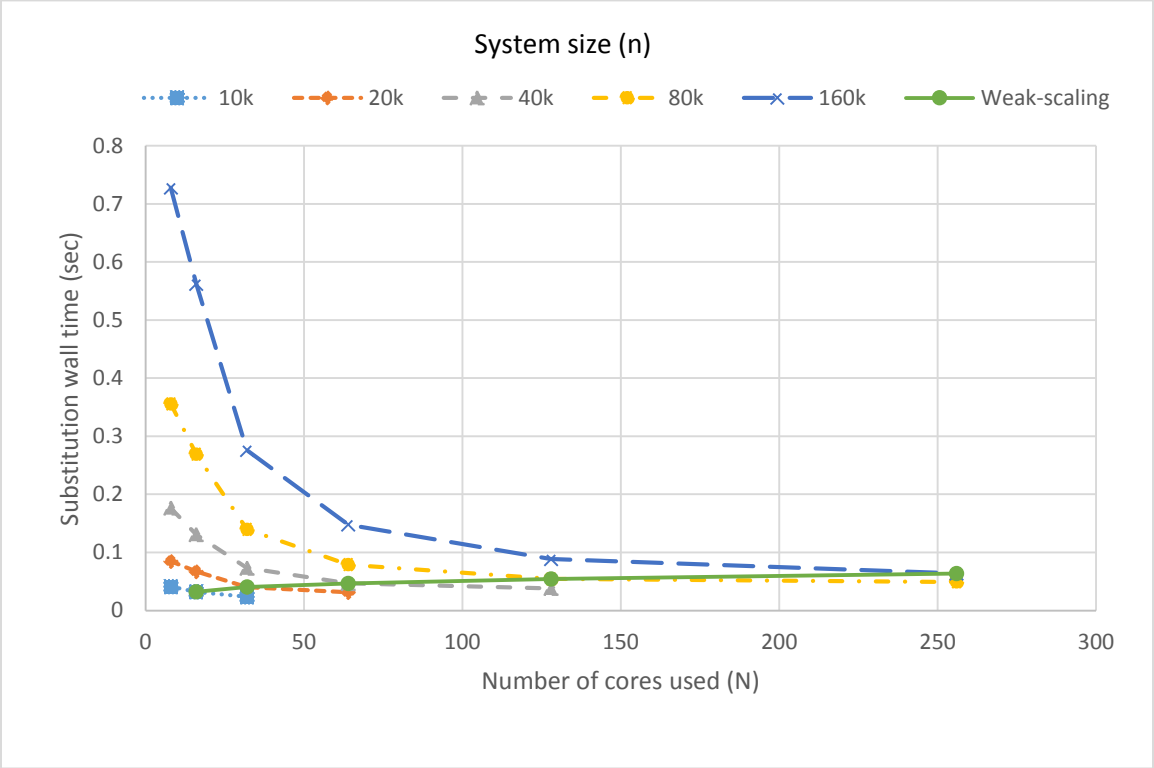

Figure 5.4: Wall times (sec) of divide-and-conquer substitution with 8 to 256 cores. Each curve corresponds to a different system size n with m=1000. With 8 cores, the multi-threaded blocked substitution from §5.3 is used. A weak-scaling curve (solid green) is constructed (where workload is $n = 5000$ *per 8 cores).*

The divide-and-conquer solver is designed for narrow-band systems, or $m \ll n$ (Cleary and Dongarra 1997). $[A]$ is divided into "large blocks" (1 block per process), as shown in Figure 5.5 and Figure 5.6, where each block is (mostly) factored locally and independently. ($[A]$ is in symmetric band form $m \times n$, locally stored in p processes as $m \times n_b$, where $n_b \approx \frac{n}{p}$. Here, p also equals the number of "large blocks" used.) A permutation matrix $[P]$, which depends on n, m, and p, determines how $[A]$ is uncoupled. To solve the linear equation:

(1) Left multiply $[A]\{x\} = \{b\}$ with $[P]$ to get

$$[P][A]([P]^T[P])\{x\} = [P]\{b\} \quad \text{(Eq. 5.12)}$$

(2) Factor

$$[P][A][P]^T = [L][L]^T \quad \text{(Eq. 5.13)}$$

(3) Solve

$$[L][L]^T\{\hat{x}\} = \{\hat{b}\} \quad \text{(Eq. 5.14)}$$

where $\{\hat{x}\} = [P]\{x\}$ and $\{\hat{b}\} = [P]\{b\}$,

(4) Recover

$$\{x\} = [P]^T\{\hat{x}\}. \quad \text{(Eq. 5.15)}$$

The permuted $[A]$ matrix is stored locally (e.g., as shown in Figure 5.7). Each local matrix is factored independently (e.g., to Figure 5.8) using

$$[A_i] = [L_i][L_i]^T \quad \text{(Eq. 5.16)}$$

$$[L_i][B_i']^T = [B_i]^T \quad \text{(Eq. 5.17)}$$

$$[C_i'] = [C_i] - [B_i'][B_i]^T \quad \text{(Eq. 5.18)}$$

$$[L_i][G_i]^T = [D_i] \quad \text{(Eq. 5.19)}$$

$$[E_i] = [G_i][G_i]^T \quad \text{(Eq. 5.20)}$$

$$[F_i] = [B_i'][H_i]^T \quad \text{(Eq. 5.21)}$$

where $[H_i]$ are the last m columns of $[G_i]$. At this point, it is worth noting that the "interface" blocks ($[E_i]$, $[F_i]$, and $[C_i']$) are not completely factored yet. Figure 5.9 shows that, as the final step in divide-and-conquer factorization, these "interface" blocks are combined as a tridiagonal block system and factored. The local storage of the factored permuted matrix is shown in Figure 5.10, ready for substitution.

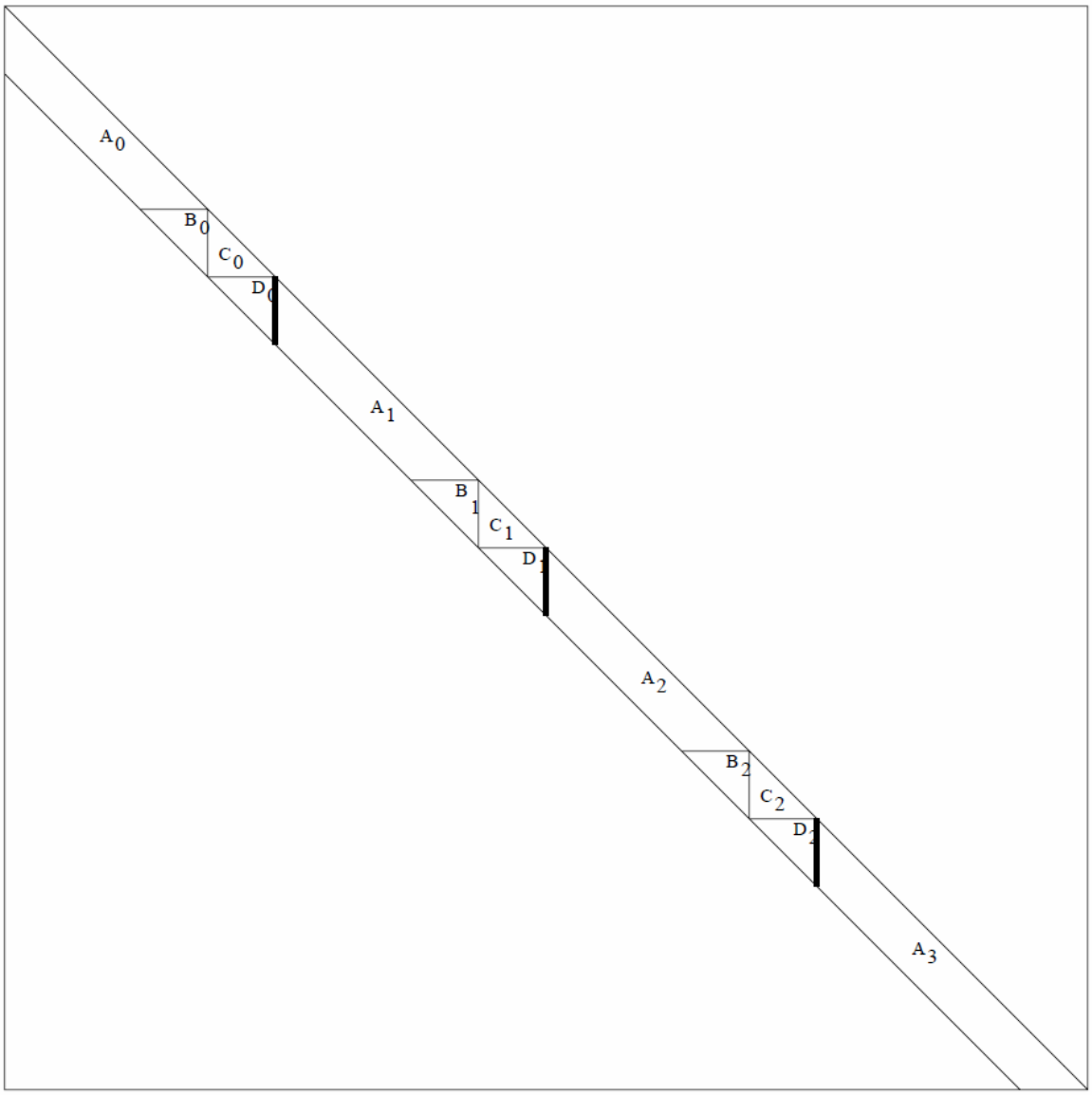

Figure 5.5: [A] matrix before divide-and-conquer permutation (Cleary and Dongarra 1997, numbering convention adjusted). Shown are the diagonal and lower half of the matrix. This example uses 4 processes.

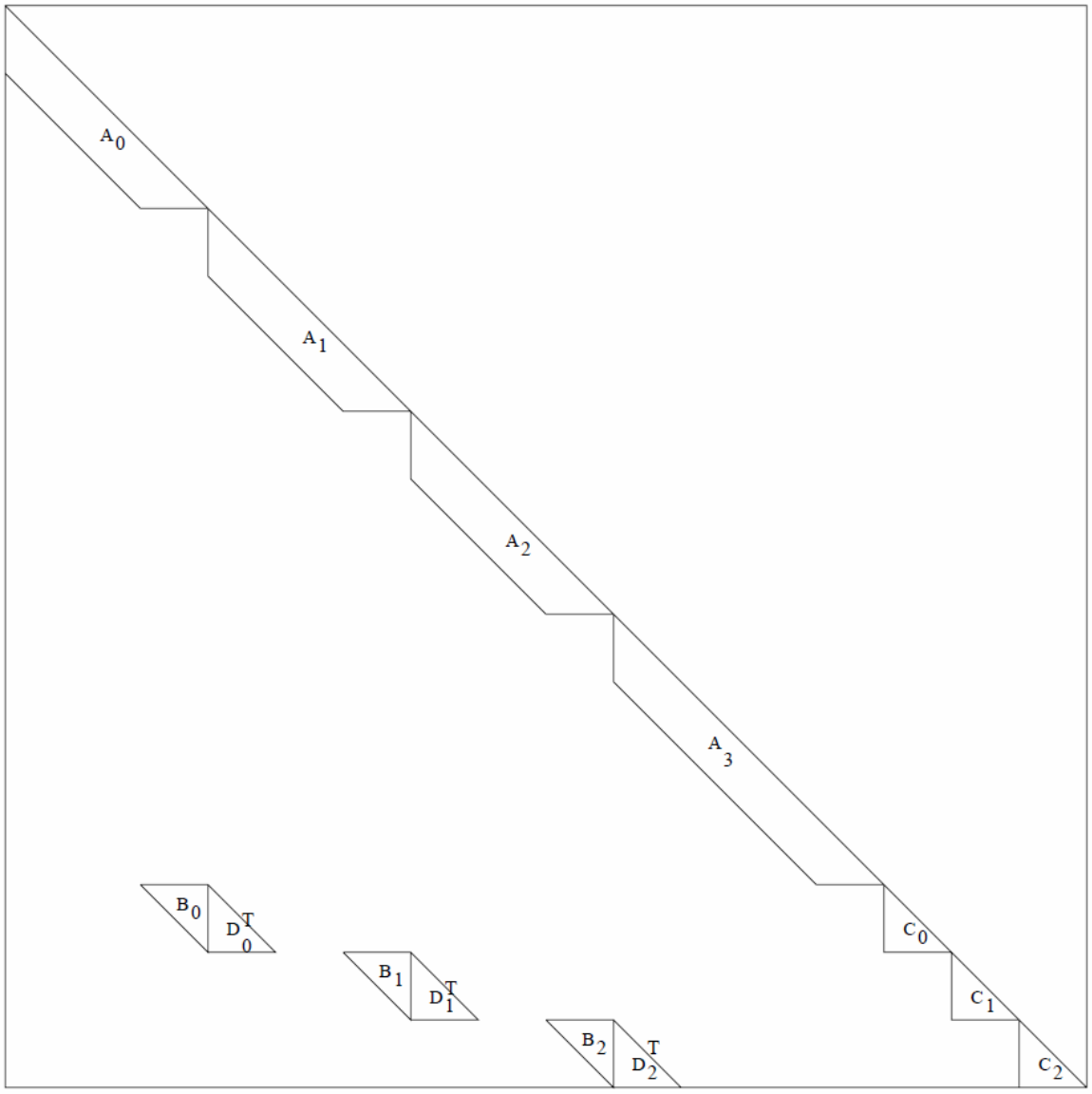

Figure 5.6: [A] matrix after divide-and-conquer permutation (Cleary and Dongarra 1997, numbering convention adjusted). Shown are the diagonal and lower half of the permuted matrix. This example uses 4 processes.

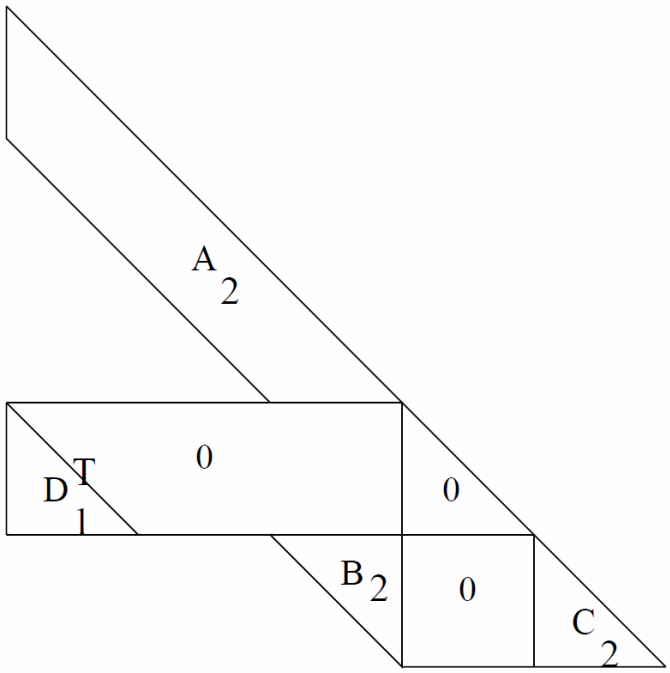

Figure 5.7: Local storage of process 2 after divide-and-conquer permutation, before factorization (Cleary and Dongarra 1997). Only the diagonal and lower half of the matrix are stored.

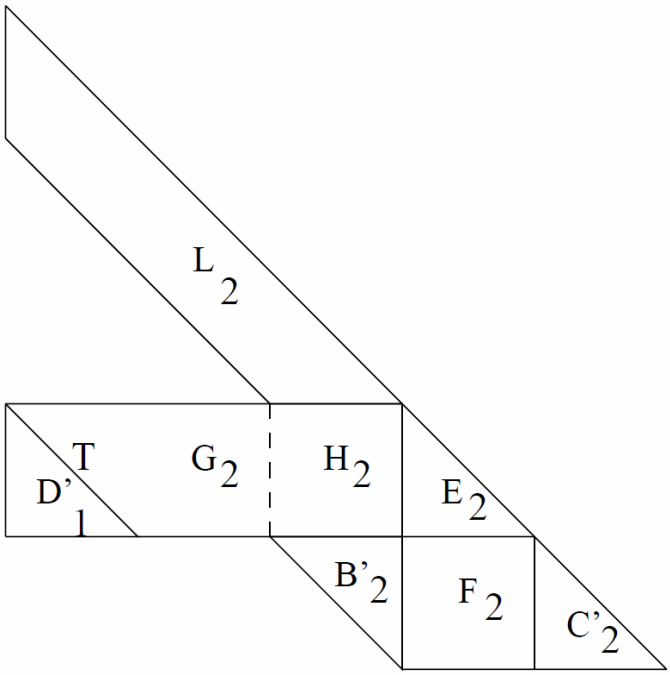

Figure 5.8: Local storage of process 2 after the independent portion of factorization (Cleary and Dongarra 1997). Only the diagonal and lower half of the matrix are stored.

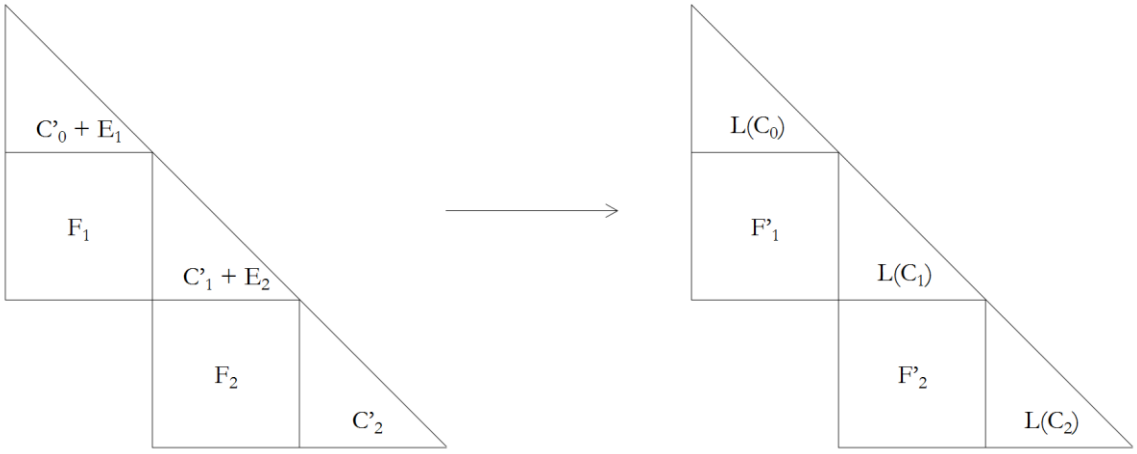

Figure 5.9: Final step for the factorization of the "interface" blocks combined as a tridiagonal block system. Shown are the diagonal and lower half of the matrix. This example shows 3 interfaces (4 processes are assumed).

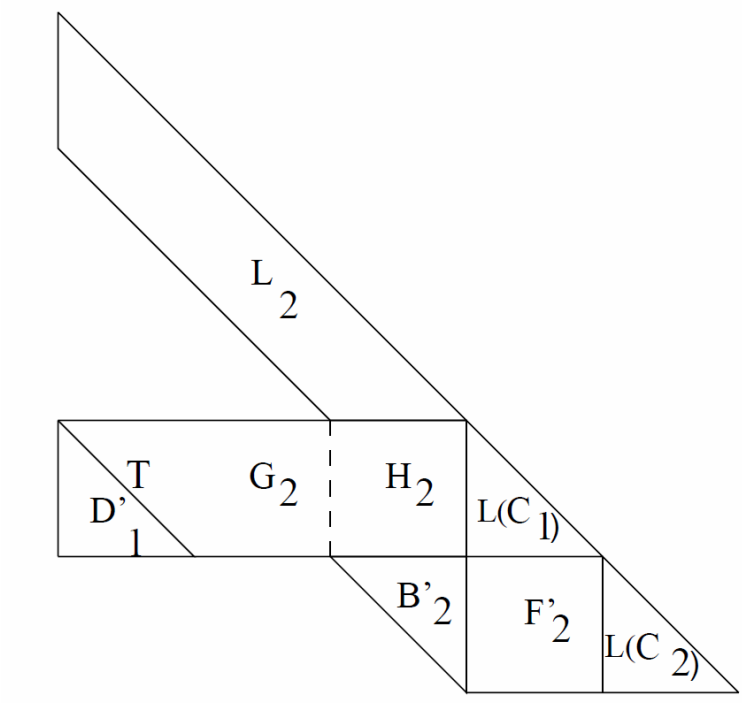

Figure 5.10: Local storage of process 2 at the end of factorization (Cleary and Dongarra 1997, edited). Only the diagonal and lower half of the matrix are stored.

$[A]$ can be divided successfully only if $2(m-1) \leq n_b$. In other words, p has the upper limit

$$p \leq \frac{n}{2(m-1)} \quad \text{(Eq. 5.22)}$$

after which additional parallelization is not possible. For example, if $n = 40{,}000$ and $m = 1000$, $[A]$ may be split into a maximum of 20 local blocks. So as to not limit the divide-and-conquer solver to (for this example) 20 cores, a hybrid-parallel implementation is used, where

- p is the number of computer nodes used (1 process per computer node), and
- the local operations (e.g., Eq. 5.16 – 5.21) are performed in parallel (8 cores per process).

Thus for the current example, up to 160 cores may be used. It is worth noting, however, that for a fixed problem size, as p is increased to approach the limit set by Eq. 5.22, the divide-and-conquer solver becomes less efficient. This is due to the increasing cost to factor the "interface" blocks (as p is increased, there are overall more "interface" blocks) relative to cost of performing the independent calculations of Eq. 5.16 – 5.21. Fortunately, if problem size is assumed to grow with n, more cores may be used for larger problems (e.g., 320 cores if $n = 80{,}000$ and $m = 1000$, etc.).

The primary drawback of the divide-and-conquer solver is "fill-in." Due to the permutation, matrices $[E_i]$, $[F_i]$, and $[G_i]$ must also be factored, increasing the overall operation count to about 4 times greater than sequential Cholesky factorization (Cleary and Dongarra 1997). This effect is observable in Figure 5.3, where the divide-and-conquer solver is slower than the 1-process (8-core) blocked solver if 4 processes (32 cores) or less are used.

But for increasing n with constant m, the operation count per process can be bounded. Each process operates on its own local matrix (e.g., Figure 5.8), which is $n_b \times n_b$. Eq. 5.16, computed by the multi-threaded blocked factorization from §5.3, operates on a band matrix of size $m \times (n_b - 2m)$. Eq. 5.17, 5.18, 5.19, and 5.21 operate on $m \times m$ matrices. And Eq. 5.19 and 5.20 operate on matrices smaller than $m \times n_b$. Increasing p reduces n_b, so as long as m is constant, the per-process operation counts for Eq. 5.16 – 5.21 can be bounded. Additionally, it can be seen from Figure 5.9 that the cost to finish factoring the "interface" blocks is a function of m and p. Finally, because the factored permuted system is stored locally, substitution can be done independently with costs related to n_b and m. In other words, the cost of the divide-and-conquer algorithm is bounded by a function of n_b, m, and p—not n directly.

Communication, which occurs three times, has a cost that is bounded by a function of m. First, at the initial permutation, each process gives $[D_i]^T$, an $m \times m$ matrix, to its neighbor. Second, in order to finish factoring the "interface" blocks, each process gives $[C_i']$, an $m \times m$ matrix, to its neighbor. Third, before substitution begins, each process gives a $2m \times 1$ vector to its neighbor. These communication costs are independent of n.

Finally, the divide-and-conquer solver has a major advantage that is more thoroughly discussed in the next chapter: preparation and communication costs are low when inserted into the context of PFRAME3D's global iterations. Other distributed-memory solvers, such as the Cho (2012) parallel pipelined solver (§B.1) are considered, too, but the divide-and-conquer approach is found to be more suitable for large narrow-band systems.

5.5 Conclusion

In this chapter, several Cholesky direct solvers are considered and one is chosen for PFRAME3D. First, serial optimizations are shown to be significant, e.g., for the $n = 80{,}000$ and $m = 1000$ system, factorization wall time is reduced from 753 sec (row-based) to 12.9 sec (1-core blocked, §5.2). Next, shared-memory parallelization is shown to further reduce wall time of the same computation to 3.47 sec (8-core blocked, §5.3). Finally, distributed-memory parallelization is shown to reduce it even further to 2.10 sec (divide-and-conquer with 256 cores, §5.4).

Recall (§4.6) that the 60-story building dynamic time-history collapse simulation, with $n = 30{,}606$, $m = 514$, would take 650 hrs (27 days) to complete if run with Part I's unoptimized FRAME3D. Recall also that the row-based direct solver would use about 89% of those 27 days. If serial optimizations are applied to the direct solver, the overall 1-core simulation would take only 83.6 hrs (3.5 days). Out of the 83.6 hrs, 14.2 hrs are spent in the optimized 1-core direct solver. Parallelization of the direct solver reduces the 14.2 hrs (1-core blocked) to 3.74 hrs (128-core divide-and-conquer).

In other words, the direct solver is no longer the most time-consuming part of the overall simulation. 69.4 hrs (i.e., 83.6 hrs minus 14.2 hrs) are spent outside of the direct solver. Therefore, the next challenge is to speed up the rest of FRAME3D. This is the topic of §6.

Chapter 6

Domain Decomposition and Parallel Updating

6.1 General

So far, Step 3 in §4.6 is sped up. §6, which focuses on the remaining steps, is organized as follows:

- Domain decomposition (§6.2)
- Parallel updating of $\{b\}_i$ (§6.3; Step 5 in §4.6)
- Parallel updating of $[A]_i$ (§6.4; Step 2 in §4.6)

- Parallel geometric updating (§6.5; Step 4 in §4.6)
- Parallel convergence check (§6.6; Step 1 in §4.6)
- Parallel input-output (§6.7)
- Miscellaneous considerations (§6.8).

The result of this chapter is an efficient hybrid-parallel FRAME3D.

For clarity in this chapter, the term *node* is used in the finite-element sense, a joint in the structural model. The parallel-computing *node* is referred to as a *process* to avoid confusion. (A *process* is a single instance of a computer program being run. In a typical hybrid-parallel program, each computer *node* in a computer cluster starts a *process*. See §A.1 for more on terminology usage.)

6.2 Domain decomposition

6.2.1 General

This section shows how domain decomposition—the splitting up of a structural model across processes as shown in Figure 6.1—is implemented in PFRAME3D. The primary reason to conduct domain decomposition is to address the fact that a single computer may not have enough RAM to hold all of the nodal, element, fiber, hysteretic, etc. data of a very large model. Fortunately in the distributed-memory context, domain decomposition can bound the per-process (i.e., per-computer) storage requirements. Even if this RAM limit is not reached, domain decomposition still provides a more efficient use

of computing resources because parallelization eliminates the need for a given process to access the entire data set (describing the structural model).

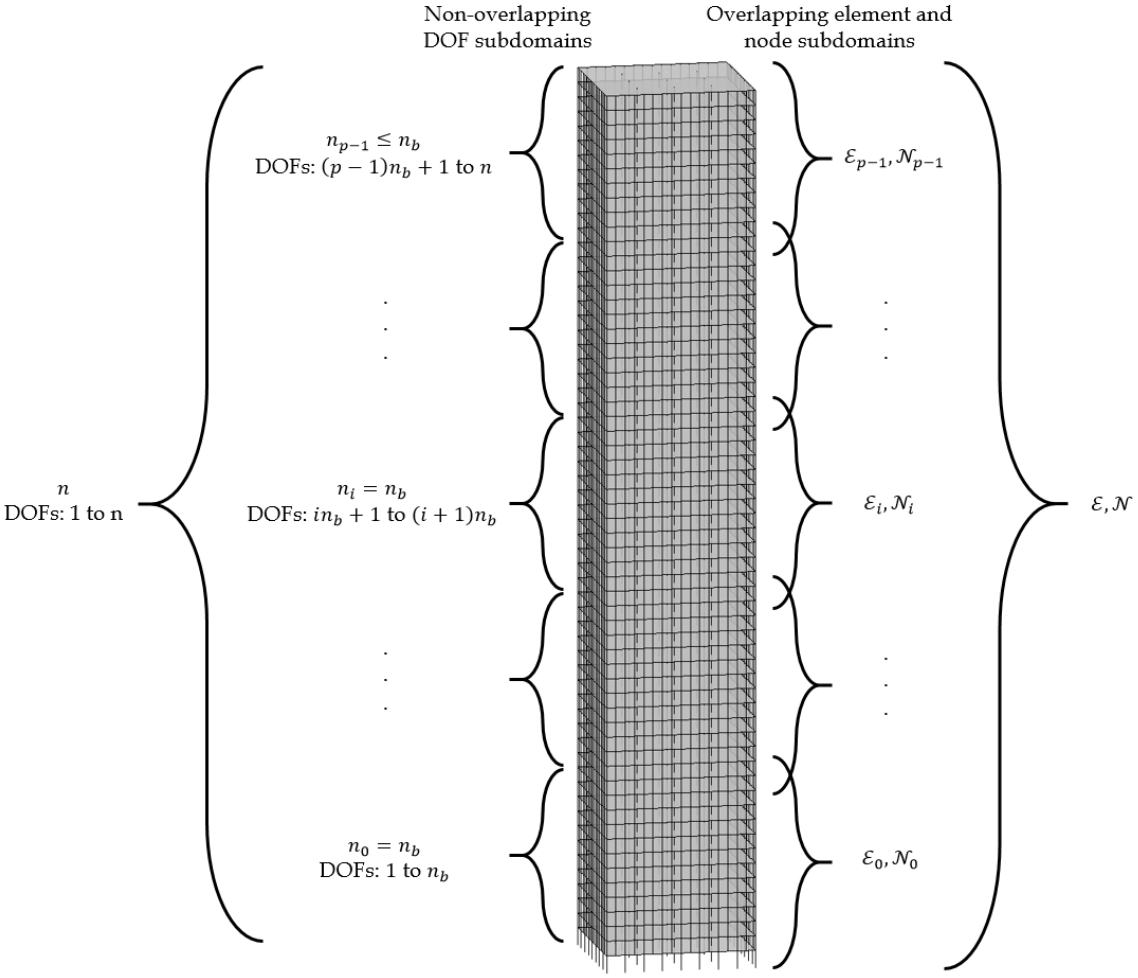

Figure 6.1: Domain decomposition of a structure.

Previous parallel implicit programs address domain decomposition in two parts: one scheme for element-state updates, and another for the equation solver. OpenSeesSP and the Cho (2012) parallel program approach domain decomposition in this manner. This approach, however, results in additional "preparation" costs. For example, Cho (2012) noted that n communication steps are needed to transition from the element-state

updates to the parallel-pipelined solver. He showed that these costs are asymptotically negligible for wide-band systems (as n and $m \to \infty$, compared to the overall factorization costs). But for narrow-band systems, which are of interest in the present work, these costs are non-negligible.

A "unified" approach is developed for PFRAME3D. Domain decomposition is most effective when inter-process communication is minimized between subroutines, e.g., between element-state updates and the direct solver of an implicit program. The "preparation" costs noted in Cho (2012) are a non-issue for parallel explicit programs because there is no linear equation solver in the explicit algorithm. The extent of communication in explicit programs is between "nearest neighbors." That is, a process communicates only data from the boundary of its subdomain to the neighboring process that shares the same boundary. This paradigm, which is well suited for parallel computing, is applied to PFRAME3D, an implicit program. Domain decomposition is implemented such that, between the element-state updates and the global solver, processes need only to communicate $m \times 1$ vectors (the boundary) to their nearest neighbors. Essentially, the domain decomposition scheme for the element-state updates is made to match that of the divide-and-conquer solver. This "unified" domain decomposition scheme results in the "nearest neighbor" communication pattern that is rarely accomplished in parallel implicit programs, making PFRAME3D unique. It is achieved in three parts:

- DOF allocation (§6.2.2)
- Element allocation (§6.2.3)
- Node allocation (§6.2.4).

Additional notes on domain decomposition are presented in §6.2.5. The "DOF" data set is distinct from the "node" data set in the following way: the "DOF" data set refers to any global array that is stored in either $m \times n$ or $n \times 1$ form, e.g., $[A]$, $\{x\}$, and $\{b\}$, whereas the "node" data set contains the coordinates, dimensions, deformation, etc. of every building joint.

6.2.2 DOF allocation

Start with the fact that the divide-and-conquer solver uncouples the DOFs in $[A]$ as shown in Figure 5.6. Before this permutation, $[A]$ is represented as an $m \times n$ band (Figure 5.5), and process $i \in [0, p-1] \subset \mathbb{Z}$ gets a non-overlapping $m \times n_i$ block of $[A]$— where m is the half-bandwidth, n is the total number of DOFs, p is the number of processes used, and n_i is the number of DOFs assigned to a process i as defined by Eq. 6.1 – 6.2. For process $i \neq p-1$,

$$n_i = n_b = \begin{cases} \text{int}\left(\frac{n}{p}\right), & \text{if mod}\left(\frac{n}{p}\right) = 0 \\ \text{int}\left(\frac{n}{p}\right) + 1, & \text{if mod}\left(\frac{n}{p}\right) \neq 0 \end{cases} \qquad \text{(Eq. 6.1)}$$

where n_b is the standard block size. For process $i = p-1$,

$$n_{p-1} = n - (p-1)n_b \leq n_b. \qquad \text{(Eq. 6.2)}$$

Denote process i's block as $[A]_i$. ($[A]_i$ is different from $[A_i]$ in Figure 5.5 to Figure 5.7; the former refers to the entire local block, while the latter refers to a sub-block and is irrelevant in the present chapter.)

The divide-and-conquer solver also requires that $\{x\}$ and $\{b\}$ be split up. To use it, process i gets an $n_i \times 1$ portion of both vectors, denoted $\{x\}_i$ and $\{b\}_i$.

Other $m \times n$ and $n \times 1$ arrays are split similarly—into $m \times n_i$ and $n_i \times 1$ blocks, respectively. Recall (§4.6) that $[A]\{x\} = \{b\}$, is simplified from the dynamic equation of motion. Thus, process i gets a non-overlapping block from $[M]$, $[C]$, $\left[K_T^l\right]$, $\{\Delta U\}$, $\left\{f_g\right\}$, $\{R^l\}$, $[r]$, $\{U(t)\}$, and $\{U^l\}$, denoted $[M]_i$, $[C]_i$, $\left[K_T^l\right]_i$, $\{\Delta U\}_i$, $\left\{f_g\right\}_i$, $\{R^l\}_i$, $[r]_i$, $\{U(t)\}_i$, and $\{U^l\}_i$. Process i also gets $[K]_i^{ps}$, a non-overlapping block from $[K]^{ps}$, the global stiffness matrix due to PS elements (§2.7). No process ever has a complete global copy of any of the above arrays.

6.2.3 Element allocation

Recall (§2.2) that $\left[K_T^l\right]$ & $\{R^l\}$ are assembled from beam, PZ, diaphragm, and/or spring elements. In parallel, process i assembles $\left[K_T^l\right]_i$ & $\{R^l\}_i$ only. Thus it needs only the set of elements that contribute to at least 1 DOF of $\left[K_T^l\right]_i$ & $\{R^l\}_i$, denoted $\mathcal{E}_i \subset \mathcal{E}$, where $\mathcal{E}$ is the set of elements in the entire model. If an element contributes to $\left[K_T^l\right]_i$ & $\{R^l\}_i$ and $\left[K_T^l\right]_{i+1}$ & $\{R^l\}_{i+1}$, it belongs to both $\mathcal{E}_i$ and $\mathcal{E}_{i+1}$; multiple copies are allowed because the element-level calculations are deterministic. As shown in Figure 6.2, element subdomains can overlap by up to 1 story worth of elements. The percent of overlap is smaller for taller buildings.

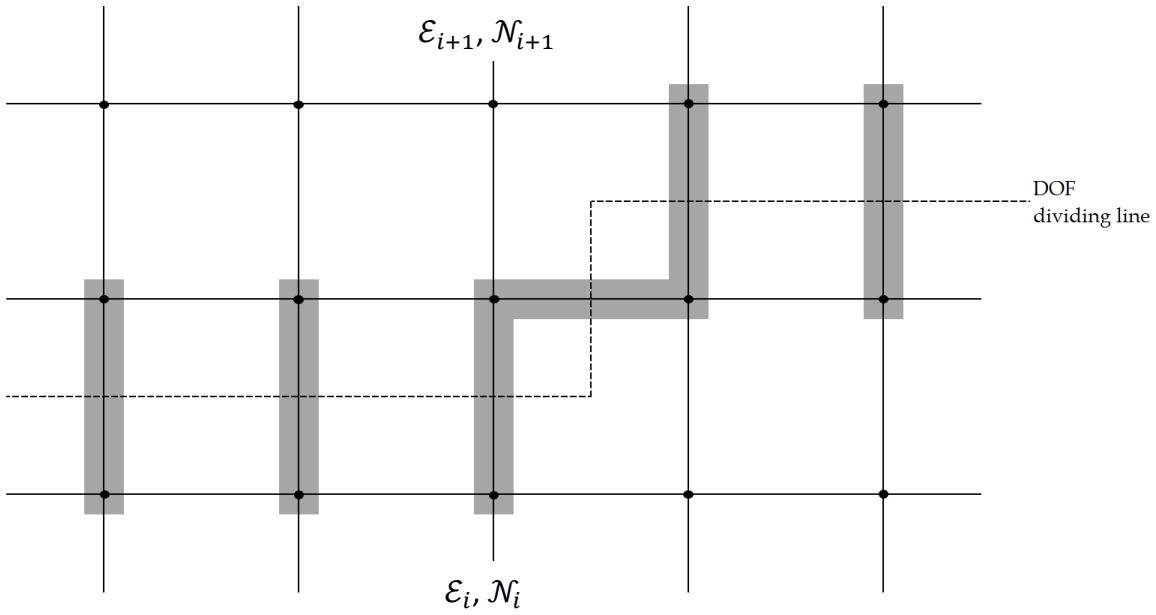

Figure 6.2: Two-dimensional example illustrating element and node subdomain overlap. The solid lines represent beam elements and the dots represent nodes. The dashed line marks the division between the non-overlapping DOF subdomains of processes i and i+1. The highlighted (grey) elements and nodes belong to both processes i and $i+1$, i.e., are overlapping.

6.2.4 Node allocation

Recall (§§2.3 – 2.8) that the element-level calculations depend on the incremented displacements of the global nodes. To perform a local-level beam calculation, the positions/rotations of the beam's two end nodes—which are based on the coordinates and deformations of attached PZs—must be known. Similarly, a PZ calculation accesses data from one node, a PS calculation from four nodes, and a spring calculation from one node. Process i needs only the set of nodes necessary for the calculation of at least one element in $\mathcal{E}_i$, denoted $\mathcal{N}_i \subset \mathcal{N}$, where $\mathcal{N}$ is the set of nodes in the entire model. If a node is necessary for the calculation of both an element in $\mathcal{E}_i$ and an element in $\mathcal{E}_{i+1}$, it belongs

to both $\mathcal{N}_i$ and $\mathcal{N}_{i+1}$. As shown in Figure 6.2, node subdomains can overlap by up to two floors worth of nodes. The percent of overlap is small for taller buildings.

6.2.5 Additional notes

The DOF, element, and node domain decomposition happens at the start of PFRAME3D, before analysis. Each process reads the same user-input files, skips irrelevant data, and saves relevant data. The more levels a building has, the more it can be split up.

It is shown in §§6.3 – 6.8 that up to m-sized vectors are communicated (because of non-overlapping DOF subdomains). Element and node data, on the other hand, are never communicated.

The domain-decomposition scheme here allows for hybrid-parallel computations. Process i computes its subdomain i in parallel using multiple cores. There is no core-to-core communication in this shared-memory parallel layer. This approach is often superior to a pure Message Passing Interface (MPI) scheme, where each core has its own subdomain, requiring core-to-core communication within a computer.

6.3 Parallel updating of $\{\boldsymbol{b}\}$

6.3.1 General

This section shows how $\{b\}$ is updated in parallel (Step 5 in §4.6). Updating $\{b\}$ (Step 5 in §4.6, which also includes most of the work for updating $[A]$; see note for Step 2 in §4.6) is the most computationally expensive step outside of the direct solver. Recall

(§5.6) that for the optimized 1-core 60-story collapse simulation, 69.4 hrs (out of 83.6 hrs) are spent outside of the direct solver. Updating $\{b\}$ uses 56.1 hrs of the 69.4 hrs. Table 6.1 shows that the parallelization of the $\{b\}$ calculation results in a significant reduction in wall time and high speedups (vs. 1 core).

Recall (Eq. 4.5) that

$$\{b\} = \{f_g\} - \{R^l\} - [M][r]\{\ddot{U}_g(t)\} + [M]\left\{\frac{4}{(\Delta t)^2}U(t) + \frac{4}{\Delta t}\dot{U}(t) + \ddot{U}(t)\right\}$$
$$+ [C]\left\{\frac{2}{\Delta t}U(t) + \dot{U}(t)\right\} - \left[\frac{4}{(\Delta t)^2}M + \frac{2}{\Delta t}C\right]\{U^l\}$$

and that process i updates $\{b\}_i$ only (§6.2). Thus,

$$\{b\}_i = \{f_g\}_i - \{R^l\}_i - \left([M][r]\{\ddot{U}_g(t)\}\right)_i + \left([M]\left\{\frac{4}{(\Delta t)^2}U(t) + \frac{4}{\Delta t}\dot{U}(t) + \ddot{U}(t)\right\}\right)_i$$
$$+ \left([C]\left\{\frac{2}{\Delta t}U(t) + \dot{U}(t)\right\}\right)_i - \left(\left[\frac{4}{(\Delta t)^2}M + \frac{2}{\Delta t}C\right]\{U^l\}\right)_i. \qquad \text{(Eq. 6.3)}$$

The following subsections describe how each term in $\{b\}_i$ is updated with a shared-memory parallel layer. The discussion is organized by descending computational cost:

- Parallel updating of $\{R^l\}_i$ (§6.3.2)
- Parallel updating of $\left(\left[\frac{4}{(\Delta t)^2}M + \frac{2}{\Delta t}C\right]\{U^l\}\right)_i$ (§6.3.3)
- Parallel updating of other terms in $\{b\}_i$ (§6.3.4)
- Additional notes (§6.3.5).

Table 6.1: Wall time and speedup of parallel {b} calculation, from 60-story dynamic time-history collapse simulation.

Number of cores used	Wall time (hrs)	Speedup vs. 1-core
1	56.1	1.00
2	32.5	1.73
4	19.9	2.81
8	12.7	4.43
16	5.01	11.2
32	2.84	19.8
64	1.78	31.5
128	1.28	43.9

6.3.2 Parallel updating of $\{R^l\}_i$

The most costly term in $\{b\}_i$ is $\{R^l\}_i$. For the same 1-core 60-story simulation, it uses about 99% of the $\{b\}_i$ calculation. $\{R^l\}_i$ is summed from the internal forces of every element in $\mathcal{E}_i$. Let $\mathcal{E}_i = \mathcal{E}_i^b + \mathcal{E}_i^{pz} + \mathcal{E}_i^{ps} + \mathcal{E}_i^s$, the sets of beam, panel-zone, plane-stress, and spring elements, respectively, in $\mathcal{E}_i$. The summation is handled in parts, based on element type; i.e., there is a different summation loop for each set $\mathcal{E}_i^b$, $\mathcal{E}_i^{pz}$, $\mathcal{E}_i^{ps}$, and $\mathcal{E}_i^s$ (called *beam loop*, *panel-zone loop*, etc.).

Beam elements

Consider the contribution of beam elements $\mathcal{E}_i^b$ on $\{R^l\}_i$. (A "beam element" is a beam, column, or brace in a structural model.) For efficiency, the beam loop is multi-threaded with 1 thread per core. Three types of load-balancing are considered: (1) static,

(2) dynamic, and (3) sorted dynamic. To understand how each type works, let c be the number of cores used by a process (e.g., $c = 8$ in the present cluster) and let each core be identified by j (an integer from $[0, c-1]$). The set of beam elements that core j calculates for $\{R^l\}_i$ is $\mathcal{E}_{i,j}^b \subset \mathcal{E}_i^b$.

In static load-balancing, beam elements are evenly distributed among cores when the beam loop begins; i.e., $\mathcal{E}_{i,j}^b$ is predetermined such that $\left|\mathcal{E}_{i,j}^b\right| \approx \frac{|\mathcal{E}_i^b|}{c}$, $\forall j$. ($|*|$ is the number of elements in set $*$.) Static load-balancing implies that $\mathcal{E}_{i,j}^b$ is generally constant for the entire simulation. Its overhead is cheaper than dynamic load-balancing, but computations may be highly imbalanced.

Due to nonlinearity, internal forces may be calculated quickly for some beam elements, but slowly for other beam elements. Denote the former as a *fast element* and the latter as a *slow element*; e.g., a PH element with elastic deformations is a *fast element*, and an EF3 or EF5 element with highly nonlinear deformations is likely a *slow element*. The solution procedures of EF elements are iterative (§§2.4 – 2.5), so it is possible for 1 slow element to have the same computational cost as hundreds or thousands of fast elements. Thus, dynamic-load balancing is considered.

In dynamic load-balancing, elements are added gradually to $\mathcal{E}_{i,j}^b$ during the beam loop itself. For global iteration l, when the beam loop begins, only 1 (or a few) beam elements are in $\mathcal{E}_{i,j}^b$; i.e., $\left|\mathcal{E}_{i,j}^b\right| = 1$. Beam elements are added to $\mathcal{E}_{i,j}^b$ whenever every element in $\mathcal{E}_{i,j}^b$ has contributed to $\{R^l\}_i$. (In PFRAME3D, beam elements are added one at a time.) The procedure continues until every element in $\mathcal{E}_i^b$ has contributed to $\{R^l\}_i$; i.e.,

$\sum_{j=0}^{c-1} \mathcal{E}_{i,j}^{b} = \mathcal{E}_{i}^{b}$. The $\mathcal{E}_{i,j}^{b}$ when the beam loop finishes is likely different from one global iteration to the next.

To improve dynamic load-balancing, the beam elements in $\mathcal{E}_{i,j}^{b}$ are sorted from slowest to fastest using the Intel MKL *dlasrt* routine every few global iterations or time steps. (In PFRAME3D, the beam elements are re-sorted every time step and every 10th consecutive unconverged global iteration.) The slowest elements are computed first, and the fastest elements last. For the 60-story simulation with 128 cores, the $\{b\}$ calculation takes 1.55 hrs with static load-balancing, and 1.28 hrs with sorted dynamic load-balancing. 15 sec were spent sorting the elements. It is possible to study the optimum re-sort frequency, but this is not done here.

Panel-zone elements

Next, consider the contribution of panel-zone elements $\mathcal{E}_{i}^{pz}$ on $\{R^l\}_i$. Like the beam loop, the PZ loop is multi-threaded, where core j computes the contributions of $\mathcal{E}_{i,j}^{pz} \subset \mathcal{E}_{i}^{pz}$ to $\{R^l\}_i$. But unlike the beam loop, all PZ calculations are direct (non-iterative). Thus, static load-balancing is implemented.

Plane-stress elements

Next, consider the contribution of plane-stress elements $\mathcal{E}_{i}^{ps}$ on $\{R^l\}_i$. Recall (§2.7) that $[K]^{ps}$, the global stiffness matrix due to PS elements, is computed only once, before analysis begins. The internal force vector due to PS elements is

$$\{R^l\}^{ps} = [K]^{ps}\{U^l\}. \qquad \text{(Eq. 6.4)}$$

The goal of process i is to compute $\{R^l\}_i^{ps}$.

To get $\{R^l\}_i^{ps}$, a hybrid-parallel matrix-vector operation (using a banded symmetric matrix) is created here because it is not found to exist in parallel linear-algebra libraries such as ScaLAPACK. Performance results (Figure 6.3) of this hybrid-parallel operation suggest nearly "ideal" weak-scaling (as defined in §4.4). For example, if workload doubles from $n = 80{,}000$ to $n = 160{,}000$ with a constant $n = 10{,}000$ workload per 8 cores, the matrix-vector operation's wall time increases by about 1%.

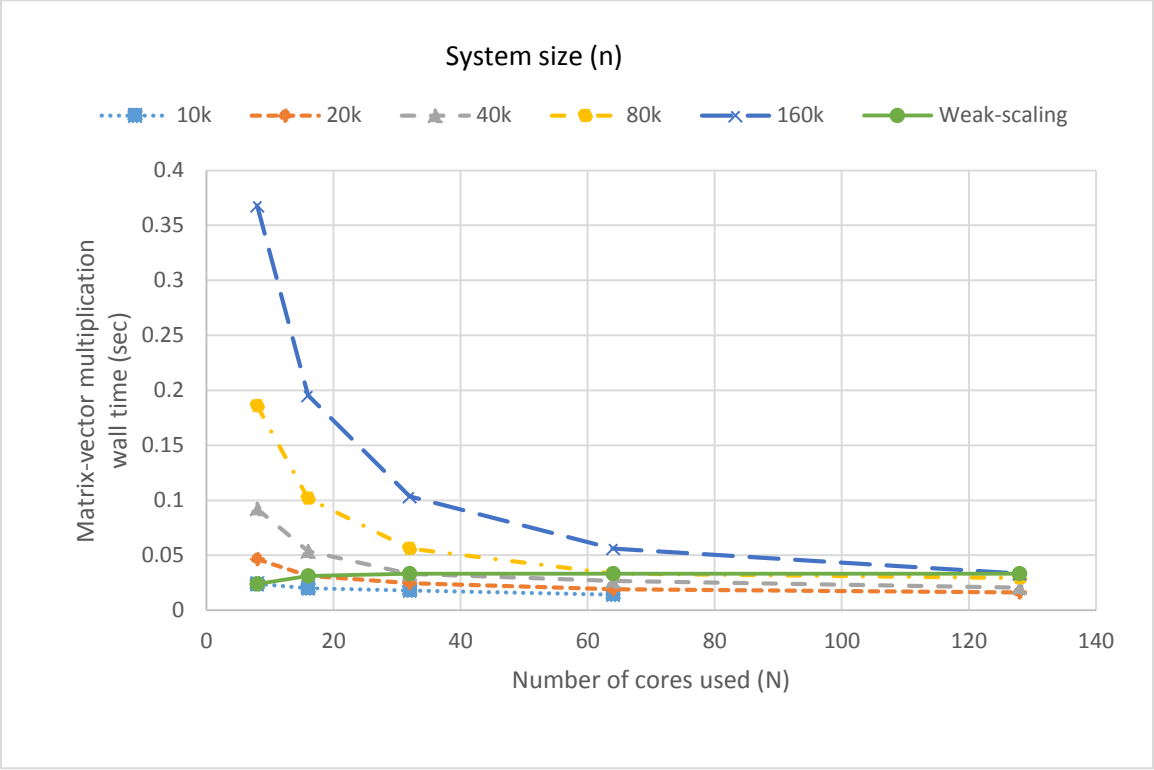

Figure 6.3: Wall times (sec) of matrix-vector multiplication with 8 to 128 cores. Each curve corresponds to a different system size n with m=1000. With 8 cores, the multi-threaded matrix-vector routine from Intel MKL (dsbmv) is used. A weak-scaling curve (solid green) is constructed (where workload is $n = 10{,}000$ *per 8 cores).*

To understand the parallel matrix-vector operation, recall (§6.2) that process i has $[K]_i^{ps}$ and $\{U^l\}_i$. However,

$$\{R^l\}_i^{ps} = \left([K]^{ps}\{U^l\}\right)_i \neq [K]_i^{ps}\{U^l\}_i \qquad \text{(Eq. 6.5)}$$

because $\{R^l\}_i^{ps}$ depends on some terms in $\{U^l\}$ that are not in $\{U^l\}_i$. Rather, if $[K]^{ps}$ is decomposed into

$$[K]^{ps} = [K]^{ps1} + [K]^{ps2} \qquad \text{(Eq. 6.6)}$$

as shown in Figure 6.4, where the white portion of the band belongs to $[K]^{ps1}$ and the grey portion of the band belongs to $[K]^{ps2}$, a large portion of the computation can be done independently. For process i, Eq. 6.4 becomes

$$\{R^l\}_i^{ps} = \left([K]^{ps1}\{U^l\}\right)_i + \left([K]^{ps2}\{U^l\}\right)_i. \qquad \text{(Eq. 6.7)}$$

The first term in Eq. 6.7 can be computed without communication using the multi-threaded Intel MKL routine *dsbmv* (double-precision symmetric band matrix-vector operation) because

$$\left([K]^{ps1}\{U^l\}\right)_i = [K]_i^{ps1}\{U^l\}_i. \qquad \text{(Eq. 6.8)}$$

To compute $\left([K]^{ps2}\{U^l\}\right)_i$, process i gets $m-1$ terms from processes $i-1$ and $i+1$.

Communication is handled in two steps:

$$\text{process } 0 \xrightarrow{\{R_*^l\}_0^{last}} \ldots \xrightarrow{\{R_*^l\}_{i-1}^{last}} \text{process } i \xrightarrow{\{R_*^l\}_i^{last}} \ldots \xrightarrow{\{R_*^l\}_{p-2}^{last}} \text{process } (p-1)$$

$$\text{process } 0 \xleftarrow{\{U^l\}_1^{first}} \ldots \xleftarrow{\{U^l\}_i^{first}} \text{process } i \xleftarrow{\{U^l\}_{i+1}^{first}} \ldots \xleftarrow{\{U^l\}_{p-1}^{first}} \text{process } (p-1).$$

The superscripts indicate that only the last or first $m-1$ terms are passed, and the $\{R_*^l\}_i^{last}$ indicates that $\{U^l\}_i^{last}$ is pre-multiplied to avoid passing terms from $[K]_i^{ps2}$.

To avoid deadlock due to cyclic dependency (i.e., some processes must send first while others must receive first), each step is a single *send-receive* operation and MPI assures

stability internally. It can be seen that each step can be done in parallel, and that processes communicate with their "nearest neighbor" only; thus, the cost of the communication algorithm depends on m, not n or p. Additionally, the first term in Eq. 6.7 is more significant for narrow-band systems (e.g., very tall buildings), making it suited for PFRAME3D. A pseudocode for the hybrid-parallel matrix-vector operation can be found in §B.2.

Spring elements

Finally, consider the contribution of spring elements $\mathcal{E}_i^s$ on $\{R^l\}_i$. The typical number of spring elements does not require a multi-threaded spring loop.

6.3.3 Parallel updating of $\left(\left[\frac{4}{(\Delta t)^2}\boldsymbol{M}+\frac{2}{\Delta t}\boldsymbol{C}\right]\{\boldsymbol{U}^l\}\right)_i$

Like $\{R^l\}_i$, $\left(\left[\frac{4}{(\Delta t)^2}M+\frac{2}{\Delta t}C\right]\{U^l\}\right)_i$ is also updated in every global iteration. The update of $\{U^l\}$, covered in §6.5, is known prior to the update of $\{b\}$. Because process i has $[M]_i$, $[C]_i$, and $\{U^l\}_i$, $\left(\left[\frac{4}{(\Delta t)^2}M+\frac{2}{\Delta t}C\right]\{U^l\}\right)_i$ is calculated using the same hybrid matrix-vector operation in §6.2 (for the $\mathcal{E}_i^{ps}$ contributions to $\{R^l\}_i$; pseudocode in §B.2).

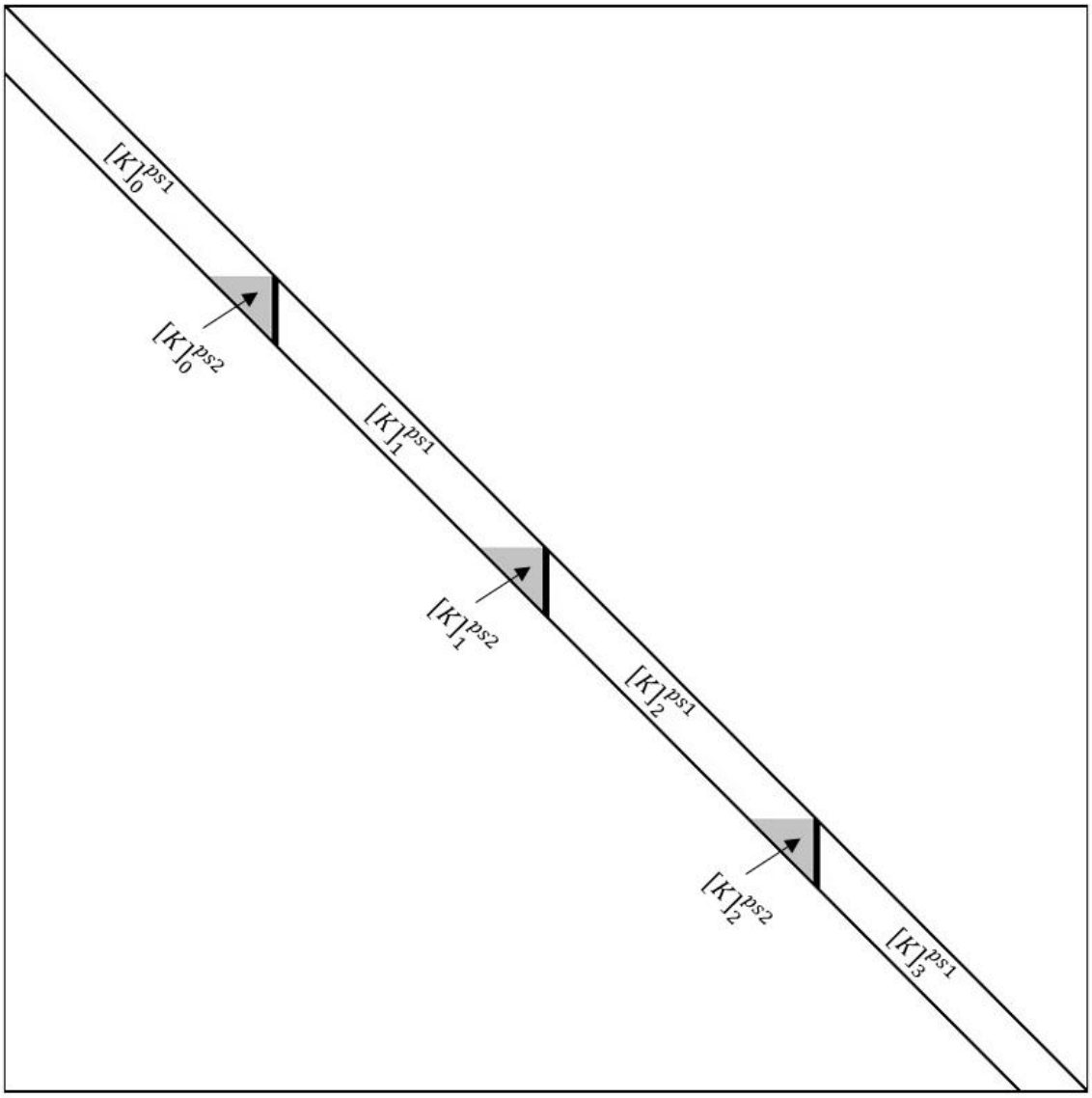

Figure 6.4: $[K]^{ps}$ decomposition for hybrid-parallel matrix-vector operation. The thick black lines mark the subdomain divisions. The white portion of the band belongs to $[K]^{ps1}$ and the grey portion of the band belongs to $[K]^{ps2}$. Shown are the diagonal and lower half of the matrix. The example uses 4 processes.

6.3.4 Parallel updating of other terms in $\{b\}_i$

$\{U(t)\}_i$ and its time derivatives are updated at the start of each time step based on the converged $\{U^l\}_i$ of the previous time step. Because $[M]_i$ is diagonal, process i calculates $\left([M]\left\{\frac{4}{(\Delta t)^2}U(t)+\frac{4}{\Delta t}\dot{U}(t)+\ddot{U}(t)\right\}\right)_i$ without communication using

$$\left([M]\left\{\frac{4}{(\Delta t)^2}U(t)+\frac{4}{\Delta t}\dot{U}(t)+\ddot{U}(t)\right\}\right)_i=[M]_i\left(\frac{4}{(\Delta t)^2}\{U(t)\}_i+\frac{4}{\Delta t}\left\{\dot{U}(t)\right\}_i+\left\{\ddot{U}(t)\right\}_i\right). \quad \text{(Eq. 6.9)}$$

To get $\left([C]\left\{\frac{2}{\Delta t}U(t)+\dot{U}(t)\right\}\right)_i$, the hybrid matrix-vector operation in §6.2 is used (pseudocode in §B.2).

$\{\ddot{U}_g(t)\}$ is read at the start of every dynamic time step. Because $[M]_i$ is diagonal, process i calculates $\left([M][r]\{\ddot{U}_g(t)\}\right)_i$ without communication using

$$\left([M][r]\{\ddot{U}_g(t)\}\right)_i=[M]_i[r]_i\{\ddot{U}_g(t)\}_i. \quad \text{(Eq. 6.10)}$$

Finally, recall that $\{f_g\}$ needs no updating; hence, $\{f_g\}_i$ is constant throughout analysis.

6.3.5 Additional notes

Every term that contributes to $\{b\}_i$ is considered above. Except in the hybrid-parallel matrix-vector operation, each process works independently. The output $\{b\}_i$ matches the DOF subdomain of the divide-and-conquer solver, so no additional "preparation" is needed.

Additional modest serial speedup of the $\{b\}_i$ calculation is achieved by reordering the EF5 interior nodes from 3-5-6-4 (Figure 2.9) to 3-4-5-6, because the half-bandwidth of the EF5 local iterations is reduced from 24 DOFs to 12 DOFs; §5.1 has more discussion on the effect of bandedness.

6.4 Parallel updating of $[A]$

6.4.1 General

This section shows how $[A]$ is updated in parallel (Step 2 in §4.6). Fortunately, updating $[A]_i$ is similar to updating $\{b\}_i$. Table 6.2 shows that the parallelization of the $[A]$ calculation results in a reduction in wall time and high speedups (vs. 1 core).

Recall (Eq. 4.3) that

$$[A] = \left[\frac{4}{(\Delta t)^2} M + \frac{2}{\Delta t} C + K_T^l\right]$$

and that process i updates $[A]_i$ only (§6.2). Thus,

$$[A]_i = \frac{4}{(\Delta t)^2}[M]_i + \frac{2}{\Delta t}[C]_i + \left[K_T^l\right]_i. \qquad \text{(Eq. 6.11)}$$

The first two terms $\frac{4}{(\Delta t)^2}[M]_i$ and $\frac{2}{\Delta t}[C]_i$ are constant, so only $\left[K_T^l\right]_i$ needs to be updated.

6.4.2 Parallel updating of $\left[K_T^l\right]_i$

$\left[K_T^l\right]_i$ is summed from the stiffness matrices of every element in $\mathcal{E}_i$. There is a different summation loop for each set $\mathcal{E}_i^b$, $\mathcal{E}_i^{pz}$, $\mathcal{E}_i^{ps}$, and $\mathcal{E}_i^s$. All summations loops are multi-threaded using static load-balancing because all stiffness matrix calculations are non-iterative and well-balanced, a result of the fact that element tangent stiffnesses were determined during the update of $\{R^l\}_i$ (see note for Step 2 from §4.6).

After $\left[K_T^l\right]_i$ is computed, the Eq. 6.11 summation is multi-threaded. There is no communication needed to compute $[A]_i$. The output $[A]_i$ matches the DOF subdomain of the divide-and-conquer solver, so no additional "preparation" is needed.

Table 6.2: Wall time and speedup of parallel [A] calculation, from 60-story dynamic time-history collapse simulation.

Number of cores used	**Wall time (*hrs*)**	**Speedup vs. 1-core**
1	11.5	1.00
2	7.98	1.44
4	5.02	2.29
8	3.49	3.28
16	1.76	6.63
32	0.89	12.9
64	0.45	25.6
128	0.25	46.6

6.5 Parallel geometric updating

This section shows how geometric updating is performed in parallel. Table 6.3 shows that parallelization reduces geometric updating wall time. Recall (§4.6) that the input to the geometric updating step is the newly solved $\{\Delta U\}$ (i.e., $\{x\}$ from Eq. 4.4) from Step 3.

Geometric updating has 4 parts:

(1) Update geometric parameters of elements

(2) Update coordinates/rotations of nodes

(3) Update $\{U^l\}$

(4) Avoid artificial unloading (adjust $\{\Delta U\}$).

Process i needs only to update its subdomain $\mathcal{E}_i$, $\mathcal{N}_i$, $\{U^l\}_i$, and $\{\Delta U\}_i$. For parts (1) and (2), multi-threaded loops across $\mathcal{E}_i$ and $\mathcal{N}_i$ are used with static load-balancing. For parts (3) and (4), $\{U^l\}_i = \{U^{l-1}\}_i + \{\Delta U\}_i$ and $\{\Delta U\}_i = \{U^l\}_i - \{U^{l-1}\}_i$ may be multi-threaded if n_b is large enough; but even if it is not multi-threaded, the operation is already parallel in the distributed-memory sense.

Before geometric updating can occur in parallel, a communication step is needed. Recall (§6.2) that process i has $\{\Delta U\}_i$. Also recall (§6.2) that some elements in $\mathcal{E}_i$ attach to DOFs outside of process i's DOF subdomain. Because $\mathcal{N}_i$ depends on $\mathcal{E}_i$ (§6.2), some nodes in $\mathcal{N}_i$ are outside of process i's DOF subdomain, too. Thus, to update some elements in $\mathcal{E}_i$ and some nodes in $\mathcal{N}_i$, process i needs some values from $\{\Delta U\}$ that are outside of $\{\Delta U\}_i$ — specifically, from the m closest DOFs from $\{\Delta U\}_{i-1}$ and $\{\Delta U\}_{i+1}$. An efficient communication subroutine is created here (pseudocode in §B.3), similar to the two-step communication used in the hybrid-parallel matrix-vector operation:

$$\text{process } 0 \xrightarrow{\{\Delta U\}_0^{last}} \dots \xrightarrow{\{\Delta U\}_{i-1}^{last}} \text{process } i \xrightarrow{\{\Delta U\}_i^{last}} \dots \xrightarrow{\{\Delta U\}_{p-2}^{last}} \text{process } (p-1)$$

$$\text{process } 0 \xleftarrow{\{\Delta U\}_1^{first}} \dots \xleftarrow{\{\Delta U\}_i^{first}} \text{process } i \xleftarrow{\{\Delta U\}_{i+1}^{first}} \dots \xleftarrow{\{\Delta U\}_{p-1}^{first}} \text{process } (p-1).$$

The superscripts indicate that only the last or first m terms of $\{\Delta U\}_i$ are passed.

The cost of the communication algorithm depends on m and is independent from n. It is also independent from p because each step can be done in parallel, and processes communicate with their "nearest neighbors" only. Relative to the rest of the geometric updating procedure ($m \ll n_i$), the communication costs are small enough to result in noticeable speedups relative to 1-core wall times, as observed in Table 6.3.

Table 6.3: Wall time and speedup of geometric updating, from 60-story dynamic time-history collapse simulation.

Number of cores used	**Wall time (hrs)**	**Speedup vs. 1-core**
1	0.28	1.00
2	0.16	1.76
4	0.08	3.39
8	0.05	6.09
16	0.21	1.34
32	0.11	2.63
64	0.06	4.51
128	0.03	8.28

6.6 Parallel convergence check

This section shows that the convergence check (Step 1 in §4.6) is automatically performed in parallel due to the parallelization of Steps 2 – 5.

Convergence occurs if every DOF in $\{b\}$ converges. Because $\{b\}$ is split up, process i checks $\{b\}_i$ only. Process i then reports a convergence status (whether subdomain i converged) to the community of processes. If at least one process reports non-convergence, then another global iteration is needed. Every process makes the same global decision. In other words, global convergence occurs only if every DOF in every $\{b\}_i$ converges.

The program has another check. Recall (§3.1) that if the maximum force residual $\|\{b\}\|_\infty$ grew in iteration $l-1$, then an elastic $\left[K_T^l\right]$ is used for iteration l. Like the

convergence check, this check is already parallel. Process i determines and reports $\|\{b\}_i\|_\infty$ to the community of processes. Every process determines the same global maximum force residual $\|\{b\}\|_\infty = \max_{i\in[0,p-1]} \|\{b\}_i\|_\infty$.

Both checks use a very small *collective* communication step, where each process shares a scalar with the community of processes.

6.7 Parallel input-output

This section shows how input-output is handled in parallel.

The user-input files for PFRAME3D are identical to FRAME3D. Each process determines internally whether data is relevant for it. No additional parameter files are needed; the user simply runs the program as shown in Table 6.4, specifying the number of processes.

Other parallel programs, such as OpenSeesSP, make input "go through" a head-node. The head-node reads input files then distributes the data to each process before analysis begins—which may be a bottleneck. A head-node is not used in PFRAME3D. Rather, each process independently reads the input files, skips irrelevant data, and keeps relevant data, which reduces startup communication costs and the above-mentioned bottleneck.

Table 6.4: User interface to run FRAME3D and PFRAME3D. In this example, PFRAME3D uses 128 cores (16 processes). Vary "16" to adjust core utilization.

Program	Command
FRAME3D	./frame3d
PFRAME3D	mpirun –np 16 --bynode pframe3d

Output files are distributed. Process i saves results from its subdomain only to a process-i-specific set of files. These results include various response histories like nodal displacements, story drifts, internal forces, times of fiber fracture, times of element failure, and other user-defined response histories (Krishnan 2009b). Thus, there are p nodal-displacement files, p story-drift files, p response time history files, etc. As p increases for a fixed problem size, process i prints less because its subdomain is smaller. The files can be quickly and easily combined in post-processing (e.g., in MATLAB).

By distributing the output files, the bottleneck that comes from every process printing to the same set of files is avoided. This bottleneck can be significant for a very large model. Additionally, race conditions where the results are printed in a non-deterministic order are avoided.

6.8 Miscellaneous considerations

6.8.1 General

This section addresses parallelization issues not already covered in §§6.2 – 6.7. These are:

- Speedup of miscellaneous computational costs (§6.8.2)

- Load-balancing in the distributed-memory layer (§6.8.3)
- Conditional multi-threading (§6.8.4)
- Race condition (§6.8.5)
- Probabilistic fracture assignments (§6.8.6)
- Shared-memory-only version of PFRAME3D (§6.8.7).

6.8.2 Speedup of miscellaneous computational costs

Table 6.5 shows that parallelization can speed up the miscellaneous computational costs relative to 1-core wall times (i.e., everything except for §4.6's Steps 2 – 5). These costs include the convergence check (§6.6) and input-output (§6.7). While these speedups are modest, they reflect a small portion of the total wall time.

Table 6.5: Wall time and speedup of miscellaneous computational costs, from 60-story dynamic time-history collapse simulation.

Number of cores used	**Wall time (*hrs*)**	**Speedup vs. 1-core**
1	1.54	1.00
2	1.53	1.01
4	1.50	1.02
8	1.50	1.02
16	0.89	1.72
32	0.62	2.50
64	0.45	3.39
128	0.40	3.88

6.8.3 Load-balancing in the distributed-memory layer

Load-balancing is an important consideration in the computation of $\{R^l\}_i$, due to the possibly imbalanced local iterations of multi-segmented elements. The shared-memory layer accounts for this imbalance with the sorted dynamic load-balancing scheme (§6.3.2). A similar type of imbalance can be observed in the distributed-memory layer. If one process is slower than others (e.g., because some parts of the building yield more than others), the other processes must wait. But if dynamic load-balancing is implemented for the distributed-memory layer, large amounts of element and node data must be communicated (e.g., the fiber histories of every fiber from every fiber segment in each element), which may increase the $\{b\}$ calculation's overall wall time. It is a concern for future study.

6.8.4 Conditional multi-threading

There are minor loops that are not multi-threaded because overhead likely costs more than the loop itself. It is possible to study the tipping-point size (where parallelization outweighs multi-threading overhead cost) and implement conditional threads—parallel only if past the tipping point. This study is not done here, and results are expected to be processor-specific.

6.8.5 Race condition

Parallel programs with a shared-memory layer may suffer from the so-called race condition, where core j may edit a variable that core k is using. This type of bug is not deterministic and difficult to track because it depends on the relative computational

speeds of cores j and k. Although not detailed here, considerable effort is taken to avoid race conditions. §7 indicates that race-condition problems are absent from PFRAME3D.

6.8.6 Probabilistic fracture assignments

Recall that FRAME3D simulates probabilistic beam fractures (§2.4). At the start of the program, a random number generator is used. A user may want a reproducible "random" sequence of numbers, and hence specify a *seed*. Thus, for a given seed, the fiber fracture assignments in PFRAME3D match FRAME3D. The random number generator in PFRAME3D produces identical results to that of FRAME3D, regardless of process or core count.

6.8.7 Shared-memory-only version of PFRAME3D

A shared-memory-only version of PFRAME3D is also created using the special case of $p = 1$. Here, the multi-threaded blocked solver (§5.3) is used for Step 3 (instead of the divide-and-conquer solver). Thus, $i = 0$, $[A] = [A]_0$, $\{x\} = \{x\}_0$, $\mathcal{E} = \mathcal{E}_0$, $\mathcal{N} = \mathcal{N}_0$, etc. This version is suitable for solving small problems in parallel.

6.9 Conclusion

In this chapter, the entirety of FRAME3D has been made parallel. Reductions in wall time are observed for every step outside of the direct solver (Steps 1, 2, 4, and 5).

Recall (§5.6) that for the 60-story building dynamic time-history collapse simulation, Steps 1, 2, 4, and 5 take 69.4 hrs to complete with 1 core. Due to 128-core parallelization, the 69.4 hrs is reduced to 1.95 hrs. Also recall (§5.6) that, for the same simulation, the 128-core divide-and-conquer solver uses 3.74 hrs. Thus, combining §5 and §6, the overall 128-core simulation wall time is (1.95 + 3.74) hrs = 5.69 hrs.

The remainder of Part II (i.e., §7) demonstrates PFRAME3D's ability to produce the same results as FRAME3D, and further showcases PFRAME3D's computational performance, using three example structures of varied sizes.

Chapter 7

Overall Parallelization Results

7.1 General

PFRAME3D is described in §4 – 6. In the present chapter, two types of comparisons are made between PFRAME3D and an optimized 1-core version of FRAME3D (that also includes the revisions made in Part I). The first comparison demonstrates that PFRAME3D produces time-history structural responses that are nearly identical to that of FRAME3D and that any discrepancies are negligible. The second comparison demonstrates that PFRAME3D uses less overall wall time due to parallelization. Three example structures are used:

- the water-tank tower from Bjornsson and Krishnan (2014) (§7.2)
- an 18-story building from Mourhatch (2015) (§7.3)
- the 60-story tube building from §8 (§7.4).

All three structures are subjected to collapse-causing dynamic time-history ground motions. In all cases, displacement response histories are saved and simulations are timed with various degrees of parallelism (i.e., core usage). The performance results from the three simulations are compared in §7.5.

7.2 Results using a small structure

This section shows that the output of the shared-memory-only PFRAME3D is nearly identical to that of FRAME3D and that wall time reductions due to parallelization are significant even for a small structure.

The water-tank tower from Bjornsson and Krishnan (2014) is a braced-frame structure with:

- $n = 252$
- $m = 102$
- 144 EF5 elements
- 18 PS elements
- 12 spring elements
- 44 nodes.

Details regarding the water-tank tower's elevation, plan, and member sizes can be found in Bjornsson and Krishnan (2014). It was not designed according to any particular building code. The water-tank tower is subjected to the Kobe earthquake ground motion at Takatori (Figure E.1), scaled at 37.3% — the same 3-component ground motion in §3.7. The simulation is terminated at $t = 38\,sec$ (7600 dynamic time steps are used), when the water-tank tower is clearly collapsing. The collapse configuration at termination is shown in Figure 7.1 for visualization.

Because the number of processes p allowed by the divide-and-conquer solver (§5.4) is limited according to Eq. 5.22, or $p \leq \frac{n}{2(m-1)} = \frac{252}{2(102-1)} \approx 1.24$, only 1 process may be used; thus, the shared-memory-only version of PFRAME3D (§6.8.7) is used with up to 8 cores (1 process).

This example indicates that the shared-memory layer of PFRAME3D produces consistent results; Figure 7.2 shows that the roof displacement histories agree regardless of core usage. Against the 1-core "X Displacement" history shown in Figure 7.2, the root-mean-squared error of the 8-core "X Displacement" history is $6.55 \times 10^{-5}\,m$, which can be considered as negligible for the present context.

In terms of performance, Table 7.1 shows that the 1-core 3.58 hr simulation is reduced with 8 cores to 1.23 hrs.

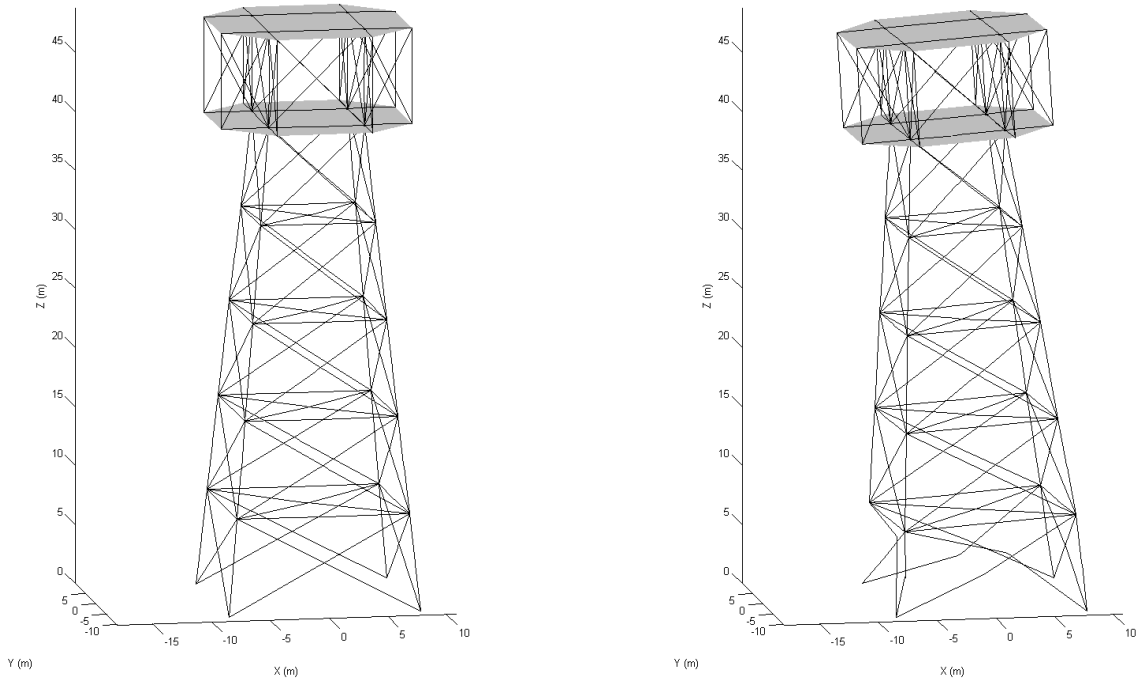

Figure 7.1: Isometric views of water-tank tower at t=0 sec (left) and t=38 sec (right) using 37.3% Kobe earthquake ground motion at Takatori (Figure E.1). Elements that failed during analysis are not shown. Deformations are unamplified.

Table 7.1: Overall parallelization speedup for water-tank tower collapse simulation.

Number of cores used	**Wall time (*hrs*)**	**Speedup vs. 1-core**
1	3.58	1.00
2	2.27	1.58
4	1.55	2.31
8	1.23	2.89

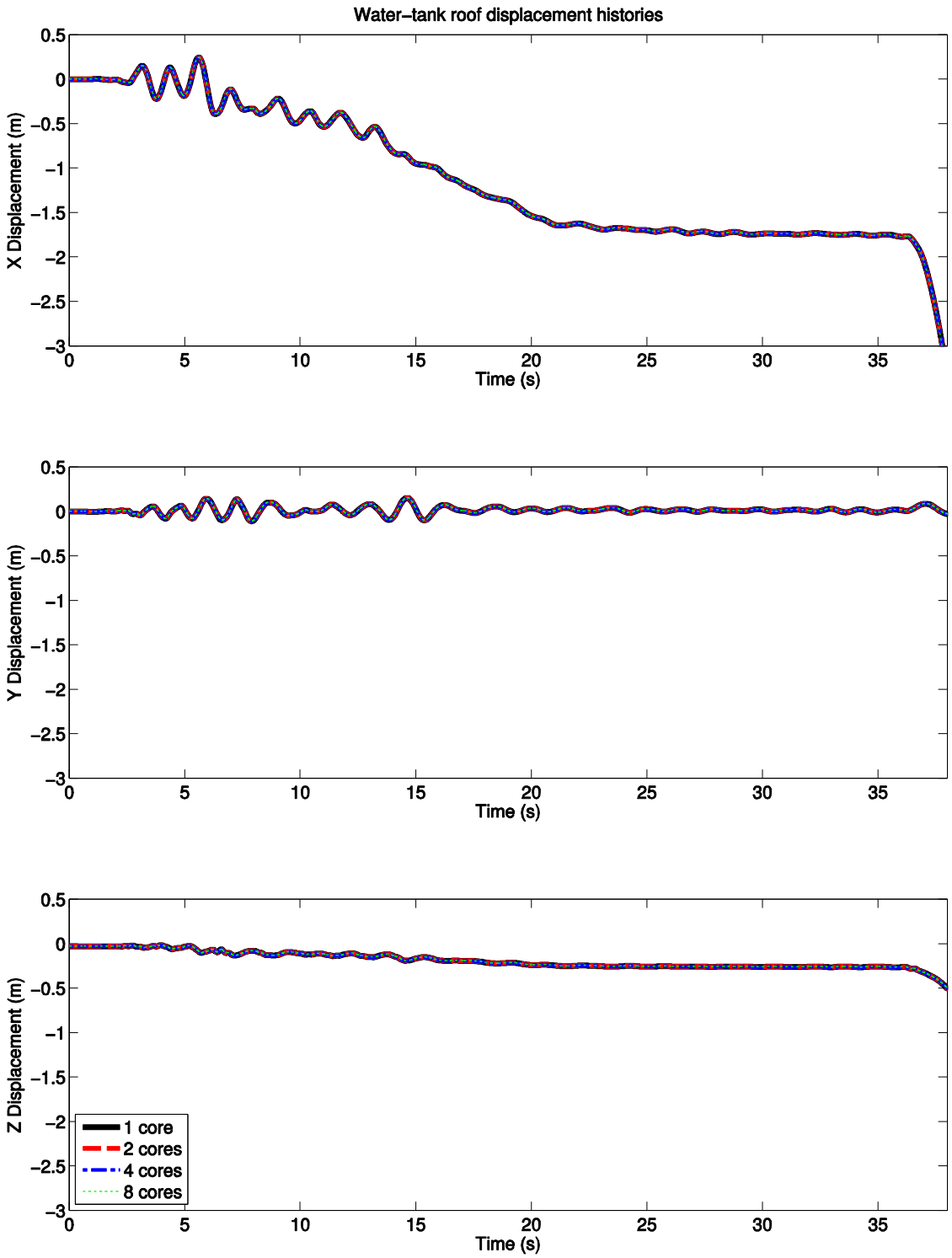

Figure 7.2: Roof displacement histories of water-tank tower (from the node initially at X=4.064 m, Y= 8.128 m, Z= 48.768 m) subjected to 37.3% Kobe earthquake ground motion at Takatori (Figure E.1). The results from 1-, 2-, 4-, and 8-core analysis are nearly identical.

7.3 Results using an 18-story building

This section shows that the output of PFRAME3D (the complete hybrid-parallel version) matches that of FRAME3D and that wall time is reduced more for a medium-sized tall building structure. The 18-story building (often referred to as the Canoga Park building), designed according to the UBC 94 with S2 soil conditions, from Mourhatch (2015), is a braced-frame building with:

- $n = 3966$
- $m = 289$
- 258 PH elements
- 282 EF3 elements
- 492 EF5 elements
- 216 PZ elements
- 517 PS elements
- 30 spring elements
- 760 nodes.

Details regarding the 18-story building's elevation, plan, and member sizes can be found in Mourhatch (2015). This building is subjected to a five-cycle idealized acceleration square wave with peak ground velocity $PGV = 1.375\, m/s$ and period $T = 5.75\, sec$ (Figure E.2). The simulation is set to terminate when the peak displacement history exceeds 300 in (~7 m), when the building is clearly collapsing. The collapse configuration at termination is shown in Figure 7.3 for visualization. Because $\frac{n}{2(m-1)} = \frac{3966}{2(289-1)} \approx 6.88$ (Eq. 5.22), up to 48 cores (6 processes) are used.

Figure 7.4 shows that the roof displacement histories agree regardless of core usage. 76 displacement histories (from throughout the building) are used to compare the 1-core and 48-core results, and the maximum observed root-mean-square error is $3.77 \times 10^{-11}\ m$, which can be considered as negligible for the present context.

Figure 7.5 (top) shows that the parallelization of the $\{b\}$ & $[A]$ update calculations contributes the most to the "Total" wall time reduction from 30.5 hrs with 1 core, to 2.95 hrs with 48 cores. The shift to distributed-memory computing begins with 16 cores, so a penalty can be seen then (i.e., from 8 cores to 16 cores in Figure 7.5). For example, the parallel geometric updating, in which communication is significant, slows down at 16 cores but speeds up as 48 cores is approached. Additionally, the divide-and-conquer factorization is slower than the 8-core blocked factorization, as a result of "fill-in" and the fact that p is nearing the Eq. 5.22 limit (recall §5.4). Nevertheless, because the parallel speedup of the $\{b\}$ & $[A]$ update calculations is more significant than the parallel slowdown of the divide-and-conquer solver and parallel geometric updating, the lowest wall time of 2.95 hrs is achieved with 48 cores, a speedup of 10.3.

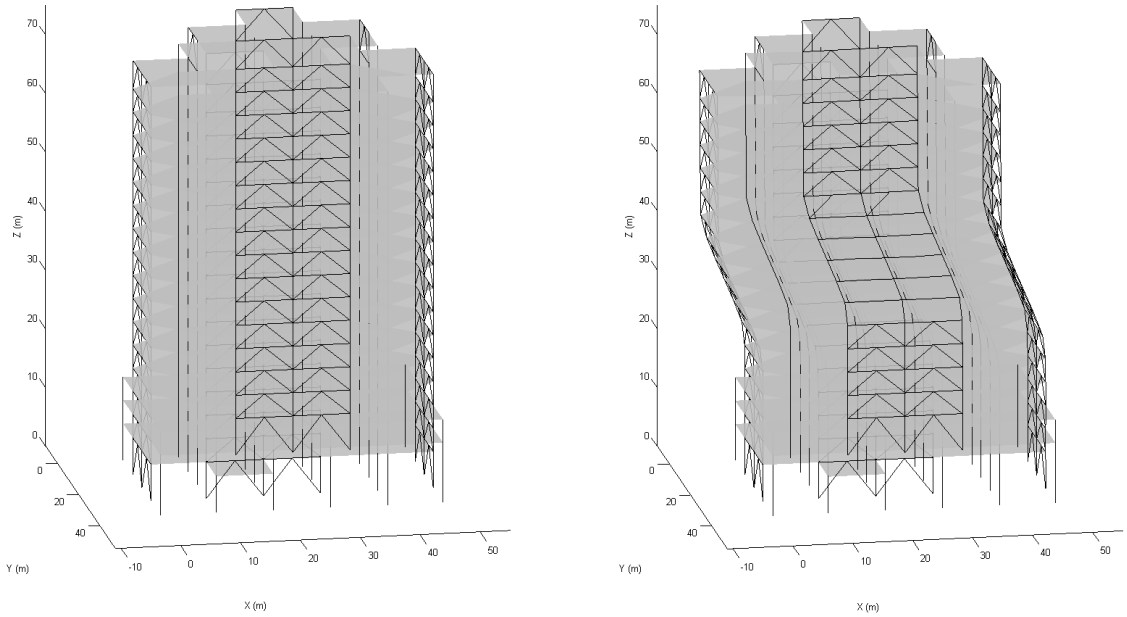

Figure 7.3: Isometric views of 18-story building at t=0 sec (left) and t=22.7 sec (right) subjected to the acceleration square wave ground motion (Figure E.2). Elements that failed during analysis are not shown. Deformations are unamplified.

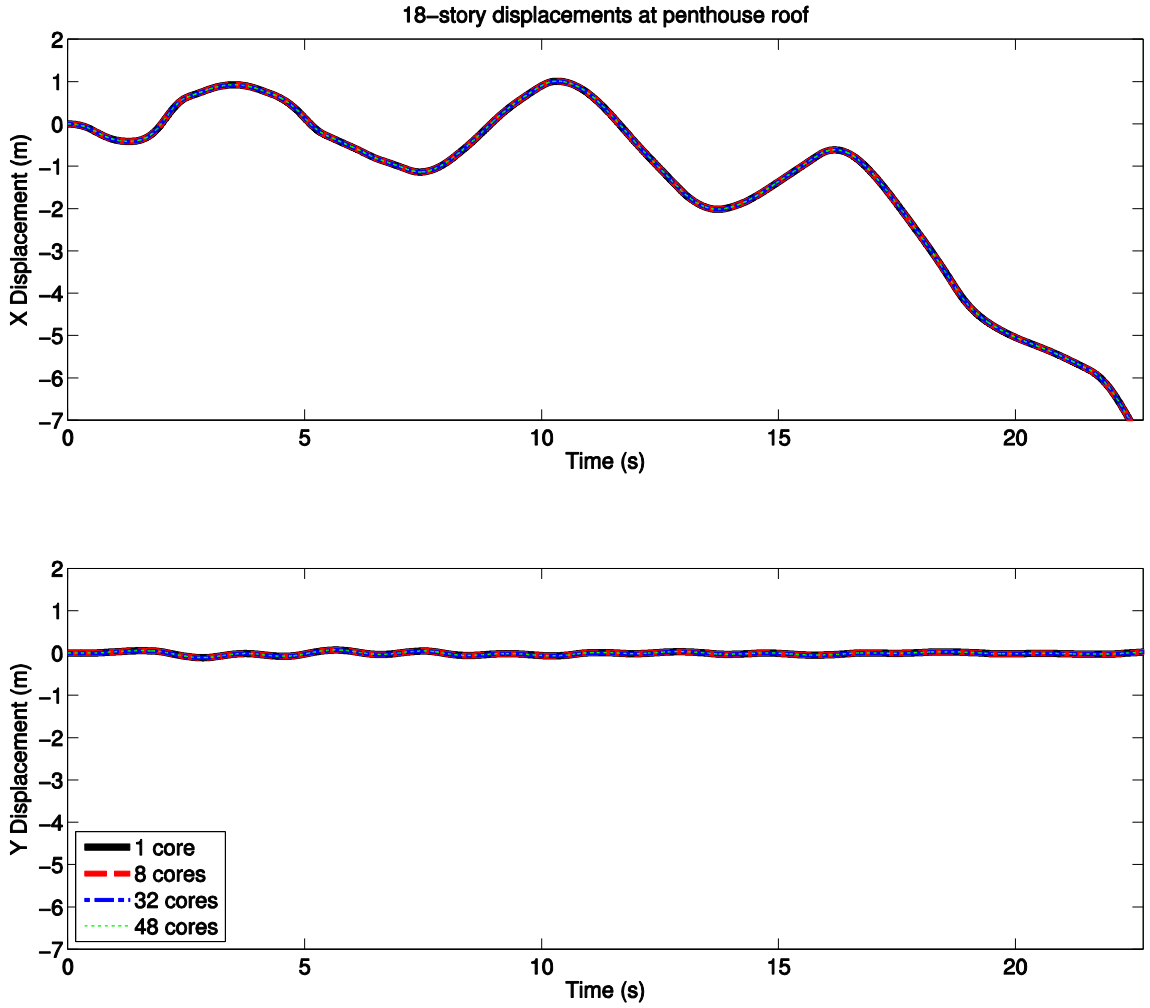

Figure 7.4: Displacement histories at penthouse roof of 18-story building subjected to an idealized five-cycle acceleration square wave with peak ground velocity PGV=1.375 m/s and period T=5.75 sec (Figure E.2). The results from 1-, 8-, 32-, and 48-core analysis are nearly identical.

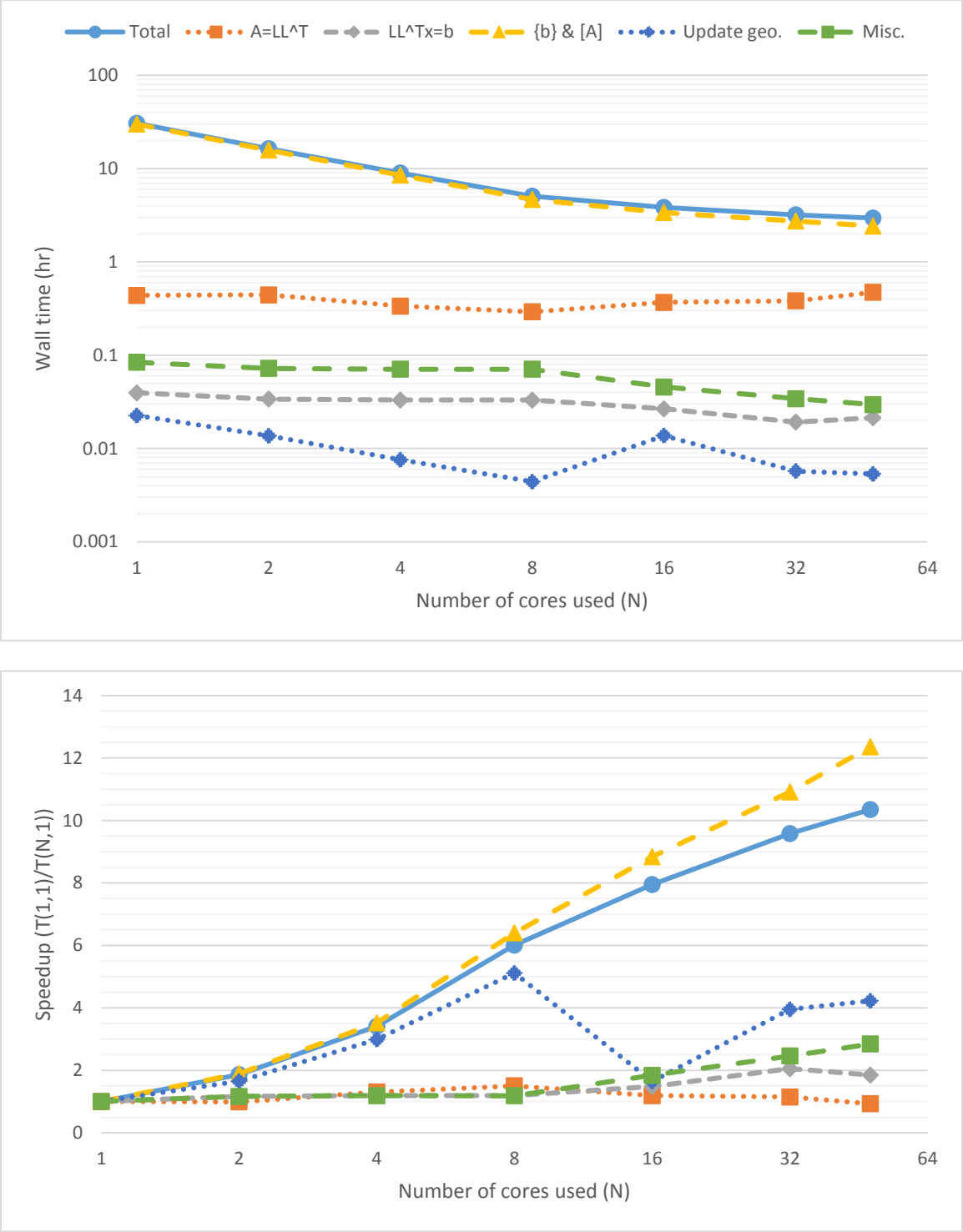

Figure 7.5: Performance summary for 18-story collapse simulation. Wall time of total and various steps (top), and speedup vs. optimized 1-core code (bottom).

7.4 Results using a 60-story building simulation

This section further shows that the output of PFRAME3D (the complete hybrid-parallel version) agrees with that of FRAME3D and that wall time is reduced even more for very tall building structures. The large structure considered here is the 60-story moment-frame tube building designed according to the UBC 94 from §8 of the current report, with:

- $n = 30{,}606$
- $m = 514$
- 1496 PH elements
- 3840 EF3 elements
- 4348 EF5 elements
- 4080 PZ elements
- 4320 PS elements
- 77 spring elements
- 4421 nodes.

The EF3 and EF5 elements have probabilistic fiber fracture assignments (§§8.3.2 – 8.3.3, brittle case with $seed = 1$). Details regarding the 60-story building's elevation, plan, and member sizes can be found in §8.2. The building is subjected to the Denali earthquake at Pump station #10 (Figure E.3). This ground motion is chosen because the building approaches collapse slowly (~40 sec in earthquake time), providing greater opportunity to check whether unforeseen race conditions are present. The simulation is set to terminate when the peak displacement history exceeds 300 in (~7 m), when the building is clearly

collapsing. The collapse configuration at termination is shown in Figure 7.6 for visualization. Because $\frac{n}{2(m-1)} = \frac{30606}{2(514-1)} \approx 29.8$ (Eq. 5.22), up to 232 cores (29 processes) are used.

Figure 7.7 shows that the roof displacement histories agree regardless of core usage. 122 displacement histories (X and Y displacements from the centroids of the 61 floors) are used to compare the 1-core and 128-core results, and the maximum observed root-mean-square error is $2.78 \times 10^{-6}\ m$, which can be considered as negligible for the present context. It is worth noting that every element type (§2) is included in this model, and that probabilistic fiber fracture assignments are included in the EF3 and EF5 elements.

Figure 7.7 (top) shows that parallelization reduces the "Total" wall time from 83.6 hrs (1-core) to 5.69 hrs (128-cores). At 1 core, the $\{b\}$ & $[A]$ update calculations are the most expensive, but once extended to distributed-memory computing (≥16 cores), the divide-and-conquer factorization becomes the most expensive step.

Unfortunately, the divide-and-conquer factorization does not exhibit speedups as impressive as that of the parallel $\{b\}$ & $[A]$ update calculations. Nevertheless, the parallelization of $\{b\}$ & $[A]$ calculations is significant enough that the "Total" speedup reaches 14.7 with 128 cores. Additionally, as shown in Figure 7.9 (plot of the wall time of each step as a function of earthquake time, from the 128-core simulation of the 60-story building collapse), the $\{b\}$ & $[A]$ update calculations become more significant as the building yields and elements are more nonlinear, especially at the last time steps of the simulation (as collapse is approached).

The slight "parallel slowdown" of the "Total" computation at 232 cores ("Total" wall time is 5.69 hrs with 128 cores and 5.74 hrs with 232 cores) is attributed to the divide-

and-conquer, which as mentioned in §5.4, is less efficient as p nears the Eq. 5.22 limit for a fixed problem size. Still, it should be noted that for an even taller building, the Eq. 5.22 limit is increased (assuming that n increases much faster than m), such that higher core counts may be used effectively. Additionally, the other steps in Figure 7.8 are shown to be faster with 232 cores. It is of interest in a future study to either improve the divide-and-conquer solver (e.g., by accounting for sparsity within the narrow band) or altogether remove the direct solver (e.g., by solving the global equation of motion using a nonlinear conjugate gradient approach). The present hybrid-parallel framework is expected to be able to accommodate such changes.

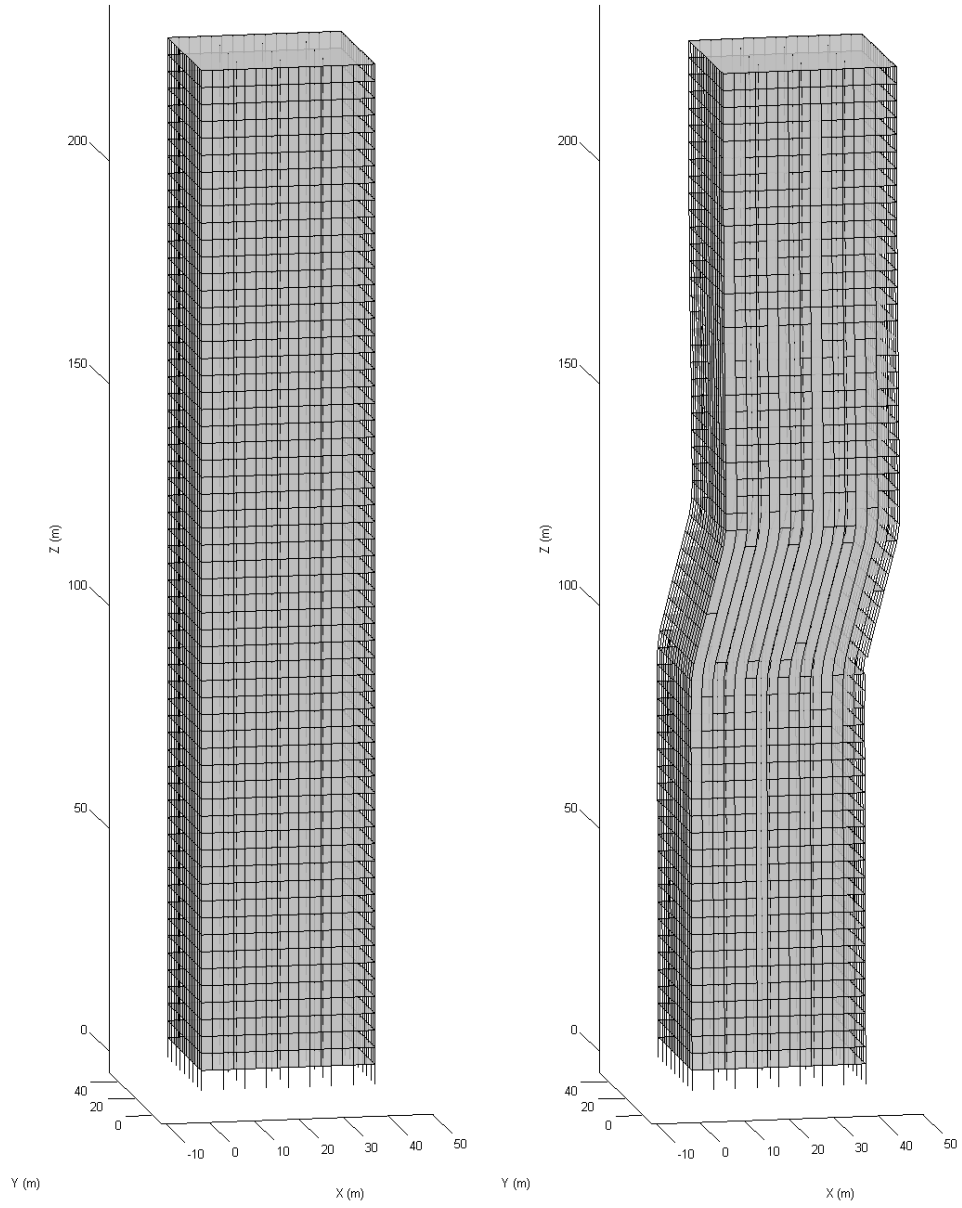

Figure 7.6: Isometric views of 60-story building at t=0 sec and t=41.9 sec subjected to the Denali earthquake ground motion at Pump station #10 (Figure E.3). Elements that failed during analysis are not shown. Deformations are unamplified.

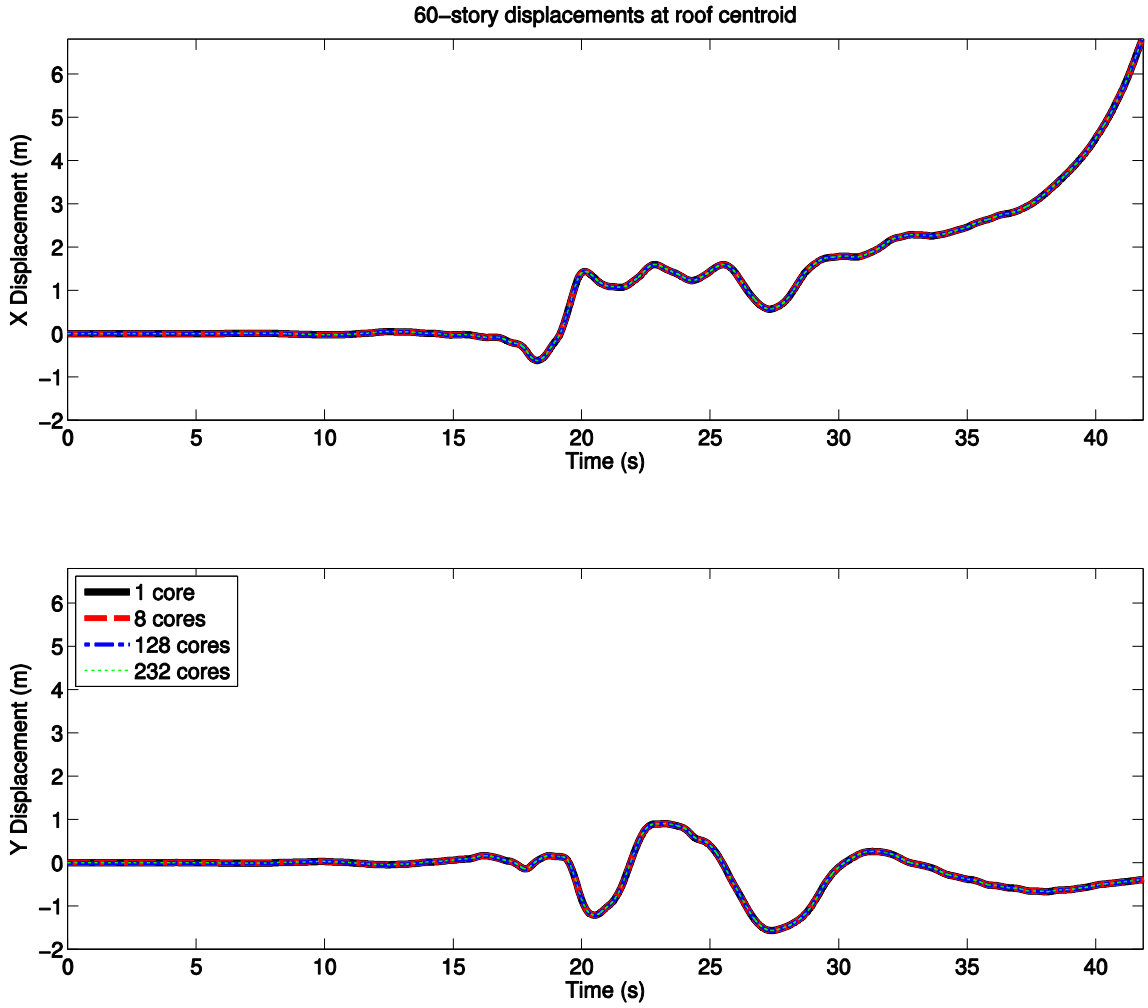

Figure 7.7: Displacement histories at the roof centroid of the 60-story building subjected to the Denali earthquake ground motion at Pump station #10 (Figure E.3). The results from 1-, 8-, 128-, and 232-core analysis are nearly identical.

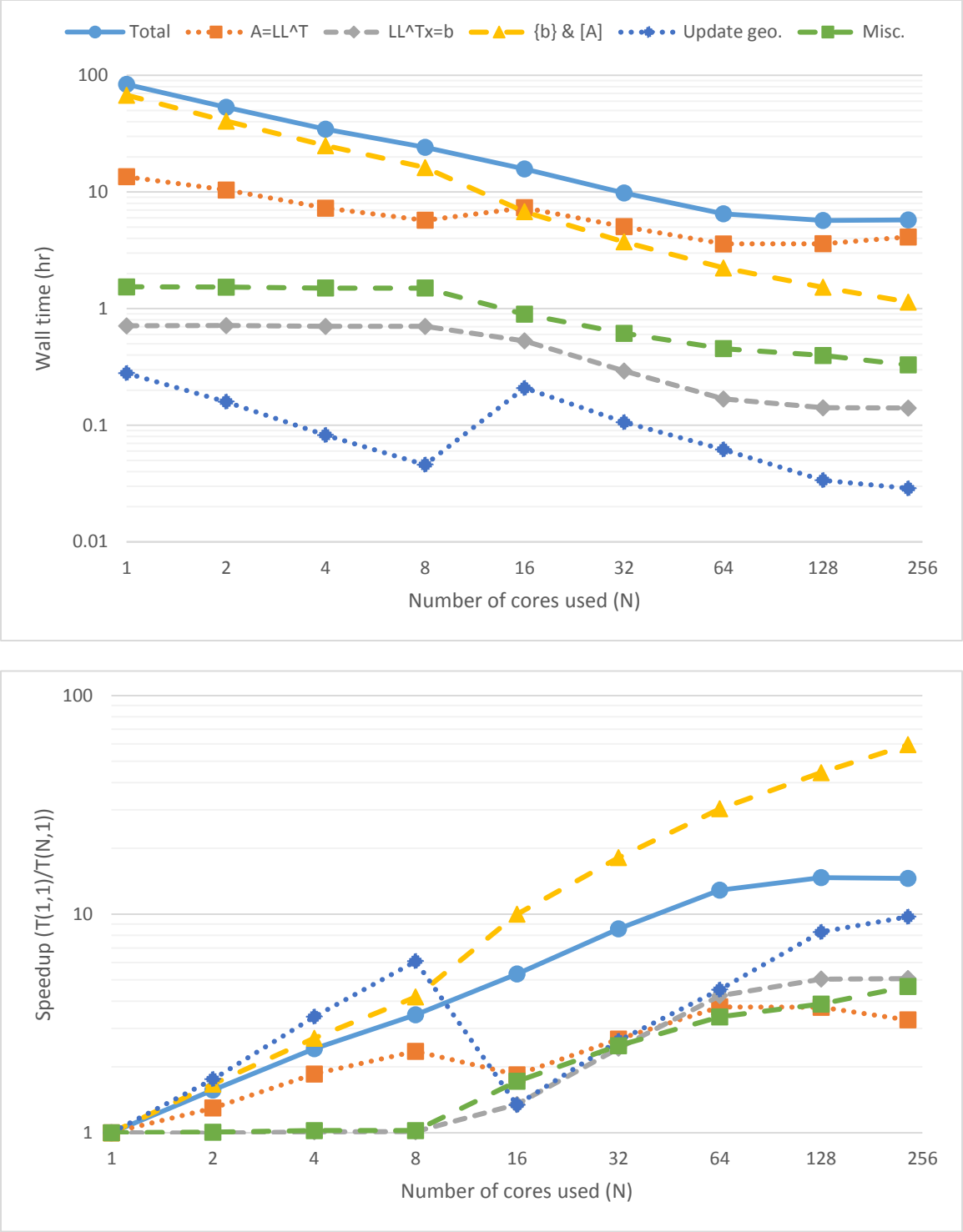

Figure 7.8: Performance summary for 60-story collapse simulation. Wall time of total and various steps (top), and speedup vs. optimized 1-core code (bottom).

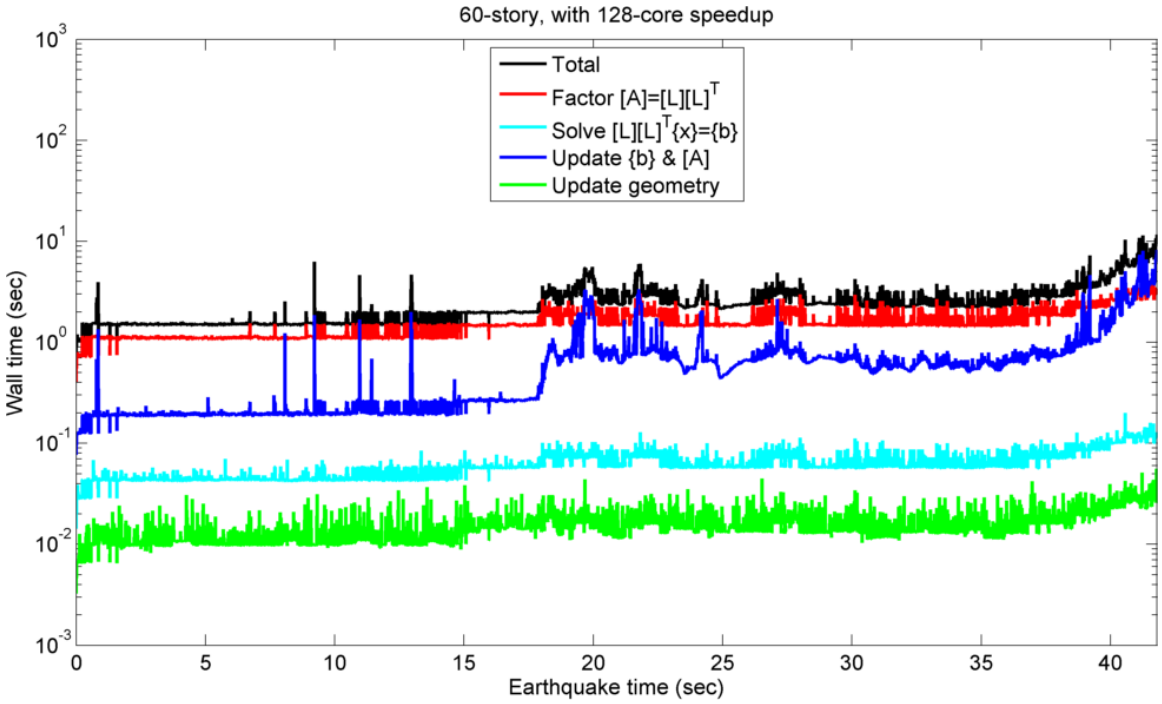

Figure 7.9: Wall time (sec) per earthquake-simulation time step, from 60-story building subjected to the Denali earthquake ground motion at Pump station #10 (Figure E.3). PFRAME3D with 128 cores is used. The "spikes" in the {b} & [A] update wall times are a result of load imbalances in the distributed-memory layer (§6.8.3).

7.5 Maximum speedups

A more holistic understanding of PFRAME3D's performance can be obtained by comparing the "Total" performance results of the three buildings with each other, as is done in Figure 7.10. For the water-tank tower collapse simulation, PFRAME3D achieves a maximum speedup of 2.89 with 8 cores; for the 18-story building collapse simulation, it achieves a maximum speedup of 10.3 with 48 cores; and for the 60-story building collapse simulation, it achieves a maximum speedup of 14.7 with 128 cores.

An additional curve is constructed on Figure 7.10 (bottom) by connecting the maximum speedups attained for the three structures. An upward trend can be seen, which suggests that as building height increases, additional cores may be used to achieve a higher speedup.

The above comparison is similar to a weak-scaling study. However, it cannot be appropriately classified as such because the per-core workloads vary between the three cases. For example, because each structure has a different bandwidth, the divide-and-conquer per-core workload varies. Or, the number of elements per floor is varied; e.g., the 60-story building has more frame elements per floor than the 18-story building. It is also important to note that the three simulations themselves are very different. Three different ground motions are used, the collapse mechanisms form at different times, and the water-tank tower and 18-story building are braced-frame buildings while the 60-story building is a moment-frame tube building.

Nevertheless, Figure 7.10 indicates that parallel speedup increases with building height. It is not unreasonable to suggest that even higher speedups than shown in Figure 7.10 are possible if PFRAME3D is applied to even taller buildings (e.g., a 100-story building).

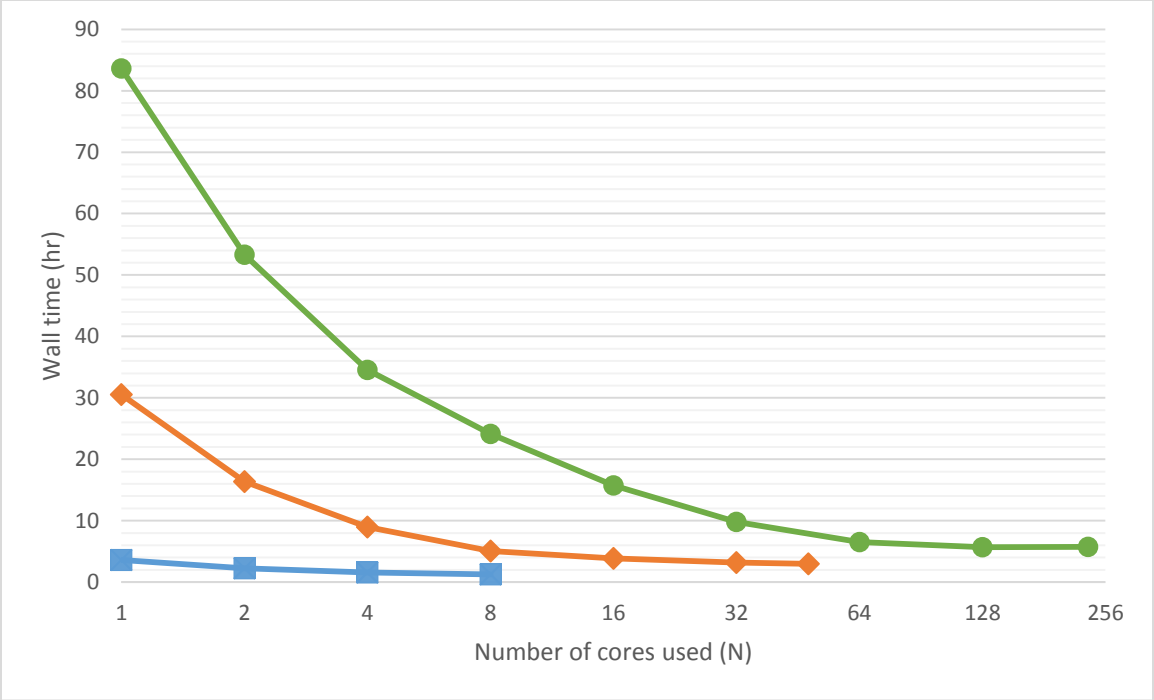

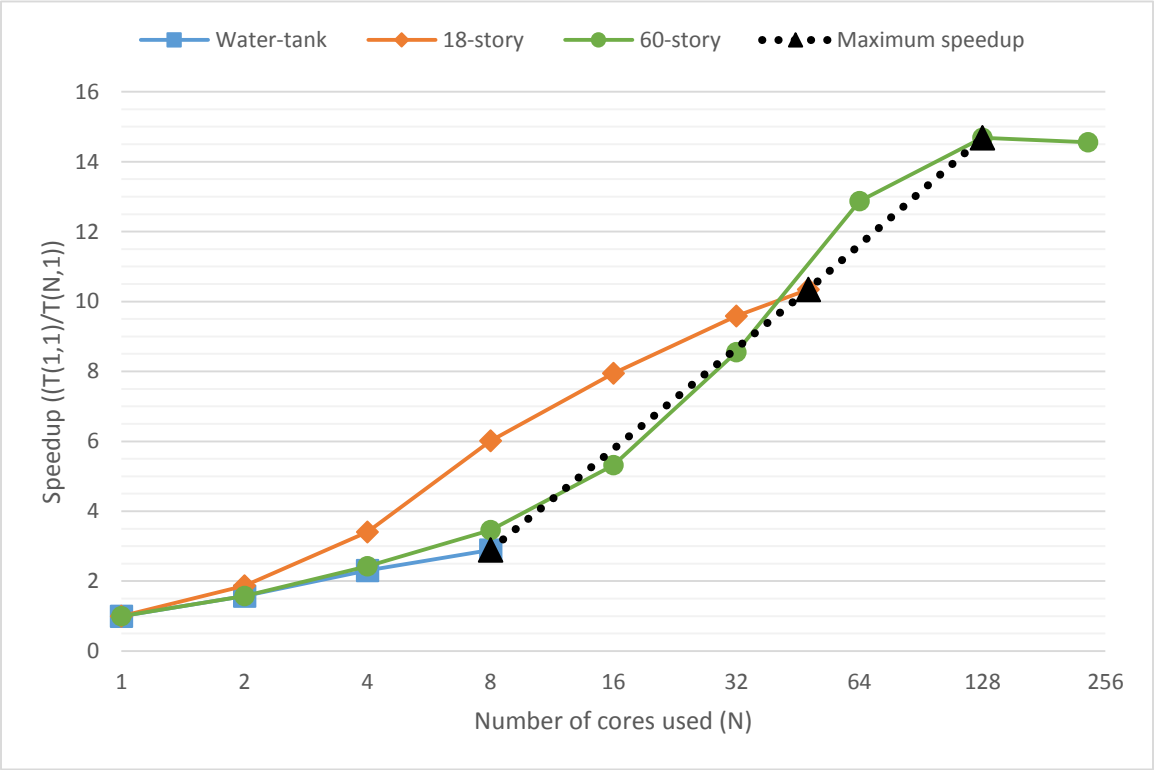

Figure 7.10: Summary of "Total" wall time (top) and speedup vs. 1-core (bottom) for the water-tank tower, 18-story building, and 60-story building collapse simulations. Also plotted (bottom) is a curve connecting the maximum speedups achieved for each of the three simulations.

7.6 Conclusion

Therefore, using the three example dynamic time-history collapse simulations in §§7.2 – 7.4, PFRAME3D is shown to produce output that is nearly identical to that of FRAME3D. Race condition problems are not observed in any of the three cases.

Still, it should be noted that round-off errors due to floating-point arithmetic can cause parallel computations to produce slightly different results than that of the 1-core computations (Goldberg 1991, Villa et al. 2009). For example, the mathematical property of associativity does not necessarily hold in optimized parallel libraries like Intel MKL. Or, elements may update the global $\{R^l\}$ (§6.3.2) and $\left[K_T^l\right]$ (§6.4.2) in a different order than the 1-core case, leading to a slightly different $\{R^l\}$ and $\left[K_T^l\right]$ (again, due to non-associativity). It is possible to use fully deterministic versions of the Intel MKL routines, or use static load-balancing such that $\{R^l\}$ and $\left[K_T^l\right]$ are assembled by the same sequence of elements as the 1-core case. However, these fixes are not optimal in terms of parallel performance, and so are not implemented here. Additionally, displacement-history root-mean-square errors are observed to be $\sim 10^{-5}\ m$ or less, and Figure 7.2, Figure 7.4, and Figure 7.7 show that the resulting collapse mechanisms are reproducible regardless of parallelization. Therefore, it can be stated that these discrepancies are negligible in the overall context of building analysis.

Maximum speedups are shown to grow with the height of the building, and a 60-story dynamic time-history collapse simulation is completed in 5.69 hours with 128 cores. Thus, it can be said that PFRAME3D is suited for the efficient computation of tall building response due to ground motion.

PART III

Application and Conclusions

Chapter 8

Application to a 60-story steel building

8.1 General

In this chapter a 60-story example building is developed and analyzed, in order to showcase PFRAME3D's capability to perform collapse analysis on very tall buildings. The design satisfies UBC 94 load and stiffness criteria, and has a typical mass distribution for office buildings. It has a 6.16-second fundamental period, which is typical for buildings of its height. However, the building shows atypical moment-frame behavior because of the use of very closely spaced columns (8 ft or 2.4384 m center-to-center) and very deep beams (up to 30 in or 0.762 m). Beams in this configuration are likely to yield in shear, but

neither the EF3 (§2.4) or EF5 (§2.5) element can capture nonlinear shear. A more realistic building model, with shallower beams and columns less closely spaced, will be designed in a future project. Nevertheless, this test case is sufficient for the current report and PFRAME3D is shown to be useful for studying very tall buildings subjected to strong ground motions. Observations such as multi-story quasi-shear band collapse mechanisms (similar to Krishnan and Muto 2012) are noted. This chapter is organized as follows:

- Building design and description (§8.2)
- Modeling considerations (§8.3)
- Building analyses and results (§8.4).

8.2 Building description and design

8.2.1 Building description

The building considered in this chapter is a moment-frame (MF) tube structure. The general behavior of tube structures is well explained in Smith and Coull (1991) and briefly recounted in §C for convenience.

The 60-story example building is designed with typical and 1st-story plans shown in Figure 8.1 and Figure 8.2, respectively. Story height is 12.5 ft (3.81 m) at levels 2 – 60, and 15 ft (4.572 m) at level 1. The plan is a square to take advantage of symmetry. Beam and column sizes are chosen every 4 stories as shown in Table 8.1. The properties of non-standard sections can be found in §D. For simplicity, all MF beams are identical within a floor level, all interior MF columns are identical within a story level, all gravity columns

are identical within a story level, etc. Column splices are located at every odd story level above first story. Design considerations are discussed in §8.2.2. Modal characteristics and mode shapes of the building are shown in Table 8.2 and Figure 8.3, respectively.

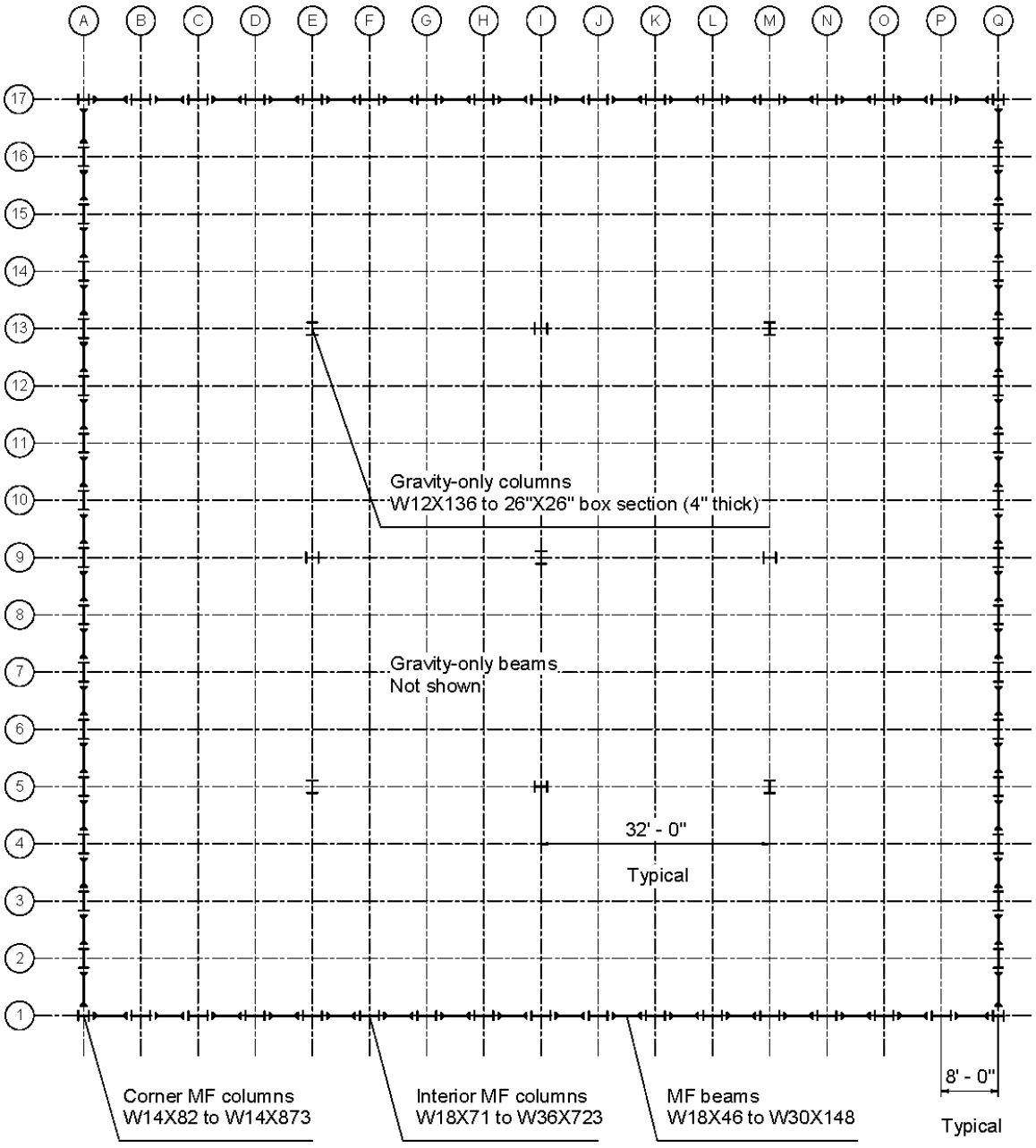

Figure 8.1: Typical plan (3rd floor to Roof) of 60-story example tube building, featuring closely-spaced columns.

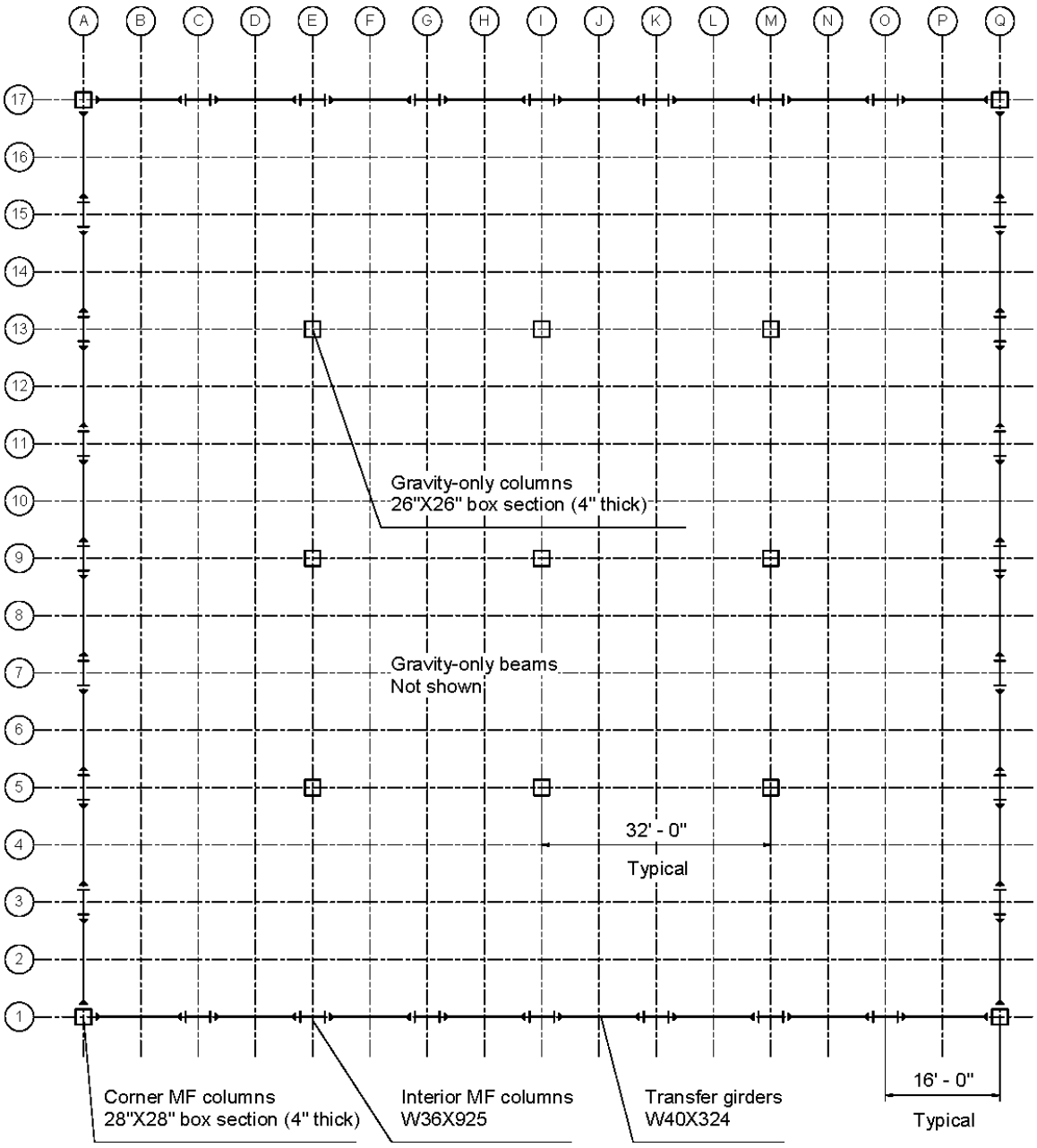

Figure 8.2: Plan for 2nd floor of 60-story example tube building, featuring transfer girder.

Table 8.1: Summary of column and beam sizes for 60-story example building.

Story levels	Moment frame		Gravity frame
	Corner columns	Interior columns	Columns
57 – 60	W14X82	W18X71	W12X136
53 – 56	W14X159	W18X97	W14X193
49 – 52	W14X176	W18X119	W14X257
45 – 48	W14X211	W21X147	W14X342
41 – 44	W14X233	W24X176	W14X426
37 – 40	W14X283	W27X194	W14X500
33 – 36	W14X342	W30X211	W14X550
29 – 32	W14X370	W30X261	W14X605
25 – 28	W14X398	W33X291	W14X665
21 – 24	W14X426	W33X318	W14X730
17 – 20	W14X455	W33X354	W14X808
13 – 16	W14X500	W36X395	W14X873
9 – 12	W14X550	W36X441	24″X24″ box*
5 – 8	W14X665	W36X529	24″X24″ box*
2 – 4	W14X873	W36X723	26″X26″ box*
1	28″X28″ box*	W36X925**	26″X26″ box*

Floor levels	Moment frame
	Beams
58 – Roof	W18X46
54 – 57	W18X60
50 – 53	W21X62
46 – 49	W21X62
42 – 45	W21X62
38 – 41	W21X68
34 – 37	W21X73
30 – 33	W21X73
26 – 29	W21X83
22 – 25	W21X93
18 – 21	W24X103
14 – 17	W24X103
10 – 13	W27X114
6 – 9	W27X114
3 – 5	W30X148
2	W40X324***

* Non-standard section, see §D.

** For column lines that extend to the ground.

*** Transfer girder.

Table 8.2: Modal periods of 60-story example building.

Mode	**Type**	**Period (s)**
1, 2	1st translational	6.16
3	1st torsional	3.18
4, 5	2nd translational	2.12
6	2nd torsional	1.32
7, 8	3rd translational	1.26

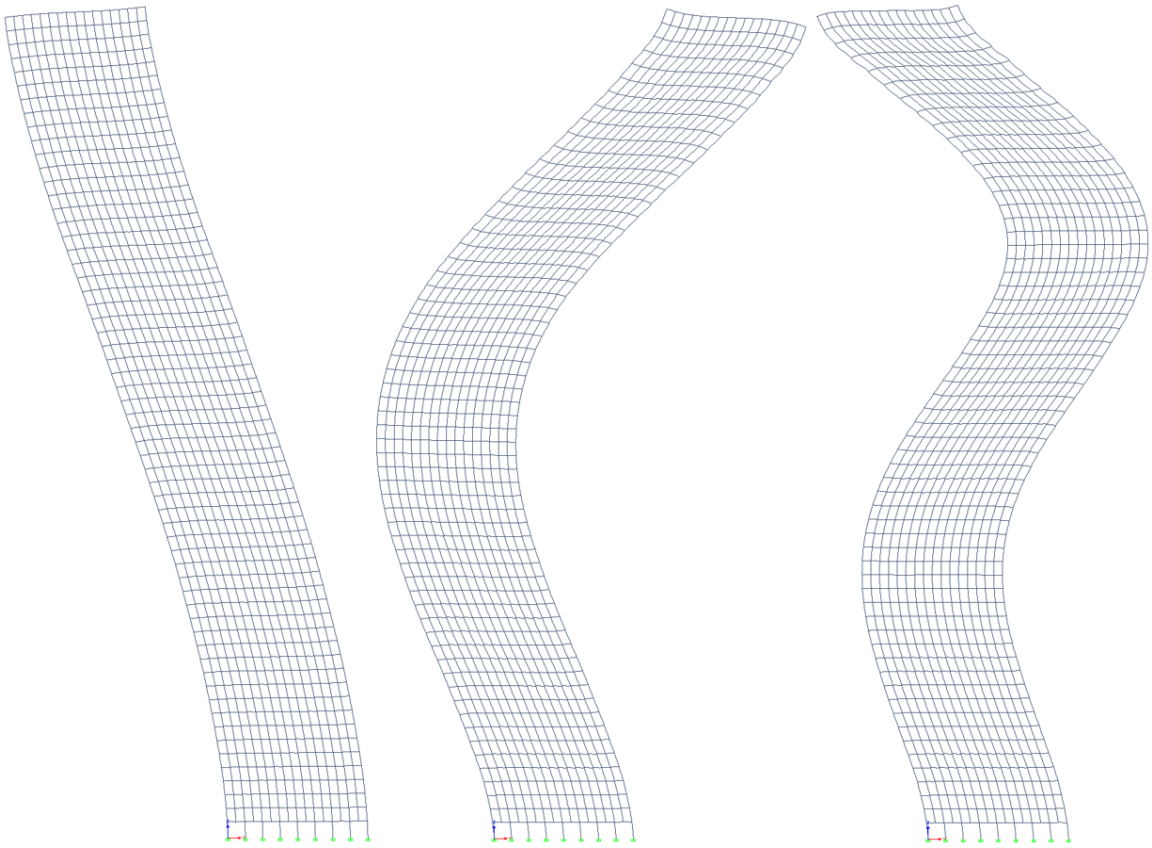

Figure 8.3: Elevation view of the 60-story example building's first three translational modes along a single direction.

8.2.2 Building design

The 60-story building is assumed to be located in downtown Los Angeles (DTLA). Because some high-rise DTLA buildings were designed according to pre-Northridge building code, design loads are determined according to the *1994 Uniform Building Code* (UBC 94). The building's beams and columns are proportioned using the Allowable Stress Design (ASD) procedure found in the *Specification for Structural Steel Buildings: Allowable Stress Design and Plastic Design* (AISC 335-89). Design software ETABS is used throughout the entire design procedure.

The basic ASD load combinations (UBC 94 §1603.6) considered are:

- $D + L$
- $D + L \pm W$
- $D + L \pm E$

where D, L, W, and E are dead, live, wind, and earthquake loads, respectively. Columns also satisfy (UBC 94 §2211.5.1):

- $1.0D + 0.7L \pm 3\left(\frac{R_w}{8}\right)E$
- $0.85D \pm 3\left(\frac{R_w}{8}\right)E$

where R_w accounts for material overstrength.

Design dead loads are according to Table 8.3. Combined, the typical floor dead load (without beam/column self-weight and cladding) is $76\,psf$ $\left(3.64\frac{kN}{m^2}\right)$ and the roof dead load (without beam and column self-weight) is $64\,psf$ $\left(3.06\frac{kN}{m^2}\right)$. Cladding is applied around the building perimeter.

Table 8.3: Design dead loads.

Dead load	$\boldsymbol{psf}\left(\frac{\boldsymbol{kN}}{\boldsymbol{m^2}}\right)$
MF beams and columns	Self-weight
Gravity columns	Self-weight
(Primary) gravity beams	Self-weight
(Secondary) gravity beams	6 (0.29)
Concrete slab	50 (2.39)
Carpet/finish	2 (0.096)
Mechanical, ceiling, etc.	8 (0.38)
Partitions	10 (0.48)
Cladding	15 (0.72)

The building is intended to be an office building, and the design floor live loads are 50 psf $\left(2.39\frac{kN}{m^2}\right)$ uniformly distributed (UBC 94, Table 16-A), except at the roof where live loads are 20 psf $\left(0.96\frac{kN}{m^2}\right)$ uniformly distributed (UBC 94, Table 16-C).

Design wind loads are applied as static forces according to the national standard ASCE 7-93 §6 (UBC 94 §1613). The wind-design parameters used are summarized in Table 8.4 as defined in the ASCE 7-93 §6. Story-drift ratios are checked to be within $\frac{1}{400}$ using the 10-year wind and a 1st order analysis (Griffis 1993).

Seismic consideration is important in DTLA. A static lateral-force procedure (UBC 94 §1628.2) is an approximation of earthquake loads; while it is convenient for short buildings, earthquakes are dynamic and often bring out the higher-mode effects in tall buildings. Thus, the code requires a dynamic lateral-force procedure for buildings taller than 240 ft (73.152 m) (UBC 94 §1627.8.3). Beams and columns are proportioned according to the Response Spectrum Method (UBC 94 §1629.5) scaled to 90% of the static procedure base shear. Overall building stability (P-Δ), individual column stability (P-δ), and accidental torsion are considered. The seismic design parameters used are summarized in Table 8.5 as defined in the UBC 94. Story drifts due to seismic loads are checked to remain below a maximum allowable limit of $\Delta_a = 0.0025h_{sx}$ using $C_s = 0.012$ (UBC 94 §1628.8).

Beams are proportioned to satisfy biaxial bending and shear strength demands. Although it is not uncommon for designers to proportion MF beams to yield in flexure (before shear), this check is not found to be explicitly specified in the UBC 94 as a beam proportioning issue and is not done here. Columns are proportioned to satisfy combined

axial and biaxial bending stresses using the Effective Length Method (AISC 335-89 §C2.2) and strong-column-weak-beam criteria. Beams and columns are also proportioned to satisfy acceptable width-thickness ratios. Doubler plates are added to PZs as prescribed by the code.

At the upper story levels, wind drifts and seismic stresses govern the beam design, and seismic stresses govern the column design. At the lower story levels, seismic stresses govern the column design, and beam sizes are increased so as to limit the Effective Length Method K-factor enough to satisfy the allowable column stress criteria.

Figure 8.4 shows that the maximum wind drift ratios due to the 10-year wind load are under $\frac{1}{400} = 0.0025$, and the maximum seismic drift ratios are under $\frac{0.03}{R_w} = 0.0025$. Due to symmetry only one loading direction is shown. The "total" drift is reported by the design program ETABS and scaled to reflect the appropriate drift-level loads. The "bending" drift is approximated based on the rotation of the entire story level. The "shear" drift is the difference between "total" and "bending" drifts.

Table 8.4: ASCE 7-93 wind design parameters for the 60-story example building.

Parameter	**Value**
V	70 mph (31.3 m/s)
Exposure category	B
I	1.00
$\bar{G}$	1.20
C_p	0.8 (windward) -0.5 (leeward)

Table 8.5: UBC 94 seismic design parameters for the 60-story example building.

Parameter	Value
C_s	0.030 (strength) 0.012 (drift)
Z	0.40
I	1.00
C	0.36
S	1.00
T	6.54
R_w	12

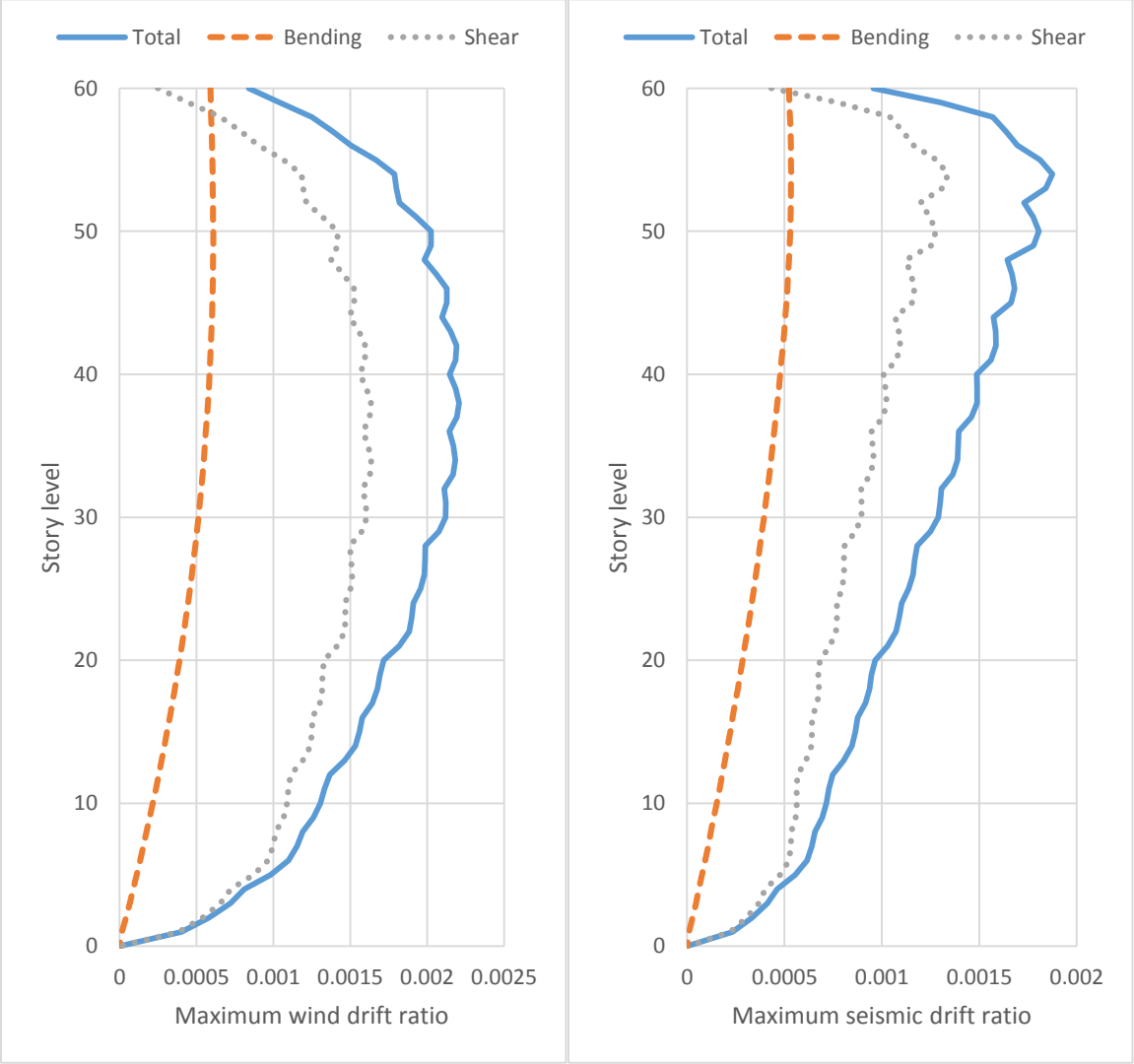

Figure 8.4: Maximum wind drift ratios using ASCE 7-93 (left) and maximum seismic drift ratios using UBC 94 Response Spectrum Method (right) for the 60-story building.

8.3 Modeling considerations

8.3.1 General

This section outlines the assumptions used to model the 60-story example building in PFRAME3D. It is organized as follows:

- Beams (§8.3.2)
- Columns (§8.3.3)
- Beam-column joints (§8.3.4)
- Floor/roof slabs (§8.3.5)
- Foundations (§8.3.6)
- Soil-structure interaction (§8.3.7)
- Gravity loads and mass (§8.3.8)
- Damping (§8.3.9)
- Miscellaneous parameters (§8.3.10).

3D models are created because 3D effects are present in tube buildings. Corner columns belong to two orthogonal frames, and so may be subject to biaxial bending. Torsion may be present due to probabilistic weld-fracture assignments, which can result in asymmetric yielding from bi-directional shaking.

8.3.2 Beams

MF beams are modeled as EF3 elements (§2.4), where each fiber segment is 3% of the total beam length (calibrated in Krishnan 2003, based on material properties). The material model of each fiber (Figure 3.7) is defined by

- $E = 29000\ ksi\ (200\ GPa)$
- $\sigma_y = 50.0\ ksi\ (345\ MPa)$
- $E_{sh} = 580\ ksi\ (4.00\ MPa)$
- $\varepsilon_{sh} = 0.012$
- $\sigma_u = 65\ ksi\ (448\ MPa)$
- $\varepsilon_u = 0.160$
- $\sigma_{fin} = 0.60\sigma_u$.

MF beams have rigid end connections. Perfect and brittle weld cases are considered. The perfect case assumes full ductility in a steel fiber, i.e., the tensile fracture strain is set to the tensile rupture strain, or $\varepsilon_f = \varepsilon_r$ (§3.7). But using perfect welds may be unconservative, especially for pre-Northridge buildings (Hall 1998, Krishnan and Muto 2012). That is partly because MF assemblages used in experiments were smaller than in real buildings, and the stress intensity factor K (in fracture mechanics) scales unconservatively with size. Additionally, field conditions may be non-ideal for producing perfect welds.

Thus, fracture-prone (brittle) welds are also modeled; if the tensile fracture strain (ε_f) is exceeded, the fiber can no longer carry tensile stresses. ε_f is handled according to a probabilistic 10-point distribution (10% probability for each point). The distribution used in Krishnan and Muto (2012) is used here. For a beam's bottom flange, $\varepsilon_f = 0.9\varepsilon_y$, $2\varepsilon_y$, $5\varepsilon_y$, $15\varepsilon_y$, and $40\varepsilon_y$ each have a 20% probability of assignment. For a beam's web and top flange, $\varepsilon_f = 10\varepsilon_y$ & $20\varepsilon_y$ each have a 30% probability of assignment, and $\varepsilon_f = 40\varepsilon_y$ & $80\varepsilon_y$ each have a 20% probability of assignment.

Gravity-only beams are modeled as PH elements (§2.3) with pinned end connections. Only primary gravity beams (that attach directly to columns) are included; no secondary beams (beams framing into beams) are modeled.

8.3.3 Columns

MF and gravity columns are modeled as EF5 elements (§2.5) to efficiently account for geometric nonlinearity and column splices. Each fiber segment is 3% of the total column length. Material properties match that of the beams. The center fiber segment is used to model column splices with two weld cases: perfect and brittle. For brittle column splices, $\varepsilon_f = 10\varepsilon_y$ & $20\varepsilon_y$ each have a 30% probability of assignment, and $\varepsilon_f = 40\varepsilon_y$ & $80\varepsilon_y$ each have a 20% probability of assignment.

8.3.4 Beam-column joints

The joints between beams and columns are modeled as PZ elements (§2.6). Its linear-quadratic ellipsoidal material model (Figure 2.11) is defined by

- $G = 11600.0\ ksi$ $(80.0\ GPa)$
- $\tau_y = 28.8675\ ksi$ $(199.03\ MPa)$.

8.3.5 Floor/roof slabs

Slabs are modeled as diaphragm elements (§2.7). Its linear-elastic material model is defined by

- $E = 3605.0\ ksi$ $(24.86\ GPa)$
- $\nu = 0.30$.

Each slab is 6.25 in (0.159 m) thick, and configured to laterally constrain every node at a floor without adding global nodes, as shown in Figure 8.5. If the beams on both sides of a column fail, the diaphragm prevents the column from two-story buckling.

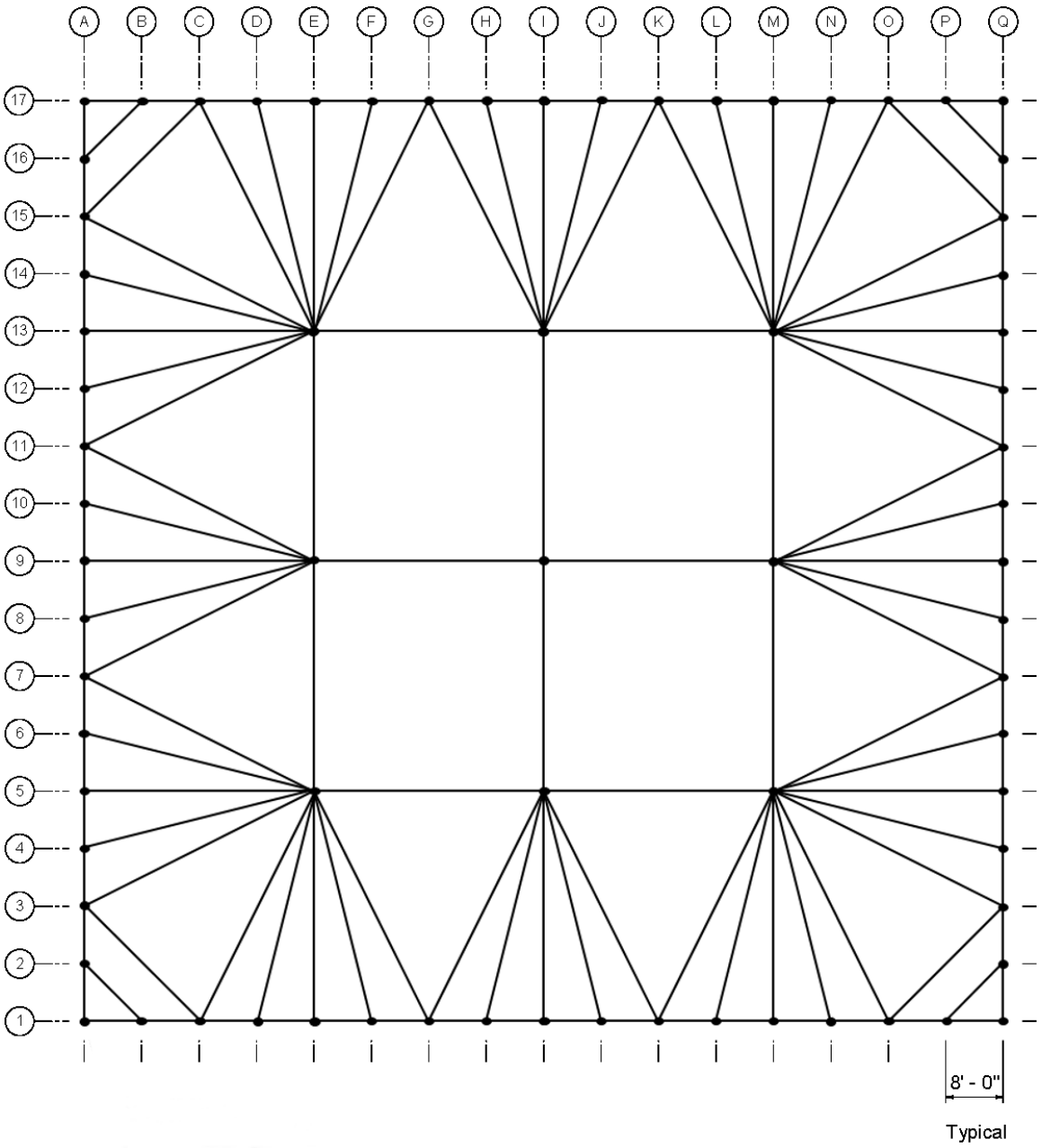

Figure 8.5: Layout of diaphragm elements in a typical floor level.

8.3.6 Foundation

A mat foundation, typical in DTLA, is approximated using elastic beams (§2.3) at ground level (Figure 8.6). The beams have stiffness properties that match a 10 ft (3.3 m) deep foundation with an elastic material model where $E = 3605.0\ ksi$ (24.86 GPa). The beams are rigidly connected. Subterranean levels are not modeled.

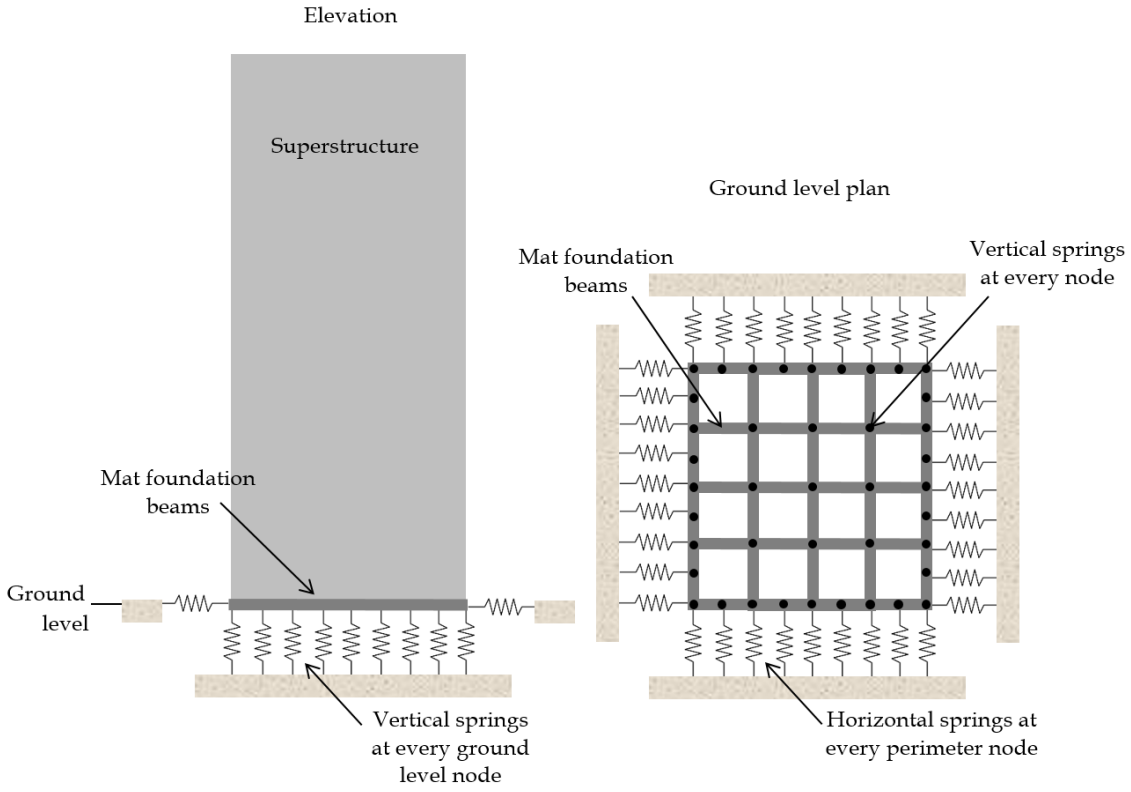

Figure 8.6: Foundation and soil modeling for 60-story example building.

8.3.7 Soil-structure interaction

To model soil-foundation-structure interaction, springs (§2.8) are attached at ground level to the foundation beams (§8.3.6) as shown in Figure 8.6. Horizontal springs are placed orthogonal to the perimeter at the base, and vertical springs are distributed

throughout the footprint of the base. The vertical springs automatically account for rocking. All springs are elastic. The springs' combined effect is tuned to yield a 10% fundamental-period increase for Building 1 (the 6.16 sec fundamental period in Table 8.2 includes soil-structure interaction), whilst maintaining a horizontal-to-vertical soil stiffness ratio of 1-to-1.27 determined by the shallow-foundation equations from NIST GCR 12-917-21 §2.2; these equations depend on the soil's shear modulus G, Poisson's ratio ν, and the dimensions of the shallow foundation. The stiffness of an individual spring is directly proportional to its "tributary" perimeter (horizontal springs) or area (vertical springs).

8.3.8 Gravity loads and mass

Vertical gravity forces are applied at every global node (to form $\{f_g\}$ in Eq. 2.2), before and throughout dynamic analysis. Additionally, masses that represent the inertia of the building are applied at every global node (to form $[M]$ in Eq. 2.2). 100% dead loads and 25% live loads are used for both gravity loading and masses. Rotational-DOF masses are not included.

8.3.9 Damping

Rayleigh damping is used. As mentioned in §3.6, there are some unrealistic effects associated with Rayleigh damping that are significant before and during collapse but are not addressed here. These effects should be taken into consideration when interpreting results (Hall 2005; ATC 72 §2.4.4.3). 2% damping is used because it is typical for a 60-story building (ATC 72 §2.4.3.1). To capture the effects of significant higher modes, the 2%

damping limits are anchored as shown in Figure 8.7 at the fundamental period T_1 and at $0.2T_1$ (ATC 72 §2.4.4). Because $T_1 = 6.16\ sec$ and $0.2T_1 = 1.23\ sec$, $a_0 = 0.0340$ and $a_1 = 0.00654$. In other words, the first three translational and first two torsional modes are damped at or below 2%. For future work, capped dampers will be included into the PFRAME3D framework.

8.3.10 Miscellaneous parameters

The tolerance, convergence, and Newmark parameters used in analysis are shown in Table 8.6. Also, analysis is automatically terminated if any node's displacement exceeds $300\ in\ (7.62\ m)$, when the building is clearly collapsing.

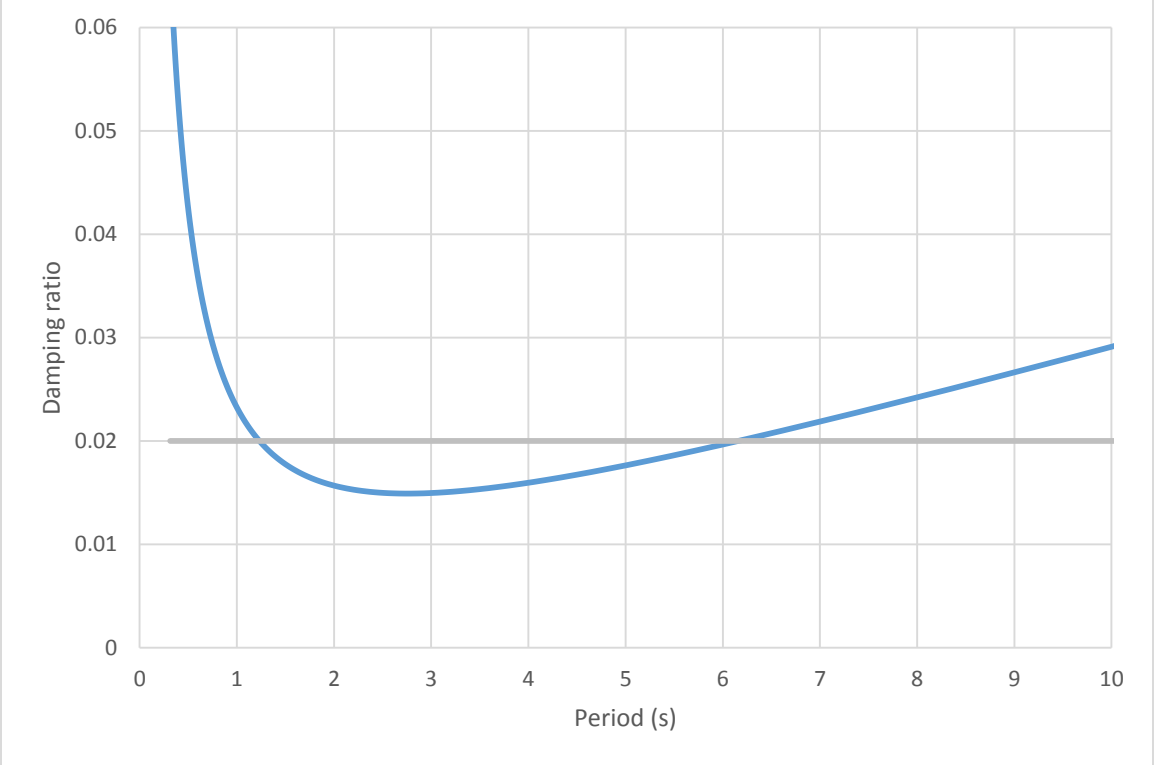

Figure 8.7: Damping ratio vs. period for 60-story example building.

Table 8.6: Tolerance, convergence, and Newmark parameters

Parameter	Value
Global force tolerance	0.1 k
Global moment tolerance	0.1 $k\ in$
EF3/EF5 force tolerance	0.005 k
EF3/EF5 moment tolerance	0.005 $k\ in$
% stiffness* for PH elements	5%
% stiffness* for EF3/EF5 elements	5%
% stiffness* for PZ elements	5%
Newmark β	0.25
Newmark α	0.50

*The percent elastic stiffness matrix added to every tangent stiffness matrix during global iterations.

8.4 Building analyses and results

8.4.1 General

To understand the nonlinear behavior of the 60-story example tube building, two types of analysis are conducted:

- Dynamic pushover analysis (§8.4.2)
- Dynamic time-history analysis (§8.4.3).

It must be noted that these results reflect preliminary results (due to potential shear yielding, not captured in the current model, of the deep beams between very closely spaced columns) and that a more realistic building will be designed in the near future.

8.4.2 Dynamic pushover analysis

A pushover analysis is useful for determining the strength and ductility of a structure. During a pushover, lateral loads are increased gradually until the building collapses. In a dynamic pushover, a ramped horizontal ground acceleration causes the lateral loads (e.g., as done in Krishnan 2003). It rises at a rate of $0.3g/min$ in the present case, which allows for a gradual deterioration of members. Masses are distributed according to §8.3.8 (not according to a building code's vertical distribution of force, e.g., UBC 94 §1628.4). Damping is removed. Due to plan symmetry, only one direction of loading is considered (the X-direction). Four pushover analyses are run: 1 perfect-weld case, and 3 brittle-weld cases (called "brittle weld cases 0 – 2"), each with a different distribution of fracture strains.

To interpret results, pushover curves are constructed in Figure 8.8, which has three subplots:

(1) The base shear (as a percentage of overall building weight, see §8.3.8) is plotted vs. the displacement at the roof centroid. This force-deformation relationship is known as the "pushover curve." It shows the building's ultimate strength, which is defined here at the peak base shear. It also shows ductility, which is defined here as the ratio between the ultimate and yield displacements (same definition as in Krishnan 2003).

(2) The base shear is plotted vs. time. This plot is useful for determining when ultimate strength is achieved, so that the building state at the ultimate point can be further studied. It is approximately linear until collapse because it

reflects the 0.3 g/min loading; the dynamic nature of analysis prevents it from being perfectly linear.

(3) The roof X-displacement is plotted vs. time. This plot shows the rate at which the buildings approach collapse.

A summary of the pushover curves is shown in Table 8.7. The perfect weld case can withstand a 13.3% base shear, which is 4.43 times larger than the 3% design base shear. This "over-strength" factor is typical compared to previously studied high-rise buildings; e.g., the approximately 20-story UBC 97 buildings in Krishnan (2003) were reported to have over-strength factors ranging from 1.5 to 5.5. The perfect weld case also has a ductility ratio of $\frac{3.65}{1.81} = 2.02$, which is near the lower limit of "ductile behavior." (According to the FEMA 356 standard for the assessment of seismic performance, a building is "ductile" if its ductility ratio exceeds 2.) The example building is less ductile than previously studied high-rise buildings; e.g., Krishnan (2003) reported ductility ratios ranging from 2.4 to 5.6. The pushover curve never bottoms out to 0% because there is still some shear resistance in the first story after the collapse mechanism forms in the upper stories (see Figure 8.12). The brittle weld cases can withstand base shears roughly 2/3rds than that of the perfect case. They exhibit non-ductile behavior (ductility ratios are under 2). Brittle weld case 1 showed the median ultimate base shear, so it is used for further analysis. Brittle weld cases 0 and 2 are no longer considered.

Table 8.7: 60-story example building pushover results. Roof displacement (m), percent base shear (% of building weight), and ductility ratio (ultimate roof displacement/yield roof displacement).

	Yield		Ultimate		Ductility ratio
	Roof disp.	**Base shear**	**Roof disp.**	**Base shear**	
Perfect	1.81 m	10.4%	3.65 m	13.3%	2.02
Case 0	1.38 m	8.47%	1.45 m	8.75%	1.05
Case 1	1.38 m	8.47%	1.55 m	8.90%	1.12
Case 2	1.40 m	8.56%	1.57 m	8.93%	1.12

By examining the story drift ratios at the ultimate state (Figure 8.9), it is shown that the collapse mechanism is localized to the mid-height story levels. For the perfect case, stories 25 – 33 exceed 3% drift, and for the brittle weld cases (case 1 shown in Figure 8.9), stories 26 – 32 exceed 1% drift. The perfect case shows a maximum of over 6% drift (at story 29) before instability (the steep drop in base shear in Figure 8.8), and the brittle weld case shows a maximum of less than 1.5% drift (at story 30) before instability.

More specifically, Figure 8.10 and Figure 8.11 show that the collapse mechanism forms as nearly all the web-frame beams from several floors fracture (or, for the perfect weld case, reach the rupture strain ε_r). Shown are:

(1) An isometric view of the frame at the ultimate state to provide context (upper left of Figure 8.10 and Figure 8.11).

(2) A zoomed-in planar view of the web-frame at the ultimate state (right of Figure 8.10 and Figure 8.11), with plastic hinges and flange fractures marked by square and triangle markers, respectively, as shown in the legend (bottom left of Figure 8.10 and Figure 8.11). Black markers are relevant for frame elements and white markers are relevant for PZ elements. The square markers vary in size depending on the plastic rotation in percent radians. Flange fractures

represent a more severe state, in which the fibers can only contribute in compression. Plastic rotations are not plotted for a segment if at least 1 of its flanges has fractured.

The perfect weld case (Figure 8.10) shows that beams within the band of concentrated lateral displacement are plastically hinging with rotations exceeding 6%; many of these beams also have fractured flanges. Although barely visible in Figure 8.10, column plastic hinges have formed at story levels 25, 26, 31, and 32. The brittle weld case (Figure 8.11) shows more fractured flanges. Because fractures occur sooner, the brittle weld case collapses sooner. Column hinging is not observed at the ultimate state. Almost no PZ plastic rotations are observed in either perfect or brittle weld cases.

Isometric snapshots of the building (Figure 8.12) when nodal displacements exceed 300 in ($\sim$7 m) show that the mechanism is of the shear band type confined to story levels 25 – 32 (perfect) or 20 – 33 (brittle). Many beams in the brittle weld case are shown to have completely failed. The observed collapse mechanism indicates that, although the tube-frame design intends for flange-frame columns to resist lateral loads axially (§C), when it comes to nonlinear deformations, web-frame beams are the first to yield and fail. This effect can largely be attributed to the strong-column/weak-beam design philosophy and the result is that the collapse mechanism resembles a shearing (not a bending) beam. It should be stated that the author still agrees with the philosophy; the failure of a single beam is likely less catastrophic than the failure of a single column, and the observed collapse mechanisms form only after many beams over many floors fracture. Additionally, more analyses will be conducted in the near future to confirm any trend.

The "somewhat brittle" behavior of the 60-story example building's "perfect case" can be attributed to its very closely spaced columns and very deep beams. This is illustrated by considering the strain of a fiber n in a pure bending beam, as shown in Figure 8.13 and summarized by

$$\varepsilon_n = Z'_n \kappa \qquad \text{(Eq. 8.1)}$$

where ε_n is the strain of fiber n, Z'_n is the position of fiber n relative to the neutral axis, and κ is curvature (the reciprocal of the radius of curvature). It can be seen (Figure 8.13) that Z'_n increases with beam depth, thus for a given κ, ε_n increases, too. It can also be seen (Figure 8.14) that for a given beam rotation θ (which approximately correlates to story drift), κ increases (radius of curvature decreases) as beam span decreases, thus ε_n increases, too. Therefore, ε_n increases "more quickly" in a building with deep beams and closely spaced columns, which results in fibers rupturing at smaller story drifts. Overall, the building is less ductile.

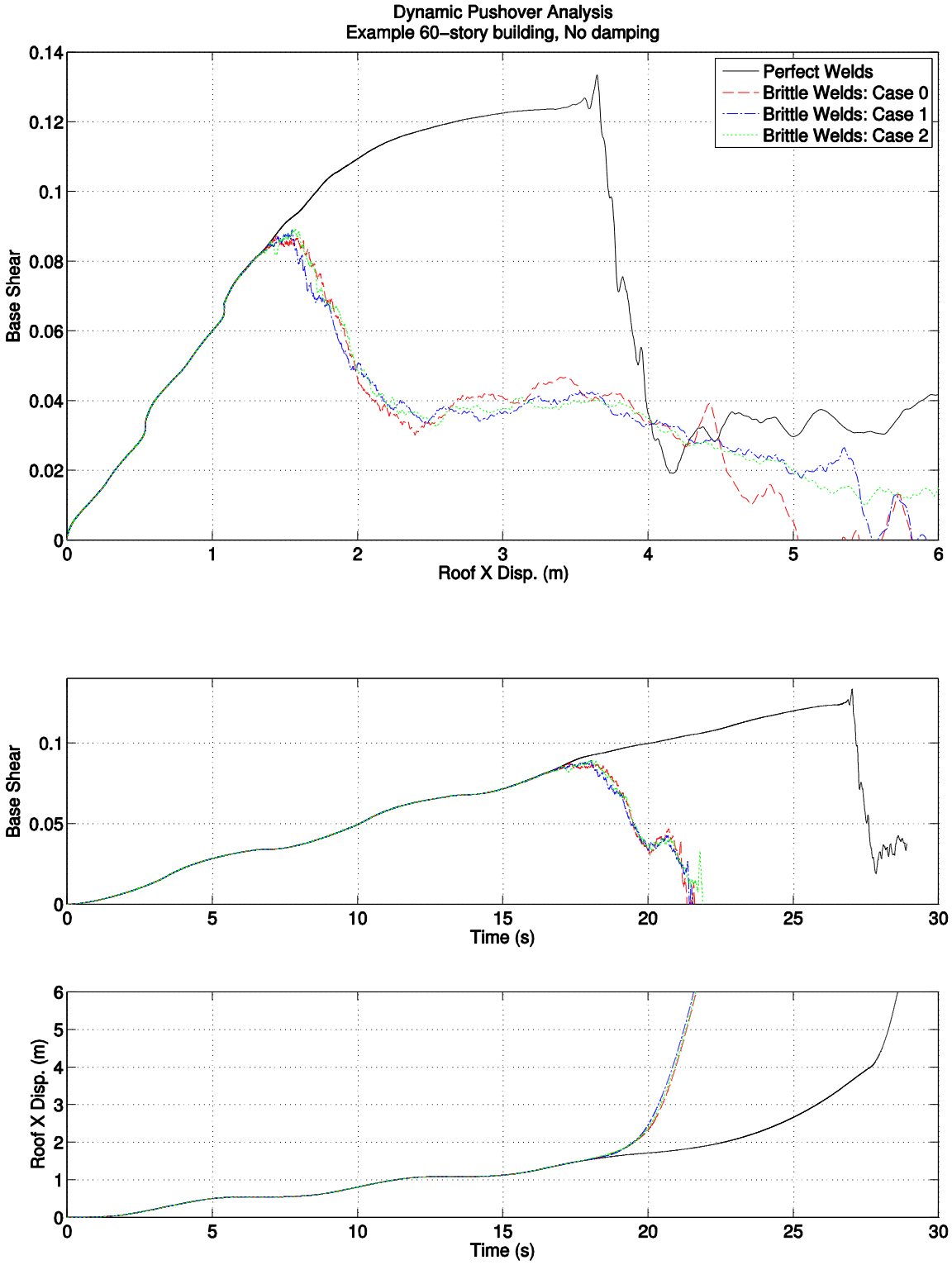

Figure 8.8: 60-story example building pushover curve (top), base shear history (middle), and roof $|X|$ displacement history (bottom), using perfect welds and 3 cases of brittle welds.

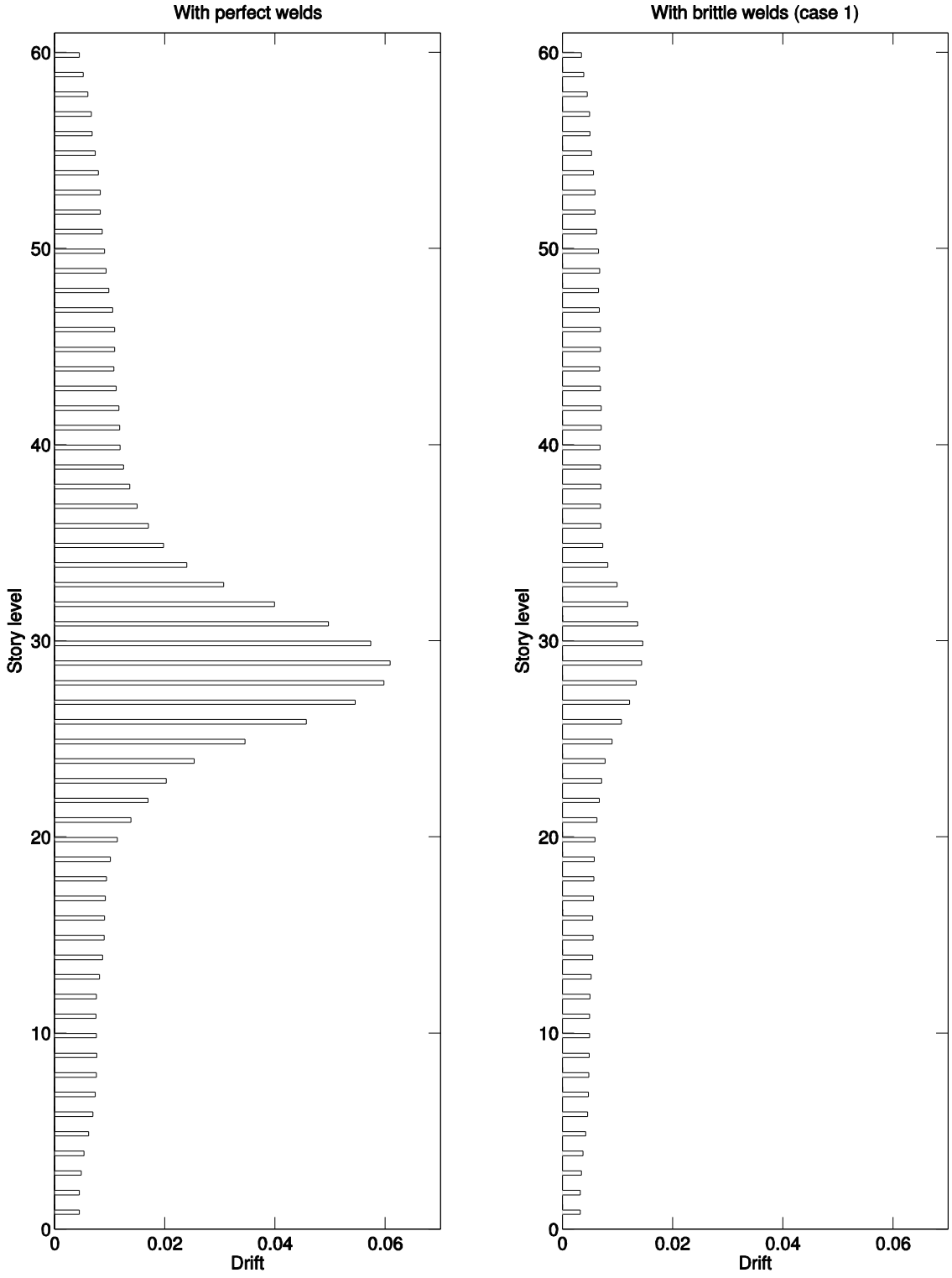

Figure 8.9: Story drift ratios at maximum pushover base shear. Shown are the perfect weld case (left) and the brittle weld case 1 (right).

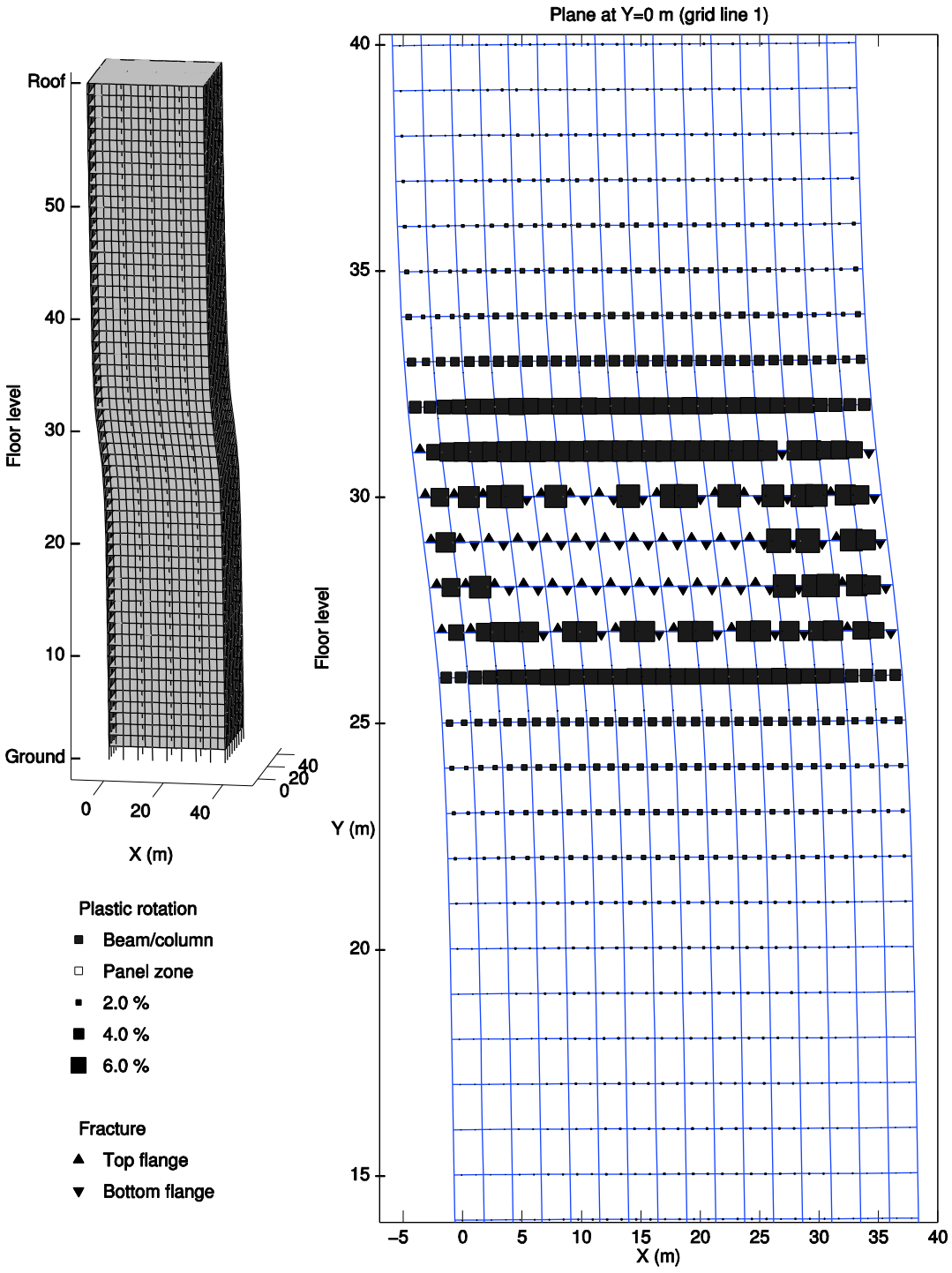

Figure 8.10: 60-story example building with perfect welds at ultimate state, t=27.0 sec. Web frame shown on right for the middle portion of the building. Deformations are amplified by 2 for both views.

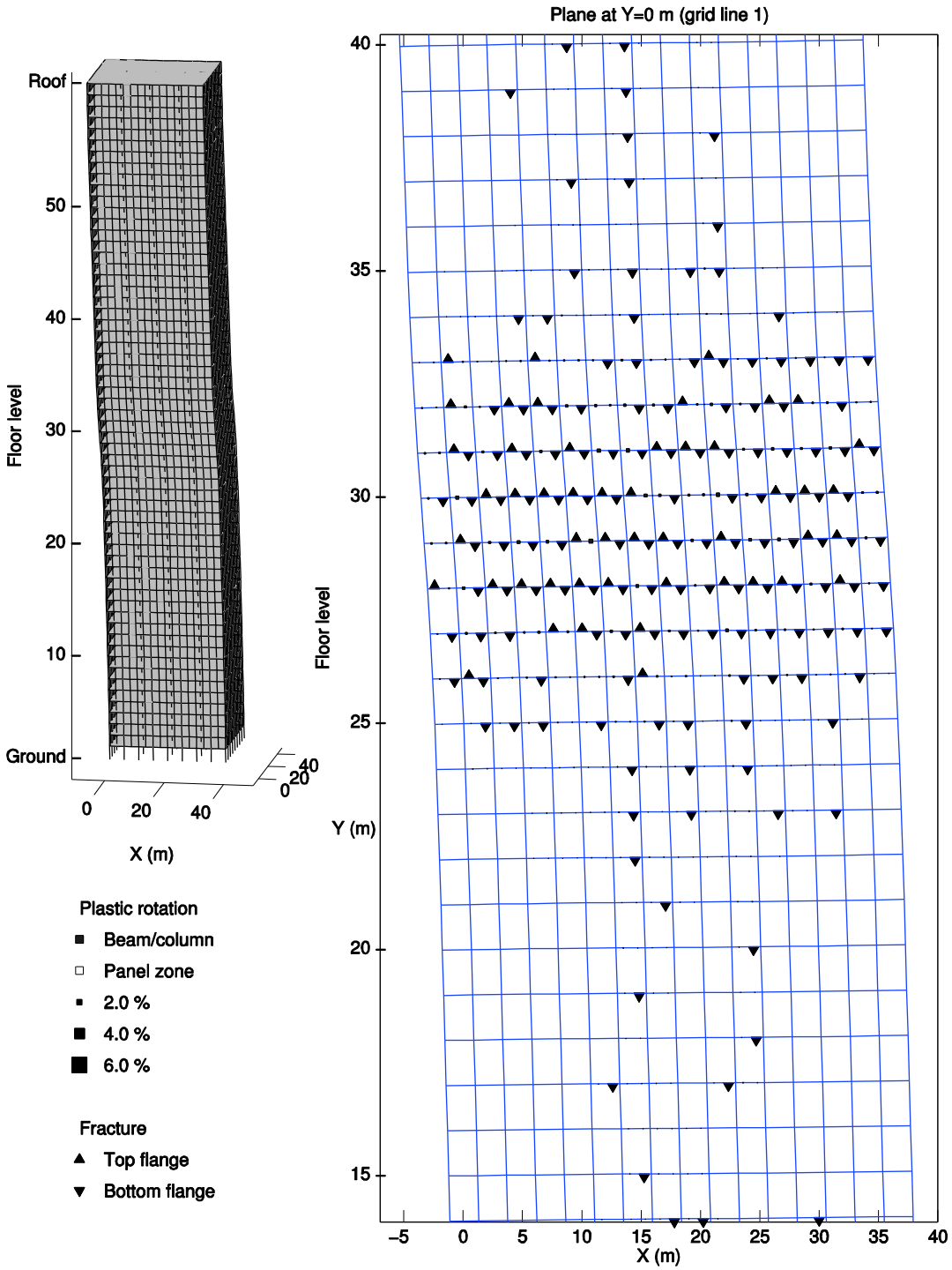

Figure 8.11: 60-story example building with brittle welds (case 1) at ultimate state, t=18.0 sec. Web frame shown on right for the middle portion of the building. Deformations amplified by 5 for both views.

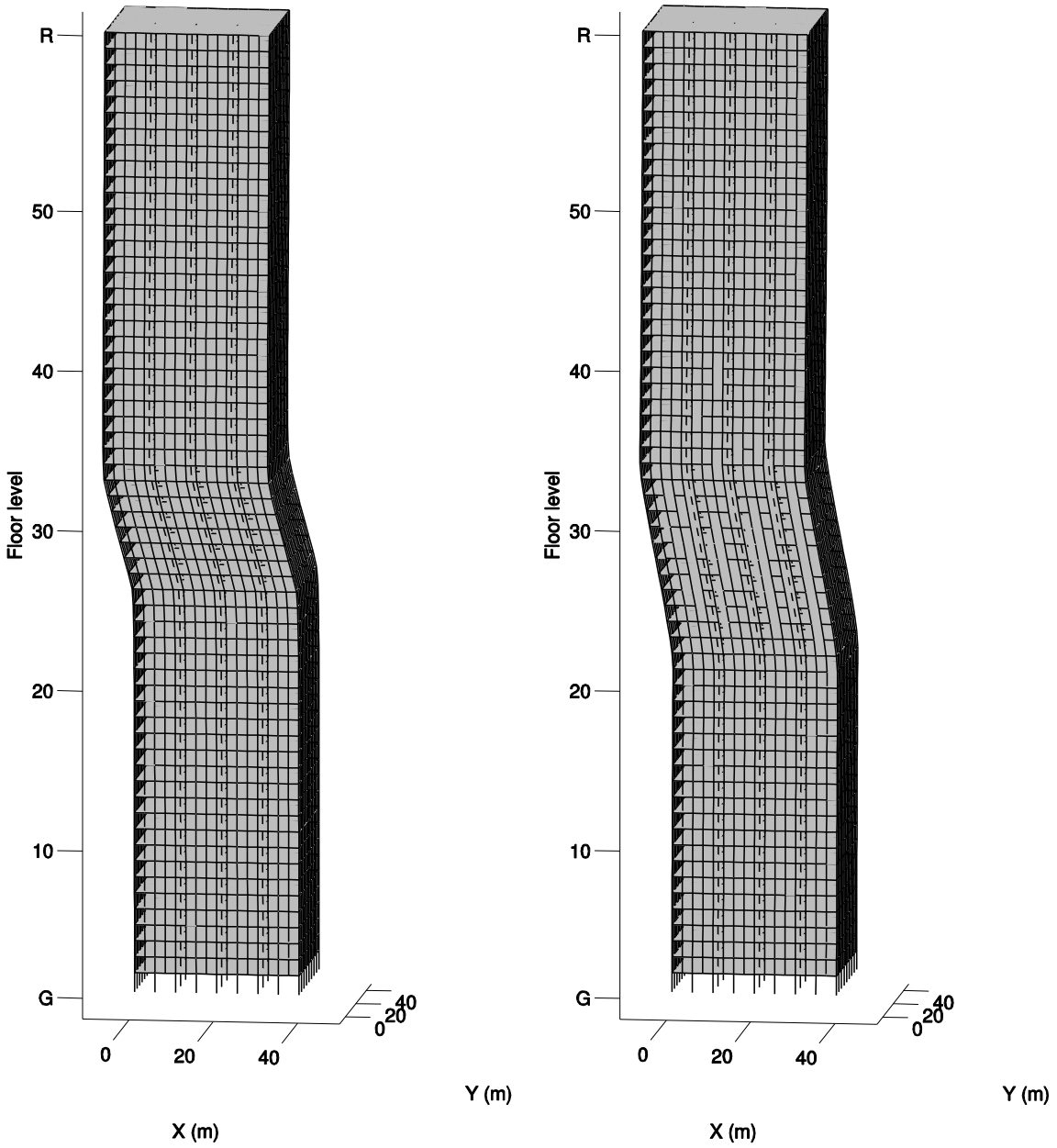

Figure 8.12: Pushover collapse mechanisms of 60-story example building with perfect (left) and brittle (right) welds. Snapshots are taken when nodal displacement exceeds 300 in (~7 m; at t=28.9 sec and t=21.9 sec, respectively). Unamplified deformations shown. Failed elements are not shown as they are omitted from analysis.

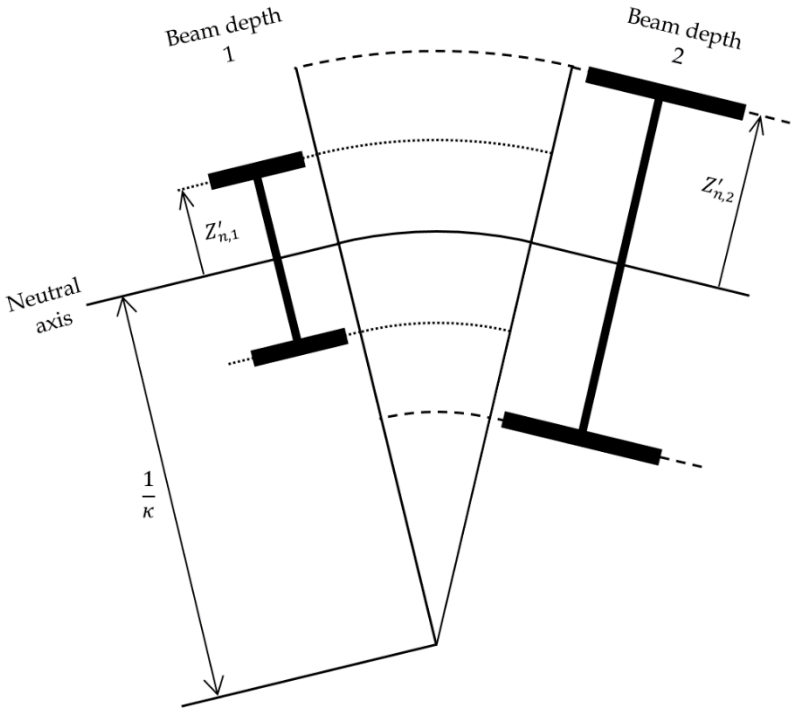

Figure 8.13: Illustration showing pure-bending of a beam, from which the relationship between fiber strain ε_n, fiber position Z'_n (relative to the neutral axis), and curvature κ can be derived.

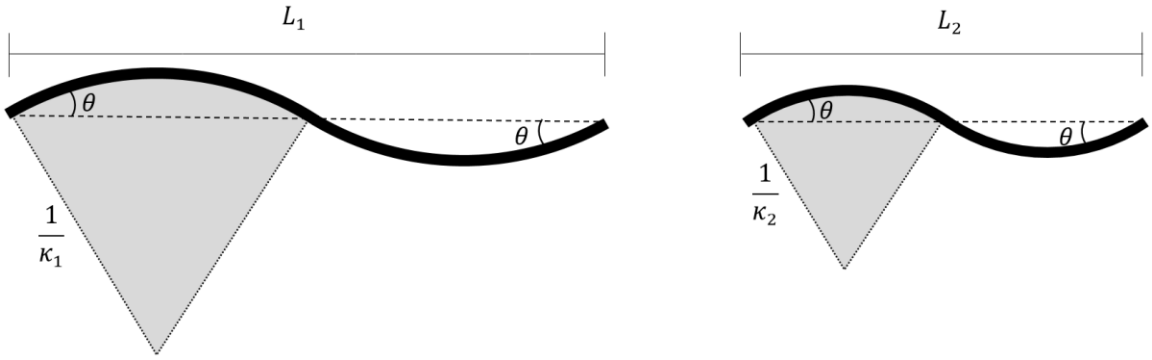

Figure 8.14: Illustration showing that for a given end rotation θ, curvature κ is larger when beam length L is shorter, i.e., because $L_1 > L_2$, $\kappa_1 < \kappa_2$.

8.4.3 Dynamic time-history analysis

The 60-story example building is subjected to the 2002 M_w 7.9 Denali earthquake ground motion at Pump station #10 (Figure E.3). Figure E.3, which includes the pseudoacceleration spectra of this ground motion (corresponding to a 1-DOF system with 2% and 5% damping), shows that this ground motion exceeds the UBC 94 design spectra significantly.

Floor displacement and story drift time histories are plotted to help assess the performance of the example building (Figure 8.15 and Figure 8.16). Each figure has four subplots: X and Y displacements from the centroid of each floor, and X and Y story drifts, based on the relative centroidal displacements of adjacent floors. The floor displacements reflect the motions relative to the shaking ground, not the absolute displacements. The story drifts reflect the total story-drift ratios, not a bending or shear component. Time histories from every floor/story are shown, where the floor/story is defined by the color bar. Deep blue corresponds to the base of the building, and deep red corresponds to the top of the building. From these plots it is clear that the building with perfect welds remains stable, while the building with brittle welds collapses.

The perfect weld case experiences highest X story drifts of over 2% at the upper stories (levels 46 – 54; peak at level 49 with 2.87%). Residual story drifts of up to about 1% are observed in the X direction. In the Y direction, peak and residual drifts are under 2% and 0.3%, respectively. Most of the damage can be attributed to the large pulse around $t = 20\ sec$.

The brittle weld case collapses with a shear-band mechanism at mid-height (levels 20 – 37). The large pulse around $t = 20\ sec$ is observed to not fully travel up the height of

the building; instead it is observed to contribute to the mid-height damage that eventually leads to collapse. Although the building does not collapse in the Y direction, upper mid-height stories (around level 43) experience a peak Y drift of 4.7%.

A story-drift summary is shown in Figure 8.17. The white and black bars correspond to X and Y drifts, respectively. Peak story-drifts are shown for the perfect case, and collapse-mechanism story drifts (at $t = 30\ sec$) are shown for the brittle weld case. The brittle weld case collapse mechanism resembles the one observed in pushover analysis, but the peak drifts of the perfect weld case do not, a result of higher mode effects.

To help understand what is happening at the element level, column P/P_y and beam M/M_p time histories are plotted in Figure 8.18 & Figure 8.19 and Figure 8.20 & Figure 8.21, respectively. P and P_y are the current and yield axial forces, respectively, in the column. M and M_p are the current and plastic moments, respectively, in the beams.

There are five subplots in Figure 8.18 and Figure 8.19 (the P/P_y plots). Each subplot corresponds to a unique column line as shown in Figure 8.1 and Figure 8.2. Shown are column lines A1, E1, I1, A5, and A9. Specific story-levels can be extracted based on the colorbar. The corner column experiences higher peak P/P_y values than the interior MF columns (0.48 vs. 0.30 for the perfect-weld case), which can be attributed to a combination of shear lag (§C) and bi-directional shaking. P/P_y is not observed to approach unity.

There are six subplots in Figure 8.20 and Figure 8.21 (the M/M_p plots). Each subplot corresponds to a unique set of beams. Specific floor-levels can be extracted based on the colorbar. Figure 8.21 (the brittle weld case) represents failed beams as horizontal lines, extended from the time and M/M_p at failure. Many perfect-weld beams are shown to exceed the plastic moment, and only a few brittle-weld beams exceed the plastic moment.

Building damage is shown using plastic-rotation and flange-fracture plots (Figure 8.22 and Figure 8.23). For the perfect case, peak plastic rotations are shown (Figure 8.22) because the damage represents the envelope of the time history and not a particular time step; thus, the plastic rotations are plotted on an undeformed configuration. The highest damage occurs at level 48 with beam plastic rotations of 2.39% radians and PZ plastic rotations of 1.36% radians. For the brittle weld case, collapse-mechanism damage (Figure 8.23) is mapped on a deformed configuration (at $t = 30.0\ sec$). Damage is severe as many beams have failed, and many remaining beams have one or multiple fractured flanges. Columns are observed to not yet develop significant plastic rotations.

For the perfect weld case, a summary of plastic rotations is presented in Table 8.8. All hinges are under 3% radians and about half of the beam components experience almost no plastic rotations (less than 0.1% radians). "Beam minor axis" plastic rotations can be attributed to diaphragm inertial effects.

If compared to performance assessment criteria such as FEMA 356 or ASCE 41, which were developed after 1994, the perfect weld case building would be classified as "collapsed" because some beams exceed major-axis plastic-rotation limits; e.g., from FEMA 356, the major-axis plastic-rotation "collapse prevention" limit is $8\theta_y$, where $\theta_y = \frac{M_p L}{6EI}$. ($M_p$, L, E, and I are the beam's major-axis plastic moment, clear length, elastic modulus, and major-axis moment of inertia, respectively.) For the 60-story example building, θ_y ranges from 0.12% to 0.29% radians, which is much smaller than the 0.5% to 1.1% radians range reported for the 19-story buildings in Krishnan (2003). The small θ_y can be attributed to the closely spaced columns (small L) and deep beams (large I, although this second point is complicated by the fact that M_p is also larger for deep beams);

i.e., θ_y is smaller for beams near the base and larger for beams near the roof. In other words, the $8\theta_y$ "collapse prevention" limit is reached at plastic rotations of 0.96% to 2.3% radians.

It is important to restate, however, that shear yielding is not included in the EF3/EF5 formulation, so the nonlinear behavior of the MF beams in the example building is not fully captured. A more realistic building will be designed in the near future, featuring wider column spacing and beams with shear capacities greater than $2M_p/L$. Results from that analysis will be presented in a subsequent paper.

Still, the 60-story example building is useful in the present research for showcasing the ability of PFRAME3D to perform highly nonlinear and collapse analyses efficiently.

Table 8.8: Summary of plastic rotations from time-history analysis (due to the Denali earthquake ground motion at Pump station #10), with perfect welds.

Component	≤ 0.1%	(0.1, 1.0]%	(1.0, 2.0]%	(2.0, 3.0]%	(3.0, 4.0]%	(4.0, 5.0]%	> 5.0%
Panel zone	2586	1361	133	0	0	0	0
Beam major axis	3678	3818	288	8	0	0	0
Beam minor axis	7561	231	0	0	0	0	0
Column major axis	8687	0	0	0	0	0	0
Column minor axis	8682	5	0	0	0	0	0

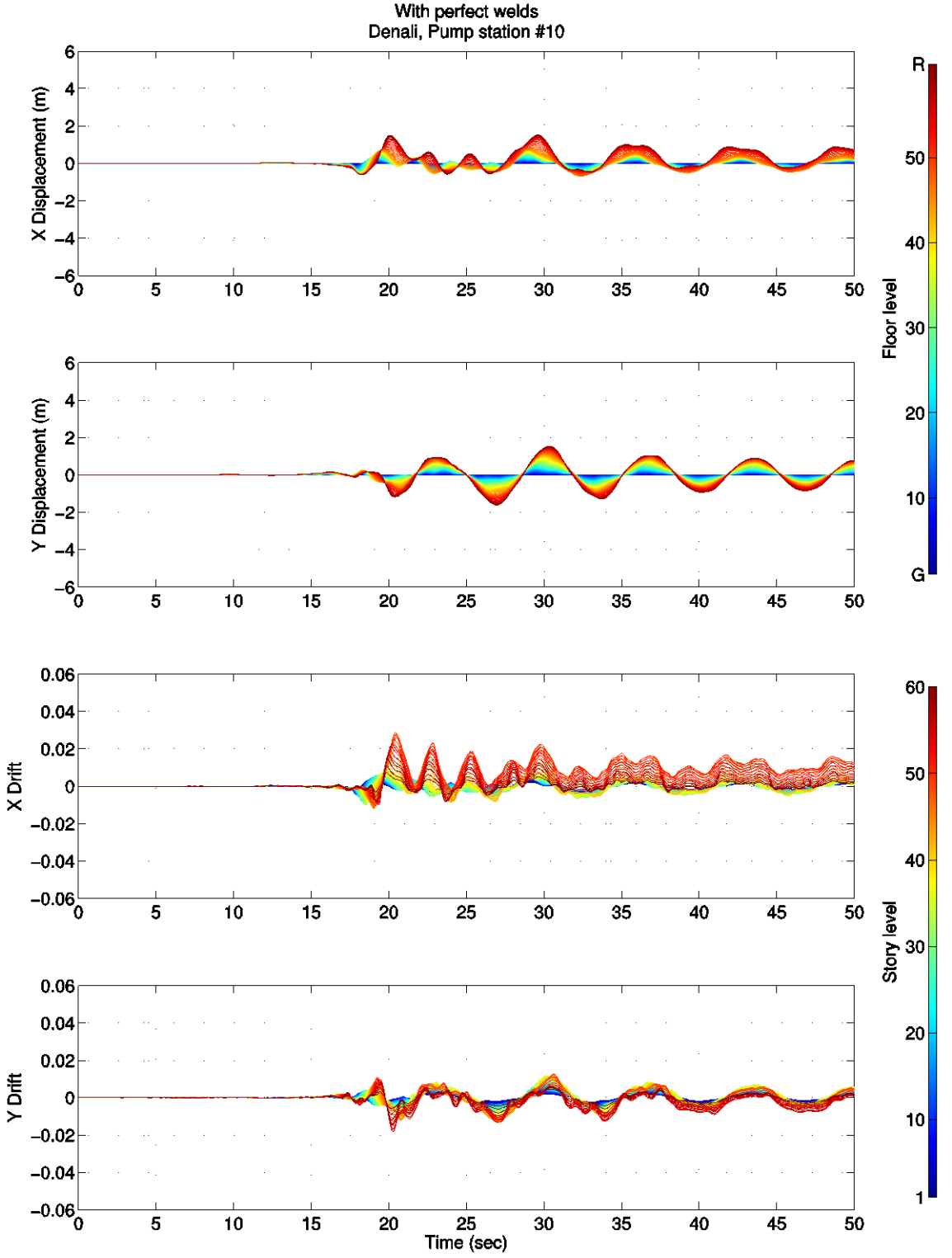

Figure 8.15: Displacement and drift histories of 60-story example building with perfect welds, subjected to the Denali earthquake ground motion at Pump station #10.

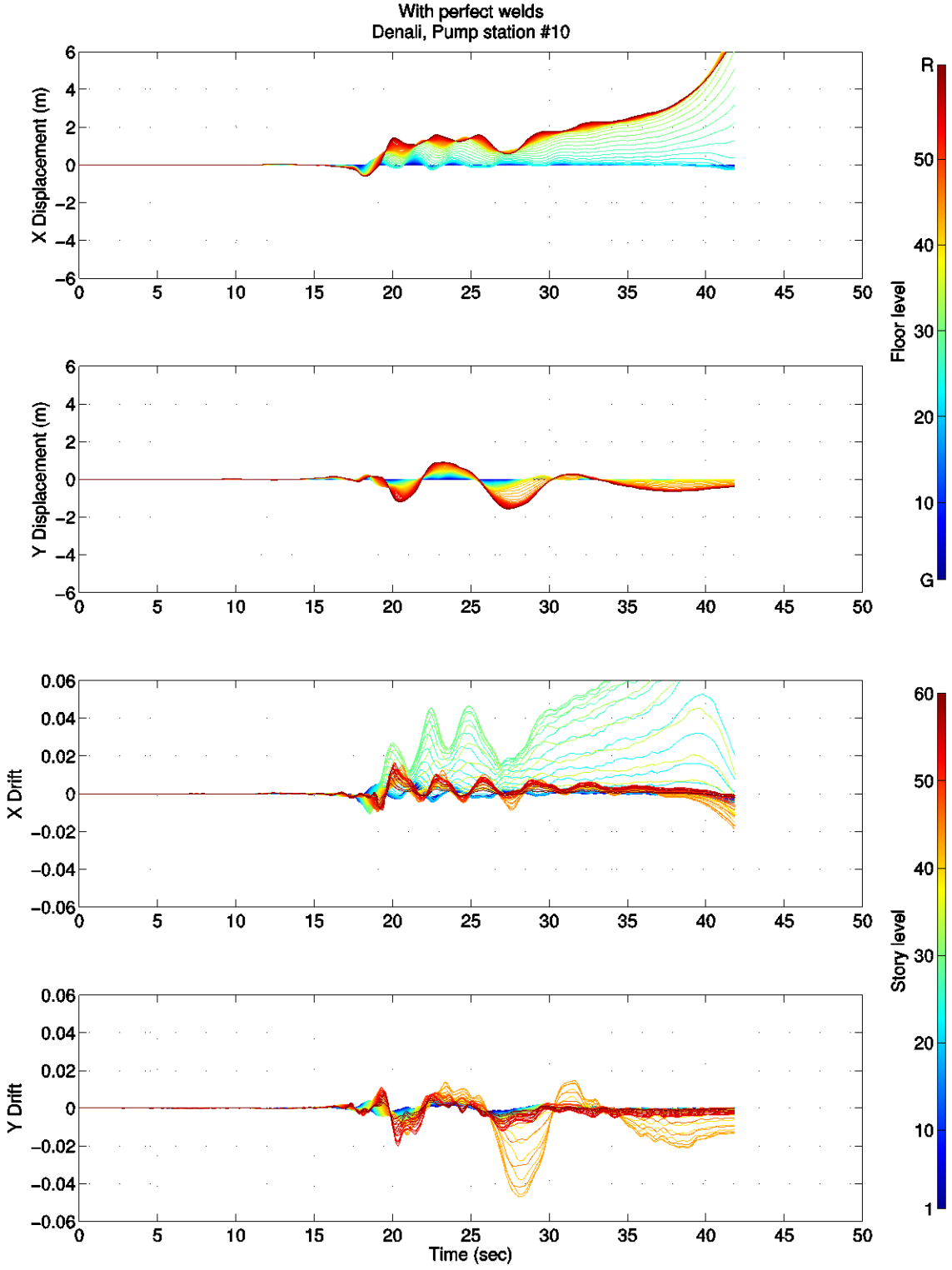

Figure 8.16: Displacement and drift histories of example 60-story building with brittle welds, subjected to the Denali earthquake ground motion at Pump station #10.

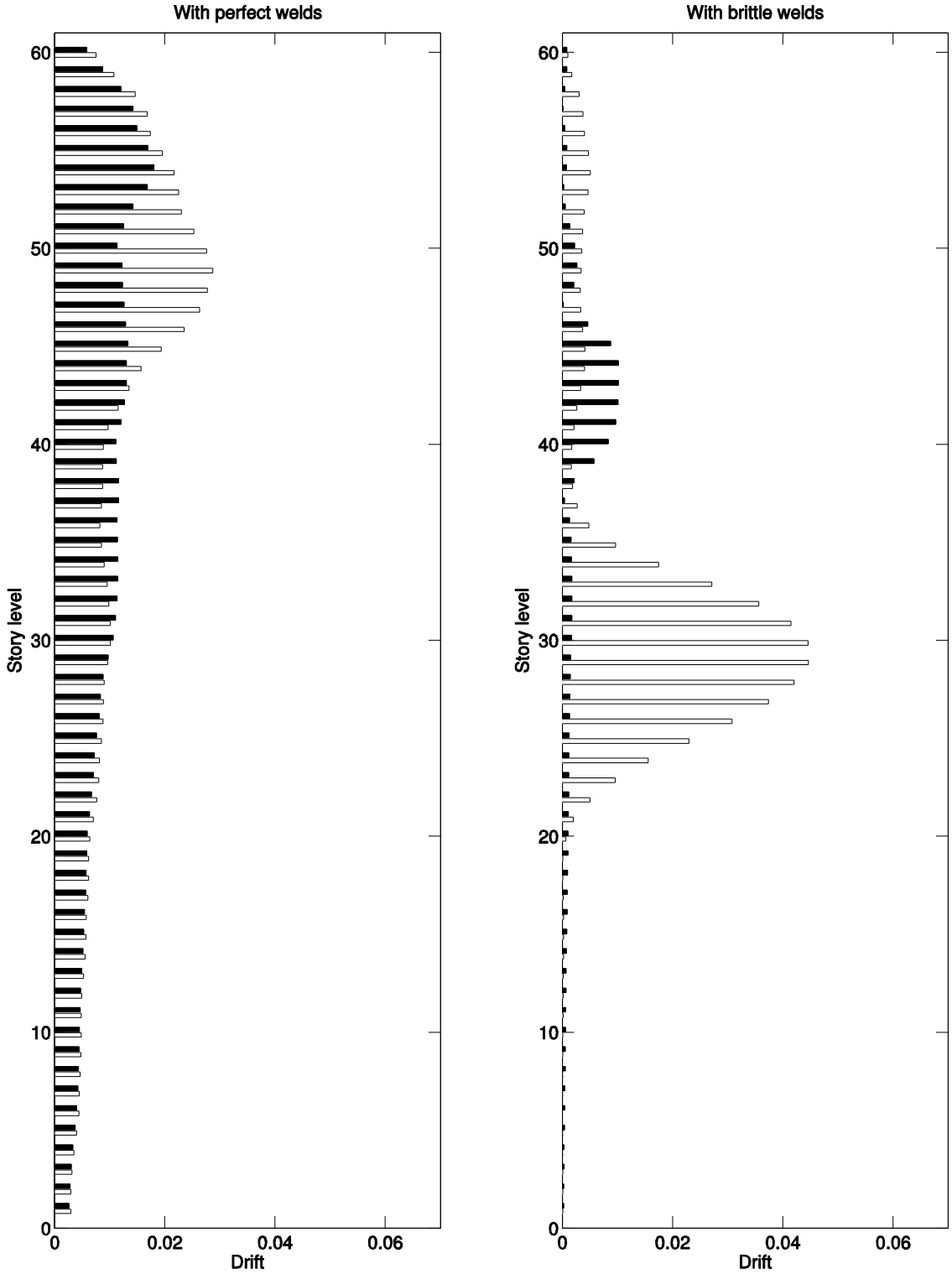

Figure 8.17: Story drift summary of time-history analysis with perfect (left) and brittle (right) welds. In the left, peak drifts are plotted. In the right, collapse mechanism drifts (at t=30.0 s) are plotted. Shown are drifts in the X (white) and Y (black) directions.

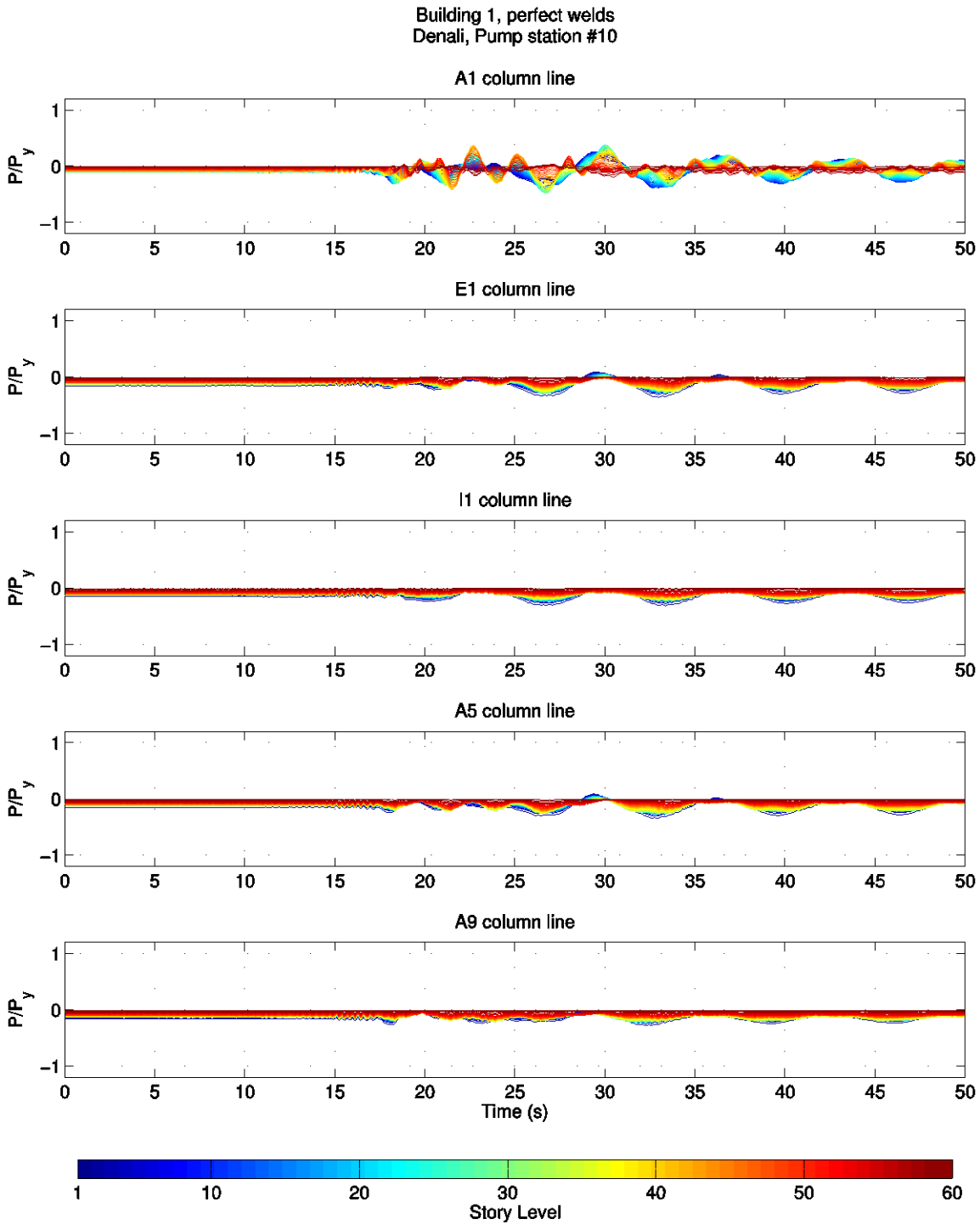

Figure 8.18: P/P_y histories of 60-story example building with perfect welds, subjected to the Denali earthquake ground motion at Pump station #10.

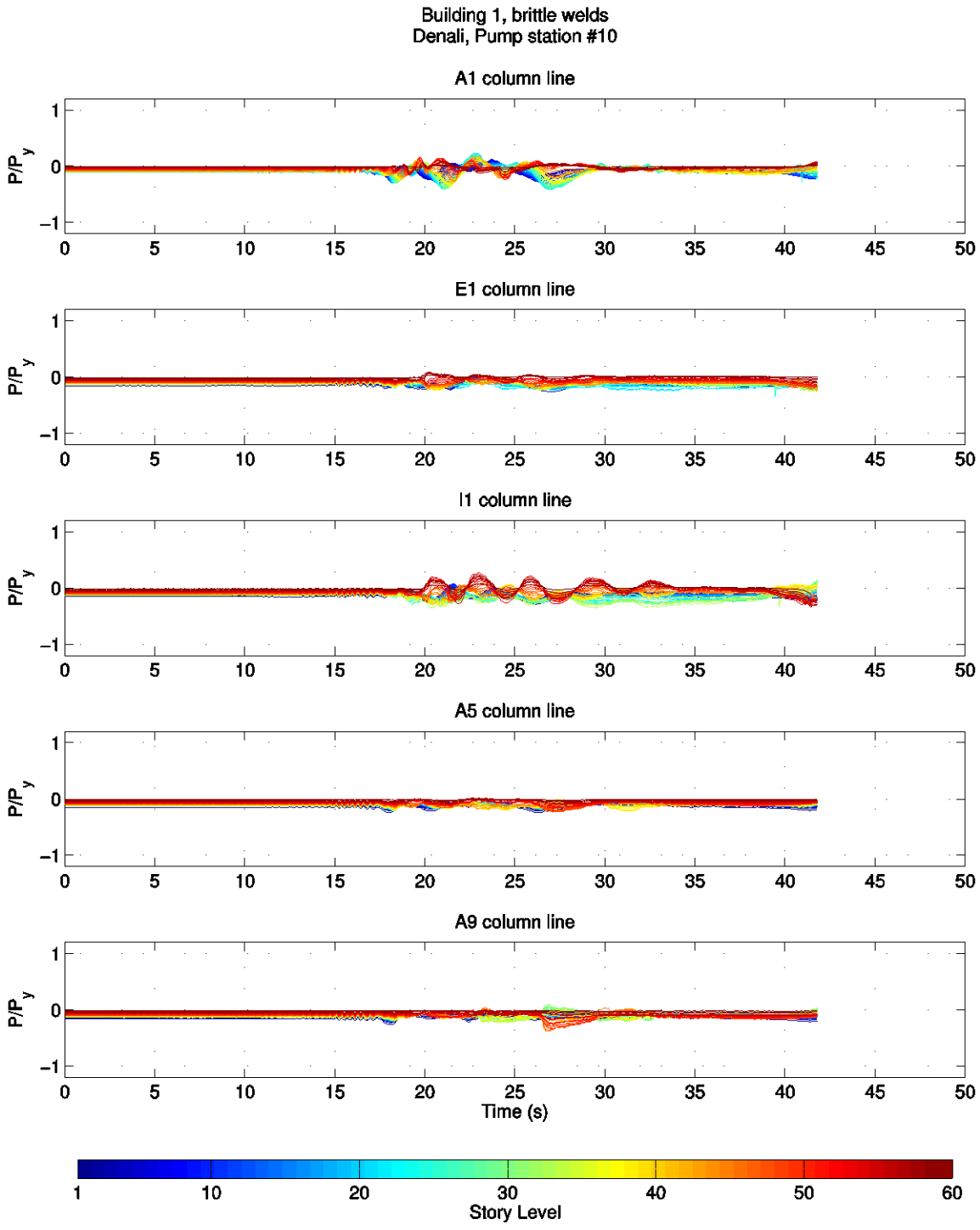

Figure 8.19: P/P_y histories of 60-story example building with brittle welds, subjected to the Denali earthquake ground motion at Pump station #10.

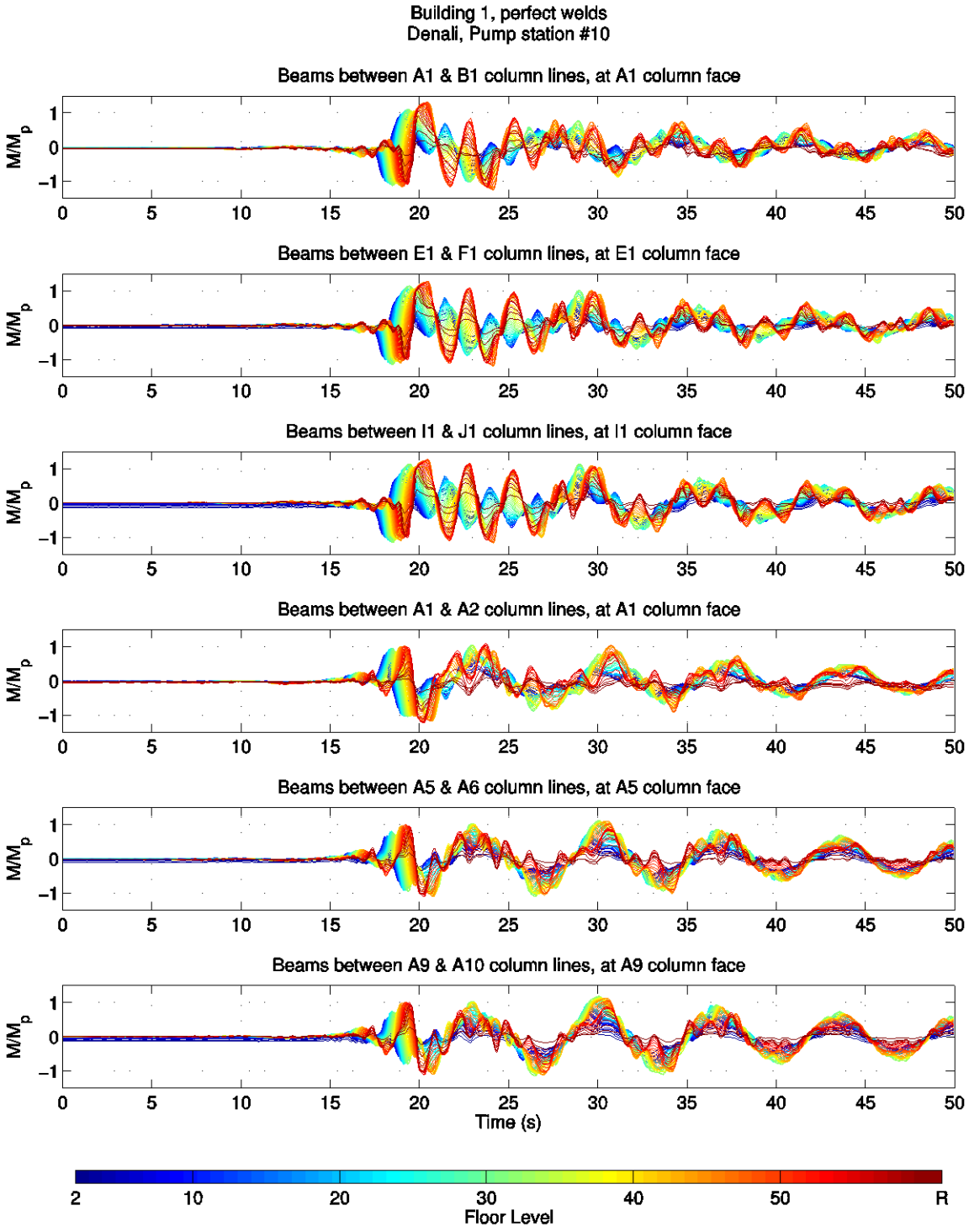

Figure 8.20: M/M_p histories of 60-story example building with perfect welds, subjected to the Denali earthquake ground motion at Pump station #10.

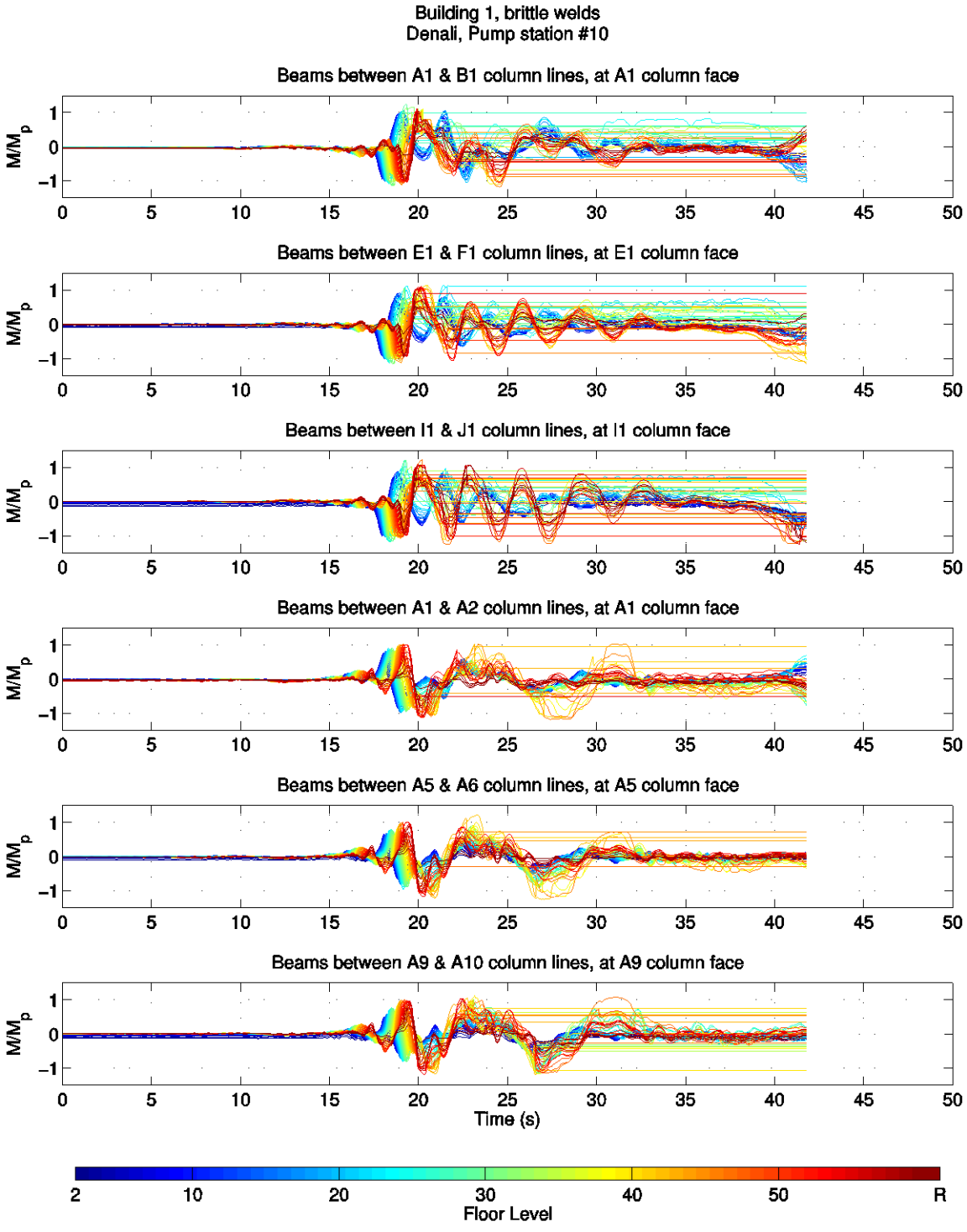

Figure 8.21: M/M_p histories of 60-story example building with brittle welds, subjected to the Denali earthquake ground motion at Pump station #10.

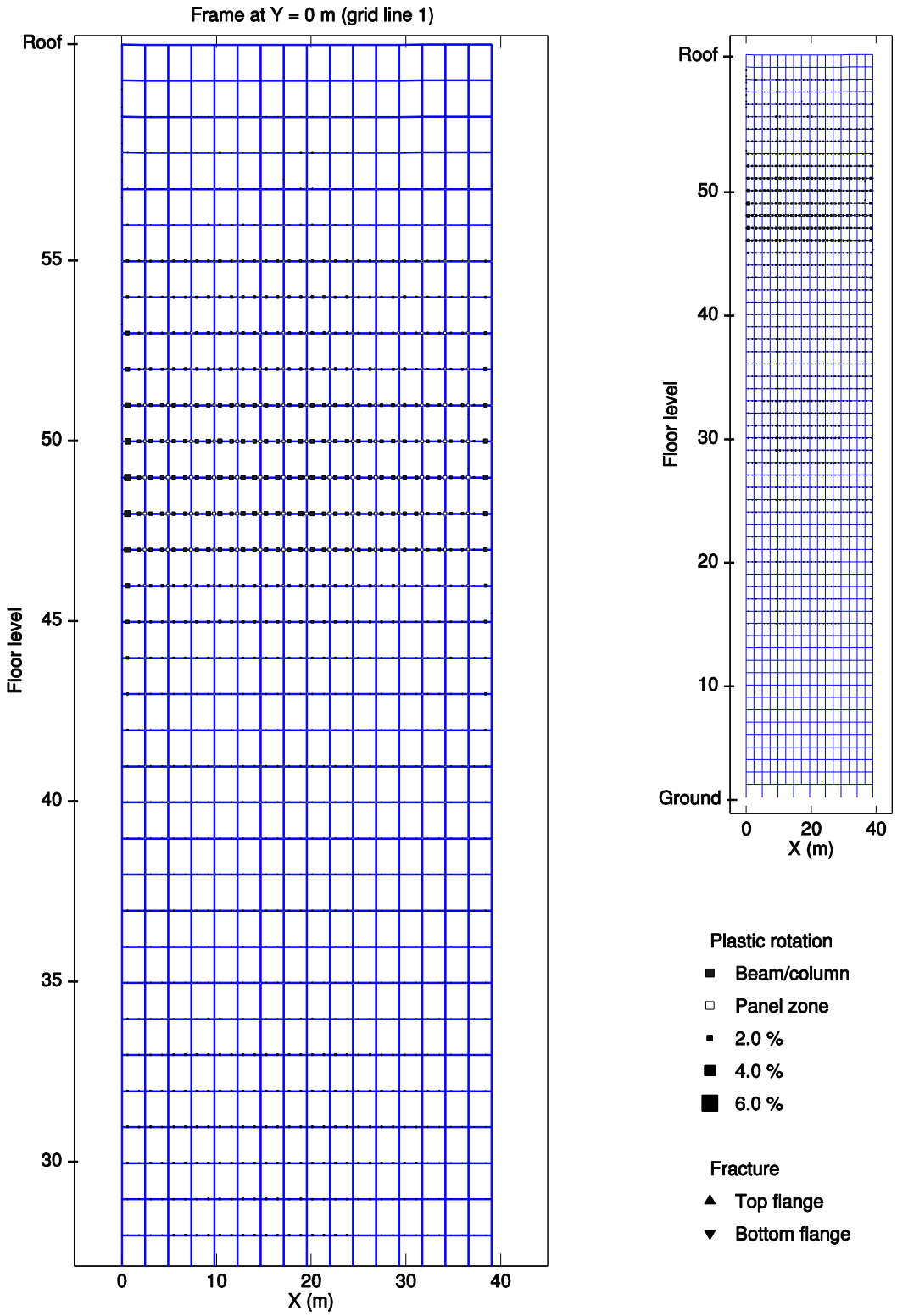

Figure 8.22: Peak plastic rotations in perfect weld case time-history analysis (due to the Denali earthquake ground motion at Pump station #10).

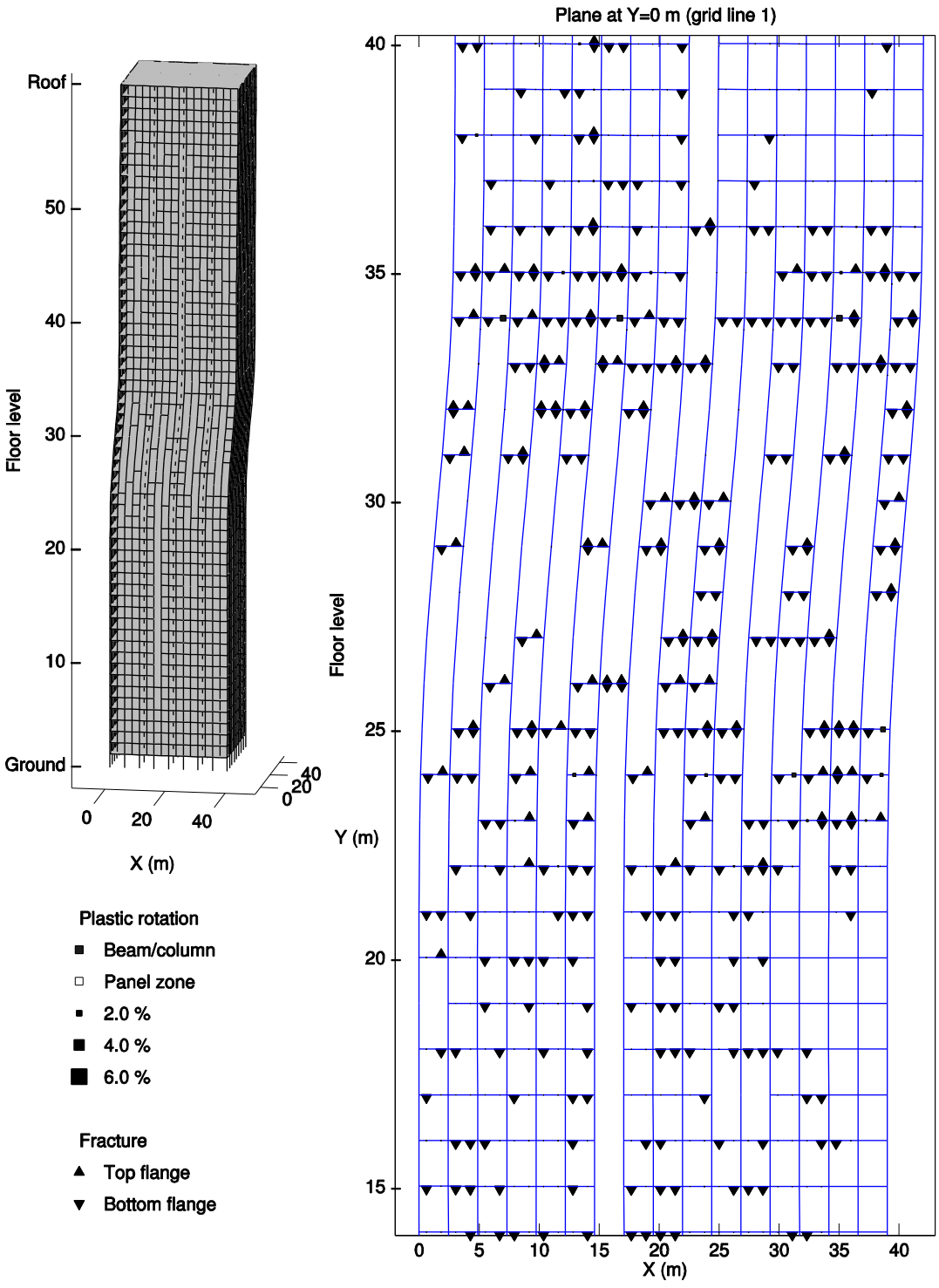

Figure 8.23: Collapse mechanism (at t=30.0 sec) and plastic rotations and flange fractures (right) in brittle weld case time-history analysis (due to the Denali earthquake ground motion at Pump station #10).

Chapter 9

Conclusions and Future Directions

9.1 Conclusions

In Part I, a comprehensive finite element program for the highly nonlinear analysis of steel buildings, FRAME3D, is reviewed then revised. The review covers the iterative global solution procedure and the formulations of various elements.

The revisions address specific nonlinear situations involving large displacement/rotation increments, the backup-subdivide algorithm, element failure, and extremely narrow joint hysteresis. The result of the revisions is superior convergence capabilities compared to the previous version of FRAME3D, as shown through a water-

tank tower dynamic time-history collapse simulation. The structure can collapse "to the ground." Although it is reasonable to expect that this convergence capability applies to other structural collapse simulations, it is noted that the structural models themselves may not capture all of the behavioral features of extremely large deformations associated with collapse conditions.

The fiber backbone curve is modified to allow for post-rupture compressive strength, which provides a more realistic representation of fiber behavior at large compressive strains while addressing a sometimes non-convergent situation in the fiber-segment formulation. The result of this modification is an overall increase in the strength of the water-tank tower (no longer collapses with the 32% Kobe earthquake ground motion at Takatori). It is found that whether a model collapses is sensitive to the additional parameters defined by the modified backbone curve; thus, experimental validation is needed to further improve realism.

In Part II, FRAME3D is sped up using serial optimizations and parallel computing. Serial optimizations alone result in an overall wall time reduction (for the collapse of a 60-story building due to the Denali at Pump station #10 ground motion) from 650 hrs to 83.6 hrs. The improvement due to serial optimization is primarily attributed to a reduction in cache-misses, most notably by switching to column-major and blocked code.

A parallel framework to efficiently analyze highly nonlinear behavior of very tall buildings is developed, further reducing the same 60-story simulation wall time to 5.69 hrs with 128 cores. A divide-and-conquer approach is used for both the global direct solver and element-state updates. The divide-and-conquer solver is found to be most suitable for problems where m is relatively small compared to n. The element-state

updates are distributed to "match" that of the divide-and-conquer solver, resulting in communication costs that are generally limited by the half-bandwidth m of the global matrix. PFRAME3D is one of if not the first implicit finite-element hybrid-parallel program with a "unified" domain decomposition scheme that takes advantage of the narrow-band nature of very tall buildings and uses nearest-neighbor-only communication patterns.

Using three structures of varied sizes, PFRAME3D is shown to compute reproducible results that agree with that of the optimized 1-core version with much less wall time. Displacement-history results of parallel computations have root-mean-squared errors (against 1-core computations) of up to about $\sim 10^{-5}\ m$, which are negligible in the context of building structures. Maximum speedups are shown to increase with building height (as the total number of cores used also increases), and the parallel framework can be expected to be suitable for buildings taller than the ones presented here.

In Part III, PFRAME3D is applied to a 60-story example building. The building is designed according to the UBC 94 and has a fundamental period of 6.16 sec. Modeling considerations are presented. Dynamic pushover and time-history (Denali at Pump station #10) analyses are conducted using "perfect" and "brittle" weld cases. It is noted, however, that the very short span beams in the 60-story example building are found to be inappropriately modeled because shear yielding is not captured by the current element formulation. The conclusions below must be considered as "preliminary" until a more realistic building model is developed for more detailed analyses in the near future.

Dynamic pushover analysis reveals multi-story shear-band collapse mechanisms around mid-height of the building. The dynamic time-history brittle weld case collapses

with a similar mechanism. This collapse mode is attributed to the strong-column/weak-beam design philosophy, and it is not unreasonable to expect a similar shear-band collapse mechanism for other MF tube buildings. Still, more analyses should be conducted first to confirm any trend.

The dynamic pushover analysis indicates that the use of closely spaced columns and deep beams can lead to "somewhat brittle" behavior (ductility ratio of 2.02). This is explained by considering the relationship between fiber strain, beam depth, and curvature—essentially that for deep short-span MF beams, fibers will rupture/fracture at smaller story drifts.

Both pushover and time-history analyses show that overall building strength is sensitive to whether a model is fracture-capable. This result is consistent with previous studies (e.g., Hall 1998, Carlson 1999, Krishnan and Muto 2012) and shown here to apply to very tall steel buildings, too. In the pushover analysis, the brittle weld case has an ultimate base shear that is roughly two-thirds that of the perfect weld case. In the time-history analysis, the brittle weld case collapses while the perfect weld case does not when subjected to the Denali earthquake ground motion at Pump station #10.

The perfect weld case remains stable (from the Denali time-history) with peak transient story drifts of 2.87% at story level 49, peak transient column $P/P_y = 0.48$, and peak transient beam plastic rotations of 2.39% radians. Although seismic assessment criteria (e.g., FEMA 356) would classify the building as "collapsed" due to excessive beam plastic rotations, the computed model remains stable at the end of the ground motion.

9.2 Future Directions

It is of interest to develop steel building models to study with the current framework. In the near future, realistic very tall MF buildings will be developed for highly nonlinear analysis. A tube design with wider column spacing will be considered. A bundled-tube building will also be designed to further avoid the short beam modeling limitations found presently. These building models will be subjected to a variety of strong ground motions. Very tall braced-frame and dual-frame steel buildings can also be studied with PFRAME3D, which may prove to be useful for the structural engineering community.

It will be beneficial to implement a more accurate damping formulation. This is a topic that must be addressed especially for nonlinear and collapse dynamic analysis. Rayleigh damping with constant coefficients can overestimate damping forces. Damping elements will soon be incorporated into PFRAME3D, similarly to how they are already implemented in FRAME2D, to remove errors from Rayleigh damping assumptions.

Because PFRAME3D introduces significant speedups, it is of interest to develop more detailed element types. For example, fiber elements (composed of only fiber segments, e.g., in FRAME2D) can replace the elastofiber elements used in PFRAME3D, which were originally created for efficiency and calibrated for MF beams. One such advantage of fiber elements is a more realistic representation of plastic axial deformation, which is especially useful for brace members.

To be able to more accurately study a greater variety of structures (e.g., eccentric braced-frames or even the 60-story example building), it is of interest to generalize the

segment formulation to account for shear yielding. Or, to study composite structures, additional fibers (representing the composite floor slab) can be added to each fiber segment as is done in FRAME2D.

Future work can include the revision of the PZ formulation to include an axial DOF—so that the PZ can participate in the axial deformation of columns.

The consideration of the post-rupture compressive strength of a fiber as presented in §3.7 can be improved. Building response and collapse potential is shown to be sensitive to the inclusion of post-rupture compressive strength. Although including some post-rupture strength is more realistic than ignoring it, the $\sigma_{fin} = 0.6\sigma_u$ strength and the $\varepsilon_{sf} = -0.9$ segment failure strain presently used were not thoroughly substantiated by experimental data. More realistic values should be selected and verified in future work.

Future work may also include the direct modeling of local flange buckling and its effect on the global response of structures. With the parallel computing framework of this thesis, modeling structures with greater detail is achievable.

Regarding the hybrid-parallel framework presented in this thesis, future work may include improving the divide-and-conquer solver (e.g., by accounting for sparsity within the narrow band), exploring alternate solution algorithms (e.g., nonlinear conjugate gradient method), investigating efficient methods for distributed-memory dynamic load-balancing, or implementing a GPU-cluster version of PFRAME3D.

There is still much to improve in terms of the structural engineering community's ability to more accurately and efficiently model buildings in earthquakes. This thesis is a step towards that goal.

Appendix A

Computer Architecture

A.1 Terminology

A.1.1 General

The reader may not be familiar with some of the terminology used by the parallel computing (PaC) and/or structural finite element modeling (FEM) communities. To add confusion, word usage may overlap between these two disciplines. For example, *node* refers to a computer in a computer cluster in PaC, but to a joint in a FEM model. Or, *local* refers to a single node in PaC, but to the element-level calculations in FEM. And *global* refers to a set of nodes in PaC, but to the structure-level calculations in FEM. The context

of usage determines which definition is used and Figure A.1 & Figure A.2 illustrate the relationships between some terms.

A.1.2 Hardware

- A *computer cluster* is a set of computers that is configured to work as a unit (Figure A.1). Each computer (with its local processors, RAM, and disk) is often called a *node*.
- A PaC node may have 1 or more *processors*; e.g., a dual quad-core computer has 2 processors (Figure A.2). A *processor* is the computer's calculator; it executes the instructions. A processor may have 1 or many *cores*, e.g., a quad-core processor has 4 cores.
- A *core* can execute a single stream (*thread*) of commands, though it often does so in a *single instruction multiple data (SIMD)* manner using *vector registers*. For the purposes here, consider a core capable of doing sequential operations.
- There are three general types of memory storage: disk, RAM, and cache.
- The *disk*, or hard drive, can store the most amount of data, but is the slowest to access. Usually, it is accessed only when reading from or writing to a file.
- The *RAM (Random Access Memory)* is accessed faster than the disk but can hold less data. A computer program generally works from the RAM to eliminate the need to search for variables in the disk.
- The *cache* is accessed faster than the RAM but can hold less data. When a program accesses a variable in the RAM, it transfers neighboring variables to its cache, which reduces the need to re-access the RAM in the near future.

There are multiple levels of cache in modern computers—L1, L2, and L3—where L1 is the fastest-but-smallest and L3 is slowest-but-largest. More discussion on the cache is found below (§A.2).

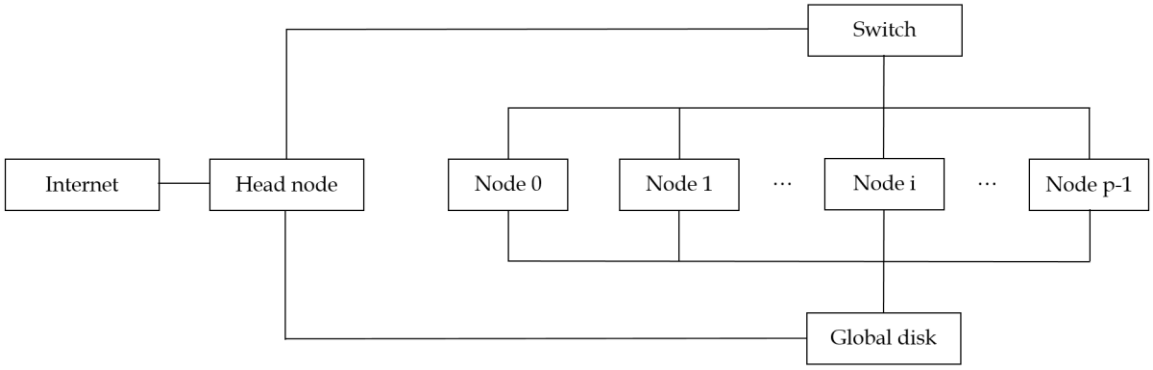

Figure A.1: Typical computer cluster schematic with p nodes.

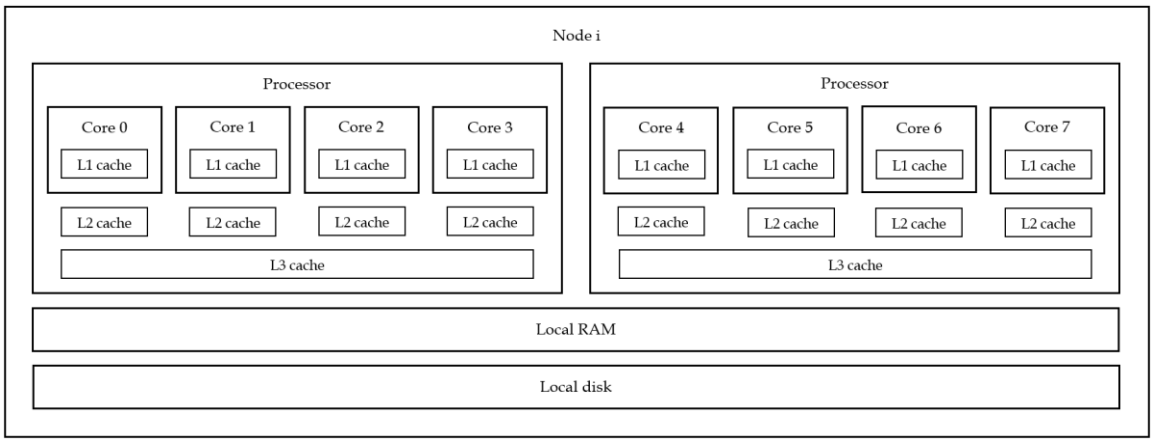

Figure A.2: Typical schematic of computer node i, featuring dual quad-core processors and 3 levels of cache.

A.1.3 Software

- A *process* is a single instance of a computer program being run. One type of parallel program is actually a set of multiple processes; i.e., multiple serial programs running concurrently. Another type of parallel program is a single process with multiple threads, a.k.a. a *multi-threaded process*.
- The latter is also called a *shared-memory (SM)* program because the threads share the same RAM. SM parallelism is usually fast because there is little overhead and no communication cost. However, a SM program is usually not scalable because the number of cores per node tends to be limited (at least for CPU-based nodes).
- *OpenMP (Open Multi-Processing)* is an interface to implement SM programs and is especially suited for parallelizing loops.
- The *Linear Algebra Package (LAPACK)* is another way to implement SM parallelism. It is a library of vector-vector, matrix-vector, and matrix-matrix operations—many of which are parallelizable in the SM context.
- The *Intel Math Kernel Library* (Intel MKL) is a library that contains LAPACK routines optimized for Intel processors.
- OpenMP and LAPACK are both used in the present research.
- A *distributed-memory (DM)* program is another type of parallel program. Here, data is distributed among multiple processes. A process cannot access the data of another process, unless the latter sends it. A DM program can be scalable because node count is potentially limitless (by connecting more computers).

However, communication in a DM program can slow it down—enough that DM-only programs are often slower than SM programs.

- *MPI (Message Passing Interface)* is a library of communication subroutines for the DM context, so that processes can send/receive data to/from other processes. It has two basic types of subroutines: (1) point-to-point (between two processes); and, (2) collective (among many processes).
- The *Scalable Linear Algebra Package (ScaLAPACK)* is another useful library for the DM context; it is the DM equivalent of LAPACK.
- MPI and ScaLAPACK are both used in the present research.
- A *hybrid parallel program (HPP)* is a DM program with a SM layer. In the DM layer, each node runs a process. In the SM layer, each process is multi-threaded. A HPP uses all available cores without needing all cores to communicate; therefore, HPP programs are often fast and scalable. PFRAME3D is a HPP.

A.2 The cache effect

When a processor retrieves a variable from the RAM, it puts the variable, plus neighboring variables, into its cache. It does this because getting a variable in the cache (*cache hit*) is much faster than getting a variable in the RAM (*cache miss*). A programmer can take advantage of this feature by writing cache-friendly code.

In a cache-friendly code, data arrangement matches the algorithm's access pattern. Consider the access pattern of a FORTRAN code that accesses an $n \times n$ matrix $[A]$, where n is large. FORTRAN is a *column-major* language, which means that 2D arrays are stored as columns—column 1, then column 2, etc. This means that $A(i,j)$ is adjacent to $A(i+1,j)$ and far (n entries away) from $A(i,j+1)$. A cache-friendly FORTRAN pseudocode would revise the algorithm as shown in Table A.1. Various nested loops in FRAME3D are revised to account for cache-friendliness.

Table A.1: Original and cache-friendly pseudocodes of a 2D matrix update.

Original	**Cache-friendly**

do i=1,n
  do j=1,n
  update A(i,j)
  continue
continue
	do i=1,n
	  do j=1,n
	  update A(j,i)
	  continue
	continue

Similarly, the matrix factorization in §5.2 is updated as shown in Table 5.3. The same concept can be applied to speed up the solution procedure of $[L][D][L]^T\{x\} = \{b\}$. Further, using *blocked code* (e.g., the blocked solver in §5.2) can reduce cache misses, which improves performance.

A.3 Regarding GPUs

Graphics processing units (GPUs) are gaining acceptance as the future of high performance computing. GPUs allow for massively parallel computations—often hundreds or thousands of cores per node. One GPU core is usually slower than one CPU core. So if an algorithm is inherently serial, CPU computing may still be the faster choice. It is not uncommon to use both GPUs and CPUs; e.g., GPUs for the global linear-equation solver and CPUs for non-parallelizable computations.

The present research uses a CPU cluster that yielded sufficient performance speed up; thus, GPU computing was not considered. Still, it may be interesting to study how GPUs can further speed up PFRAME3D. The same principles apply, but with many more cores per node.

Appendix B

Miscellaneous Parallel Algorithms

B.1 Parallel pipelined solver

A "cache-friendly" version of the Cho (2012) parallel pipelined factorization is shown in Table B.1. (It is "cache-friendly" because it is a column-based algorithm written in FORTRAN, a column-major language; the Cho (2012) pipeline, too, was column-based but written in C++, a row-major language. See §A.2 for more about cache effects.) A benchmark comparison (Table B.2) shows that the "cache-friendly" version is an improvement of the Cho (2012) parallel pipeline, as seen in the less-than-half wall times

to solve a system (size $n = 32400$ and $m = 8145$) using the same computational resources (i.e., the same computer cluster).

Table B.1: "Cache-friendly" parallel pipelined factorization, based on Cho (2012).*

```
nextprocbefore=myproc-1
nextprocafter=myproc+1
lastproc=nproc-1
if (myproc.eq.lastproc) nextprocafter=0
if (myproc.eq.0) nextprocbefore=lastproc
iproc = 0
istart = 1
do 10 i = 1,nj
  minrow = min0(mbd,ni-i+1)
  if (myproc.eq.iproc) then
    buffer(1) = A(1,istart)
    do 20 j = 2,minrow
      buffer(j) = A(j,istart)
      A(j,istart) = buffer(j)/buffer(1)
    continue
    call mpi_send(buffer to nextprocafter)
    istart = istart+1
  else
    call mpi_recv(buffer to nextprocbefore)
    if (myproc.ne.lastproc) call mpi_send(buffer to nextprocafter)
  endif
  jstart = myproc-iproc+1
  if (jstart.le.1) jstart = jstart+nproc
  ii = istart
  do j = jstart,minrow,nproc
    st = buffer(j)/buffer(1)
    do k = j,minrow
      A(k-j+1,ii) = A(k-j+1,ii) - buffer(k)*st
    continue
    ii = ii+1
  continue
  lastproc = iproc
  iproc = iproc+1
  if (iproc.eq.nproc) iproc = 0
continue
```

*Before this algorithm begins, the $m \times n$-sized $[A]$ (symmetric banded storage) is distributed "column-cyclically" among the different processes. For example, consider 3 processes and $n = 7$. Process 0 gets columns 1, 4, and 7; process 1 gets columns 2 and 5; and process 2 gets columns 3 and 6.

Table B.2: Benchmark comparison wall times (sec) with the Cho (2012) parallel pipelined solver using n=32,400 and m=8145.

Solution step	Version of parallel pipeline	Number of cores used				
		16	**32**	**64**	**128**	**256**
Factorization	**Cho (2012)**	2356.0	1177.5	581.9	266.3	128.3
	Cache-friendly	1005.7	503.2	231.1	70.9	22.4
Substitution	**Cho (2012)**	4.47	4.99	6.32	6.90	7.12
	Cache-friendly	2.33	2.10	1.99	1.97	2.18

However, for the present work the parallel pipeline has two main drawbacks. First, it is based on the un-optimized column-based solver (§5.2), a much slower "starting point" for parallelization than the blocked solver from §5.2. For example, the parallel pipelined solver factors the $n = 80{,}000$ and $m = 1000$ system in 9.53 sec (with 32 cores), whereas the 1-core blocked solver factors the same system in 12.9 sec.

Second, if system half-bandwidth is narrower than the Table B.2 benchmark example (e.g., $m = 1000$), Figure B.1 shows that weak-scaling (as defined in §4.4) is nearly "poor"; e.g., if workload doubles from $n = 80{,}000$ to $n = 160{,}000$ with a constant $n = 5000$ per core, wall time increases by a factor of roughly 1.9. (Recall from §4.4.2 that weak-scaling is "ideal" if this factor is 1.0 and "poor" if it is 2.0).

The second drawback is attributed to the high communication costs in the parallel pipeline. Each process sends and receives n messages. Cho (2012) compared this cost with $\frac{n^3}{3p}$, which asymptotically governed as $n \to \infty$. (p is the number of processes used, which for the pipeline equals the number of cores used.) For his wide-band systems (reinforced concrete walls), this comparison is adequate. But for narrow-band systems ($m \ll n$), the

costs should be compared with $\frac{nm^2}{3p}$, which grows at the same rate as n, assuming constant m. Also, as p increases, $\frac{nm^2}{3p}$ decreases, making communication costs govern. There are additional "preparatory" communication costs that grow by n when the solver allocates $[A]$ column-cyclically (see note in Table B.1) and $\{b\}$ & $\{x\}$ row-cyclically among processes; these preparatory costs are not included in Figure B.1, but would reduce the overall performance if the pipeline is implemented into a finite element program.

Therefore, although the parallel pipeline solver was adequate for Cho (2012), it is not suitable for the large narrow-band systems likely used in PFRAME3D. §5.4 shows that a divide-and-conquer solver is better suited for PFRAME3D.

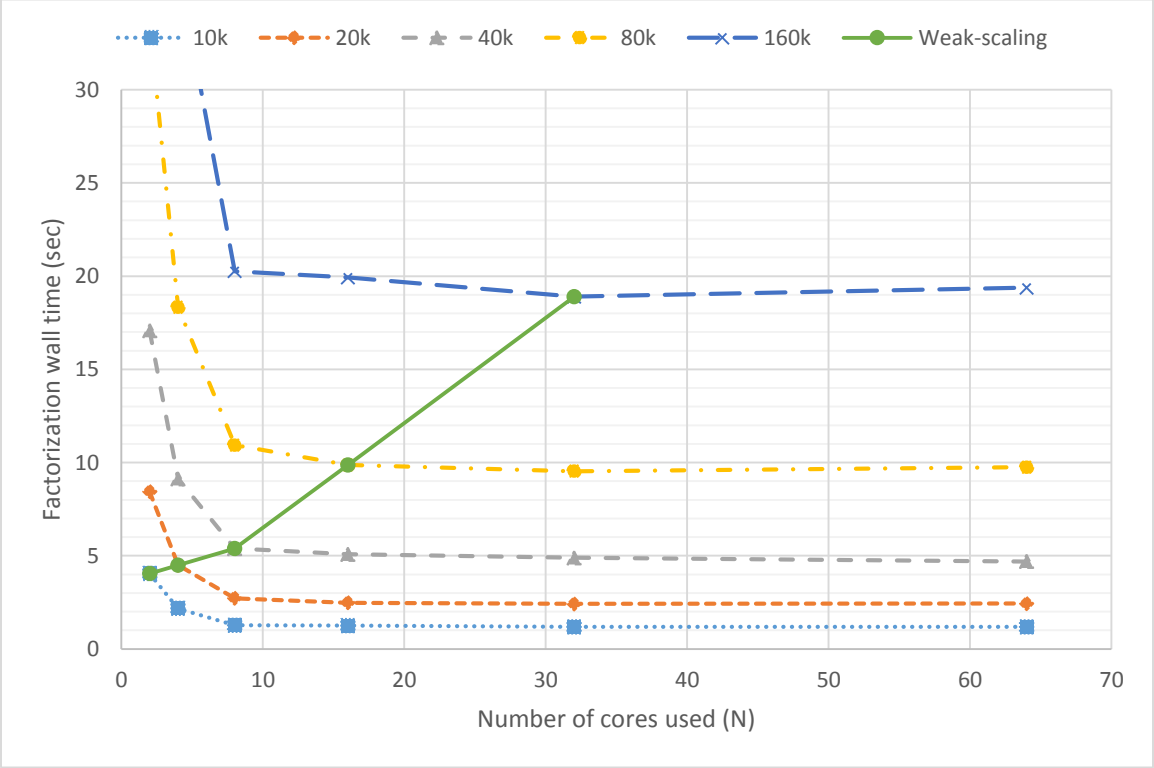

Figure B.1: Wall times (sec) of parallel-pipelined factorization with 2 to 64 cores. Each curve corresponds to a different system size n with m=1000. A weak-scaling curve (solid green) is constructed (where workload is n=5000 per core).

B.2 Hybrid-parallel matrix-vector multiplication

The pseudocode in Table B.3 computes

$$\{a\} = \{a\} + [B]\{c\} \quad \text{(Eq. B.1)}$$

in parallel where $\{a\}$, $[B]$, and $\{c\}$ are distributed among p processes as $\{a\}_i$, $[B]_i$, and $\{c\}_i$, as is done in §6.2.2. If

$$[B] = [B_1] + [B_2] \quad \text{(Eq. B.2)}$$

as shown in Figure 6.4, then Eq. B.1 becomes

$$\{a\} = \{a\} + [B_1]\{c\} + [B_2]\{c\} \quad \text{(Eq. B.3)}$$

or for process i,

$$\begin{aligned} \{a\}_i &= \{a\}_i + ([B_1]\{c\})_i + ([B_2]\{c\})_i \\ &= \{a\}_i + [B_1]_i\{c\}_i + ([B_2]\{c\})_i \end{aligned} \quad \text{(Eq. B.4)}$$

The implementation in PFRAME3D computes Eq. B.4 accounting for symmetry, bandedness, and cache-friendliness. It can be seen that nearest-neighbor-only communications is used.

Table B.3: Hybrid-parallel matrix-vector multiplication.

```
! Use Intel MKL dsbmv to compute {a}_i = {a}_i + [B_1]_i{c}_i
call dsbmv('l', ni, m-1, 1.d0, B, m, c, 1, 1.d0, a, 1)

! Determine what to send to neighbors
do i=1,m-1
  if (myproc.ne.0) sendleft(i)=c(i)
  if (myproc.ne.(nproc-1)) then
    sendright(i) = 0.d0
    mm=m-i
    do j=1,mm
      sendright(i)=sendright(i)+c(ni-j+1)*B(i+j,ni-j+1)
    continue
  endif
continue

! Send-receive operations
if (myproc.eq.0) then
  call mpi_sendrecv(sendright to myproc+1, and recvright from myproc+1)
elseif (myproc.eq.(nproc-1)) then
  call mpi_sendrecv(sendleft to myproc-1, and recvleft from myproc-1)
else
  call mpi_sendrecv(sendright to myproc+1, and recvleft from myproc-1)
  call mpi_sendrecv(sendleft to myproc-1, and recvright, from myproc+1)
endif

! add ([B_2]{c})_i to {a}_i
do i=1,m-1
  if (myproc.ne.0) a(i)=a(i)+recvleft(i)
  if (myproc.ne.(nproc-1)) then
    mm=m-i
    do j=1,mm
      a(ni-i+1)=a(ni-i+1)+recvright(j)*B(i+j,ni-i+1)
    continue
  endif
continue
```

B.3 Share interface

Assuming that dx is an n-DOF vector distributed as dxi (n_i-DOF vector), the pseudocode in Table B.4 generates a dxg vector, where dxg is dxi with m-DOFs (from neighboring processes) concatenated to its front and back, i.e., an $(n_i + 2m)$-DOF vector. It can be seen that nearest-neighbor-only communication is used.

Table B.4: Share interface routine, used in parallel geometric updating.

```
! Determine what to send to neighbors
do i=1,mbd
  if (myproc.ne.0) sendleft(i)=dxi(i)
  if (myproc.ne.(nproc-1)) sendright(i) = dxi(ndof-mbd+i)
continue

! Send-receive operations
if (myproc.eq.0) then
  call mpi_sendrecv(sendright to myproc+1, recvright from myproc+1)
elseif (myproc.eq.(nproc-1)) then
  call mpi_sendrecv(sendleft to myproc-1, recvleft from myproc-1)
else
  call mpi_sendrecv(sendright to myproc+1, recvleft from myproc-1)
  call mpi_sendrecv(sendleft to myproc-1, recvright from myproc+1)
endif

! Create dxg
do i=1,mbd
  dxg(i) = recvleft(i)
  dxg(mbd+ndof+i) = recvright(i)
continue
do i=1,ndof
  dxg(mbd+i) = dxi(i)
continue
```

Appendix C

General behavior of tube buildings

The 60-story example building in §8 is a moment-frame (MF) tube structure. The general behavior of tube structures is well explained in Smith and Coull (1991), but a brief overview is recounted here for convenience. This appendix is intended as a qualitative discussion.

A tube structure has four exterior frames (assuming a rectangular floor-plan) connected at the corners (Figure C.1). It is often idealized as a hollow bending beam, where the frames parallel to the loading direction act like beam webs, and the frames orthogonal act like beam flanges. The intention of the tube is that opposite flange frames provide the most stiffness through the axial tension and compression in columns.

In a MF tube building, the web frames produce a shear-like (i.e., racking) component of building response due to beam bending. The web frames' response also has a bending component, where web columns are stretched/compressed based on their distance from the neutral axis.

Corner columns are important to the tube frame because they belong to both web and flange frames. A simple elastic analysis of the fundamental mode of the §8 example building (Figure C.2 and Figure C.3) shows that when the web frame bends, the corner columns (C1) are stretched/compressed, and because they are rigidly connected to flange-frame beams (B1), they cause the adjacent flange-frame columns (C2) to participate. In the same way, flange-frame beams (B2) transfer load from C2 to the next column line (C3), and so on. The overall result is that the flange-frame columns help resist lateral loads through axial deformation.

But due to non-rigid beams, Figure C.3 shows that $\Delta_1 > \Delta_2 > \cdots > \Delta_9$. This effect, known as *shear lag*, results in highly stressed corner columns and underutilized interior columns. (For the 60-story example building, C9's axial loads are less than 25% of C1's axial load.) Engineers typically try to minimize this effect, so that the columns are more evenly utilized. Shear lag may be reduced by stiffening beams or using closer column spacing (e.g., every $2 - 4\ m$). Another way to reduce shear lag is to use variants of the tube structure, such as the bundled-tube or braced-tubed structure. In the present example, only the tube structure is considered.

It is not uncommon for tube structures to have wider column-spacing at ground level. For aesthetic and/or practical reasons, architects and owners often want large

entrances. A transfer girder or truss is needed to accommodate this feature and redistribute loads to the 1st story columns.

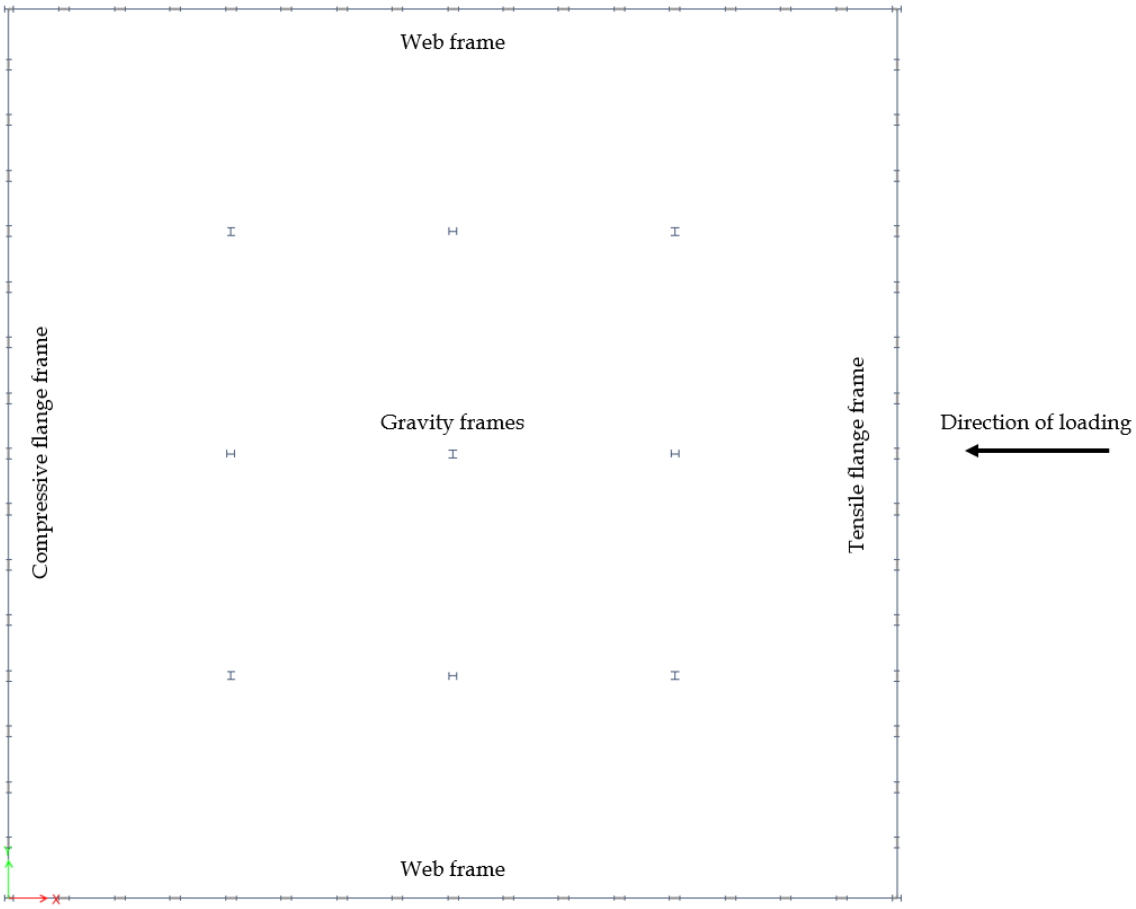

Figure C.1: Example plan of a moment-frame tube building.

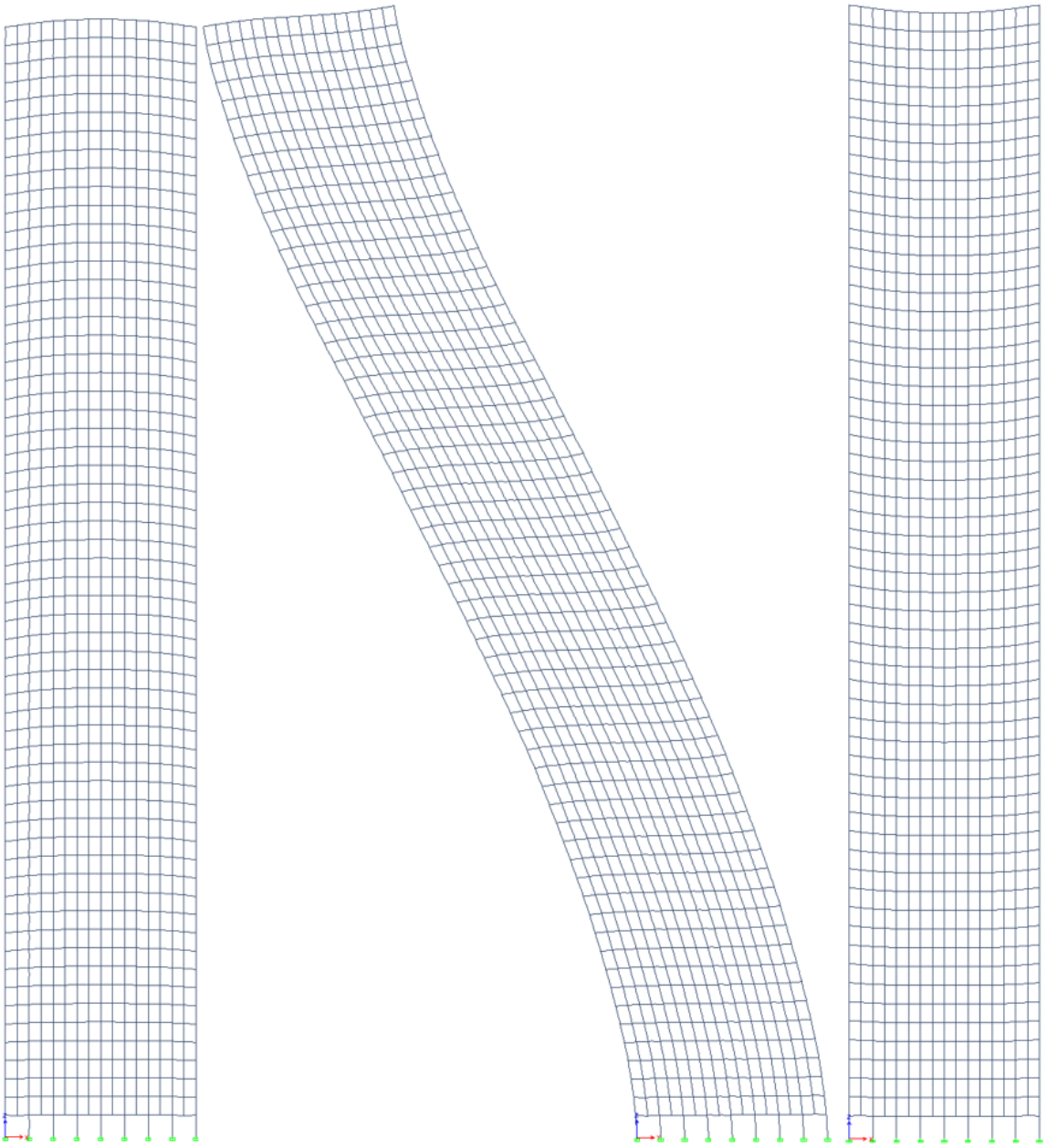

Figure C.2: Exaggerated fundamental mode of the 60-story example tube building (§8). Compressive flange frame (left), web frame (center), and tensile flange frame (right).

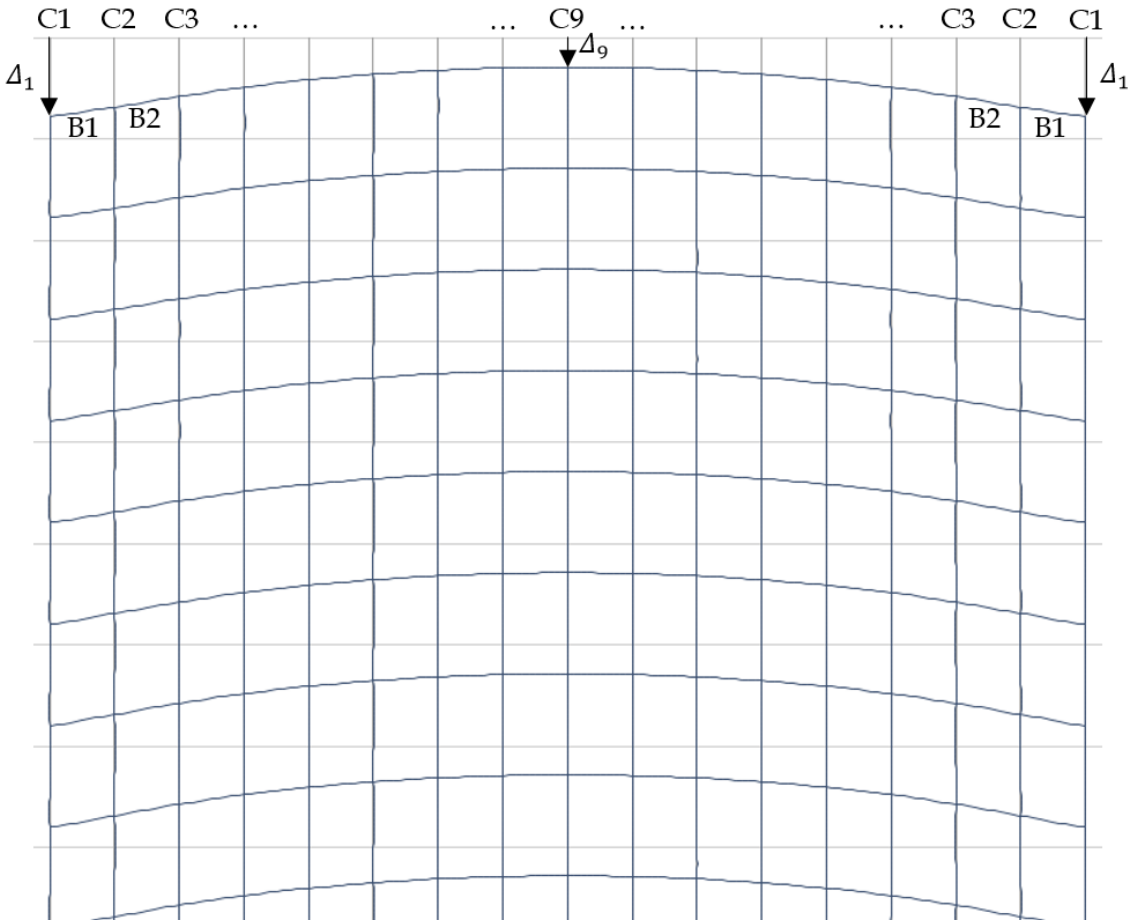

Figure C.3: Upper stories of a compressive flange frame. Due to shear lag, outer columns are compressed more than interior columns.

Appendix D

Non-standard Section Properties

Most beams and columns in the 60-story example building are sized using standard sections according to the *AISC Steel Construction Manual, 14th Edition* (2010). Refer to this manual to get the properties of standard sections. However, a few sections are non-standard and are listed in Table D.1, where

- A is the cross-sectional area in in^2
- I_y and I_z are the major- and minor-axis moment of inertias, respectively, in in^4
- S_y and S_z are the major- and minor-axis section moduli, respectively, in in^3
- Z_y and Z_z are the major- and minor-axis plastic section moduli, respectively, in in^3

- d is the depth of the section in $inches$
- t_w is the web thickness in $inches$
- b_f is the flange width in $inches$
- t_f is the flange thickness in $inches$
- J is the torsional constant in in^3.

Table D.1: Non-standard section properties used in the example 60-story building.

Section	A (in^2)	I_y (in^4)	I_z (in^4)	S_y (in^3)	S_z (in^3)	Z_y (in^3)	Z_z (in^3)	d (in)	t_w (in)	b_f (in)	t_f (in)	J (in^3)
24″X24″ box	319.8	22155.1	22155.1	1846.3	1846.3	2429.3	2429.3	24.0	4.0	24.0	4.0	32000
26″X26″ box	351.8	29296.2	29296.2	2253.6	2253.6	2933.1	2933.1	26.0	4.0	26.0	4.0	42592
28″X28″ box	383.8	37844.9	37844.9	2703.2	2703.2	3484.9	3484.9	28.0	4.0	28.0	4.0	55296

Appendix E

Ground Motions

Three ground motions are used in the current report and presented in this appendix. Shown (Figure E.1 to Figure E.3) are acceleration, velocity, and displacement histories, and pseudoacceleration spectra. East-West (EW), North-South (NS), and vertical components are applied along the global X, Y, and Z directions, respectively. The velocity and displacement histories are integrated from the acceleration histories; artifacts from discrete integration (MATLAB's *cumtrapz*) may be present. The pseudoacceleration spectra reflect the single-DOF response with 2% and 5% damping. The UBC 94 design spectrum is plotted for comparison.

The first (Figure E.1) is the Kobe earthquake ground motion at Takatori, which can be accessed from the Center for Engineering Strong Motion Data (CESMD) website, www.strongmotioncenter.org. This ground motion is used for the water-tank tower analyses in §3 (scaled to 32% and 37.3%) and §7.2 (scaled to 37.3%).

The second (Figure E.2) is a five-cycle idealized acceleration square wave with peak ground velocity $PGV = 1.375\, m/s$ and period $T = 5.75\ sec$. NS and vertical motions are zero. It is used for the 18-story building analysis in §7.3.

The third (Figure E.3) is the Denali earthquake ground motion at Pump station #10, which can be accessed from the CESMD website. This ground motion is used for the 60-story example building analyses in §7.4 and §8.

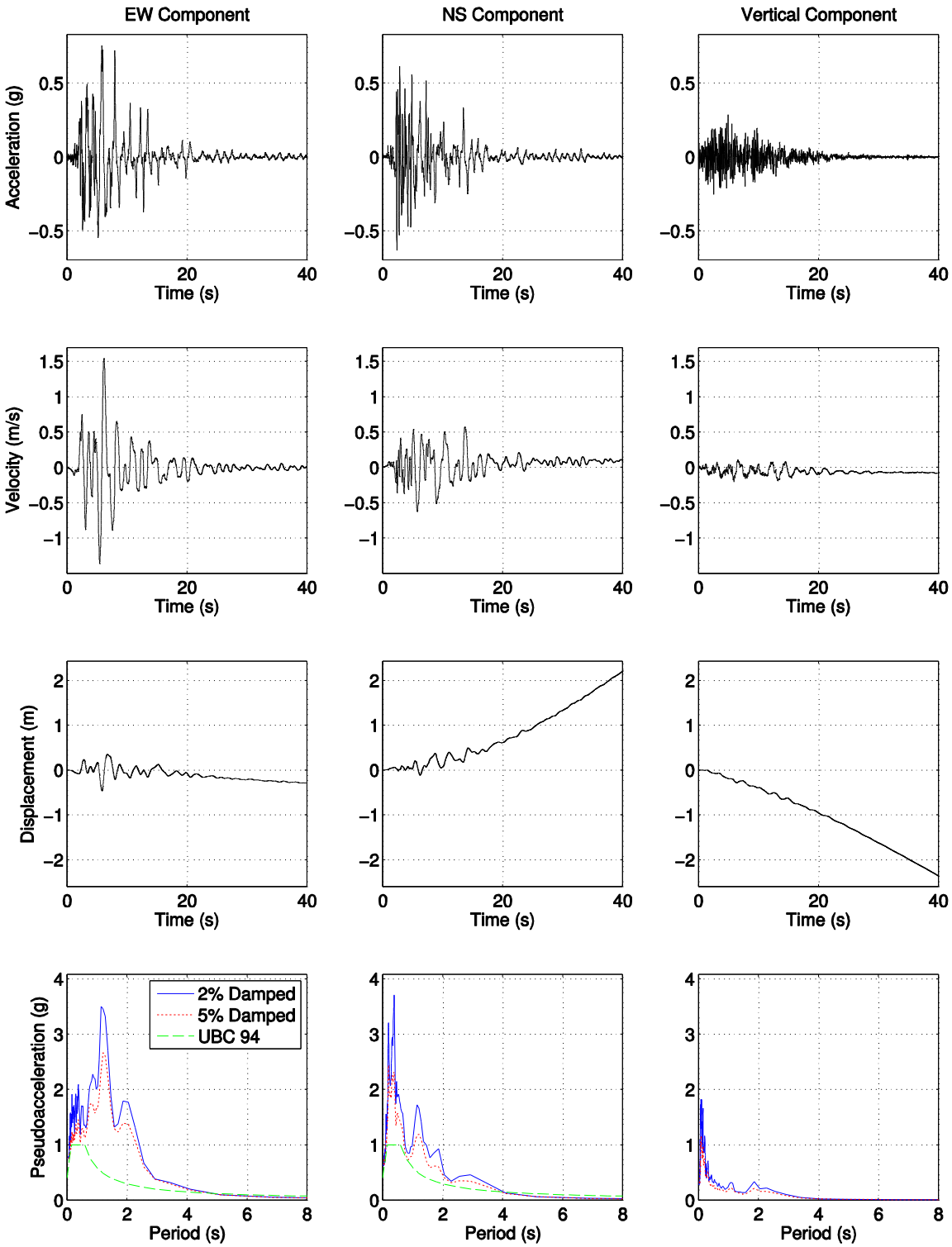

Figure E.1: Kobe earthquake ground motion at Takatori. Shown are acceleration, velocity, and displacement histories, and pseudoacceleration spectrum. EW, NS, and vertical components are applied along the water-tank tower's global X, Y, and Z directions, respectively.

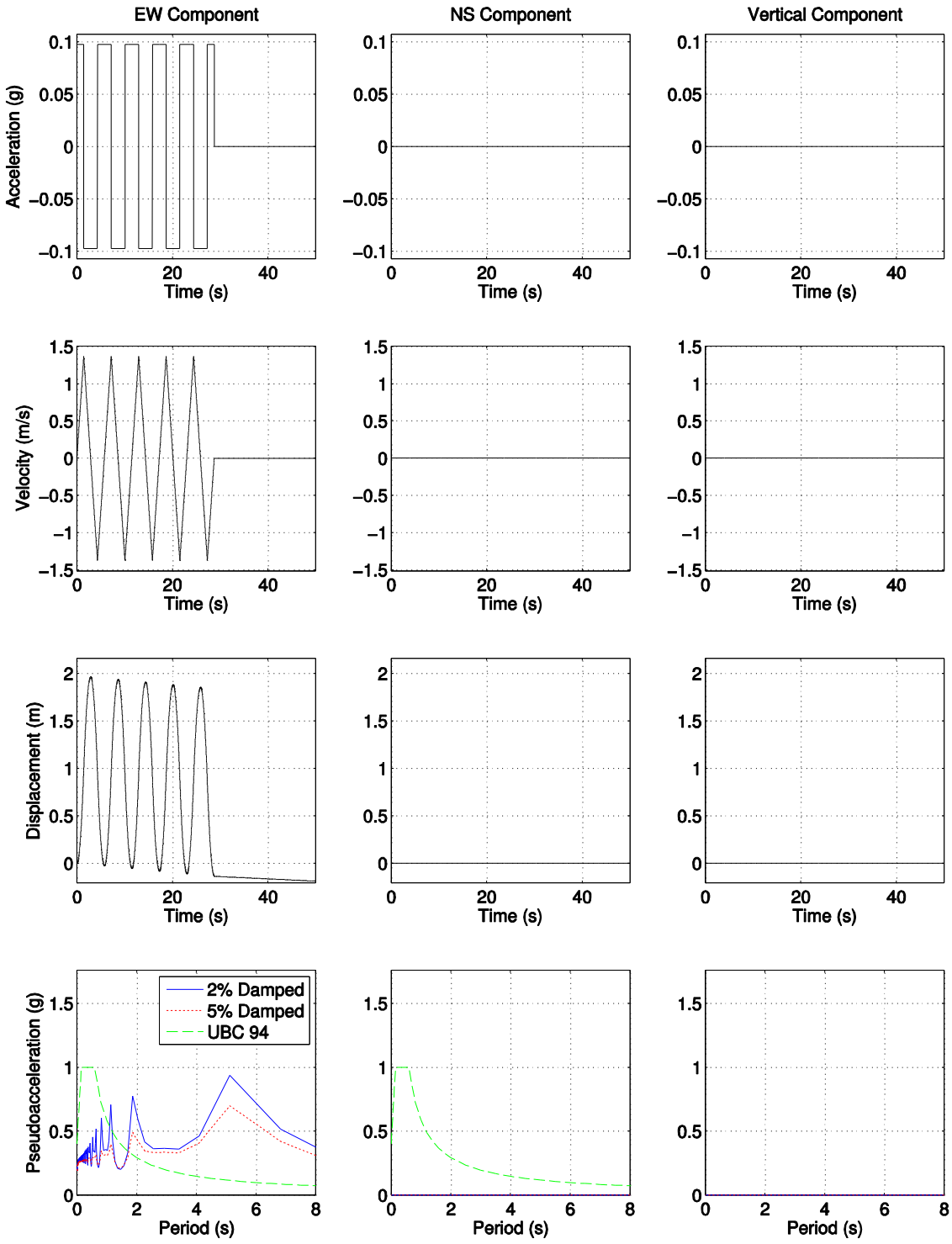

Figure E.2: Five-cycle idealized acceleration square wave with peak ground velocity PGV=1.375 m/s and period T=5.75 sec. Shown are acceleration, velocity, and displacement histories, and pseudoacceleration spectrum. EW, NS, and vertical components are applied along the 18-story building's global X, Y, and Z directions, respectively.

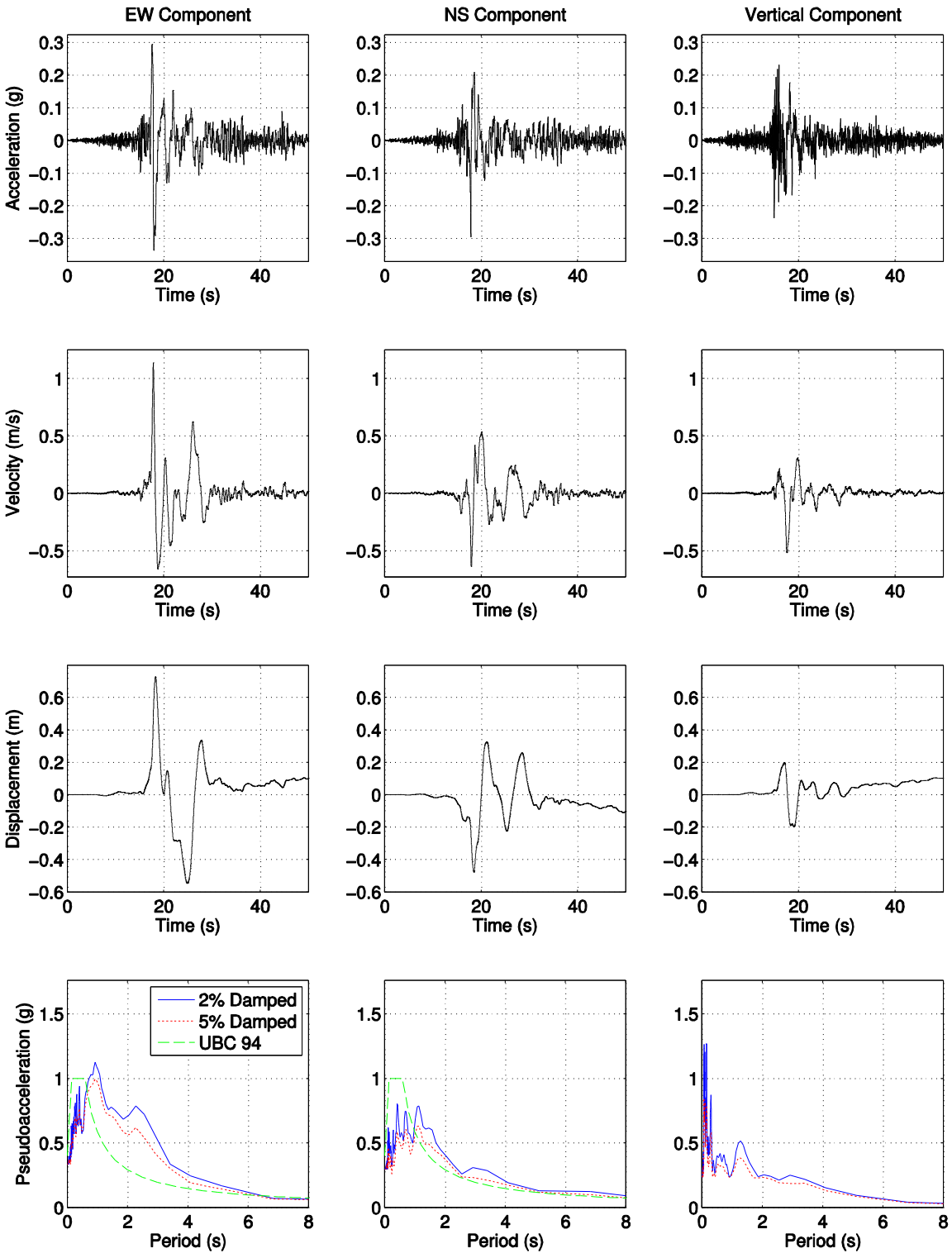

Figure E.3: Denali at Pump station #10 acceleration, velocity, and displacement histories, and pseudoacceleration spectrum. EW, NS, and vertical components are applied along the 60-story example building's global X, Y, and Z directions, respectively.

Bibliography

AISC (1989). *Specification for Structural Steel Buildings: Allowable Stress Design and Plastic Design*. American Institute of Steel Construction, Inc., Chicago, IL.

ASCE (1993). *Minimum Design Loads for Buildings and Other Structures*. American Society of Civil Engineers, New York, NY.

ATC (2010). *Modeling and Acceptance Criteria for Seismic Design and Analysis of Tall Buildings*. Applied Technology Council, Redwood City, CA.

Amdahl, G. M. (1967). "Validity of the single-processor approach to achieving large scale computing capabilities." *AFIPS Conference Proceedings*, Vol. 30. AFIPS Press, Reston, VA, 483-485.

Ballard, G., et al. (2009). "Communication-optimal parallel and sequential Cholesky decomposition." *Technical Report No. UCB/EECS-2009-29*, Electrical Engineering and Computer Sciences, University of California at Berkeley, Berkeley, CA.

Bjornsson, A. B. and Krishnan, S. (2014). "A low-complexity candidate for benchmarking collapse-prediction of steel braced structures." *Special Issue on Computational Simulation in Structural Engineering, Journal of Structural Engineering*, Vol. 140(8), 2014.

Carlson, A. E. (1999). "Three-dimensional nonlinear inelastic analysis of steel moment-frame buildings damaged by earthquake excitations." *Technical Report EERL 1999-02*, Earthquake Engineering Research Laboratory, California Institute of Technology, Pasadena, CA.

Carlson, A. E., and Hall, J. F. (1997). "Three-dimensional analysis of a tall building under Northridge earthquake." *Proceedings of the NEHRP Conference and Workshop on Research on the Northridge, California Earthquake of January 17, 1994*, Volume III-A, 330-337.

Challa, V. R. M. (1992). "Nonlinear seismic behavior of steel planar moment-resisting frames." *Technical Report EERL 1992-01*, Earthquake Engineering Research Laboratory, California Institute of Technology, Pasadena, CA.

Cho, I. H. (2012). "Virtual earthquake engineering laboratory with physics-based degrading materials on parallel computers." *Ph.D. Thesis*, California Institute of Technology, Pasadena, CA.

Cleary, A., and Dongarra, J. (1997). "Implementation in ScaLAPACK of divide-and-conquer algorithms for banded and tridiagonal linear systems." *Technical Report No. CRPC-TR97717*, Center for Research on Parallel Computation, University of Tennessee, Knoxville, TN.

Computers and Structures, Inc. (2011). *Components and Elements for PERFORM-3D and PERFORM-Collapse Version 5*, Computers and Structures, Inc., Berkeley, CA.

Cook, R. D., Malkus, D. S., and Plesha, M. E. (1989). *Concepts and applications of finite element analysis*, 3rd ed., Wiley, New York, NY.

Goldberg, D. (1991). "What every computer scientist should know about floating point arithmetic." *ACM Computing Surveys*, 23, 5-48.

Griffis, L. G. (1993). "Serviceability limit states under wind load." *Engineering Journal*, 30(1), American Institute of Steel Construction, Chicago, IL.

Hall, J. F. (1995). "Parameter study of the response of moment-resisting steel frame buildings to near-source ground motions." *Technical Report EERL 1995-08*, Earthquake Engineering Research Laboratory, California Institute of Technology, Pasadena, CA.

Hall, J. F. (1998). "Seismic response of steel frame buildings to near-source ground motions." *Earthquake Engineering Structural Dynamics*, 27(12), 1445-1464.

Hall, J. F. (2005). "Problems encountered from the use (or misuse) of Rayleigh damping." *Earthquake Engineering and Structural Dynamics*, 35(5), 525-545.

Hall, J. F., and Challa, V. R. M. (1995). "Beam-column modeling." *Journal of Engineering Mechanics*, 121(12), 1284-1291.

Haselton, C. B., Liel, A. B., and Deierlein, G. G. (2009). "Simulating structural collapse due to earthquakes: Model idealization, model calibration, and numerical solution algorithms." *Computational Methods in Structural Dynamics and Earthquake Engineering (COMPDYN)*, Rhodes, Greece, June 22-24, 2009.

ICBO (1994). *Uniform Building Code*. International Conference of Building Officials, Whittier, CA.

Intel (2013). *Intel Math Kernel Library for Linux OS: User's Guide*. Intel Corporation, Santa Clara, CA.

Kent, D. C. (1969). *Inelastic behavior of reinforced concrete members with cyclic loading*. Univ. of Canterbury, Christchurch, New Zealand.

Krishnan, S. (2003). "Three-dimensional nonlinear analysis of tall irregular steel buildings subject to strong ground motion." *Technical Report EERL 2003-01*, Earthquake Engineering Research Laboratory, California Institute of Technology, Pasadena, CA.

Krishnan, S. (2009a). "On the modeling of elastic and inelastic, critical- and post-buckling behavior of slender columns and bracing members." *Technical Report EERL 2009-03*, Earthquake Engineering Research Laboratory, California Institute of Technology, Pasadena, CA.

Krishnan, S. (2009b). "FRAME3D V2.0 – A program for the three-dimensional nonlinear time-history analysis of steel structures: User guide." *Technical Report EERL 2009-04*, Earthquake Engineering Research Laboratory, California Institute of Technology, Pasadena, CA.

Krishnan, S., and Hall, J. F. (2006a). "Modeling steel frame buildings in three dimensions – Part I: Panel zone and plastic hinge beam elements." *Journal of Engineering Mechanics*, 132(4), 345–358.

Krishnan, S., and Hall, J. F. (2006b). "Modeling steel frame buildings in three dimensions – Part II: Elastofiber beam element and examples." *Journal of Engineering Mechanics*, 132(4), 359–374.

Krishnan, S., and Muto, M. (2012). "Mechanism of collapse of tall steel moment-frame buildings under earthquake excitation." *Journal of Structural Engineering*, 138(11), 1361-1387.

Mazzoni, S., McKenna, F., and Fenves, G. L. (2009). "Opensees command language manual." *Technical Report*, <opensees.berkeley.edu>, Pacific Earthquake Engineering Research (PEER), Berkeley, CA.

McKenna, F. (2012). "Parallel and Grid Computing." *OpenSees Parallel Workshop*. University of California, Berkeley, CA.

McKenna, F., and Fenves, G. L. (2007). "Using the OpenSees interpreter on parallel computers." *NEESit Report No. TN-2007-16*. University of California, Berkeley, CA.

Mourhatch, R. (2015). "Quantifying earthquake collapse risk of tall steel braced frame buildings using rupture-to-rafters simulations." *Ph.D. Thesis*, California Institute of Technology, Pasadena, CA.

Message Passing Interface Forum (2012). *MPI: A Message-Passing Interface Standard, Version 3.0*. University of Tennessee, Knoxville, TN.

NEHRP Consultants Joint Venture (2012). *Soil-Structure Interaction for Building Structures*. Applied Technology Council and the Consortium of Universities for Research in Earthquake Engineering, Redwood City and Richmond, CA.

Newmark, N. M. (1959). "A method of computation for structural dynamics." *Journal of Engineering Mechanics*, ASCE, 85(EM3) 67-94.

OpenMP Architecture Review Board (2013). *OpenMP Application Program Interface, Version 4.0*. <openmp.org>.

Popov, E. P., and Petersson, H. (1978). "Cyclic metal plasticity: experiments and theory." *Journal of the Engineering Mechanics Division, Proceedings of the ASCE,* 104(6).

Remon, A., Quintana-Orti, E. S., and Quintana-Orti, G. (2007). "Cholesky factorization of band matrices using multithreaded BLAS." *Applied Parallel Computing: State of the Art in Scientific Computing*, Springer Berlin Heidelberg, 608-616.

Smith, B. S., and Coull, A. (1991) *Tall Building Structures: Analysis and Design*. John Wiley and Sons, Inc., New York, NY.

Tsai, K. C., and Popov, E. P. (1988). "Steel beam-column joints in seismic moment-resisting frames." *Report Number UCB/EERC 88-19*, Earthquake Engineering Research Center, University of California, Berkeley, CA.

United States Geological Survey, and California Geological Survey (2015). "Center for Engineering Strong Motion Data." <strongmotioncenter.org>.

Villa, O., et al. (2009). "Effects of floating-point non-associativity on numerical computations on massively multithreaded systems." *Technical Report*, Pacific Northwest National Laboratory, Richland, WA.